THE FULL TWO-BODY-PROBLEM: SIMULATION, ANALYSIS, AND APPLICATION TO THE DYNAMICS, CHARACTERISTICS, AND EVOLUTION OF BINARY ASTEROID SYSTEMS

by

Eugene Gregory Fahnestock

A dissertation submitted in partial fulfillment
of the requirements for the degree of
Doctor of Philosophy
(Aerospace Engineering)
in The University of Michigan
2009

Doctoral Committee:

      Professor Daniel J. Scheeres, Chair
      Professor Michael R. Combi
      Professor N. Harris McClamroch
      Senior Research Scientist Steven J. Ostro, Jet Propulsion Laboratory

DEDICATION

To the Creator of the Universe, including the many small worlds I have had the joy

and pleasure of studying in conducting the work herein, and many more worlds yet

to become known to mankind.

ACKNOWLEDGEMENTS

I would like to acknowledge all those who have made it possible for me to produce this dissertation, directly and indirectly. Foremost, I would like to thank my advisor, Dan Scheeres, for his encouragement, guidance, and constructive oversight in pursuing my graduate studies. I also wish to thank him for making possible so many opportunities that have shaped my professional development, and for his advice both in matters of academic research and otherwise.

I would also like to thank all of those who instructed me and mentored me both at the Ohio State University and at the University of Michigan, thereby enabling and encouraging me to embark on the path of conducting this research.

In addition I would like to thank the members of my committee for taking the time and effort from their busy schedules and professional pursuits to give input for this dissertation, and in most cases collaborating with me earlier in research and paper-writing. In particular I would like to thank Steve Ostro for providing valuable data for the work described herein, supercomputer access, advice, and the example of someone playing a key role in shaping the field of asteroid studies as it is today.

I also thank others in various fields with whom I've had the privilege of collaborating, including Alan W. Harris (the elder), Taeyoung Lee, Jean-Luc Margot, Melvin Leok, Petr Pravec, and many more. I would also like to thank R. Scott Erwin, Seth Lacy, and others at AFRL for helping to persuade me to pursue my graduate studies in the first place, and Scott in particular for his unflagging support since then.

Finally, but most importantly, I would like to thank my parents for their strong and unwavering support in all of my pursuits and endeavors over all the years, and without which this dissertation would never have come about.

TABLE OF CONTENTS

LIST OF FIGURES

LIST OF TABLES

LIST OF APPENDICES

Appendix

ABSTRACT

The Full Two-Body-Problem (F2BP) describes the dynamics of two unconstrained rigid bodies in close proximity, having arbitrary spatial distribution of mass, charge, or similar field quantity, and interacting through a mutual potential dependent on that distribution. While the F2BP has applications in areas as wide ranging as molecular dynamics to satellite formation flying, this dissertation focuses primarily on the F2BP's application to natural bodies in space with nontrivial mass distribution interacting through mutual gravitational potential, i.e. binary asteroids. A significant fraction ($\approx 15\pm4\%$) of near-Earth objects (NEOs) and a small percentage of the main-belt asteroids are such binary systems, whose study has potential to significantly enhance understanding of solar system formation and evolution beyond the study of solitary asteroid bodies.

This dissertation first describes further development and implementation of methods for accurate and efficient F2BP propagation based upon a flexible method for computing the mutual potential between bodies modeled as homogenous polyhedra. Derivation of the mutual potential gradients with respect to relative position and relative attitude, incorporation of these into simulation code, progression to flexible parallel implementations used on cluster computing platforms, and use of specialized geometric integration algorithms with better numerical properties are all detailed, demonstrating an overall numerical simulation performance gain of 4-5 orders of magnitude.

Next application of these numerical tools to the study of binary asteroid (66391) 1999 KW4 is summarized. This system typifies the largest class of NEO binaries, which includes nearly half of them, and is characterized by a roughly oblate spheroid primary rotating rapidly and roughly triaxial ellipsoid secondary remaining in (on-average) synchronous rotation. Thus KW4's dynamics generalize to any member of that class. Using detailed radar-observation-derived polyhedral shape models and system parameters, KW4's behavior is explored over a range of parameter values placing the system in more or less energetically excited configurations. Multiple dynamic modes of motion are detailed, as is the discovery that the actual KW4 system exists not in the most energetically relaxed configuration, but is moderately excited. Using the same models, the most likely excitation mechanism for this system, solar tide during perihelion passage, is demonstrated.

Analytical formulae are developed which separately describe the effects of primary oblateness and of secondary triaxial ellipsoid shape on frequencies of certain system motions revealed through the F2BP simulation. These formulae are useful for estimating inertia elements and highest-level internal mass distributions of bodies in any similar system, simply from standoff observation of these motion frequencies.

Finally precise dynamical simulation and analysis of the motion of test particles within the time-varying gravity field of the F2BP system is detailed. This Restricted Full-detail Three-Body-Problem encompasses exploration of three types of particle motion within a binary asteroid: 1) Orbital motion such as that for a spacecraft flying within the system about the primary, secondary, or system barycenter at large distance; 2) Motion of ejecta particles originating from the body surfaces with substantial initial surface-relative velocity; 3) Motion of particles originating from the primary surface near the equator, with no initial surface-relative velocity, but when

primary spin rate exceeds the "disruption spin rate" for which material on the surface will be spun off. This latter regolith lofting motion is demonstrated to serve as a mechanism for angular momentum transfer between binary system components when the primary is spun up to its disruption rate by external torque such as the Yarkovsky-O'Keefe-Radzievskii-Paddack (YORP) effect. This mechanism leads to rapid orbit expansion over timescales comparable to or several times faster than standard orbital evolution due to solid body tides. Such dynamical evolution for binary asteroids has many interesting implications within planetary science.

CHAPTER I

Introduction

In the development of the field of astrodynamics, there has been a tendency toward categorization of most of the natural and artificial systems studied as falling into one of several major "problem types", according to the dynamics governing the essential behavior of those systems. Then one makes various modifications of, or perturbations to, the usually relatively clean mathematical representation of the basic problem type into which a system is categorized, in order to recover the true observed system's more complex behavior with greater accuracy.

The Full Two-Body-Problem (hereafter F2BP) is one of these principal problem types. A very general formal definition for the F2BP is that it describes the dynamics of two otherwise unconstrained rigid bodies in close proximity, having arbitrary spatial distribution of mass, charge, or similar scalar field quantity, and interacting through a mutual potential dependent upon that distribution. According to this definition, the F2BP has very broad applicability in numerous engineering and scientific fields, beyond just the field of astrodynamics.

The F2BP's applications range from very small to very large spatial scale, from natural systems to artificially engineered ones to hybrid systems that have one natural body and one artificial body. At one extreme of scale lie basic problems in molecular

dynamics, in which sets of atoms that are (to first approximation) rigidly linked to form large molecules or parts of molecules have mass and charge distribution according to their constituent atoms' internal arrangement. They then interact through mutual electrostatic (Coulomb) potential, mutual van der Waals potentials (e.g. the Lennard-Jones potential), and so forth, which dominates over interaction through the also present mutual gravitational potential. This is an area of ongoing research with important implications for topics in the biosciences, such as protein formation and folding.

Another interesting application at intermediate scale is the problem of relative dynamics between pairs of spacecraft flying within a close satellite formation, when the two spacecraft have a differential charge applied to portions of them. The tunable charge distribution gives a mutual electrostatic potential that governs the relative position and attitude dynamics of the satellite pair, allowing for control of those dynamics through charge variation, to maintain the satellites in their formation. This so-called "Coulomb formation flying" topic has been well studied in the literature [1, 2, 3, 4, 5].

The familiar gravity-gradient satellite configuration is another example of the F2BP, with one of the bodies in the hybrid system being at a very much larger scale. However it is a poor example because the mass distribution of the planet about which the satellite orbits is usually very close to spherical and can be modelled as such, producing a restricted special case of the F2BP. An example without this feature is the more comparably scaled system of a solitary asteroid body and a spacecraft, large or small in mass but with significantly large physical dimension relative to the asteroid size and its own distance from the asteroid. The spacecraft in this hybrid system may or may not be in a gravity gradient pose, and would potentially be constructed for

the the purpose of altering the trajectory of the combined asteroid-spacecraft system within the solar system, to accomplish deflection of the asteroid from Earth impact. This so called "gravity tractor" impact mitigation strategy would make use of the virtual towline interaction between the asteroid and spacecraft that results from their mutual gravitational potential due to their mass distributions, offset by continuous low-thrust force upon the spacecraft produced by electric propulsion, solar sails, etc. The dynamic features of this problem have also been examined recently (e.g. refer to [6, 7]).

At the other extreme of scale lie large planet-moon or even binary star systems with mass distributions within each body interacting through their mutual gravitational potential. But again, parts of the definition of the F2BP above break down once the bodies involved become large enough and spin slowly enough that their self gravity gives them nearly spherical shapes. Their average distance of separation also is likely large relative to the body sizes (at least for most systems stable enough to exist for timescales characteristic of planetary and stellar system lifetimes). The bodies are no longer in close proximity and their mass distribution is no longer very arbitrary, but uniformly spherical. This is a limiting case for the F2BP, tending toward the classical Keplerian Two-Body-Problem.

In contrast to the broad range of applications for the F2BP, this dissertation focuses primarily on the F2BP's application to pairs of two natural planetary bodies in space of a smaller scale, with nontrivial mass distribution relative to their size, interacting through mutual gravitational potential; in other words the dynamics of binary asteroids. These systems generally preserve the key aspect of interest to us in the F2BP, that distinguishes it from the Keplerian problem. This is the feature of full coupling between the relative translational (orbital) dynamics and relative

rotational (body attitude) dynamics which is not weakened as in the limits of large separation and spherical distribution of the field quantity (mass). Also examined within this dissertation are the dynamics of test particles within the presence of the time-evolving binary asteroids themselves, which for each particle is described by the restricted but full-detail Three-Body-Problem (RF3BP) introduced later.

There are several motivations for studying the dynamics of binary asteroids in particular. To begin with, there is the abundance of them within the solar system. The possible existence of binary asteroids or satellites of a primary asteroid body had been discussed for some time [8], but the first definitive discovery of a binary asteroid system, the main-belt asteroid (MBA) designated 243 Ida, came in 1993 through the Galileo spacecraft mission [9]. Since the first discovery of a binary **near-Earth** asteroid (NEA), which was 1994 AW1 in 1994 according to [10], there has been a steady increase in the number of both MBA and NEA binaries discovered. These have been found through the use of ground-based imaging with adaptive optics [11, 12, 13], optical photometry [14], radar observation [15], and even Hubble Space Telescope imaging. As of May 2007, Pravec and Harris tabulated in an online database (at http://www.asu.cas.cz/∼asteroid/binastdata.htm) 82 discovered binary asteroids including 29 binary NEAs, 16 of which are further profiled in [14]. Over a similarly recent time frame, and using the same passive observation methods from among those mentioned above, binaries have also been discovered among the Trojan asteroids, Centaur objects, and Kuiper belt objects. In short, they have been found within almost every population of small solar system bodies across the whole range of distances from the sun.

The fraction of binarity has also been found to vary greatly between these small body populations, and to be significantly large within the NEA population that is

dynamically closest to Earth. The current best estimate for the binary fraction of the NEA population is $\approx$15$\pm$4%. This estimate has developed over time (see for example Bottke et. al. [16, 17], Margot et. al. [18], and Pravec et. al. [14]) and is significantly higher than the current best estimate of a $\approx$2-3% binary fraction for the MBA population [19]. In addition, it has recently been estimated that another approximately 9% of the NEA population consists of "contact binaries", bodies which may have previously existed as a binary pair but have now joined through collapse of their mutual orbit and low-speed collision [20]. The picture that emerges is that an appreciable fraction of all NEAs have been, are, or will become binary systems, as governed by complex dynamical evolution mechanisms. A key scientific question in the exciting and rapidly developing field of asteroid science, and in planetary science in general, is what gives rise to these differing rates of binarity between small body populations. That is, understanding what the processes for binary formation and destruction are, how each of those processes occur, and how frequently or how fast they occur, across the populations. These processes are in turn governed by the dynamics of the progenitor bodies and the binary systems produced.

A number of attempts to fully describe these processes of binary formation, evolution, and destruction have been made. And to a lesser extent, a number of studies of the dynamics of binaries independent of long-term evolution, at any given epoch, have been made. Both are complicated by the fact that the system of two rotating and co-orbiting irregularly shaped bodies, an example of the full two rigid bodies problem, has fully coupled rotational and translational dynamics, and can possibly exhibit exotic motions consistent with excited coupled dynamical configurations.

The originally favored model for binary formation was tidal disruption during planetary flyby. Such tidal disruption of rubble-pile progenitor bodies has been sim-

ulated using packed-sphere asteroid models [21, 22] and also treated indirectly by Holsapple and Michel [23]. But recent results indicate planetary encounter tidal disruption alone cannot account for more than a 1-5% incidence of binaries among the NEA population [24]. Put simply, this is because tidal encounters disrupt already formed binaries just as or more easily than they create binaries in the first place through pulling apart single progenitor bodies. Concurrent with this finding, the Yarkovsky-O'Keefe-Radzievskii-Paddack (YORP) effect has come to be viewed as a very important mechanism. It was originally brought to the attention of the asteroid community by Rubincam [25], has been further studied by Vokrouhlický and Čapek [26, 27] and Scheeres [28], and has recently been directly measured and confirmed to be acting on NEAs [29, 30]. Studies of binary formation due to either sudden bifurcation or gradual mass shedding in response to spin-up under accumulated YORP torque include Bottke et al [31], Scheeres et al [32, 33], and Walsh et al [34]. The subsequent evolution of already separated binary systems under the effects of YORP, or more properly under the net effective torque on the binary's mutual orbit due to solar flux absorption and re-radiation, has been discussed by Cuk et al [35, 36]. They compute very short timescales for binary evolution under this net effect, which they call BYORP (for "binary" YORP). This supports the conclusion that these effects apparently overwhelm those of basic tidal dissipation evolution [37] within the NEA population.

Aside from the abundances of binary asteroid systems and the associated scientific questions about their formation, evolution, and destruction, another motivation for studying their dynamics is the necessity of doing so in preparation for safely conducting mission operations within a binary system once it is visited by a spacecraft.

Visiting a binary asteroid with a spacecraft is in turn becoming more likely, in part

6

because of the unique opportunity that a binary asteroid presents to obtain valuable scientific information that cannot be obtained from visiting a solitary asteroid body alone. Of course more information can be gleaned from a binary using an equivalent (in size and budget) mission, the so-called "two bodies for the price of one" paradigm. But also more particularly, a binary presents two bodies with different sizes and usually different spin rates, and possibly with different densities, porosities, and internal structures too, yet subject to the same heliocentric orbit history and the same average bulk composition (if produced from a single progenitor body). So it is an ideal natural laboratory for making comparative studies of the effects of size, spin, structure, etc. on various phenomena, controlling for the other factors that would otherwise be different between two solitary asteroids. One such phenomena is space weathering. If the binary was formed through YORP torque spin-up, then depending on the fashion in which that occurred, the resulting binary's components may have had different portions of their surfaces exposed for different time periods. This and different spin rates and thermal loadings of the two components may produce observable differences in space weathering effects, controlling for the same solar flux exposure history because of the the same heliocentric orbit conditions [38]. Other phenomena include the fundamental geophysical response of asteroids to rotation, and the micro- vs. macro-nature of porosity in asteroidal bodies plus dependence of macro-porosity on dynamics (particularly the body spin rate and angular acceleration). Binary systems allow for more in-depth exploration of these features, improving understanding of those features for all asteroids and significantly enhancing understanding of solar system formation and evolution. In addition, only binary systems may allow for interesting active dynamical experiments involving liberation of surface material that then would be size-sorted by solar radiation pressure, would possibly comprise temporary

planetary debris ring structures evolving on very rapid timescales (compared to usual planetary systems), and would be distributed throughout the system subject to **both** bodies' gravity.

There are a few additional pragmatic reasons for sending spacecraft to binary asteroids in particular, and hence for prerequisite study of the dynamics of binary asteroids. The frequency of binaries among the NEAs noted above is inherited by the subset of NEAs that pose the greatest likelihood of impact with the Earth, designated Potentially Hazardous Asteroids (PHAs, formally defined as NEAs whose Minimum Orbit Intersection Distance (MOID) with the Earth's orbit is less than 0.05 AU, or about 4.6 million miles, and whose absolute magnitude is $H \leq 22.0$ or brighter, meaning the body diameter is larger than about 150 m given typical albedo). Earth has suffered impacts by such bodies in the past, with significant effects on the development and evolution of Earth's biosphere from the highest energy impacts, and local landform creation or significant localized destruction on the surface from respectively lower energy impacts. In consideration of that, survey programs were initiated to identify and determine high-precision orbits for 90% of the asteroids larger than 1 km in diameter by the end of 2008. Further follow on surveys authorize doing the same task for 90% of bodies larger than about 140 m in diameter. While these surveys have not yet uncovered any immediate impact threat from any of the discovered asteroids with probability larger than what most deem insignificant, on long enough timescales impact is still inevitable without successful asteroid deflection mission capability. Humanity must become prepared to successfully accomplish just such mitigation efforts, which requires knowledge about how to interact with all types of NEAs. This includes the binary PHA systems, whose frequency among PHAs means that for any mission mounted to a small (less than roughly kilometer sized) deflection target with no prior

indication of whether or not the target is a binary system, there is approximately a 1 in 7 chance that the target would be a binary system. In light of that, and of how such a binary system's complex dynamics pose special challenges and risks to the success of impact mitigation missions, it may be wise to send a spacecraft to such a system to develop how to interact with it and prove those methods beforehand.

In addition to the threat element, the NEAs are natural next stepping stones and intermediate destinations between Earth's moon and Mars for the progression of manned spaceflight. Indeed they may be essential for obtaining the resources (particularly volatiles for propellant manufacture) required to enable human spaceflight to Mars and setting up any permanent manned infrastructure in space. These are eventual goals of multiple nations. The same argument as above applies for needing to understand the dynamics, both for the binary asteroid systems themselves and for spacecraft operating within them, in order to know how to safely interact with any member of the significant binary fraction of NEAs to conduct in-situ resource utilization missions there.

Previous work of relevance on the dynamics of binary asteroids, and the F2BP in general, includes Maciejewski's presentation of continuous equations of motion of the F2BP in inertial and relative coordinates [39]. He also provides some discussion of the existence of relative equilibria. A relative equilibrium can always exist for the two arbitrary mass distributions (bodies) involved, in the absence of exogenous disturbances, i.e. for just the system of two bodies considered in isolation. However no binary system in nature, with its truly arbitrary mass distributions and rotational and co-orbital states, actually occupies its relative equilibrium, so that a relative equilibrium configuration isn't found in nature. Even if a system were hypothetically placed in one of its relative equilibrium configurations, that equilibrium is usually

unstable for the true system unless it is the one with minimum energy. Scheeres has derived a stability condition for the full two body problem [40], and also studied the planar stability of an ellipsoid-sphere model which approximates the true system [41]. Spacecraft motion about binary asteroids has also been discussed before using the approximate restricted three body model (R3BP) [42, 43], and four body model (R4BP) [44].

In this dissertation, the dynamics of binary asteroid systems, and of loose material within them, are studied as a specific application of the F2BP and extensions of it. The rest of this dissertation is structured as follows: First, the further development and implementation of methods for accurate and efficient F2BP propagation, based upon a flexible method for computing the mutual gravity potential between bodies modeled as polyhedra, is presented in Chapter II. This encompasses derivation of the mutual potential gradients with respect to absolute or relative position and absolute or relative attitude, incorporation of these into simulation code using specific sets of equations of motion and integration schemes, parallelization for use with cluster computing, and validation of the resulting numerical simulation tools through several test cases. Next application of these numerical tools to the study of binary asteroid (66391) 1999 KW4 is summarized in Chapter III. This system typifies the largest class of NEA binaries, which includes nearly half of them, so that its (KW4's) dynamics generalize to any member of that class. KW4's behavior is explored over a range of parameter values placing the system in more or less energetically excited configurations. Multiple dynamic modes of motion are detailed, and the actual KW4 system is found to not exist in the most energetically relaxed configuration, but rather be moderately excited. Using the same system models, the most likely excitation mechanism for this system, solar tide during perihelion passage, is also demonstrated. Next

some analytical formulae, which separately describe the effects of primary oblateness and of secondary triaxial ellipsoid shape on frequencies of certain system motions (as revealed through the F2BP simulation) are given in Chapter IV. These formulae are useful for estimating inertia elements and highest-level internal mass distributions of bodies in any similar system, simply from standoff observation of the motion frequencies. Finally precise dynamical simulation and analysis of the motion of test particles within the time-varying gravity field of the F2BP system is detailed in Chapter V. Three types of particle motion within a binary asteroid system are explored in Chapter V in particular: 1) Orbital motion such as that for a spacecraft flying within the system about the primary, secondary, or system barycenter at large distance; 2) Motion of ejecta particles originating from the body surfaces with substantial initial surface-relative velocity; 3) Motion of particles originating from the primary surface near the equator, with no initial surface-relative velocity, but when primary spin rate exceeds the "disruption spin rate" for which material on the surface will be spun off. This latter regolith lofting motion is demonstrated to serve as a mechanism for angular momentum transfer between binary system components, expanding binary system orbits over timescales comparable to or several times faster than standard orbital expansion evolution due to solid body tides. Finally Chapter VI contains some concluding remarks about the study of binary asteroids herein and promising directions for further investigation related to the work presented here.

CHAPTER II

Development and Implementation of F2BP Simulation Methodology

As mentioned earlier, the dynamics of the F2BP focused on in this dissertation are governed by the mutual gravitational potential between the two rigid extended celestial bodies involved. This is distinct from, but associated with, the simpler mutual gravitational potential between a single rigid extended body and an ideal point mass, normalized by the mass of the point mass. For clarity, the latter may simply be called the gravitational potential of a single body. For background, it is useful to survey the various approaches commonly used to model this single body potential. The most highly popular approach is to represent it with a set of coefficients for the orthogonal basis of spherical harmonic functions up to a given degree and order (see any common astrodynamics text, e.g. [45]). However, this method has a key limitation when applied to small irregularly shaped bodies, namely that the spherical harmonic expansion diverges for all points within the Brillouin sphere, which is the sphere that circumscribes the body centered on the body's center of mass (or centroid).

Another common representation for the single body gravitational potential comes from filling the body's volume with a set of N point masses rigidly fixed to one another and with total mass equal to the body's mass (the so-called rigid "packed sphere" model) and then summing the potential contributions of each point mass and

the one mass-normalized material point at the position where the potential value is being calculated. Unlike the spherical harmonics method, this method is theoretically convergent at all exterior locations for the material point, yet convergence is suspect at the body surface, unless one takes the limit as $N \to \infty$ (see Werner and Scheeres [46]). Like the spherical harmonics method, the packed sphere model never exactly recovers the true gravity potential, only approximates it. Although in the limit as $N \to \infty$ one can approximate the true gravity potential very well, using so many particles in the body carries great computational cost.

Another approach, which provides the intellectual foundation for most of the methodology outlined in this chapter, is the method outlined by Werner and Scheeres [46] in which the single body is modeled as a homogenous polyhedron. Then an expression for the potential results which is **exact** to the geometry captured in the polyhedron mesh, though that is itself an approximation to true body shape. For context, this formulation for the force potential is, summarized from [46]:

$$U_{\text{single}} = -G\,\rho\,\left(-\frac{1}{2}\sum_{e \in edges\ in\ body} \mathbf{r}_e \cdot \mathrm{E}_e \cdot \mathbf{r}_e\, L_e + \frac{1}{2}\sum_{f \in faces\ in\ body} \mathbf{r}_f \cdot \mathrm{F}_f \cdot \mathbf{r}_f\, \omega_f\right)$$

(2.1)

Here G is the (possibly normalized) universal gravitational constant, and ρ is the (also possibly normalized) constant scalar body density. All of the vector, dyad, and scalar quantities within the summations over every face and every edge of the polyhedron representing the body are as defined in [46]. One may refer to Section 5.1 for the expressions for these quantities. It is important to note that the relative position vector of the particle with respect to the body centroid, **in the frame fixed to the body**, is required within the quantities $\mathbf{r}_e$, $\mathbf{r}_f$, L_e and ω_f. Associated with this formulation for the potential is the following simple expression for the Laplacian of

that potential:

$$\nabla^2 U_{\text{single}} = -G\,\rho \sum_{f \in faces\ in\ body} \omega_f \qquad (2.2)$$

This expression always evaluates to zero at all points exterior to the polyhedron and evaluates to $-4\,\pi$ at particle positions interior to that polyhedron, which makes it useful for detecting intersection of the material point at which the potential is evaluated with the polyhedral mesh (i.e. detecting impact of a particle with the body). Modeling the shape of the body as a polyhedron consisting of many triangular facets is advantageous in that it provides great flexibility for capturing geometric features of the body, even including fissures and hollow spaces, to whatever resolution in surface geometry detail is required, desired, or available, and allows for that resolution to vary over the surface.

Similar to the above, various approaches may be used to model the mutual gravitational potential of two rigid extended celestial bodies. This mutual potential has been expressed using an adaptation of the above familiar spherical harmonics [47, 48]. But again, the harmonic expansion is not guaranteed to converge. Convergence has been shown to be an unstable property of such spherical harmonic series [49]. This means that an arbitrarily small change to the mass distribution may cause a previously convergent series to diverge. Another approach for evaluating the mutual gravitational potential is to fill each rigid body's volume with a distribution of point masses, fixed with respect to one another, the sum of which equals the respective body's total mass [50, 51]. Then one pairwise sums the potential across every pairing of a point mass in one body with a point mass in the other. Although the mutual potential obtained for two rigid bodies using this approach converges to the true value in the limit as the number of point masses becomes arbitrarily large, there are significant numerical errors in the computation of gravitational forces from that mutual

potential when using very many point masses within this method [46].

Related to, yet separate from, the polyhedral formulation for single body gravity potential, is a method outlined by Werner and Scheeres [52] to compute the mutual potential when both bodies are modelled as polyhedra. This method for computing the scalar mutual potential U is also stated below, for context. But first for some notation. Observe that U is a function not only of the internal geometry of each of the irregular bodies A and B but of the relative position vector between their centroids and of the attitude of each body. This can be written as $U(\mathbf{B} - \mathbf{A},\ P,\ S)$ or $U(\mathbf{R},\ P,\ S)$. Here $\mathbf{A}$ and $\mathbf{B}$ are vectors from an inertial reference frame's origin to the centroid of body A and the centroid of body B, respectively. It follows that $\mathbf{R} = \mathbf{B} - \mathbf{A}$. Also, P and S in the above are attitude rotation matrices mapping from the frame fixed in body A to the inertial reference frame and from the frame fixed in body B to the inertial reference frame, respectively. Note that $P, S \in \mathrm{SO}(3)$.

2.1   Polyhedral Formulation for Mutual Potential

For each body in a binary, the coordinates with respect to the body centroid of the three vertices of each triangular facet of the polyhedron can be generated. A stretched and skewed tetrahedral simplex is formed by the centroid and these three vertices. Let body A be divided into a set of such simplices indexed by a and body B be divided into a set of simplices indexed by b. Evaluating a pair of iterated volume integrals over A and B is equivalent to the double summation over all a and over all b of the result of evaluating the pair of iterated volume integrals over each simplex combination (a,b). This is shown by the following expression for the mutual potential U, from [52]. Note that it is a Legendre-series expansion. Also note that at this point begins the use of tensor notation and the Einstein convention of summation

over repeated indices:

$$U = G \sum_{a \in A} \sum_{b \in B} \rho_a \, T_a \rho_b \, T_b \left\{ \left[\frac{\mathbf{Q}}{R} \right] + \left[-\frac{\mathbf{Q}_i \, \mathbf{w}^i}{R^3} \right] + \left[-\frac{\mathbf{Q}_{ij} \mathbf{r}^{ij}}{2R^3} + \frac{3\mathbf{Q}_{ij} \mathbf{w}^i \mathbf{w}^j}{2R^5} \right] \right.$$
$$\left. + \left[\frac{3\mathbf{Q}_{ijk} \mathbf{r}^{ij} \mathbf{w}^k}{2R^5} - \frac{5\mathbf{Q}_{ijk} \mathbf{w}^i \mathbf{w}^j \mathbf{w}^k}{2R^7} \right] + \cdots \right\} \quad (2.3)$$

Here the gravitational constant is G and it is through the densities ρ_a and ρ_b of simplices a and b that density variation can be accommodated in the two angular coordinates of a spherical coordinate system, i.e. latitude and longitude on the body. It is through nesting of multiple closed polyhedra fixed to each other, within a single body, that density variation in the radial coordinate can also be accommodated.

The scalars T_a and T_b are Jacobian determinants corresponding to simplex a and simplex b in the respective bodies. These scalars are independent of both relative position between centroids and relative attitude between the bodies. The $\mathbf{Q}$'s in Eq. (2.3) are tensors with rank equal to the number of indices affixed to them. They are symmetric along every dimension and each element in them is a rational number. Their form is illustrated in [52], in which they are written out explicitly up to the third rank. These tensors are also independent of both relative position between the centroids and relative attitude between the bodies. The R appearing in Eq. (2.3) is the scalar magnitude of the previous relative position vector between centroids $\mathbf{R}^j$, and the vector $\mathbf{w}^i$ and matrix $\mathbf{r}^{ij}$ are defined as

$$\mathbf{w}^i = \mathbf{R}^j \mathbf{v}^i_j \qquad , \qquad \mathbf{r}^{ij} = \mathbf{v}^i_p \mathbf{v}^j_p.$$

In turn, $\mathbf{v}^i_j$ is a 3×6 matrix defined for each simplex pair (a,b). Putting aside the tensor notation for a moment, this is defined as

$$\mathbf{v} = \left[-P \left[\Delta \mathbf{r}^{a1}, \ \Delta \mathbf{r}^{a2}, \ \Delta \mathbf{r}^{a3} \right], \ S \left[\Delta \mathbf{r}^{b1}, \ \Delta \mathbf{r}^{b2}, \ \Delta \mathbf{r}^{b3} \right] \right]. \qquad (2.4)$$

16

Each $\Delta\mathbf{r}^{(a,b)i}$ is the column-representation of the vector to the i-th face vertex of the simplex denoted by either a or b, from the centroid of the respective body. Each $\Delta\mathbf{r}^{(a,b)i}$ is expressed in coordinates of the frame fixed to the respective body. The matrices P and S in Eq. (2.4) above ensure that $\mathbf{v}$, and hence $\mathbf{w}$ and $\mathbf{r}$, are all expressed in inertial frame coordinates. Take special note that each $\mathbf{w}$ is a function of both relative position and attitude and each $\mathbf{r}$ is a function of relative attitude only. The series within the braces in Eq. (2.3) is infinite but sufficient accuracy seems to be obtained with just the first several terms in square brackets, especially as the ratio of body separation to characteristic body diameter grows.

2.2 Gradients of Polyhedral Formulation for Mutual Potential

In practice, computation of the mutual potential U between bodies A and B itself is not as useful as computation of the gradients, or partial derivatives of U. These determine the actual force and torque terms for equations of motion (EOM) that describe the dynamics of the coupled system.

2.2.1 Computing force terms for EOM describing absolute motion in inertial frame

The force vector acting on body A is computed by differentiating the mutual potential with respect to each component of the centroid coordinates of A, as expressed in an inertial reference frame. The same is done to compute the force vector acting on body B. Resuming use of the tensor notation, this can also be stated as

$$\mathbf{F}_\theta^A \; = \; \frac{\partial U}{\partial \mathbf{A}_\theta} \qquad , \qquad \mathbf{F}_\theta^B \; = \; \frac{\partial U}{\partial \mathbf{B}_\theta}, \qquad (2.5)$$

where ^{A} and ^{B} refer to the bodies and $_\theta$ is a tensor index. This requires differentiating R and $\mathbf{w}^i$ within each term in square brackets on the right hand side of Eq. (2.3) with respect to $\mathbf{A}_\theta$ or $\mathbf{B}_\theta$. Henceforth let all indices which will be eliminated by summation

17

be written with small roman letters, and all indices which will be preserved after summation be written with small Greek letters. The following two relationships are derived first as useful shortcuts:

$$\frac{\partial R}{\partial \mathbf{A}_\theta} = \frac{\partial \left(\sqrt{\mathbf{R}^j \mathbf{R}_j} \right)}{\partial \mathbf{A}_\theta} = \frac{1}{2\sqrt{\mathbf{R}^j \mathbf{R}_j}} \frac{\partial \left(\mathbf{R}^j \mathbf{R}_j \right)}{\partial \mathbf{A}_\theta} = \frac{1}{2R} \left(\frac{\partial \mathbf{R}^j}{\partial \mathbf{A}_\theta} \mathbf{R}_j + \mathbf{R}^j \frac{\partial \mathbf{R}_j}{\partial \mathbf{A}_\theta} \right) =$$

$$= \frac{1}{2R} \left(-2\delta_\theta^j \mathbf{R}_j \right) = -\frac{\mathbf{R}_\theta}{R} \qquad (2.6)$$

$$\frac{\partial \mathbf{w}^i}{\partial \mathbf{A}_\theta} = \frac{\partial \left(\mathbf{R}^j \mathbf{v}_j^i \right)}{\partial \mathbf{A}_\theta} = \frac{\partial \mathbf{R}^j}{\partial \mathbf{A}_\theta} \mathbf{v}_j^i = -\delta_\theta^j \mathbf{v}_j^i = -\mathbf{v}_\theta^i \qquad (2.7)$$

Here δ_θ^j is the rank-2 tensor defined by the Kronecker delta function. Now one may use these relationships when differentiating each of the terms in square brackets in Eq. (2.3), denoted for convenience as $\hat{U}_0$, $\hat{U}_1$, $\hat{U}_2$, and so on. It is found that for the first such term,

$$\frac{\partial \hat{U}_0}{\partial \mathbf{A}_\theta} = \frac{\partial}{\partial \mathbf{A}_\theta} \left(\frac{\mathbf{Q}}{R} \right) = -\frac{\mathbf{Q}}{R^2} \frac{\partial R}{\partial \mathbf{A}_\theta} = \frac{\mathbf{Q} \mathbf{R}_\theta}{R^3}. \qquad (2.8)$$

For the second term, $\hat{U}_1$,

$$\frac{\partial \hat{U}_1}{\partial \mathbf{A}_\theta} = \frac{\partial}{\partial \mathbf{A}_\theta} \left(-\frac{\mathbf{Q}_i \, \mathbf{w}^i}{R^3} \right) = \frac{3\mathbf{Q}_i}{R^4} \frac{\partial R}{\partial \mathbf{A}_\theta} \mathbf{w}^i - \frac{\mathbf{Q}_i}{R^3} \frac{\partial \mathbf{w}^i}{\partial \mathbf{A}_\theta} = -\frac{3\mathbf{Q}_i \mathbf{R}_\theta \mathbf{w}^i}{R^5} + \frac{\mathbf{Q}_i \mathbf{v}_\theta^i}{R^3}.$$
$$(2.9)$$

The third term, $\hat{U}_2$, is only slightly more complex:

$$\frac{\partial \hat{U}_2}{\partial \mathbf{A}_\theta} = \frac{\partial}{\partial \mathbf{A}_\theta} \left(-\frac{\mathbf{Q}_{ij} \mathbf{r}^{ij}}{2R^3} + \frac{3\mathbf{Q}_{ij} \mathbf{w}^i \mathbf{w}^j}{2R^5} \right)$$

$$= \frac{3\mathbf{Q}_{ij} \mathbf{r}^{ij}}{2R^4} \frac{\partial R}{\partial \mathbf{A}_\theta} - \frac{15\mathbf{Q}_{ij}}{2R^6} \frac{\partial R}{\partial \mathbf{A}_\theta} \mathbf{w}^i \mathbf{w}^j + \frac{3\mathbf{Q}_{ij}}{2R^5} \frac{\partial \mathbf{w}^i}{\partial \mathbf{A}_\theta} \mathbf{w}^j + \frac{3\mathbf{Q}_{ij}}{2R^5} \mathbf{w}^i \frac{\partial \mathbf{w}^j}{\partial \mathbf{A}_\theta}$$

$$= -\frac{3\mathbf{Q}_{ij} \mathbf{r}^{ij} \mathbf{R}_\theta}{2R^5} + \frac{15\mathbf{Q}_{ij} \mathbf{R}_\theta \mathbf{w}^i \mathbf{w}^j}{2R^7} - \frac{3\mathbf{Q}_{ij} \mathbf{w}^i \mathbf{v}_\theta^j}{R^5}. \qquad (2.10)$$

Note the combination of terms at the far right, which is only possible given the symmetry of the tensors $\mathbf{Q}$ along all of their dimensions. For the fourth bracketed

term in Eq. (2.3), $\hat{U}_3$, making use of similar combinations due to symmetry gives

$$
\begin{aligned}
\frac{\partial \hat{U}_3}{\partial \mathbf{A}_\theta} &= \frac{\partial}{\partial \mathbf{A}_\theta} \left(\frac{3\mathbf{Q}_{ijk}\mathbf{r}^{ij}\mathbf{w}^k}{2R^5} - \frac{5\mathbf{Q}_{ijk}\mathbf{w}^i\mathbf{w}^j\mathbf{w}^k}{2R^7} \right) \\
&= \frac{-15\mathbf{Q}_{ijk}\mathbf{r}^{ij}}{2R^6}\frac{\partial R}{\partial \mathbf{A}_\theta}\mathbf{w}^k + \frac{3\mathbf{Q}_{ijk}\mathbf{r}^{ij}}{2R^5}\frac{\partial \mathbf{w}^k}{\partial \mathbf{A}_\theta} + \frac{35\mathbf{Q}_{ijk}}{2R^8}\frac{\partial R}{\partial \mathbf{A}_\theta}\mathbf{w}^i\mathbf{w}^j\mathbf{w}^k \\
&\qquad\qquad\qquad\qquad\qquad\qquad\qquad\qquad\qquad - \frac{15\mathbf{Q}_{ijk}}{2R^7}\mathbf{w}^i\mathbf{w}^j\frac{\partial \mathbf{w}^k}{\partial \mathbf{A}_\theta} \\
&= \frac{15\mathbf{Q}_{ijk}\mathbf{r}^{ij}\mathbf{R}_\theta\mathbf{w}^k}{2R^7} - \frac{3\mathbf{Q}_{ijk}\mathbf{r}^{ij}\mathbf{v}_\theta^k}{2R^5} - \frac{35\mathbf{Q}_{ijk}\mathbf{R}_\theta\mathbf{w}^i\mathbf{w}^j\mathbf{w}^k}{2R^9} + \frac{15\mathbf{Q}_{ijk}\mathbf{w}^i\mathbf{w}^j\mathbf{v}_\theta^k}{2R^7},
\end{aligned}
$$

$$(2.11)$$

and so on. All successive terms of higher order in the Legendre series are seen to each be a linear combination of fractional sub-terms which have one of the three forms in Eqs. (2.12), (2.13), and (2.14) below. The use of small roman letters $i,j,k,...$ as indices for the tensors which are eliminated by summation is now abandoned. Numbers are used to identify these indices (**not** to represent the values assumed by those indices nor to represent powers). This allows the small roman letters to be used to designate the rules governing the sequence and arrangement of the indices.

$$
\frac{\mathbf{Q}_{123...n}}{R^X} \left(\prod_{i=1}^{n/2} \mathbf{r}^{2i-1,2i} \right)
$$

$$(2.12)$$

$$
\frac{\mathbf{Q}_{123...n}}{R^X} \left(\prod_{i=1}^{n} \mathbf{w}^i \right)
$$

$$(2.13)$$

$$
\frac{\mathbf{Q}_{123...n}}{R^X} \left(\prod_{i=1}^{(n-m)/2} \mathbf{r}^{2i-1,2i} \prod_{j=n-m+1}^{n} \mathbf{w}^j \right)
$$

$$(2.14)$$

Here X is just the power of R in the denominator, and in Eq. (2.14) the m is the number of $\mathbf{w}^j$ factors. These three forms have the corresponding three derivatives

$$
\frac{X\,\mathbf{Q}_{123...n}}{R^{(X+2)}} \left(\prod_{i=1}^{n/2} \mathbf{r}^{2i-1,2i} \right) \mathbf{R}_\theta,
$$

$$(2.15)$$

$$\frac{X\,\mathbf{Q}_{123...n}\mathbf{R}_\theta}{R^{(X+2)}}\left(\prod_{i=1}^{n}\mathbf{w}^i\right) - \frac{n\,\mathbf{Q}_{123...n}}{R^X}\left(\prod_{i=1}^{n-1}\mathbf{w}^i\right)\mathbf{v}_\theta^n, \qquad (2.16)$$

$$\frac{X\,\mathbf{Q}_{123...n}}{R^{(X+2)}}\left(\prod_{i=1}^{(n-m)/2}\mathbf{r}^{2i-1,2i}\prod_{j=n-m+1}^{n}\mathbf{w}^j\right)\mathbf{R}_\theta$$
$$-\frac{m\,\mathbf{Q}_{123...n}}{R^X}\left(\prod_{i=1}^{(n-m)/2}\mathbf{r}^{2i-1,2i}\prod_{j=n-m+1}^{n-1}\mathbf{w}^j\right)\mathbf{v}_\theta^n. \qquad (2.17)$$

According to Eqs. (2.3) and (2.5), the total force on body A is , with the previous standard tensor notation:

$$\mathbf{F}_\theta^A = G\sum_{a\in A}\sum_{b\in B}\rho_a\,T_a\,\rho_b\,T_b\left(\frac{\partial\hat{U}_0}{\partial\mathbf{A}_\theta} + \frac{\partial\hat{U}_1}{\partial\mathbf{A}_\theta} + \frac{\partial\hat{U}_2}{\partial\mathbf{A}_\theta} + ...\right). \qquad (2.18)$$

Here the expression for each additional $\partial\hat{U}_i\,/\,\partial\mathbf{A}_\theta$ is a linear combination of terms patterned after Eqs. (2.15), (2.16), and (2.17). As expected, due to $\partial\mathbf{R}^j\,/\,\partial\mathbf{B}_\theta$ being the negative of $\partial\mathbf{R}^j\,/\,\partial\mathbf{A}_\theta$ in all of the above, the force vector acting on body B is the negative of that acting on body A.

2.2.2 Computing force terms for EOM describing relative motion in a body-fixed frame

Suppose the dynamical equations of motion are instead written to describe relative motion between the bodies with all kinematic and dynamic vectors expressed in the frame fixed to body A, following the development by Maciejewski [39]. Suspend use of the tensor notation at this point, and note that earlier, the vector $\mathbf{R}$ was expressed in the coordinates of the inertial frame. Expressed in the frame fixed to body A, the same vector is simply

$$\mathbf{R} = P^T\left(\mathbf{B} - \mathbf{A}\right), \qquad (2.19)$$

with $\mathbf{B}$ and $\mathbf{A}$ still expressed in the inertial frame. Then the force term to be used in the new equations of motion as written by Maciejewski [39] is:

$$\mathbf{F}_{REL} = \frac{\partial U}{\partial \mathbf{R}} \tag{2.20}$$

Note from the form of Eq. (2.19) that any function written with the formulae above to calculate $\partial U / \partial \mathbf{B}$ can be used without any modification to calculate $\partial U / \partial \mathbf{R}$, by passing it the argument of $\mathbf{R}$ rather than $\mathbf{B}$.

2.2.3 Computing torque terms for EOM describing absolute motion in inertial frame

Recall that P is a transformation matrix mapping from the frame of body A to the inertial reference frame, and S is a transformation matrix mapping from the frame of body B to the inertial reference frame. The representations in the inertial reference frame of the torque vectors acting on each body, $\mathbf{m}_A$ and $\mathbf{m}_B$ respectively, are related to the representations of those same torque vectors in the frame of each body by

$$\mathbf{m}_A = P\,\mathbf{M}_A \quad , \quad \mathbf{m}_B = S\,\mathbf{M}_B.$$

Now define the columns of P^T and S^T as

$$P^T = \begin{bmatrix} \alpha_P & \beta_P & \gamma_P \end{bmatrix} \quad , \quad S^T = \begin{bmatrix} \alpha_S & \beta_S & \gamma_S \end{bmatrix}.$$

The torque vector acting on body A, expressed in the frame of body A, is then given by

$$\mathbf{M}_A = -\,\alpha_P \times \frac{\partial U}{\partial \alpha_P} - \beta_P \times \frac{\partial U}{\partial \beta_P} - \gamma_P \times \frac{\partial U}{\partial \gamma_P}, \tag{2.21}$$

and the torque vector acting on body B, expressed in the frame of body B, is

$$\mathbf{M}_B = -\,\alpha_S \times \frac{\partial U}{\partial \alpha_S} - \beta_S \times \frac{\partial U}{\partial \beta_S} - \gamma_S \times \frac{\partial U}{\partial \gamma_S}. \tag{2.22}$$

Here the negative signs are due to the use of potential energy rather than force potential in Maciejewski [39], from which these formulae are obtained. In Eq. (2.21), one wants to find the cross product of 1) each column of the mapping from the inertial reference frame to the frame of A with 2) the partial derivative of U with respect to that same column. The result is also desired to be expressed entirely in the frame of A. In Eq. (2.22), one wants to find the cross product of 1) each column of the mapping from the inertial reference frame to the frame of B with 2) the partial derivative of U with respect to the same column, and the result is to be expressed completely in the frame of B.

In either case, a cleaner approach is to take the partial derivative of U not with respect to each column of the relevant mapping (matrix), but with respect to that entire matrix at once. Following the chain rule, this will ultimately come down to taking the partial derivative of $\mathbf{v}$ with respect to the entire matrix at once, because the matrix represents some attitude rotation and the attitude of either or both bodies enters into the calculation of the mutual potential only through the intermediate quantity $\mathbf{v}$. The definition of this in Eq. (2.4) is repeated here for convenience:

$$\mathbf{v} = \left[\ -P \left[\ \Delta \mathbf{r}^{a1}, \ \ \Delta \mathbf{r}^{a2}, \ \ \Delta \mathbf{r}^{a3} \ \right], \ \ S \left[\ \Delta \mathbf{r}^{b1}, \ \ \Delta \mathbf{r}^{b2}, \ \ \Delta \mathbf{r}^{b3} \ \right] \right].$$

To have the result of the partial differentiation be expressed in any coordinate frame other than the inertial reference frame, $\mathbf{v}$ must be modified from the above so that it is expressed in that same coordinate frame, before the partial differentiation is performed.

Consider first the case in which the result is desired in the frame fixed to body A. Left multiplying $\mathbf{v}$ by the transpose of P, yields

$$\mathbf{v} = \left[\ - \left[\ \Delta \mathbf{r}^{a1}, \ \ \Delta \mathbf{r}^{a2}, \ \ \Delta \mathbf{r}^{a3} \ \right], \ \ P^T S \left[\ \Delta \mathbf{r}^{b1}, \ \ \Delta \mathbf{r}^{b2}, \ \ \Delta \mathbf{r}^{b3} \ \right] \right].$$

For this case, define a new rotation matrix T mapping from the frame fixed to body B to the frame fixed to body A, such that $T \triangleq P^T S$. In the special case where S is the identity, T is equivalent to P^T, but in general the new coordinates matrix is written as

$$\mathbf{v} = \left[-\left[\Delta\mathbf{r}^{a1}, \quad \Delta\mathbf{r}^{a2}, \quad \Delta\mathbf{r}^{a3} \right], \quad T\left[\Delta\mathbf{r}^{b1}, \quad \Delta\mathbf{r}^{b2}, \quad \Delta\mathbf{r}^{b3} \right] \right]. \tag{2.23}$$

Differentiating this with respect to either T or P^T forms a rank-4 tensor. The form of this tensor will not depend on whether one differentiates with respect to the matrix T as a whole or P^T within T as a whole. This is because S can be grouped in with the trio of $\Delta\mathbf{r}^{bi}$ vectors on the right half of $\mathbf{v}$ so that the form of the tensor resulting from the differentiation of $\mathbf{v}$ is unchanged, even though the physical meaning of the torque term that results in the end is very different, as will be seen later. To show the form of the tensor, just differentiate with respect to T as a whole, writing it as T_{jk} or $T_{\phi\theta}$ with a simple change of index labelling and using the tensor notation again. The result of differentiating Eq. (2.23) with respect to $T_{\phi\theta}$ is

$$\frac{\partial \mathbf{v}_j^i}{\partial T_{\phi\theta}} = \left[0_{j\theta}^{\phi\, i}, \quad \frac{\partial T_{jk}}{\partial T_{\phi\theta}}\Delta\mathbf{r}_k^{bi} \right] = \left[0_{j\theta}^{\phi i}, \quad \delta_j^\phi \delta_\theta^k \Delta\mathbf{r}_k^{bi} \right] = \left[0_{j\theta}^{\phi i}, \quad \delta_j^\phi \Delta\mathbf{r}_\theta^{bi} \right] = \mathbf{D}_{j\theta}^{\phi i}. \tag{2.24}$$

Here the index i varies $1 \ldots 6$ altogether (it varies $1 \ldots 3$ on the 0 tensor and $4 \ldots 6$ on the nonzero portion to the right). The three other indices which are not eliminated (j, ϕ, and θ) vary $1 \ldots 3$.

Consider next the other case in which the result is desired in the frame fixed to body B. Left multiplying $\mathbf{v}$ by the transpose of S, yields

$$\mathbf{v} = \left[-S^T P \left[\Delta\mathbf{r}^{a1}, \quad \Delta\mathbf{r}^{a2}, \quad \Delta\mathbf{r}^{a3} \right], \quad \left[\Delta\mathbf{r}^{b1}, \quad \Delta\mathbf{r}^{b2}, \quad \Delta\mathbf{r}^{b3} \right] \right].$$

For this case, one instead defines the rotation matrix T as mapping from the frame fixed to body A to the frame fixed to body B, such that $T \triangleq S^T P$. Again, if P

happens to be the identity, T is equivalent to S^T, but in general the new coordinates matrix is written as

$$
\mathbf{v} = \left[-T \left[\Delta\mathbf{r}^{a1}, \ \Delta\mathbf{r}^{a2}, \ \Delta\mathbf{r}^{a3} \right], \ \left[\Delta\mathbf{r}^{b1}, \ \Delta\mathbf{r}^{b1}, \ \Delta\mathbf{r}^{b1} \right] \right]. \tag{2.25}
$$

Differentiating this with respect to either T as a whole or with respect to S^T within T as a whole again does not change the form of the resulting rank-4 tensor. To obtain the tensor's form, just differentiate Eq. (2.25) with respect to $T_{\phi\theta}$, giving

$$
\frac{\partial \mathbf{v}_j^i}{\partial T_{\phi\theta}} = \left[-\frac{\partial T_{jk}}{\partial T_{\phi\theta}} \Delta\mathbf{r}_k^{ai} \ , \ 0_{j\theta}^{\phi\,i} \right] = \left[-\delta_j^\phi \delta_\theta^k \Delta\mathbf{r}_k^{ai} \ , \ 0_{j\theta}^{\phi i} \right] = \left[-\delta_j^\phi \Delta\mathbf{r}_\theta^{ai} \ , \ 0_{j\theta}^{\phi i} \right] = \mathbf{D}_{j\theta}^{\phi i}
$$

$$
\tag{2.26}
$$

Some further discussion of the rule used to get the tensors in Eqs. (2.24) and (2.26), and an alternative approach, is provided in Appendix A. For now one can postpone the choice of the frame in which one would like to obtain the result, and hence the choice of definition for T, and hence the choice of which one of Eqs. (2.24) and (2.26) to use. The following equations and notation are independent of these choices. One proceeds to take the partial derivative, with respect to a 'generic' relative attitude rotation matrix T, of each of the scalar mutual potential terms $\hat{U}_0$, $\hat{U}_1$, $\hat{U}_2$, etc. in turn. Again a few shortcut relationships can be derived first as follows:

$$
\frac{\partial \mathbf{w}^i}{\partial T_{\phi\theta}} = \frac{\partial \left(\mathbf{R}^j \mathbf{v}_j^i \right)}{\partial T_{\phi\theta}} = \mathbf{R}^j \frac{\partial \mathbf{v}_j^i}{\partial T_{\phi\theta}} = \mathbf{R}^j \mathbf{D}_{j\theta}^{\phi i} \tag{2.27}
$$

$$
\frac{\partial \mathbf{r}^{ij}}{\partial T_{\phi\theta}} = \frac{\partial \left(\mathbf{v}_p^i \, \mathbf{v}_p^j \right)}{\partial T_{\phi\theta}} = \frac{\partial \mathbf{v}_p^i}{\partial T_{\phi\theta}} \mathbf{v}_p^j + \mathbf{v}_p^i \frac{\partial \mathbf{v}_p^j}{\partial T_{\phi\theta}} = \mathbf{D}_{p\theta}^{\phi i} \mathbf{v}_p^j + \mathbf{v}_p^i \mathbf{D}_{p\theta}^{\phi j} = 2\,\mathbf{v}_p^i \mathbf{D}_{p\theta}^{\phi j} \tag{2.28}
$$

For the first mutual potential term, $\hat{U}_0$, there is no attitude dependence whatsoever, and for the second term

$$
\frac{\partial \hat{U}_1}{\partial T_{\phi\theta}} = \frac{\partial}{\partial T_{\phi\theta}} \left(-\frac{\mathbf{Q}_i \, \mathbf{w}^i}{R^3} \right) = -\frac{\mathbf{Q}_i}{R^3} \frac{\partial \mathbf{w}^i}{\partial T_{\phi\theta}} = -\frac{\mathbf{Q}_i \mathbf{R}^j \mathbf{D}_{j\theta}^{\phi i}}{R^3}. \tag{2.29}
$$

For the third term $\hat{U}_2$, one now has the presence of the matrix $\mathbf{r}^{ij}$:

$$
\begin{aligned}
\frac{\partial \hat{U}_2}{\partial T_{\phi\theta}} &= \frac{\partial}{\partial T_{\phi\theta}}\left(-\frac{\mathbf{Q}_{ij}\,\mathbf{r}^{ij}}{2\,R^3} + \frac{3\,\mathbf{Q}_{ij}\,\mathbf{w}^i\,\mathbf{w}^j}{2\,R^5}\right) \\
&= -\frac{\mathbf{Q}_{ij}}{2\,R^3}\frac{\partial \mathbf{r}^{ij}}{\partial T_{\phi\theta}} + \frac{3\,\mathbf{Q}_{ij}}{2\,R^5}\frac{\partial\left(\mathbf{w}^i\,\mathbf{w}^j\right)}{\partial T_{\phi\theta}} \\
&= -\frac{\mathbf{Q}_{ij}\mathbf{v}_p^i \mathbf{D}_{p\theta}^{\phi j}}{R^3} + \frac{3\,\mathbf{Q}_{ij}}{2\,R^5}\left(\frac{\partial \mathbf{w}^i}{\partial T_{\phi\theta}}\mathbf{w}^j + \mathbf{w}^i\frac{\partial \mathbf{w}^j}{\partial T_{\phi\theta}}\right) \\
&= -\frac{\mathbf{Q}_{ij}\mathbf{v}_p^i \mathbf{D}_{p\theta}^{\phi j}}{R^3} + \frac{3\,\mathbf{Q}_{ij}}{2\,R^5}\left(\mathbf{R}^p\mathbf{D}_{p\theta}^{\phi i}\mathbf{w}^j + \mathbf{w}^i\mathbf{R}^p\mathbf{D}_{p\theta}^{\phi j}\right) \\
&= -\frac{\mathbf{Q}_{ij}\mathbf{v}_p^i \mathbf{D}_{p\theta}^{\phi j}}{R^3} + \frac{3\,\mathbf{Q}_{ij}\mathbf{w}^i\mathbf{R}^p\mathbf{D}_{p\theta}^{\phi j}}{R^5}.
\end{aligned}
\tag{2.30}
$$

Consolidation of terms in the last line above is possible because of the symmetry of the tensors $\mathbf{Q}$ on all dimensions. Using such combination again, for the fourth term, $\hat{U}_3$, yields:

$$
\begin{aligned}
\frac{\partial \hat{U}_3}{\partial T_{\phi\theta}} &= \frac{\partial}{\partial T_{\phi\theta}}\left(\frac{3\,\mathbf{Q}_{ijk}\,\mathbf{r}^{ij}\mathbf{w}^k}{2\,R^5} - \frac{5\,\mathbf{Q}_{ijk}\,\mathbf{w}^i\,\mathbf{w}^j\,\mathbf{w}^k}{2\,R^7}\right) \\
&= \frac{3\,\mathbf{Q}_{ijk}}{2\,R^5}\left(\frac{\partial \mathbf{r}^{ij}}{\partial T_{\phi\theta}}\mathbf{w}^k + \mathbf{r}^{ij}\frac{\partial \mathbf{w}^k}{\partial T_{\phi\theta}}\right) \\
&\quad - \frac{5\,\mathbf{Q}_{ijk}}{2\,R^7}\left(\frac{\partial \mathbf{w}^i}{\partial T_{\phi\theta}}\mathbf{w}^j\mathbf{w}^k + \mathbf{w}^i\frac{\partial \mathbf{w}^j}{\partial T_{\phi\theta}}\mathbf{w}^k + \mathbf{w}^i\mathbf{w}^j\frac{\partial \mathbf{w}^k}{\partial T_{\phi\theta}}\right) \\
&= \frac{3\,\mathbf{Q}_{ijk}}{2\,R^5}\left(2\mathbf{v}_p^i\mathbf{D}_{p\theta}^{\phi j}\mathbf{w}^k + \mathbf{r}^{ij}\mathbf{R}^p\mathbf{D}_{p\theta}^{\phi k}\right) \\
&\quad - \frac{5\,\mathbf{Q}_{ijk}}{2\,R^7}\left(\mathbf{R}^p\mathbf{D}_{p\theta}^{\phi i}\mathbf{w}^j\mathbf{w}^k + \mathbf{w}^i\mathbf{R}^p\mathbf{D}_{p\theta}^{\phi j}\mathbf{w}^k + \mathbf{w}^i\mathbf{w}^j\mathbf{R}^p\mathbf{D}_{p\theta}^{\phi k}\right) \\
&= \frac{3\,\mathbf{Q}_{ijk}}{2\,R^5}\left(2\mathbf{v}_p^i\mathbf{D}_{p\theta}^{\phi j}\mathbf{w}^k + \mathbf{r}^{ij}\mathbf{R}^p\mathbf{D}_{p\theta}^{\phi k}\right) - \frac{15\,\mathbf{Q}_{ijk}\mathbf{w}^i\mathbf{w}^j\mathbf{R}^p\mathbf{D}_{p\theta}^{\phi k}}{2\,R^7}.
\end{aligned}
\tag{2.31}
$$

All higher-order series terms consist of a linear combination of fractional sub-terms conforming to one of Eqs. (2.12), (2.13), or (2.14). The derivatives of these three forms with respect to $T_{\phi\theta}$ are seen to be, in order:

$$
\frac{n\,\mathbf{Q}_{123\ldots n}}{R^X}\left(\prod_{i=1}^{n/2-1}\mathbf{r}^{2i-1,2i}\right)\mathbf{v}_{n+1}^{n-1}\,\mathbf{D}_{n+1\,\theta}^{\phi\,n},
\tag{2.32}
$$

$$
\frac{n\,\mathbf{Q}_{123\ldots n}}{R^X}\left(\prod_{i=1}^{n-1}\mathbf{w}^i\right)\mathbf{R}^{n+1}\,\mathbf{D}_{n+1\,\theta}^{\phi\,n},
\tag{2.33}
$$

25

$$\frac{(n-m)\,\mathbf{Q}_{123...n}}{R^X}\left(\prod_{i=1}^{(n-m)/2-1}\mathbf{r}^{2i-1,2i}\right)\mathbf{v}_{n+1}^{n-m-1}\mathbf{D}_{n+1\,\theta}^{\phi\,n-m}\left(\prod_{j=n-m+1}^{n}\mathbf{w}^j\right)$$

$$+\frac{m\mathbf{Q}_{123...n}}{R^X}\left(\prod_{i=1}^{(n-m)/2}\mathbf{r}^{2i-1,2i}\prod_{j=n-m+1}^{n-1}\mathbf{w}^j\right)\mathbf{R}^{n+1}\,\mathbf{D}_{n+1\,\theta}^{\phi\,n}. \quad (2.34)$$

Here too numbers are used to specify the different indices, and small roman letters are used for the rules for the sequence and arrangement of those indices. Again, X is the power of R in the denominator and m is the number of $\mathbf{w}^j$ factors in the form of Eq. (2.14).

One can now express the resulting partial derivative matrix as

$$E_{\phi\theta} \;=\; G\sum_{a\in A}\sum_{b\in B}\rho_a\,T_a\,\rho_b\,T_b\left(\frac{\partial\hat{U}_1}{\partial T_{\phi\theta}}+\frac{\partial\hat{U}_2}{\partial T_{\phi\theta}}+\frac{\partial\hat{U}_3}{\partial T_{\phi\theta}}+\ \ldots\right), \quad (2.35)$$

into which one substitute the terms given by Eq. (2.29) and up. Laying aside the tensor notation again, define the columns of this result as:

$$E \;=\; \begin{bmatrix} E^\alpha & E^\beta & E^\gamma \end{bmatrix}. \quad (2.36)$$

All torque terms of interest make use of this same formulation, incorporating either Eq. (2.24) or Eq. (2.26) as the definition of $\mathbf{D}$. In this section the interest happens to be in $\mathbf{m}_A$ and $\mathbf{m}_B$, the torque terms for equations of motion describing absolute motion in the inertial reference frame. These are found with $\mathbf{M}_A$ and $\mathbf{M}_B$ using the obvious attitude transformations.

For $\mathbf{M}_A$, the result is desired to be expressed in the frame fixed to body A, so one chooses T to be the mapping from the frame of B to the frame of A and writes $\mathbf{v}$ as in Eq. (2.23). Desiring a derivative with respect to P^T (the inertial attitude of A) one uses the form of $\mathbf{D}$ in Eq. (2.24) and then Eqs. (2.29-2.36) with P^T instead of T. Then following after Eq. (2.21) one has

$$\mathbf{M}_A \;=\; -\,\alpha_P\,\times\,E^\alpha\,-\,\beta_P\,\times\,E^\beta\,-\,\gamma_P\,\times\,E^\gamma. \quad (2.37)$$

26

For $\mathbf{M}_B$ however, the result is desired to be expressed in the frame fixed to body B, so one chooses T to be the mapping from the frame of A to that of B and writes $\mathbf{v}$ as in Eq. (2.25). Desiring the derivative with respect to S^T (the inertial attitude of B) one uses the form of $\mathbf{D}$ in Eq. (2.26) and then Eqs. (2.29-2.36) with S^T instead of T. Then following after Eq. (2.22) one has

$$\mathbf{M}_B \;=\; -\,\alpha_S \;\times\; E^\alpha \;-\; \beta_S \;\times\; E^\beta \;-\; \gamma_S \;\times\; E^\gamma. \tag{2.38}$$

2.2.4 Computing torque terms for EOM describing relative motion in a body-fixed frame

If the dynamical equations of motion are instead written to describe relative motion between the bodies within the frame fixed to body A, as in [39], little changes from the above. One chooses the T to be the mapping from the frame of B to that of A, uses Eq. (2.24) for $\mathbf{D}$ and then Eqs. (2.29-2.36) without modification, and obtains

$$\mu_A \;=\; \left(P^T\left(\mathbf{B}-\mathbf{A}\right)\right) \times \left(-\mathbf{F}_{REL}\right) - \alpha_T \times E^\alpha - \beta_T \times E^\beta - \gamma_T \times E^\gamma \tag{2.39}$$

$$\mu_B \;=\; \mathbf{M} \;=\; \alpha_T \times E^\alpha + \beta_T \times E^\beta + \gamma_T \times E^\gamma, \tag{2.40}$$

wherein α_T, β_T, and γ_T are the columns of T from left to right respectively. The observed asymmetry of Eqs. (2.39) and (2.40), with the additional cross product appearing in the former, is necessary due to the fact that equations of motion describing relative motion between the bodies are written with respect to the body frame of A and describe the relative motion within the frame of A. Note in the above that $\mathbf{B}$ and $\mathbf{A}$ are still expressed in the inertial frame.

2.3 Incorporation of Gradients into F2BP Equations of Motion

The above force and torque terms are suitable for use in differential equations of motion that yield the F2BP system's dynamics when integrated. There are several

choices for the form of these EOM, in combination with an integration scheme to use for their propagation. The EOM may describe inertial motion or relative motion, and may be continuous but discretized through the integration scheme or already in the form of a discrete map that forms the integration scheme itself. It is advisable to choose to use relative EOM for simulation of the dynamics because of the reduced-size state vector for them compared to inertial EOM. The inertial motions for both bodies can then be recovered from the inertial motion of one body propagated by separate, comparatively simple, equations.

First for the continuous relative EOM to be propagated with a standard integration algorithm, which are written with respect to the frame of body A as follows [39]:

$$\dot{\mathbf{P}} = \mathbf{P} \times \boldsymbol{\Omega}_A + \mathbf{F}_{REL}, \quad \dot{\mathbf{R}} = \mathbf{R} \times \boldsymbol{\Omega}_A + \frac{\mathbf{P}}{m}, \tag{2.41}$$

$$\dot{\boldsymbol{\Gamma}}_B = \boldsymbol{\Gamma}_B \times \boldsymbol{\Omega}_A + \mu_B, \quad \dot{\boldsymbol{\Gamma}}_A = \boldsymbol{\Gamma}_A \times \boldsymbol{\Omega}_A + \mu_A, \tag{2.42}$$

$$\dot{T} = T\hat{\boldsymbol{\Omega}}_B - \hat{\boldsymbol{\Omega}}_A T. \tag{2.43}$$

Here T is the attitude rotation matrix mapping from the frame of body B directly to the frame of body A, $\mathbf{R}$ is the relative position between centroids expressed in the frame of body A, $\mathbf{P}$ is the relative momentum in the same frame, and m is a combination of the mass of A and the mass of B,

$$m = \frac{m_A\, m_B}{m_A\, +\, m_B}. \tag{2.44}$$

Also, $\boldsymbol{\Omega}$ is angular velocity of the body indicated by the subscript, expressed in its own frame, and $\boldsymbol{\Gamma}$ is angular momentum of the body indicated by the subscript, expressed in the frame of body A in either case. The $\hat{X}$ notation is the cross-product operator. Along with the above, one has the relations [39]

$$\boldsymbol{\Omega}_A = \mathbf{I}_A^{-1}\boldsymbol{\Gamma}_A, \qquad \boldsymbol{\Omega}_B = \mathbf{I}_B^{-1}T^T\boldsymbol{\Gamma}_B,$$

in which $\mathbf{I}_A$ and $\mathbf{I}_B$ are the inertia tensors of each body expressed in its own frame. A closed system of first-order differential equations is formed by Eqs. (2.41) through (2.43), with 21 states. However, to recover the inertial behavior of the system, one more equation,

$$\dot{P} \;=\; P\,\hat{\mathbf{\Omega}}_A, \tag{2.45}$$

must be added in and solved either simultaneously with the actual relative dynamics or after the fact, i.e. after the angular velocity of A in its own frame has been propagated.

A software package to perform dynamic simulation using the above EOM was developed in the C/C++ programming language (see the next section). This package makes use of the Runge-Kutta-Fehlberg 7(8) integration routine to propagate the system, after a starting calculation of the time-invariant $\mathbf{Q}$ tensors. It is noted that the EOM are evaluated 13 times within each time step, after which the state update is performed only if the truncation error is within the tolerance specified. Time step adjustment is performed with every step. With each state update the mutual potential itself, while not required for the dynamics, is also evaluated to allow for checking the total energy conservation. The forces and torques acting on each body are also calculated again at the time of each state update in order to be output along with the mutual potential and updated state itself.

A different dynamic simulation package was also developed, instead based upon relative EOM that already form a discrete mapping, and thus comprise a specialized geometric integration algorithm with better numerical properties than most general integration algorithms. The reason why this specialized algorithm has better properties for the problem at hand has to do with the fact that the F2BP dynamics arise from Lagrangian and Hamiltonian mechanics; they are characterized by symplectic,

momentum and energy preserving properties. These geometric features determine the qualitative behavior of the F2BP dynamics. The configuration space of the those dynamics have a Lie group structure referred to as the Euclidean group, SE(3). However, general numerical integration methods, including the widely used Runge-Kutta schemes, neither preserve the Euclidean Lie group structure nor these geometric properties [53].

In contrast, the variational approach [54] and Lie group methods [55] provide systematic methods of constructing structure preserving numerical integrators. The idea of the variational approach is to discretize Hamilton's principle rather than the continuous equations of motion [54]. The numerical integrator obtained from the discrete Hamilton's principle exhibits excellent energy properties, conserves first integrals, and preserves the symplectic structure. Lie group methods consist of numerical integrators that preserve the geometry of the configuration space by automatically remaining on the Lie group [55]. A Lie group method is explicitly adopted for the variational integrator in references [56], [57], and [58]. This unified integrator, referred to as the Lie Group Variational Integrator (or LGVI for short), is symplectic and momentum preserving, and it exhibits good total energy behavior for exponentially long time periods. It also preserves the Euclidian Lie group structure without the use of local charts, re-projection, or constraints.

General integration methods are obtained by approximating continuous EOM by directly discretizing them with respect to time. With each integration step, the updates involve additive operations, so that the underlying Lie group structure is not preserved as time progresses if it is not closed under addition. And the Euclidean Lie group structure of the F2BP is not closed under addition. For example, if one uses a Runge-Kutta method for numerical integration of 2.43, then the rotation matrices

drift from the orthogonal rotation group, SO(3); the quantity $T^T T$ drifts from the identity matrix. Then the attitudes of the rigid bodies cannot be determined accurately, resulting in significant errors in the gravitational force and moment computations that depend upon the attitude, and consequently errors in the entire simulation. It is often proposed to parameterize Eq. 2.43 by Euler angles or unit quaternions. However, Euler angles are not global expressions of the attitude since they have associated singularities. Unit quaternions do not exhibit singularities, but are constrained to lie on the unit three-sphere $\mathbb{S}^3$, and general numerical integration methods do not preserve the unit length constraint. Therefore, quaternions lead to the same numerical drift problem. Re-normalizing the quaternion vector at each step tends to break the conservation properties. Furthermore, unit quaternions double cover SO(3), so that there are inevitable ambiguities in expressing the attitude.

In contrast, the LGVI has better properties because it is obtained by first directly discretizing Hamilton's principle; the velocity phase space of the continuous Lagrangian is replaced by discrete variables, and a discrete Lagrangian is chosen such that it approximates a segment of the action integral. Taking the variation of the resulting action sum yields discrete EOM referred to as a variational integrator. Since the discrete variables are updated by Lie group operations, the group structure is preserved. The resulting discrete EOM are presented here as follows, with the second subscript denoting the time steps; for the detailed development one can refer to [57].

$$\mathbf{R}_{n+1} = \Phi_{A_n}^T \left(\mathbf{R}_n + \frac{h}{m} \mathbf{P}_n - \frac{h^2}{2m} \frac{\partial U_n}{\partial \mathbf{R}_n} \right), \tag{2.46}$$

$$h \left(\widehat{\mathbf{\Gamma}_{B_n} - \frac{h}{2} \mathbf{M}_n} \right) = \Phi_n \left(T_n \mathbf{I}_{dB} T_n^T \right) - \left(T_n \mathbf{I}_{dB} T_n^T \right) \Phi_n^T, \tag{2.47}$$

$$h \left(\widehat{\mathbf{\Gamma}_{A_n} + \frac{h}{2} \mathbf{R}_n \times \frac{\partial U_n}{\partial \mathbf{R}_n} + \frac{h}{2} \mathbf{M}_n} \right) = \Phi_{A_n} \mathbf{I}_{dA} - \mathbf{I}_{dA} \Phi_{A_n}^T, \tag{2.48}$$

31

$$T_{n+1} = \Phi_{A_n}^T \Phi_n T_n, \tag{2.49}$$

$$\mathbf{P}_{n+1} = \Phi_{A_n}^T \left(\mathbf{P}_n - \frac{h}{2} \frac{\partial U_n}{\partial \mathbf{R}_n} \right) - \frac{h}{2} \frac{\partial U_{n+1}}{\partial \mathbf{R}_{n+1}}, \tag{2.50}$$

$$\mathbf{\Gamma}_{B_{n+1}} = \Phi_{A_n}^T \left(\mathbf{\Gamma}_{B_n} - \frac{h}{2} \mathbf{M}_n \right) - \frac{h}{2} \mathbf{M}_{n+1}, \tag{2.51}$$

$$\mathbf{\Gamma}_{A_{n+1}} = \Phi_{A_n}^T \left(\mathbf{\Gamma}_{A_n} + \frac{h}{2} \mathbf{R}_n \times \frac{\partial U_n}{\partial \mathbf{R}_n} + \frac{h}{2} \mathbf{M}_n \right) + \frac{h}{2} \mathbf{R}_{n+1} \times \frac{\partial U_{n+1}}{\partial \mathbf{R}_{n+1}} + \frac{h}{2} \mathbf{M}_{n+1}. \tag{2.52}$$

with the scalar step size h, m as defined before, and the non-standard inertia dyads defined as

$$\mathbf{I}_{dA} = \frac{1}{2} \mathrm{tr}[\mathbf{I}_A] I_{3\times3} - \mathbf{I}_A \quad , \quad \mathbf{I}_{dB} = \frac{1}{2} \mathrm{tr}[\mathbf{I}_B] I_{3\times3} - \mathbf{I}_B \tag{2.53}$$

where $I_{3\times3}$ is the 3×3 identity matrix.

To propagate these equations, start with a set of initial states, $(\mathbf{R}_0, \mathbf{P}_0, T_0, \mathbf{\Gamma}_{A_0}, \mathbf{\Gamma}_{B_0})$, and perform one initial evaluation of the mutual potential gradients, obtaining $\partial U_0 / \partial \mathbf{R}_0$ with

$$\frac{\partial U}{\partial \mathbf{R}_\theta} = -G \sum_{a \in A} \sum_{b \in B} \rho_a T_a \rho_b T_b \left(\frac{\partial \hat{U}_0}{\partial \mathbf{R}_\theta} + \frac{\partial \hat{U}_1}{\partial \mathbf{R}_\theta} + \frac{\partial \hat{U}_2}{\partial \mathbf{R}_\theta} + \dots \right), \tag{2.54}$$

based upon Eq. 2.18, and obtaining $\mathbf{M}_0$ with Eq. 2.40. Next find $\mathbf{R}_1$ from Eq. 2.46. Solving the implicit equations 2.47 and 2.48 yields the matrix-multiplication update matrices Φ_0 and Φ_{A_0} for the attitude rotation matrices, and T_1 follows from Eq. 2.49. After that, one uses $\mathbf{R}_1$ and T_1 in a new evaluation of the mutual potential gradients. Then one computes $\mathbf{P}_1$, $\mathbf{\Gamma}_{B_1}$, and $\mathbf{\Gamma}_{A_1}$ from equations 2.50, 2.51 and 2.52, respectively. This yields a discrete map $(\mathbf{R}_0, \mathbf{P}_0, T_0, \mathbf{\Gamma}_{B_0}, \mathbf{\Gamma}_{A_0}) \mapsto (\mathbf{R}_1, \mathbf{P}_1, T_1, \mathbf{\Gamma}_{B_1}, \mathbf{\Gamma}_{A_1})$, and this process can be repeated for each time step. Note that only one new evaluation of the potential gradients is required per time step. The discrete trajectory in reduced variables can be used to reconstruct the inertial motion of the bodies. Either concurrently with that propagation or later after completion of it, through storing values,

one can use the gradient $\partial U / \partial \mathbf{R}$, the relative attitude T, and the update matrix Φ_A with these equations:

$$\mathbf{A}_{n+1} = \mathbf{A}_n + \frac{h}{m_A} \mathbf{P}_{A_n} + \frac{h^2}{2m_A} T_n \frac{\partial U_n}{\partial \mathbf{R}_n}, \tag{2.55}$$

$$\mathbf{P}_{A_{n+1}} = \mathbf{P}_{A_n} + \frac{h}{2} T_n \frac{\partial U_n}{\partial \mathbf{R}_n} + \frac{h}{2} T_{n+1} \frac{\partial U_{n+1}}{\partial \mathbf{R}_{n+1}}, \tag{2.56}$$

$$P_{n+1} = P_n \Phi_{A_n}. \tag{2.57}$$

In the discrete map defined by the LGVI above, the only implicit parts are Eqs. 2.47 and 2.48. These two equations have the same structure, which suggests a specific computational approach. Using Rodrigues' formula, those equations are rewritten as equivalent vector equations, and those are solved numerically using Newton's iteration. Numerical simulations show that two or three iterations are sufficient to achieve a tolerance of $\epsilon = 10^{-15}$.

Since the LGVI is obtained by discretizing Hamilton's principle, it is symplectic and preserves the structure of the configuration space, SE(3), as well as the relevant geometric features of the full two rigid body problem dynamics represented by the conserved first integrals of total angular momentum and total energy. The total energy oscillates around its initial value with small bounds on a comparatively short timescale, but there is no tendency for the mean of the oscillation in the total energy to drift (increase or decrease) from the initial value for exponentially long time. In contrast, the total energy behavior with general numerical methods such as the Runge-Kutta schemes tends to drift dramatically over exponentially long time.

The LGVI preserves the group structure. By using the given computational approach, the matrices Φ_n and Φ_{A_n}, representing the change in the relative attitude and the inertial attitude of body A over a time step, are guaranteed to be rotation matrices. The group operation of the Lie group SO(3) is matrix multiplication. Hence

rotation matrices T_n and P_n are updated by the group operation in Eqs. 2.49 and 2.57, so that they evolve on SO(3) automatically without constraints or reprojection. Therefore, the orthogonal structure of the rotation matrices is preserved, and the attitude of each rigid body is determined accurately and globally without the need to use local charts (parameterizations) such as Euler angles or quaternions.

This geometrically exact numerical integration method yields a highly efficient and accurate computational algorithm, especially for the F2BP dynamics examined here. In the F2BP there is a large burden in computing the mutual gravitational force and moment for arbitrary bodies, so the number of force and moment evaluations should be minimized. It is seen that the LGVI requires only one such evaluation per integration step, the minimum number of evaluations consistent with the presented LGVI having second order accuracy (and that because it is a self-adjoint method). Within the LGVI, two implicit equations must be solved at each time step to determine the matrix-multiplication updates for T and P. However the LGVI is only weakly implicit in the sense that the iteration for each implicit equation is independent of the much more costly gravitational force and moment computation. The computational load to solve each implicit equation is comparatively negligible; only two or three iterations are required. Altogether, the entire method could be considered "almost explicit". Note that the LGVI is a fixed step size integrator, but all of the beneficial properties above are independent of the step size. Consequently, one can achieve the same level of accuracy while choosing a larger step size as compared to other numerical integrators of the same order.

More significant to computational performance is the fact that only one evaluation of the modified discrete hamiltonian relative EOM, requiring only one call to the mutual potential and gradients function, takes place per (major) time step, and there

34

is no minor time step. The mutual potential and forces and moments are already available at every (major) time step from that same function call. And in practice, solving the implicit equation for the attitude update is much less costly than an additional call to obtain the potential and gradients. Recall the $13 + 1 = 14$ such calls to obtain the potential and gradients that are needed per time step within the RKF7(8), for the 13 minor steps plus the evaluation of forces and torques at the time of the state update. Put together, all of these things mean a 14 to $1 + \delta$ reduction in computation time per time step (with $\delta \ll 1$), in switching to the LGVI from the RKF7(8). Although the time step for the LGVI that must remain fixed throughout the simulation is smaller than the mean time step selected by the RKF7(8) algorithm, there is still an order of magnitude reduction in computation time using the LGVI.

2.4   Simulation Package Implementation with Parallelization

The relative EOM above have been implemented in C/C++, resulting in four simulator versions: both a single processor version and a parallel computing version built around each of the two integration schemes used, which were both a high-order Runge-Kutta scheme applied to the continuous EOM of Eqs. 2.41-2.45 and the 2nd-order LGVI of Eqs. 2.46-2.57.

Using the above methodology, most of the computation time is associated with the evaluation of the mutual potential gradients $\partial U / \partial \mathbf{R}$ and $\partial U / \partial T$, which in turn involves performing the same operations for all of the different pairwise simplex combinations, followed by a global sum. This is well-suited for parallelization. The parallel computing versions are flexible in that any number of nodes and processors can be specified by the user. Then the process 0 assigns to each of the other processors the task of calculating the portion of the mutual potential gradient double summations

that arises from pairing a single simplex a in body A with all simplices in body B. If the number of other processors available is less than the number of simplices in the primary body model, this is done in rounds until the portion of the problem matching with every a is obtained. All operations other than the mutual potential gradient evaluations remain serial. The parallel versions were written with the addition of MPI and have been used on Myrinet clusters at the Center for Advanced Computing (CAC) at the University of Michigan and at the Supercomputing and Visualization Facility (SVF) at NASA's Jet Propulsion Laboratory, utilizing up to 256 processors in some runs. Though compiler and user environment differences produced markedly different capabilities in each cluster environment, eventually a further two-orders-of-magnitude reduction in computation time over otherwise identical single-processor runs was achieved with both integration schemes. This and the previously mentioned order of magnitude speedup from using the LGVI integrator rather than the alternative schemes means the parallel LGVI version was used for most all numerical results in the following chapters.

All simulator code versions have command line options for specifying the sizes of the two component body models involved in a simulation, in number of faces (simplices) and number of nodes. There is also a command line option to specify how many terms beyond the two point mass approximation are to be used in the Legendre series expansion behind the formulation for the mutual potential between the components. Other command line options specify whether to actually run forward with dynamic simulation or instead just evaluate and output the forces and moments at the initial time (for diagnostic purposes only), and whether to include the perturbing effects of a third body on the relative motions of the binary's components, in anticipation of examining flyby scenarios. This latter option involves modifying the

relative force term $\partial U/\partial \mathbf{R}$ in the above EOM. One can assume that to first order the effects of the third body are adequately captured through this additional force alone, i.e. through the direct effect on the translational dynamics alone. This in turn will transfer to effects on the rotational dynamics via the full coupling of the system. In other words, assume no change is needed to the relative moment $\mathbf{M}$ itself, or no direct effects on the rotational dynamics are needed to capture the third body perturbation. Ultimately, one uses the replacement rule of

$$\frac{\partial U}{\partial \mathbf{R}} \quad \Rightarrow \quad \frac{\partial U}{\partial \mathbf{R}} \;+\; \frac{m_B}{m_A \;+\; m_B}\mathbf{C}_A \;-\; \frac{m_A}{m_A \;+\; m_B}\mathbf{C}_B \tag{2.58}$$

within either set of EOM presented in the previous subsection. One has a choice as to how to obtain the potential gradients denoted by $\mathbf{C}_{(A,B)}$. One can use the partial derivative, with respect to the position vector from the third body to the primary's centroid, of the polyhedron plus point mass potential formulation (refer to [46]) using the full-detail shape model of the primary. And similarly for the secondary. Alternatively one can just use the partial derivative, with respect to the same position vector, of the two point mass potential approximating both the binary component in question and the perturbing third body as spheres. So if the command line option for including third body perturbation effects is used, another command line option exists to select whether to use the two point mass or single point mass plus single polyhedron formulation after Eq. 2.1 for the gradients $\mathbf{C}_i$ in Eq. 2.58. There is also an option for enabling or shutting off density variation between simplices within each body model. The LGVI has additional options to specify which vector equation is used with Newton's method to solve the implicit functions involved in the LGVI: the vector equation coming from the Cayley transformation parameterization of the update rotation matrices mapping attitudes from one time step to the next, or the vector equation coming from the Rodrigues' formula parameterization of the same.

MATLAB scripts are used to pre-process the body models and initial conditions for each setup, producing files read in by the main simulator codes. The first two of these files contain the properly ordered elements of the position vectors with respect to the centroid for the vertices of the simplices in each body. If a third body is included in the simulation, a file containing the six orbital elements to define the path of the binary system relative to the third body is also read in. If, further, the single point mass plus polyhedron method for the $\mathbf{C}_i$'s is selected, another data file containing some edge- and face-specific dyads, etc. is needed for each polyhedral body model. The other three input files respectively contain the initial states, other system physical data (such as body moments of inertia and body densities), and the integration parameters (starting and stopping times and truncation error tolerance).

Other MATLAB scripts are used to postprocess the state output file and the potential, forces, and torques output file produced when running the main executable for all code versions. Plots of the raw relative motion states, all motion pulled back to an inertial reference frame, and the total energy and total angular momentum integrals of motion are generated. Other quantities such as linear and angular accelerations of the bodies, the effective angular velocity, the dynamic moment of inertia, and orthonormality loss in the attitude rotation matrices T and P are also plotted for error checking purposes. The latter orthonormality loss metrics are defined as $\|T^T T - I\|$ and $\|P^T P - I\|$ where I is the 3×3 identity matrix. An option to create animations of the motion is included in the post-processing script as well.

Apart from any parallelization (e.g. with the single-processor versions), the timing results of various simulations show that total wall-clock time increases linearly with an increase in the number of faces in either one of the body models, and increases proportionally with the product of the number of simplices in the primary and the

number of simplices in the secondary. In this sense, the wall-clock time increases as $O(n^2)$, where n is representative of the mean number of facets or resolution of the models used. As mentioned before, the majority of computation time is spent evaluating the mutual potential gradients, and the time to compute those partial derivatives once increases as $O(6^r)$, where r is the number of terms with increasing-rank tensors used in the Legendre series expansion for each simplex pairing's contribution. Therefore the total wall-clock time also increases as $O(6^r)$. For satisfactory results, r will need to be increased as the proximity of the bodies in the system is reduced, but r of only four or five is sufficient for usual binary asteroid separation distances.

As for the reduction of run times through parallelization, Figure 2.1 shows normalized wall clock time and speedup ratio vs. the number of processors used, for many runs employing the parallel LGVI code version with different numbers of CPUs, both with and without the third body included and with different models of the KW4 asteroid (see the next chapter concerning that binary asteroid system). For each run the normalization of the wall-time is with respect to the product of the total number of simulation time steps taken and the product of facet counts for the two body models involved. The single-processor simulation time used for the speedup ratio calculation was obtained by running the single-processor LGVI on a single node of the same cluster environment used for all plotted runs. It can be seen that for the largest model size (the high resolution models, or data series' B and C in the plot) the speedup does not level off within the full range of processor numbers used, so that from not yet observing the limit of Amdahl's law one may estimate a very small serial fraction of operations (at least $< 0.4\%$) for simulating this particular model. It is in fact seen that in this range, the first-order fit to the speedup data points is steeper than the theoretical best linear scaling law, likely due to efficiencies from optimization of the

39
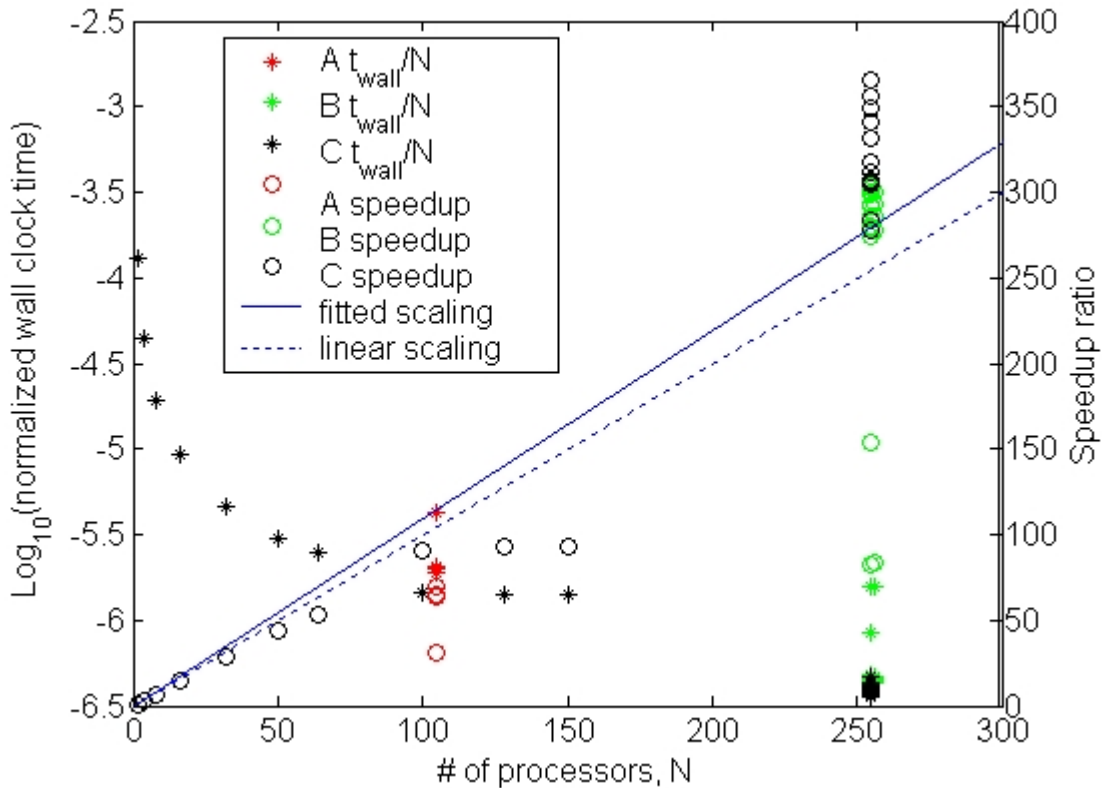
Figure 2.1: Normalized wall clock time and relative-to-single-processor speedup ratio vs. number of processors used. Here data series A is for low resolution models without 3rd body, series B is for high resolution models without 3rd body, and series C is for high resolution models with 3rd body incorporated. All three data series are used for the scaling curve fitted to the data.

code portions running on processes other than process 0.

2.5   Simulation Package Validation, and Performance Gains

Several sets of results using the above detailed simulation packages are now presented for validation purposes. These results also provide points of reference to help quantify the improvement in computational speed for similar error metric performance, or alternatively the improvement in error metric performance for roughly the same computational cost, across successive versions of the code as use of the LGVI and parallelization was added. From the very earliest (purely MATLAB) implementa-

40

Table 2.1: Properties of octahedral body models used in validation simulations.

Property	body A		body B	
Surface area (m^2)	8.839		2.002	
Volume (m^3)	1.800		0.1561	
Equiv. radius (m)	0.7546		0.3340	
Mass (kg)	4500		390.3	
Density (kg/m^3)	2500		2500	
I_{xx} (kg-m^2)	1377.0		9.24	
I_{yy} (kg-m^2)	814.5		42.99	
I_{zz} (kg-m^2)	1462.5		44.32	
Extents (m)	min	max	min	max
body frame X	-1.0	1.0	-1.0	1.0
body frame Y	-1.5	1.5	$-1/\exp(1)$	$1/\exp(1)$
body frame Z	-0.9	0.9	$-1/\pi$	$1/\pi$

tions to the implementations in hand at the time of this writing, an overall numerical simulation performance gain of 4-5 orders of magnitude has been observed.

2.5.1 Test cases with a pair of octahedral bodies

Simulation results for two octahedral rigid bodies with eight faces and eight simplices each are given for a few scenarios. Octahedra are used rather than more complex shapes because they are the simplest polyhedral shapes that manifest the coupled dynamics behavior desired in all of the scenarios. For greater simplicity, the octahedra are made symmetric about all axes, although they are of different sizes. The extents data defining the locations of the corners of each octahedron are given in Table 2.1, as are various physical parameters of each octahedron including mass and moment of inertia properties. Simulation results for three scenarios are presented here, and the initial conditions for each scenario are given in Table 2.2.

Scenario 1   The first scenario presented here is that of short-duration simulation of the two octahedra starting from initial conditions matching with a medium eccen-

Table 2.2: Initial conditions for three validation scenarios using octahedral body models.

Scenario	Attitude* (deg)	Body spin† (rad/s)	Orbital elements (m,deg) OR state vector (m,m/s)
1	(100, 9.8, 175) (160, -5, 165)	$(0, 0, 5.0 \times 10^{-5})$ $(0, 0, 9.2 \times 10^{-5})$	$(a, e, i, \Omega, \omega, \nu)=$ (4m, 0.3, 5°, 15°, 60°, 10°)
2	(180, 0, 30) (270, 0, 30)	(0, 0, 0.566) (0, 0, -0.566)	$X_0 = [0, 6, 0]^T$, $V_0 = [-0.006, 0, 0]^T$
3	(-22.6, 5, 180) (50.3, 5, -180)	$(0, 0, 1.63 \times 10^{-4})$ $(0, 0, 1.55 \times 10^{-4})$	$(a, e, i, \Omega, \omega, \nu)=$ (52.9m, 0.942, 5°, 0°, 88.2°, -107.1°)

* 3-1-3 Euler sequence for body B (first line) and body A (second line).
† Components of angular velocity of each body expressed in its own body-fixed frame for body B (first line) and body A (second line).

tricity elliptical mutual orbit. Both the RKF7(8) and LGVI integrators are used, with the intent of making a direct comparison between the trajectories of the configuration variables that result from using each integrator over a short simulation duration.

Figure 2.2 shows the difference between the output of the RKF7(8) and that of the LGVI in components of reconstructed inertial position, inertial velocity, and body-frame angular velocity vectors for A, plus the difference in body attitude parameters for A. The corresponding output difference plots for body B look very similar. The differences in vector components of Figure II.2(a) are normalized by the system's semi-major axis ($a = 4.0$ m). The differences in vector components of Figure II.2(b) are normalized by the equivalent circular velocity ($\sqrt{\mu/a} = 2.856 \times 10^{-4}$ m/s), and those of Figure II.2(c) are normalized by the equivalent meanmotion ($\sqrt{\mu/a^3} = 7.141 \times 10^{-5}$ radians/s). To obtain the results compared here, the total number of mutual potential derivatives evaluations and actual running time using the RKF7(8) routine were 70014 and 494 seconds, respectively, while the number of such evaluations and actual running time using the LGVI were 70001 and 539 seconds. Therefore the

computational effort and resources used were roughly the same in each case. All of these results show that the LGVI can be trusted to produce almost exactly the same trajectory as a standard RKF7(8) integration routine over short time scales. As the simulation duration increases the trajectories from the two integrators begin to diverge. The behavior of integrals of motion and appropriate error metrics must then be used to discern which trajectory is to be taken as the "truth".

(a) Inertial position for body A

(b) Inertial velocity for body A

(c) Angular velocity for body A

(d) 3-1-3 Euler angles for body A
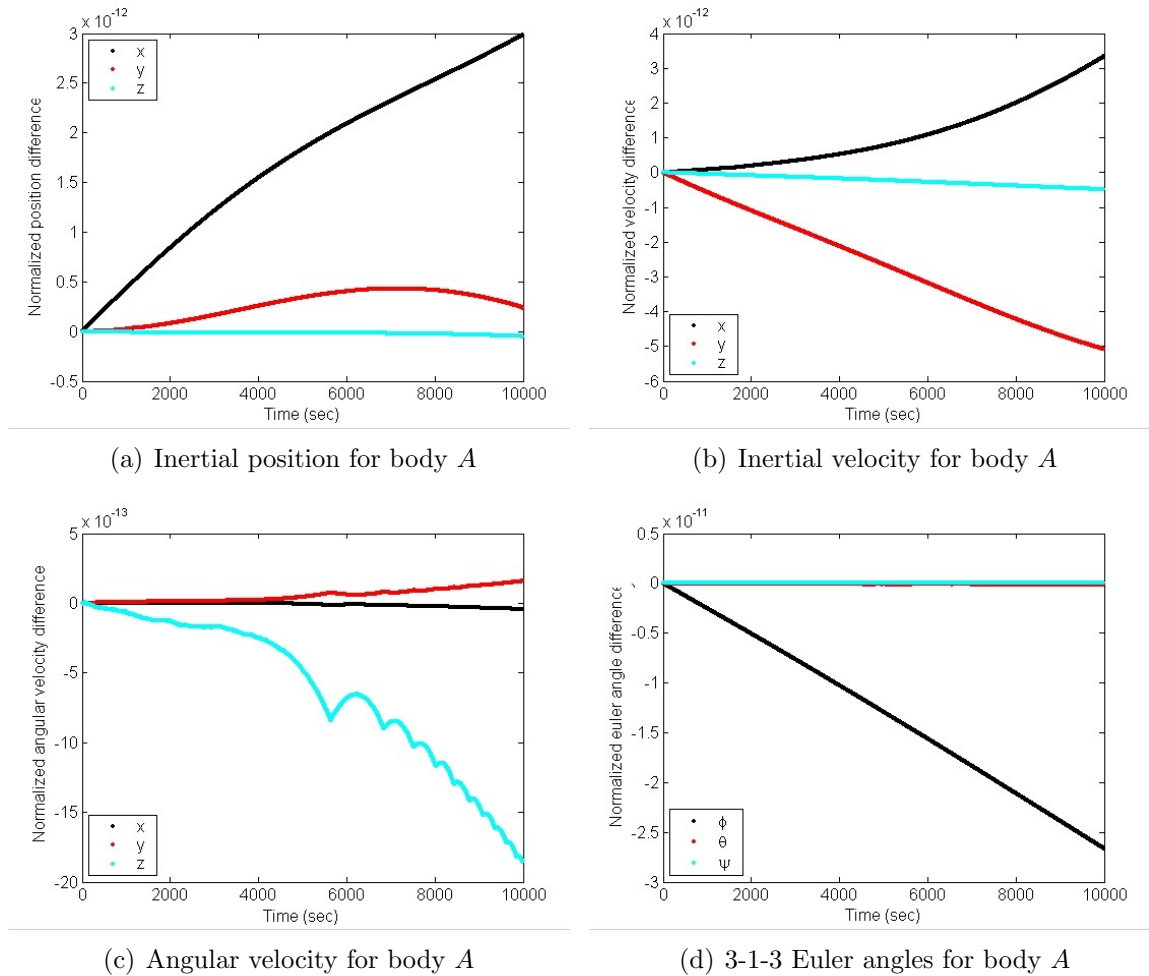
Figure 2.2: (Validation scenario 1) Difference between RKF7(8) and LGVI output.

Scenario 2   Another scenario is that of propagation from an initial condition with the bodies aligned but possessing relatively large magnitude centroid velocity vectors that are antiparallel and perpendicular to the initial line between centroids. This

43

scenario is simulated both with the LGVI at different step sizes and with the variable step size RKF7(8) at different error tolerances. This allows for a comparison between the integrators of their performance, in terms of the total energy and total angular momentum integrals and the attitude error metric growth vs. computational burden. The results in Table 2.3 illustrate the general superiority of the LGVI approach over Runge-Kutta-type approaches.

Table 2.3: (Validation scenario 2) Performance comparison between RKF7(8) and LGVI.

Method	h^*	$N_u^\star$	$t_W^\diamond$	$\epsilon^\triangleleft$	$\mathrm{E}[|\Delta\mathrm{TE}|]^{\dagger\ddagger}$	$\mathrm{E}[\|\Delta\pi_T\|]^{\dagger\ddagger}$	$\mathrm{E}[\|I - R^T R\|]^{\dagger}$
RKF	0.236	2368912	23439	10^{-12}	3.901×10^{-12}	1.493×10^{-9}	1.151×10^{-7}
RKF	0.421	1331414	9102	10^{-10}	1.274×10^{-10}	2.630×10^{-7}	1.985×10^{-5}
RKF	0.749	747376	5252	10^{-8}	2.284×10^{-8}	4.620×10^{-5}	3.173×10^{-3}
LGVI	0.0169	2370000	13511	-	1.698×10^{-11}	5.167×10^{-10}	2.525×10^{-11}
LGVI	0.04	1000000	9920	-	1.928×10^{-11}	1.189×10^{-10}	2.120×10^{-11}
LGVI	0.08	500000	5127	-	9.879×10^{-11}	4.139×10^{-11}	2.004×10^{-12}
LGVI	0.4	100000	983	-	2.234×10^{-9}	6.266×10^{-12}	3.386×10^{-14}
LGVI	0.8	50000	431	-	9.326×10^{-9}	1.279×10^{-11}	6.352×10^{-14}
LGVI	1.0	40000	335	-	1.512×10^{-8}	3.991×10^{-12}	4.786×10^{-14}

* h is integration step size, in seconds, fixed for LGVI but averaged over the run's duration for RKF7(8)

* N_u is the total number of calculations of the mutual potential derivatives made within the run

$^\diamond$ t_W is the "wall-clock" time to complete each simulation run, in seconds

$^\triangleleft$ ϵ is the error tolerance for the variable step size in RKF7(8)

‡ TE and π_T are total energy and the total angular momentum, respectively, while Δ refers to deviation from the initial value over simulation

† E[·] denotes mean

Here it is seen that for any pair of simulations, one using the LGVI and the other using the RKF7(8) scheme, for which the total energy metric performs about the same, the computation time needed to complete the simulation using the LGVI is a fraction of that needed using the RKF7(8). Simultaneous with this improvement in run time, the total angular momentum and attitude error metrics still perform better

in the LGVI run than in the RKF7(8) run by multiple orders of magnitude. Going in the other direction, as the step size for the LGVI is reduced so that the computational burden using it begins to approach that for any chosen run using the RKF7(8), all error metrics remain at the same level as or else orders of magnitude smaller than those for the chosen RKF7(8) run. For the LGVI, the round-off error accumulates when multiplying rotation matrices at 2.49. The rotation matrix error of the LGVI is caused only by the floating-point arithmetic operation, and it is increased as the number of integration steps is increased. A similar trend is observed in the total angular momentum error for the LGVI, because determination of the total angular momentum in the inertial frame from the states written to the output file makes use of the rotation matrices.

Scenario 3 The next scenario illustrates the ability of the methods herein to capture the interesting effects of coupling in a mutual orbit configuration that the Keplerian two-body approximation incorrectly predicts as being perpetual. Simulation with the LGVI yields the trajectory illustrated in Figure II.3(a), which transitions from a highly elliptical orbit to a hyperbolic escape path. This is shown by the plots in Figure II.3(b) of the semi-major axis and eccentricity change during the close encounter, which occurs roughly midway through the run duration of 60,000 seconds. The initial conditions and body configurations are symmetric about the initial orbital plane, and as such the motion of the centroids should be restricted to the initial orbital plane. This is observed numerically, as the body centroids remain within $8.6 \times v10^{-14}$ meters of the initial orbital plane throughout the simulation.

(a) Trajectory of binary octahedra system components

(b) Eccentricity and semi major axis
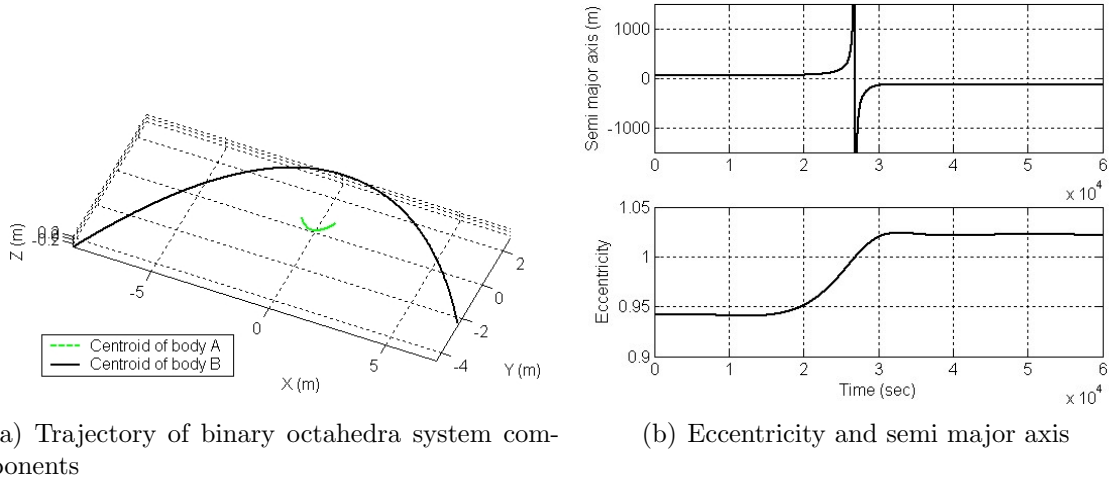
Figure 2.3: (Validation scenario 3) Disruption of the binary octahedra system.

2.5.2 Test case using a pair of artificial asteroid mesh models of intermediate size

For this test case, it was intended to stress the simulation tools more by examining a hypothetical interaction between two artificial asteroidal body models, both having irregular shapes without any planes of symmetry. This interaction was intended to involve a comparatively larger trade-off between the kinetic and potential forms of energy in the system. Therefore the initial relative translational motion state for this test case was defined as that matching a highly elliptical keplerian orbit with eccentricity of 0.4, 20° inclination, $\Omega = 15°$ RAAN, $\omega = 30°$ argument of perigee, and $\nu = 10°$ true anomaly. Body A for this test case is an asteroid model having 580 simplices, radially re-scaled to have the extents in its own body-fixed frame shown in Table 2.4. Its density is set to 2,670 kg/m^3. Body B is a different asteroid shape modelled with 380 simplices, and having the extents in its own body-fixed frame also shown in Table 2.4. Body B has density of 2,400 kg/m^3, leading to choice of the initial semi-major axis as an even 1,200 m. The initial spin of body A is twice the mean motion of the orbit matching the initial relative translational motion states,

46

about the inertial-frame $+z$ axis. This is equivalent to a period of about 20.52 hours. The initial spin of body B is 3/2 the mean motion about the inertial-frame $+z$ axis and 1/2 the mean motion about the inertial-frame $+y$ axis. This is equivalent to a period of about 25.96 hours. The initial attitudes of the bodies are each given by 3-1-3 euler rotation sequences with the randomly generated ϕ, θ, ψ angles given in Table 2.4. It should be noted that for this test case nondimensionalization was used for better scaling of the state and internal variables, even though most results plots shown herein have standard meter-kilogram-second units.

Table 2.4: Extents and initial attitude angles of asteroid models for intermediate-sized artificial asteroid model test case.

Angle (deg)	Body A		Body B	
ϕ	81.10		41.74	
θ	116.17		6.21	
ψ	71.55		-39.32	
Extents (m)	minimum	maximum	minimum	maximum
body frame X	-251.6	234.7	-100.0	98.7
body frame Y	-129.0	137.1	-69.5	72.7
body frame Z	-129.6	126.9	-51.5	55.6

A 3D plot of the trajectory in the inertial frame is shown in Figure 2.4. Because the rotational motion of the bodies is not captured in this figure, the components of the angular velocity vector in the inertial frame are also shown for each body in Figure 2.5. The deviation of the motion from the initial orbit due to coupling is perhaps best seen by examining some of the osculating orbital elements, calculated from the motion states pulled back to the inertial frame. The semi-major axis and the eccentricity are shown in Figure 2.6. The variations from initial values of the kinetic energy of each body, total kinetic energy, potential energy, and total system energy are shown together in Figure 2.7. The total energy variation from its initial value is shown separately in Figure 2.8. Note the greatly expanded scale of this total
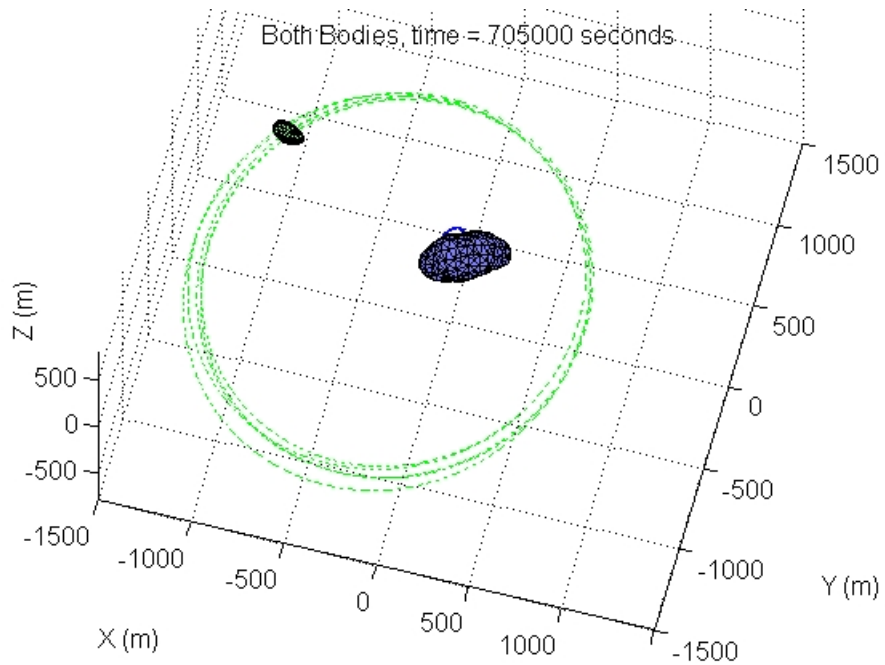
Figure 2.4: Three dimensional plot of trajectory, for intermediate-sized artificial asteroid model test case.

energy plot in Figure 2.8 in comparison to the scale of Figure 2.7. Similar variation from initial value in the components of the total angular momentum vector is also shown in Figure 2.8. Here too, the drift in each total angular momentum component is at about 14 orders of magnitude smaller than the value of the respective vector component itself. The attitude matrix errors are shown together in Figure 2.9.
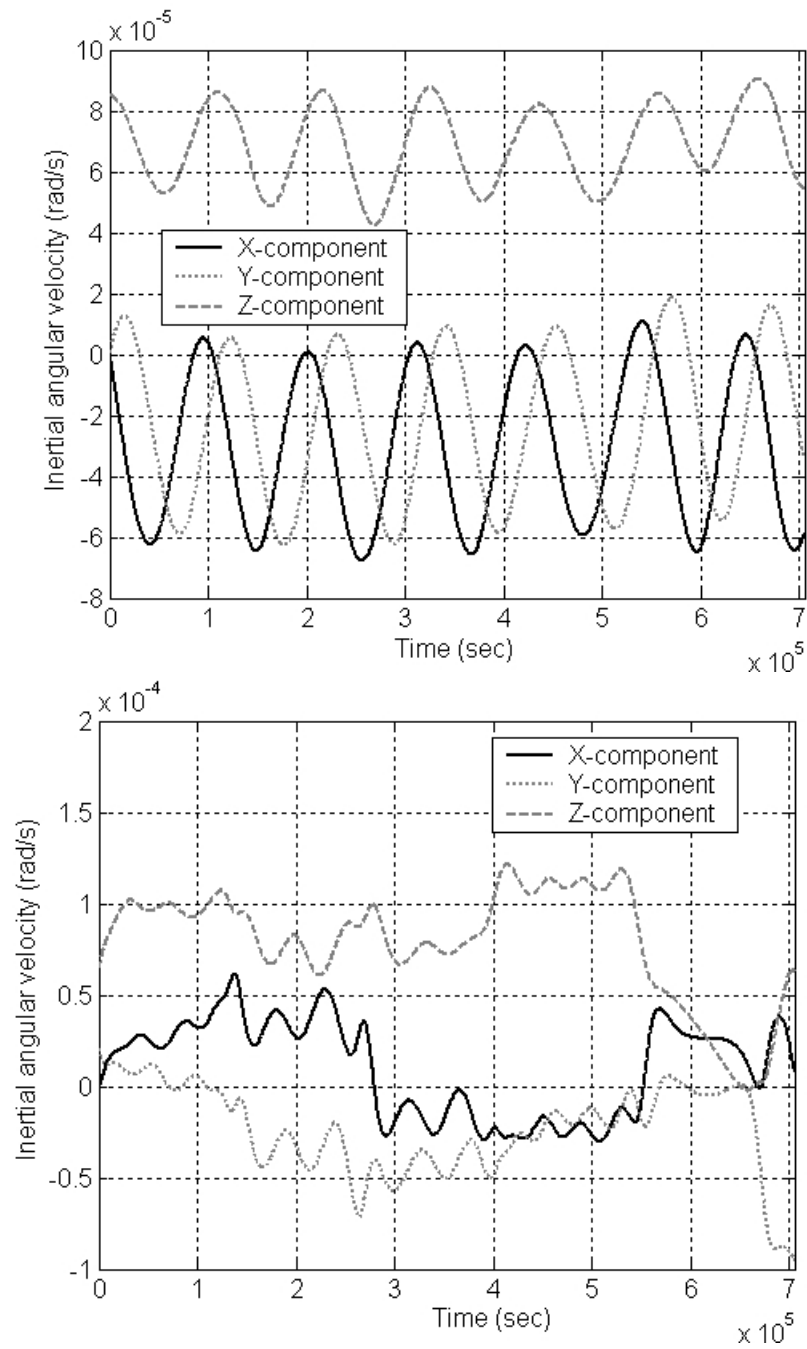
Figure 2.5: Body angular velocity vectors in inertial frame, for intermediate-sized artificial asteroid model test case. Body A is at top and B is at bottom.
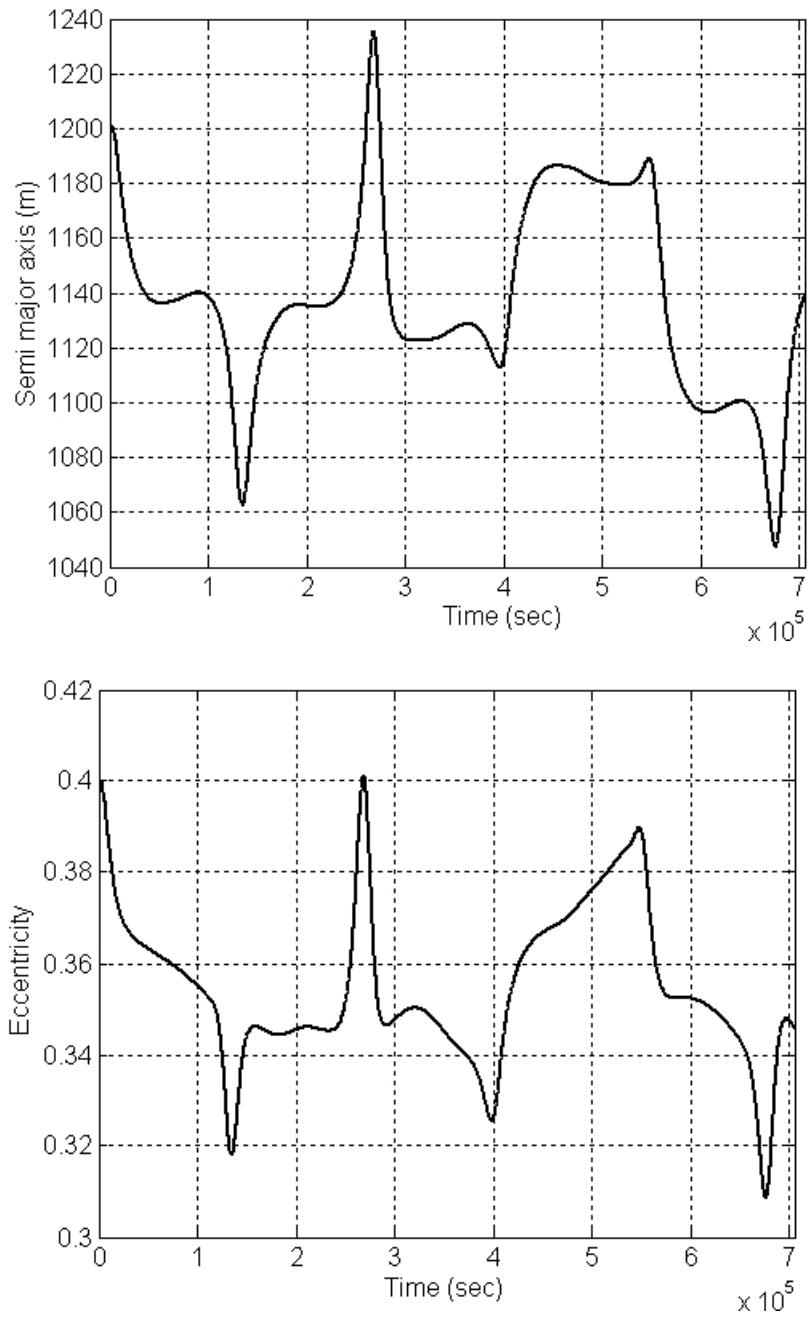
Figure 2.6: Co-orbital semi-major axis and eccentricity, for intermediate-sized artificial asteroid model test case. Semi-major axis is at top and eccentricity is at bottom.
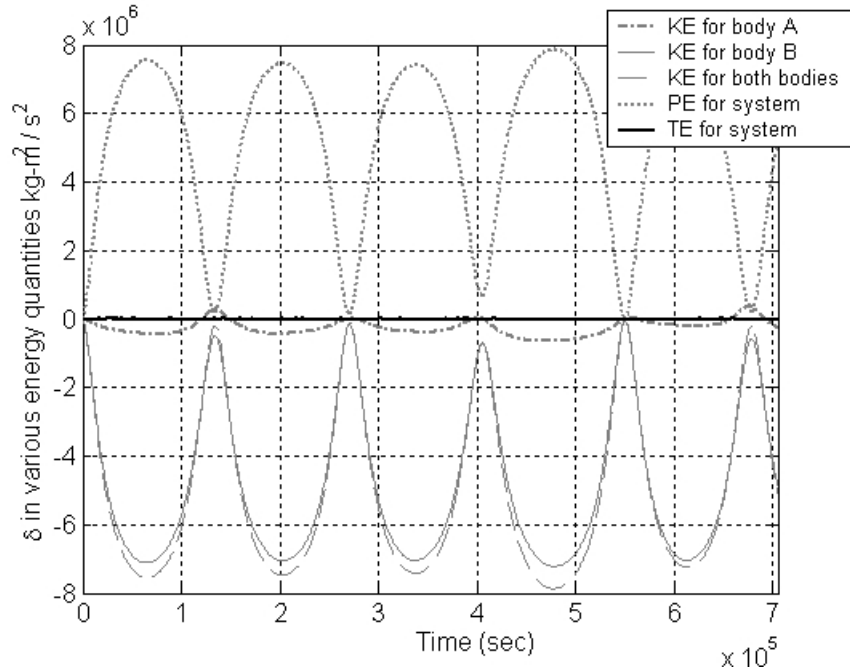
Figure 2.7: Variation from initial value of body kinetic energies, total kinetic energy, potential energy, and total system energy, for intermediate-sized artificial asteroid model test case.

In this case too, gravitational coupling produces changes in the rotational dynamics of the bodies, with the spin state of body B changing much more, and in a much more irregular fashion, than that of the more massive body A. The changes in semimajor axis and eccentricity are on the order of 20-25 percent over the approximately 5 periods covered in the duration of the run (which was again 30 nondimensionalized time units, or about 7.055×10^5 seconds in this case). Again, the total energy variation is 12 orders of magnitude less than the energy exchanged between the kinetic and potential forms, and the angular momentum variation is also about 14 orders of magnitude less than the total angular momentum magnitude (which has a mean of 2.177×10^{11} kg-m^2/s for this case). The attitude matrix errors remain small, though increasing irregularly. Interestingly, the relative attitude matrix T diverges from the orthonormality condition faster than the body-A-to-inertial attitude matrix P.

This test case was performed using a relatively early single-processor code version,
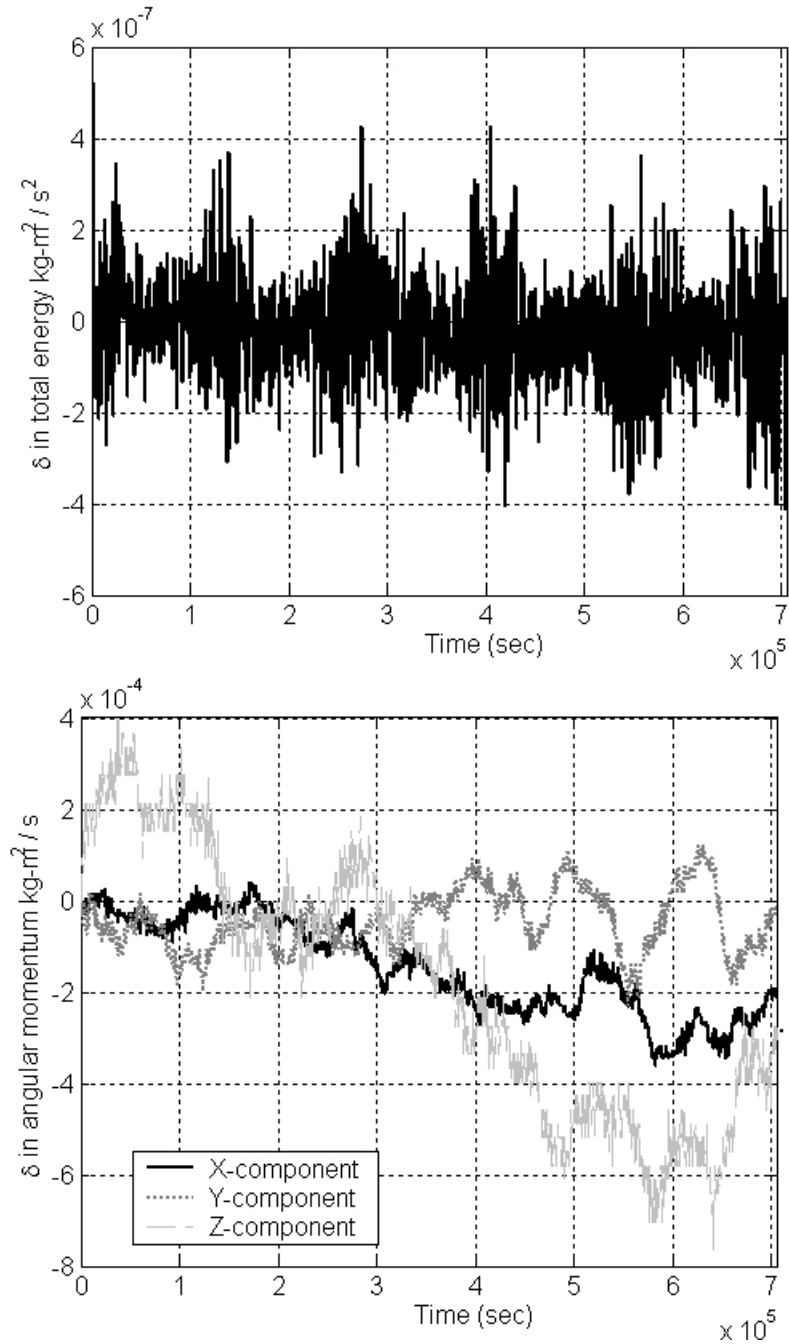
Figure 2.8: Expanded view of variation from initial value of total system energy and total angular momentum vector components, for intermediate-sized artificial asteroid model test case.

after the switch to compiled C/C++ from the initial Matlab-only code but before the further LGVI or parallelization improvements, on a 512 Mb RAM and ≈2.4GHz Intel processor laptop. The integration tolerance, for time-step control, was kept at

52
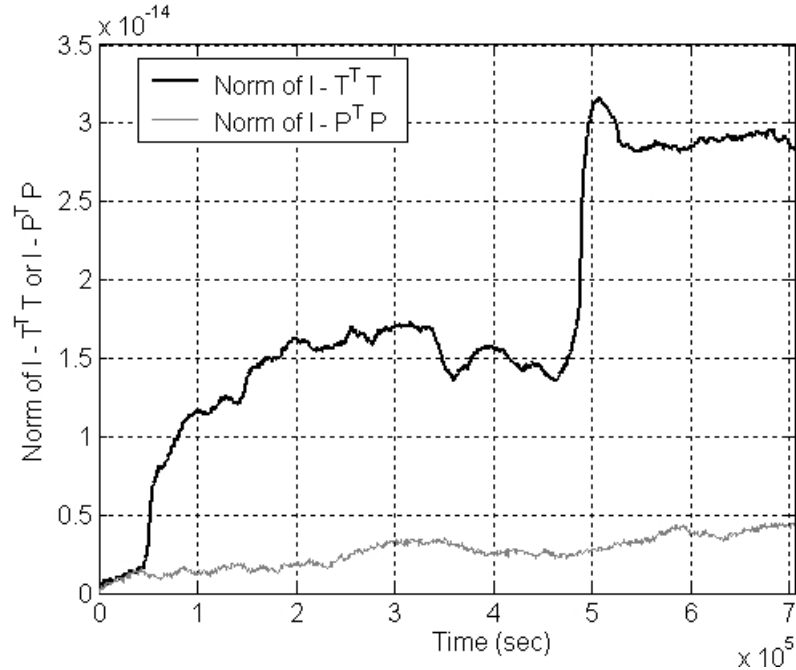
Figure 2.9: Attitude rotation matrix errors, for intermediate-sized artificial asteroid model test case.

1×10^{-14}. The number of series terms used was only four terms, such that the last term used contained fractional sub-terms proportional to $1/(R^7)$, with R again being the relative position vector magnitude. The total wall-clock time resulting with these run parameters and before the speed-up improvements was 3 days plus 22:55:52 just for this test case.

2.5.3 Test case using large-sized binary asteroid component models

Here it is sought to validate the methodology using a much more detailed model patterned after an actual binary system but with one major modification in that the smaller body, denoted body B, is rotated 180 deg about its own +Z axis from the actual system. The high-fidelity polyhedral models of both the larger body A and body B, suited for the simplex formulation, have the body-frame-axis extents shown in Table 2.5 along with several other derived body properties.

Table 2.6 shows the definition of the initial conditions for the simulations with

53

Table 2.5: Properties of high-fidelity polyhedral asteroid models.

Property	A	B
# Simplices	9168	2292
# Vertices	4586	1148
Surface area (km^2)	5.742	0.6739
Volume (km^3)	1.195	0.04803
Equiv. radius (m)	658.4	225.5
Mass (kg $\times 10^9$)	2337	134.3
Density (kg/m^3)	1955	2795
I_{xx} (kg-m^2 $\times 10^{17}$)	3.850	0.02159
I_{yy} (kg-m^2 $\times 10^{17}$)	4.032	0.03187
I_{zz} (kg-m^2 $\times 10^{17}$)	4.578	0.03758

Extents (m)	min	max	min	max
body frame X	-750.3	779.2	-288.0	283.2
body frame Y	-736.2	755.6	-235.7	227.4
body frame Z	-688.4	659.1	-177.8	171.2

Table 2.6: Initial attitudes, spins, and orbital elements for high-fidelity polyhedral asteroid models.

Quantity (units)	A	B
spin rate (deg/day)	3125	496
ϕ (deg)	-83.93	0
θ (deg)	2.063	0
ψ (deg)	-152.9511	0
a (m)	2540.5	
e	0.0	
i, Ω, ω, ν (deg.)	0.0	

results shown below. At the initial time, the body spin rates are about each body frame's +Z axis, and are equivalent to a period of $\approx$2.76 hr for A and $\approx$17.4 hr for B. An inertial reference frame is chosen with origin at the system center of mass and with +Z axis parallel to the orbit normal and +X axis parallel to the line between body centroids. Each body is oriented with respect to this frame by 3-2-3 Euler sequence angles ϕ, θ, and ψ. Note that the orbital elements of the mutual orbit of the bodies are time-varying due to the coupled rotational and translational dynamics. Since numbers for the eccentricity e, inclination i, longitude of ascending node Ω, longitude

of periapsis ω, and true anomaly ν at a specific epoch are very uncertain, one may arbitrarily choose zero in each case. The initial orbit period and the initial semimajor axis lead to a total system mass estimate of approximately 2.4713×10^{12} kg.

It is observed in the results of propagating this system from the given initial conditions that all integrals of motion which should be conserved (both total energy and the total angular momentum vector) are conserved very well for long time-span propagations with the simulator, using both the RKF7-8 and LGVI integrators. All results shown for this test case within this subsection were obtained with the LGVI integrator. Very dynamic behavior in the system is observed, indicating that it is in an excited state. The oscillations in the spin states, orbital elements, and various other quantities occur on several different timescales roughly matching: 1) the period of A body rotation, 2) the nominal orbit period (which the B body rotation period is equal to initially) 3) an $\approx$ 103 hrs intermediate period, and 4) the $\approx$ 87 days period for precession of the angular momenta of A and B and of the orbit plane. The motions on the first two timescales are driven by the asymmetry of the shape models (primarily A's longitudinal asymmetry near its equator) and conservation of total energy. The body B rotation rate varies about the orbital rate so that B librates while remaining synchronous on average. The motion on the third timescale is linked to the free precession of body B, excited by the motions on the first two timescales. This involves a variation from zero to maximum and back in the magnitude of the above mentioned libration of B. The motion on the fourth timescale is generally independent of motions on the other three timescales, and is explained by a simple conservation of total angular momentum. Table 2.7 shows the extents for oscillations of the angular velocities and angular accelerations of the bodies (both magnitude and inertial frame x,y,z components), and the extents for oscillations of the orbital

Table 2.7: Quantities of interest for propagation of high-fidelity asteroid component models. Duration covers two weeks of simulation time.

Quantity (units)	min	max	periods
Body A			
$\|\boldsymbol{\omega}_A\|$ (rad/s)	6.313e-4	6.314e-4	1,2*,4
$\boldsymbol{\omega}_{A_X}$ (rad/s)	1.073e-5	2.130e-5	1,2,4*
$\boldsymbol{\omega}_{A_Y}$ (rad/s)	-1.314e-5	-2.964e-6	1,2,4*
$\boldsymbol{\omega}_{A_Z}$ (rad/s)	6.309e-4	6.313e-4	1,2,4*
$\|\boldsymbol{\alpha}_A\|$ (rad/s^2)	3.077e-13	4.496e-11	1,2,3,4*
$\boldsymbol{\alpha}_{A_X}$ (rad/s^2)	-1.206e-11	1.024e-11	1,2,3*,4
$\boldsymbol{\alpha}_{A_Y}$ (rad/s^2)	-1.910e-11	2.116e-11	1,2,3*,4
$\boldsymbol{\alpha}_{A_Z}$ (rad/s^2)	-4.220e-11	4.116e-11	1,2*,3,4
Body B			
$\|\boldsymbol{\omega}_B\|$ (rad/s)	8.844e-5	1.165e-4	2,3*,4
$\boldsymbol{\omega}_{B_X}$ (rad/s)	-1.149e-7	6.232e-6	2,3,4*
$\boldsymbol{\omega}_{B_Y}$ (rad/s)	-4.754e-6	1.8301e-6	2,3,4*
$\boldsymbol{\omega}_{B_Z}$ (rad/s)	8.833e-5	1.164e-4	2,3*
$\|\boldsymbol{\alpha}_B\|$ (rad/s^2)	0.0	1.331e-9	2,3*,4
$\boldsymbol{\alpha}_{B_X}$ (rad/s^2)	-1.030e-10	9.627e-11	1,2,3*
$\boldsymbol{\alpha}_{B_Y}$ (rad/s^2)	-6.846e-11	6.629e-11	1,2,3*
$\boldsymbol{\alpha}_{B_Z}$ (rad/s^2)	-1.323e-9	1.327e-9	2,3*
a (m)	2535.4	2545.0	1,2,3*
e	0.0	0.0239	1,2,3*,4
i (deg)	0.0	3.195	1,2,4*
Ω (deg)	30	150	1,2,4*
ω_{peri} (deg)	secular	increase	2*
$\|\boldsymbol{a}_{REL}\|$ (m/s^2)	2.569e-5	2.718e-5	1,2,3*
$\boldsymbol{a}_{REL\,\|}$ m/s^2)	2.564e-5	2.713e-5	1,2,3*
$\boldsymbol{a}_{REL\,\perp}$ (m/s^2)	1.58e-6	1.78e-6	1,2*

elements and the relative acceleration (both magnitude and components parallel and perpendicular to the instantaneous line between centers of mass). The last column of Table 2.7 indicates which timescales, as numbered above, are influential on a quantity, with an asterisk indicating the most dominant mode for that quantity.

Figures 2.10 and 2.11 show the shorter timescale behavior of the orbit shape and size. Figure 2.12 shows the components lying in the inertial X-Y plane of the (normalized to unit length) angular momentum vectors. It is seen that the angular
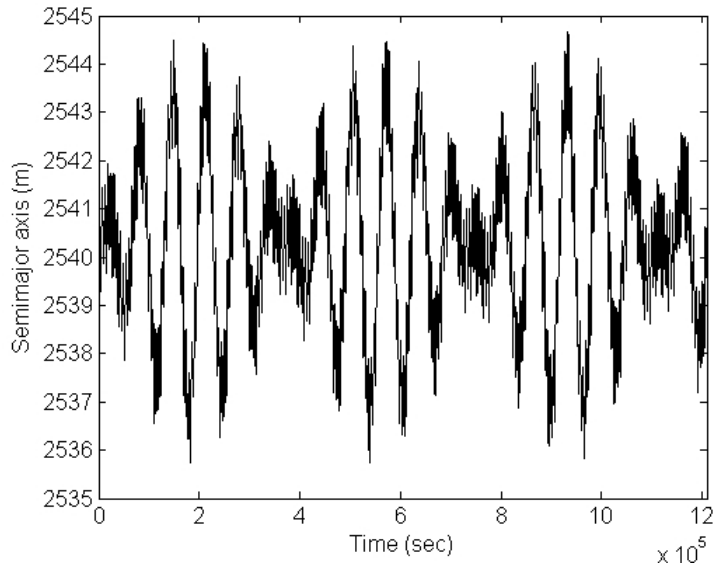
Figure 2.10: Semi-major axis behavior, over 2 week duration.
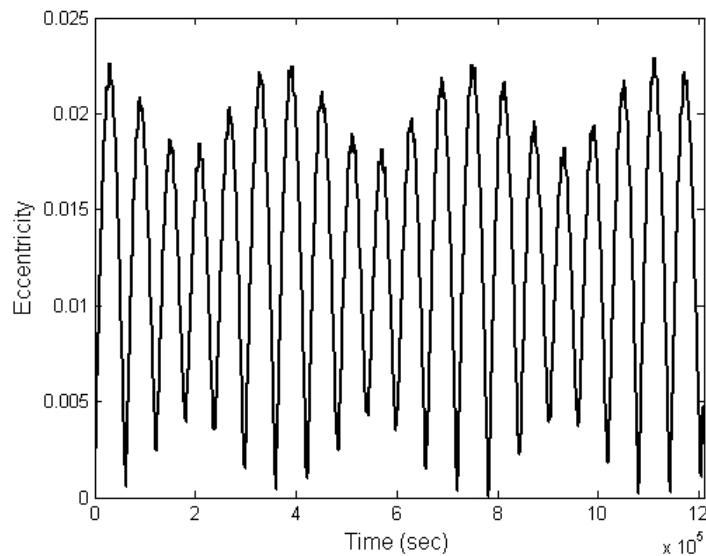
Figure 2.11: Eccentricity behavior, over 2 week duration.

momentum vector of B has a direction that remains bounded near the direction of the orbit angular momentum vector. This B angular momentum is also comparatively small in magnitude so the total angular momentum vector is effectively formed by just the vector addition of the A and orbit angular momentum vectors. Their projections in the X-Y plane trace out near-circular paths in it over time, and always lie in opposite directions from each other about the point in that plane which

57
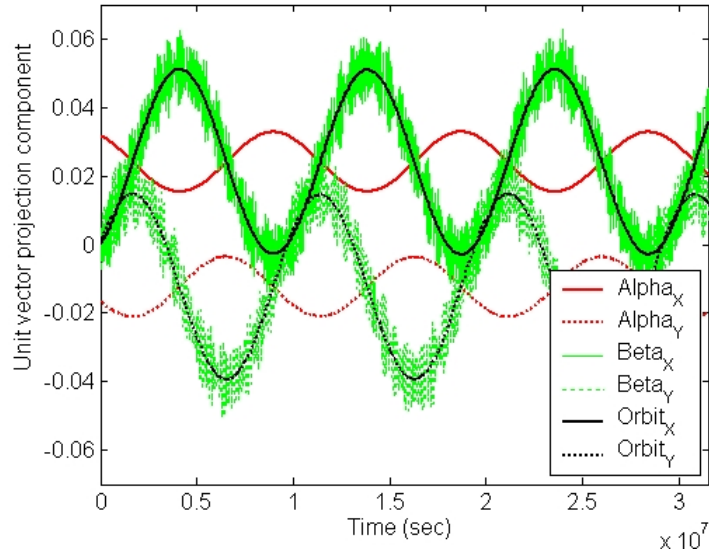
Figure 2.12: Normalized angular momentum vector projections in the inertial X-Y plane, over one year duration.

is the projection of the total angular momentum vector. As this angular momentum precession occurs, the offset between the spin pole of A and the orbit normal is invariant, because conservation of total angular momentum would be violated if it were not. Actually, approximate models with only 100 facets each but the same total
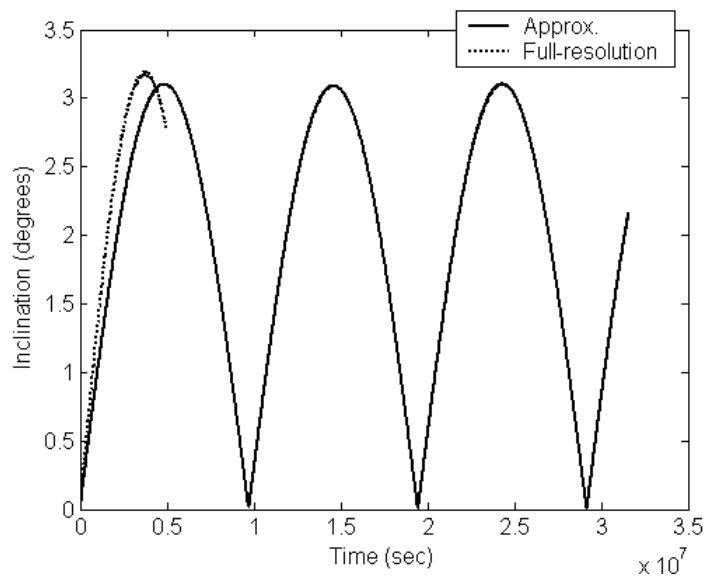
Figure 2.13: Comparison of inclination response for approximate and high-fidelity body models.

mass that approximate the shape of the high-fidelity models are used for the results in Figure 2.12. It is acceptable to use the approximate models like this to roughly characterize the longest timescale behavior of the system more efficiently, as Figure 2.13 shows there is commensurability between the high-fidelity model results and the approximate model results. All qualitative behavior is the same, although the longest and intermediate timescale behaviors require an adjustment in their amplitudes and periods in a consistent fashion, in order to quantitatively describe the true system with the results of approximate model simulations.

In the next chapter, a more complete application of all of the methodology developed in this chapter is embarked upon, to accomplish much more detailed study of an actual binary asteroid existing in nature for which shape models and relative motion parameters data was made available from various active and passive astronomical observations.

CHAPTER III

Application of F2BP Simulation Methodology to Binary NEA (66391) 1999 KW4

The F2BP simulation methodology described in the previous chapter has been used to perform a detailed study of an actual observed binary asteroid system, the binary NEA (66391) 1999 KW4. A brief introduction to this fascinating pair is in order. Discovered on May 20th, 1999 through the LINEAR program's facility at Socorro, New Mexico, this Aten-class [1] NEA is also designated a Potentially Hazardous Asteroid (PHA) [59]. Its binary nature was discovered in 2001 with radar [60], although the system had been photometrically observed earlier [61]. An extended campaign of Goldstone X-band and Arecibo S-band radar observations was conducted during this system's May 2001 Earth flyby, and Arecibo radar observations were also obtained during a more distant June 2002 Earth flyby. This entire set of radar data along with available lightcurve data for 1999 KW4 (hereafter just KW4) was used to obtain high resolution shape models of the binary's components, estimate their mutual orbit characteristics, and estimate the binary's heliocentric orbit, all according to the methods mentioned later. For context, the heliocentric orbital elements for

---

[1]Aten class refers to an orbital classification scheme that categorizes Near-Earth asteroid orbits by similarity to that of 2062 Aten (semi major axis < 1.0 AU; aphelion > 0.983 AU) or that of 1862 Apollo (semi major axis > 1.0 AU; perihelion < 1.017 AU) or that of 1221 Amor (semi major axis > 1.0 AU; 1.017 AU < perihelion < 1.3 AU).

Table 3.1: Properties of Heliocentric Orbit of KW4. These are in the form of osculating orbit elements, with respect to the ICRF93/J2000 coordinate frame of the DE-405 JPL planetary ephemeris.[*],[†]

Osculating Element	Value	Post-Fit Std. Deviation
Eccentricity	0.6883867034	± 0.0000000258
Perihelion distance (AU)	0.2001480484	± 0.0000000164
Time of perihelion (JD)	2453676.5283086650	± 0.0000142757
Time of perihelion (date)	2005-Nov-02.02831	
Longitude of ascending node (deg.)	244.9330159090	± 0.0000001442
Argument of perihelion (deg.)	192.5958593259	± 0.0000018719
Inclination (deg.)	38.8905365946	± 0.0000023616
Semi-major axis (AU)	0.6422962390	± 0.0000000030
Orbit period (days)	188.01889472	± 0.00000132
Orbit period (years)	0.514758659	± ??

[*] All angular elements are referred to the **ecliptic** J2000 frame, **unlike** the angular values and binary mutual orbit elements in the later Table 3.2.
[†] All data in this table are from Table S2 of the online supplement to Ostro et al [62] and are repeated here for context and easy reference.

this system were found to be as presented in Table 3.1. From the table, it is seen that the system passes quite close to the sun every approximately half year, possibly with significant dynamical implications.

Although KW4 was studied in detail as described in this chapter largely because it just happened to be the system for which the observation data was made available in the right time and circumstances, the KW4 system also typifies the largest class of small binary NEAs. Thus studying it was not studying an exceptional case but an easily generalized case. That is, the main results herein and comprehensive treatment of the dynamics of KW4 herein should transfer well to any member of the majority class of small binary NEAs to which KW4 belongs. This class encompasses much of the binary asteroid population in the inner solar system, according to Pravec et al [14] and Pravec and Harris [63] (in the latter reference all of groups A and B are

included). The small asteroid spin rate distributions in Pravec and Harris [64] are also consistent with this. Members of this class have a small size (primary diameter <10 km) and a secondary to primary size ratio usually between 0.18 and 0.5. For any member the larger, roughly spherical or oblate spheroid primary is spinning quite rapidly relative to the rate of the mutual orbit while the elongated, roughly triaxial ellipsoid secondary has an on-average synchronous rotation with that mutual orbit. The longest axis of the secondary is pointed toward the primary. The asynchronous rotation of the primary has led this category of systems to be called that of "small asynchronous binaries" by some. Others prefer to reserve that terminology for systems in which both bodies have asynchronous rotation, or else to use "singly synchronous binaries" or "singly asynchronous binaries" to be more specific. In any case, there is no special importance to studying KW4 over all other possible binary asteroid systems, yet the study of this particular system is very important because it has broader applicability, by similarity to other systems.

It is worth noting that while the various elements of KW4's whole system model (shapes, mutual orbit, body properties, and heliocentric orbit) which were estimated from the observation data were used in setting up and executing high-fidelity dynamic simulations of the system, in reverse some outputs from such dynamic simulation were also used to inform the interpretation of the observation data being put into the system model estimation process. This kind of collaboration between observers handling the estimation and those handling the simulations (the author) was key to enabling a better overall understanding of the KW4 system and its behavior. The approach taken for this study is to start by considering a nominal model for the system that matches with the results of this collaborative estimation process.

3.1 Nominal Model of KW4 System

First note that from this point onward, Alpha will be used to refer to the primary and Beta will be used to refer to the secondary, for convenience. The observation data mentioned previously was used to obtain polyhedral mesh shape models and body physical and spin properties of KW4's components through a least squares estimation procedure. A separate least squares estimation of orbit elements for the (originally assumed as Keplerian) mutual orbit followed by the centroids of these two components, with their shapes and spins, was also carried out. As described in detail in Ostro et al [62], these two estimation processes were performed in alternation to refine both the shapes and orbit and arrive at what is hereafter called the nominal model of the KW4 system. The final shape models arrived at have sufficiently high spatial resolutions to capture the geometric detail contained in the raw data, i.e. 4586 vertices and 9108 faces for Alpha and 1148 vertices and 2292 faces for Beta. The product of those facecounts, or over 21 million, gives the order of the number of sets of tensor operations performed for each evaluation of the mutual potential, force, and moment. To facilitate faster computation than is possible with these high resolution models, and enable some more rapid exploratory simulations, low resolution models of each body were created having 100 faces each and vertex locations fitted to the shapes of the "true" high resolution models. Note that even for the high resolution models the numbers of faces and vertices and the body sizes lead to an average edge length for the triangular faces of 39 and 26 meters, for Alpha and Beta respectively. Hence topography much smaller than this scale cannot be captured in the models, but was also not resolved in the raw data to begin with.

For the high resolution body models, the rough dimensions, densities, and a few general mass properties, plus body spin rates/periods, are indicated in Table 3.2. Note

Table 3.2: Properties of the nominal model of KW4. All component shape- or mass-related properties apply to the high resolution body models.*,†,‡

Parameter (units)	Alpha	Beta
extents along X principle axis (km)	1.532±3%	0.571±6%
extents along Y principle axis (km)	1.495±3%	0.463±6%
extents along Z principle axis (km)	1.347±3%	0.349±6%
volume (km^3)	1.195±9%	0.048±18%
mass (10^{12} kg)	2.353±0.100	0.135±0.024
density (kg m^{-3})	1970±240	2810(+820,-630)
I_x (km^2)	0.1648±3%	0.01608±7%
I_y (km^2)	0.1726±3%	0.02374±7%
I_z (km^2)	0.1959±3%	0.02799±7%
I_z/I_x	1.189±5%	1.74±10%
I_y/I_x	1.047±5%	1.48±10%
rotation period (hr)	2.7645±0.0003	17.4223 assumed
rotation rate (deg day^{-1})	3125.34±0.34	495.916 assumed
total mass (10^{12} kg)	2.488	±0.054
orbit period (hr)	17.4223	±0.036
a, semi-major axis (m)	2548	±15
e, eccentricity	0.0004	±0.0019
i, inclination (deg)	156.1	±2
Ω long. of ascend. node (deg)	105.4	±3
ω arg. periapsis (deg)	319.7	±182
MJD epoch	2055.4132	±0.88

* The given body spins are assumed to be about each body's +Z principle axis, so that axis is the same as the body spin pole.

† All angular values and binary mutual orbit elements are referred to the **equatorial** J2000 reference frame.

‡ All data in this table except for the mass-normalized principle axis inertia elements are from Tables 1 and 2 of Ostro et al [62] and are repeated here for context and easy reference.

that some difficulty was encountered in trying to precisely resolve the spin period of Beta, such that in [62], the source of the data in this table, this was assumed equal to the mean mutual orbit period on average. The dynamic behavior of the system may help explain the difficulty in obtaining a simple description of Beta's spin behavior from data taken during the observation windows. The nominal values for Keplerian mutual orbit elements determined are also shown in Table 3.2. It

should also be noted that the parametric mutual orbit elements appearing in it are only descriptive in nature and without a dynamical basis, resulting from fitting the observed system motion with a Keplerian orbit while allowing no precession of the argument of periapsis, nor orbital plane motion, in response to perturbations. Their different nature from that of the osculating orbit elements shown later as numerical simulation output implies no comparison can be made with those results.

There are several additional features of the system's model noteworthy in connection to the simulation results below. The potential of gravity for Alpha, in the geophysical context and as defined in Hofmann and Wellenhof [65], has its minimum value on Alpha's surface at the poles and maximum value near the equator, due to Alpha's fast rotation [66]. This is the same situation as for Earth (which is nearly equipotential but not exactly so) and the opposite of the situation for most solitary small solar system bodies studied to date in such detail. It means the deepest point in the geopotential is at the equator and loose material on the surface should preferentially flow toward the equator. The interesting raised equatorial band of Alpha has its highest points only several meters below the altitude at which a free particle would enter orbit, with the current rapid spin rate [66]. While Alpha has significant variation in gravitational slope across its surface, with the largest slope values at points on the equatorial band, Beta has comparatively low gravitational slopes everywhere [66]. These gravitational slopes (or more properly the angular deviation of the net acceleration vector from being antiparallel with the surface normal vector) are mapped over both bodies in Figure 3.1. For the net acceleration vector in the slope calculations shown in this figure, smooth rotation of each body about it's +Z axis at the rotation rate in Table 3.2 was included. The difference in the degree of gravitational slope variation, and estimated density, between Beta and Alpha may also be attributable

to dynamic behavior of the system (if Beta is sufficiently shaken by angular acceler-ations). Finally, note that out of the system's total angular momentum, ≈75% is in Alpha spin, ≈25% in the mutual orbit, and <0.1% in Beta spin [66].

(a) Northern hemisphere of Alpha

(b) Northern hemisphere of Beta

(c) Southern hemisphere of Alpha

(d) Southern hemisphere of Beta
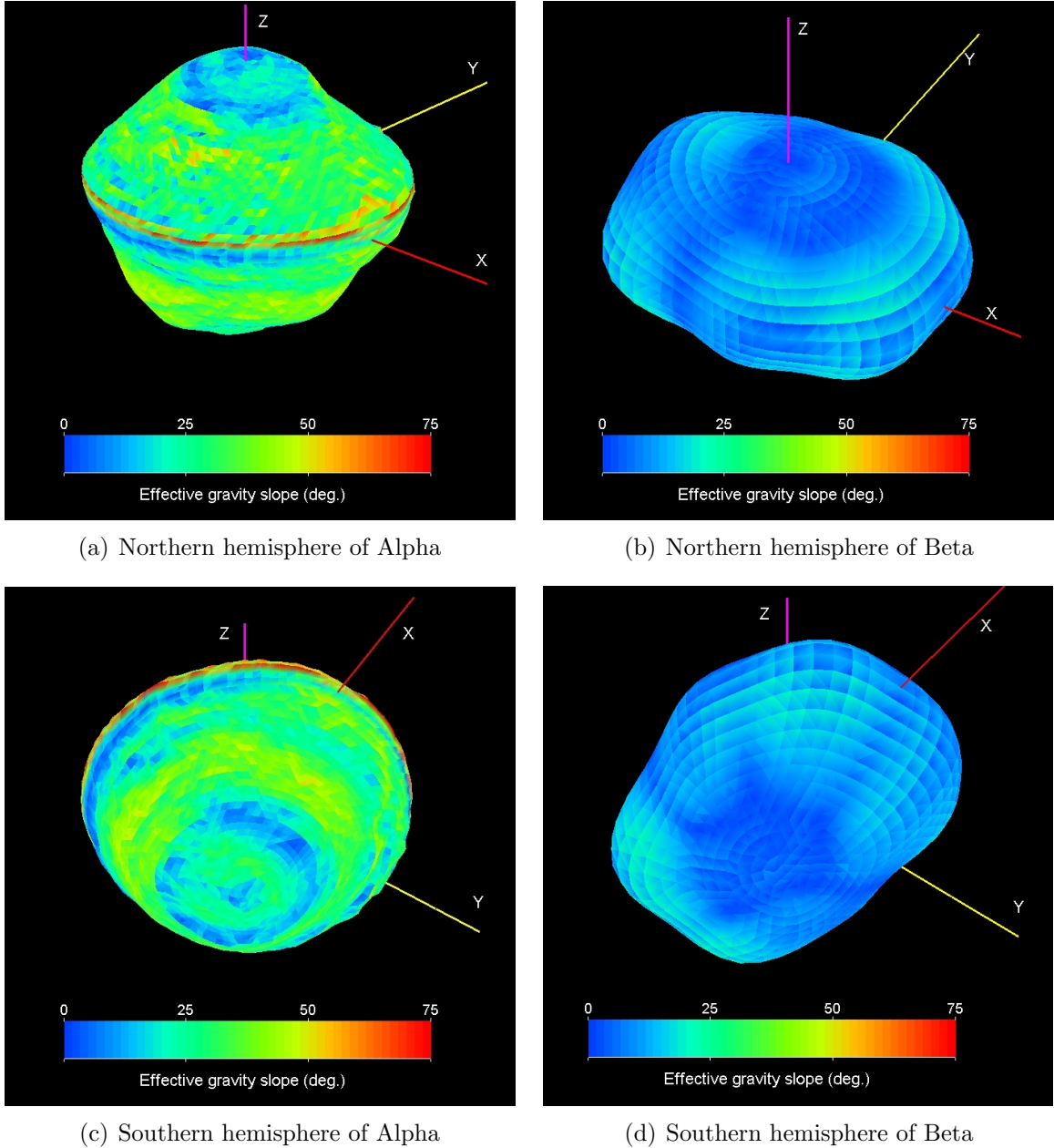
Figure 3.1: Effective gravitational slope for both Alpha and Beta according to the nominal model setup. For that, both Alpha and Beta are in rotation about their +Z axis at the constant rotation rate listed in Table 3.2. Gravitational slope is angular deviation of net acceleration vector at a surface point from the vector antiparallel to surface normal at that point.

3.2 Variations Relative to Nominal Model of KW4 to Explore System Excitation

In addition to simulating and studying the nominal model of KW4, with nominal values for the uncertain system parameters, one can also learn a great deal from simulating and studying models of KW4 that are "close" to the nominal one, in that they differ from it only by small changes in one or more of those parameters. Making these small changes leads to many models of KW4 that have different levels of energy excitation. Parametrically varying the osculating orbital elements (e, ν, etc.) and the key pole offset angle ($\Delta = \delta + i$) between Alpha's spin pole and the orbit normal at the initial simulation time is one method of exploring different cases of system excitation. Here Alpha's spin pole's obliquity, δ, and orbit plane's inclination, i, are measured relative to the system's total angular momentum direction. It was chosen to examine variation of the initial osculating eccentricity between 0 and 0.0115, and of the initial true anomaly of the system at 0° and 180°. Meanwhile values for Δ between 0 and 10 degrees were explored, the latter being close to the limit of what may plausibly exist in the natural system. These unconstrained initial conditions have formal uncertainty ranges, from observations of the system, of $0 \leq e \leq 0.0023$, $0° \leq \Delta \leq 7.5°$ and $\nu \in [0, 2\pi]$ [62].

As an alternative to directly starting the system with a certain level of excitation by adjusting the simulation initial conditions, one can instead propagate the simulation through an excitation event. In particular, one can propagate the system through an Earth flyby (which produces tidal forces on the binary components) or through a perihelion passage of the binary's orbit about the sun (which also causes a tidal interaction with the Sun's gravity). Given the current low perihelion distance of approximately 0.20 AU and the long-term Kozai resonance minimum possible perihelion

distance of 0.12 AU, regular gravitational interaction with the Sun is hypothesized as a primary mechanism for system excitation, so simulating that has more significance than simulating a comparatively infrequent Earth flyby.

3.3 Possible Relaxed and Excited Dynamical Configurations for KW4 and Similar Systems

This section presents a sampling of results from simulations of both the high and low resolution models of the KW4 system by itself (with no third-body influences), with initial conditions varied from the nominal model as mentioned above. The initial conditions for the limited selection of simulations summarized herein are presented in Table 3.3. Therein the angles ψ, θ, and ϕ correspond to a 3-2-3 Euler rotation sequence orienting each binary component relative to the initial orbital frame, in turn defined as having $+X$ axis from the system barycenter to the initial position of the center of mass of Beta, $+Z$ axis perpendicular to the initial orbital plane, and $+Y$ axis mutually orthogonal to these by the right hand rule. For all cases the tabulated values of these angles refer to Alpha's orientation, since for all cases Beta has fixed initial values of $\psi = 0°$, $\theta = 0°$, and $\phi = 180°$, i.e. Beta's spin pole is initially aligned with the orbit plane normal. For all cases, the initial spin rate of Alpha is 3125.4 deg day^{-1}, the initial semi-major axis is 2540.5 m, the initial spin rate of the orbit and Beta is the mean motion in agreement with that semi-major axis, and both bodies' initial spins are about their $+Z$ principle axes. For all cases initially $i = \Omega = \omega = 0$, because the inertial orientation of the entire system is irrelevant to internal motions, given no external influences.

In general, the binary is seen to manifest motions in four "system modes" with different periods, though the amplitude or aggressiveness of those motions varies with the level of excitation for each simulation case. The first and fastest mode has a

Table 3.3: Initial conditions and selected outputs for simulations of relaxed and excited KW4 configurations.

◇	Initial conditions[*]						Outputs[†]		
	For Alpha						max.		max.
	ψ	θ	ϕ	Δ	e	ν	amp. $\delta\eta$	E[TE]	δKE
	(deg)	(deg)	(deg)	(deg)		(deg)	(deg)	(J$\times 10^{10}$)	(J$\times 10^{8}$)
	27.04	2.06	-83.93	2.06	0	0	5.874	7.660391	1.638
l	27.04	5.00	-83.93	5.00	0	0	6.164	7.660408	1.790
o	27.04	10.0	-83.93	10.0	0	0	6.700	7.660464	2.079
w	27.04	2.06	-83.93	2.06	.0085	0	1.399	7.660343	0.2828
	27.04	2.06	-83.93	2.06	.010	180	11.149	7.660446	3.248
h	27.04	2.06	-83.93	2.06	0	0	8.279	8.711780	2.088
i	27.04	2.06	-83.93	2.06	.0085	0	2.960	8.711716	0.7129
g	27.04	10.0	-83.93	10.0	0.010	180	14.659	8.711961	3.843
h	27.04	0.00	-83.93	0.0	.01125	0	0.825	8.711685	0.3843

[*] Here the angles ψ, θ, and ϕ correspond to a 3-2-3 Euler rotation sequence orienting Alpha relative to the orbital frame, Δ is the angular offset between Alpha's spin pole and the orbit normal, and e and ν are the the mutual orbit eccentricity and true anomaly, respectively, all at the initial simulation time.

[†] For the output quantities, the first column is the maximum amplitude of variation of the libration angle, the second is the mean total energy, and the third is the maximum variation of kinetic energy, hence the largest tradeoff of energy between kinetic and potential forms during the simulation.

◇ This column indicates the resolution of the body models employed for the simulation.

period commensurate with Alpha's spin period, and is driven by the ≈4% equatorial ellipticity of Alpha (note the I_y/I_x value). The second mode has a period matching the orbital period (the same as the on-average Beta rotation period). The attitude of Beta relative to perfectly synchronous rotation, and oscillations of mutual orbital elements coupled to that libration, show motion within this mode. The third mode is an excitation of Beta's free precession dynamics through the faster oscillations of the previous modes, and has period of ≈188 hours. A "beating" of the amplitude of Beta's libration is the most noticeable manifestation of the oscillations in Beta rotation and the mutual orbit comprising this mode. It is interesting to note that

the period of the second mode is only slightly longer than the period of torque-free precession of Alpha's angular velocity vector in its own frame, while the period of the third mode is only slightly shorter than four times the period of torque-free precession of Beta's angular velocity vector in its own frame.

Mostly decoupled from these three fastest system modes is a fourth one observed to have a period of ≈90 days for the high resolution models. It is observed from the numerical simulation results that there is an on-average constant offset angle between orbit pole and the spin pole of Alpha, and matched precession at a roughly constant rate of both those poles (i.e. both the Alpha and orbit angular momenta vectors) about the total angular momentum vector's invariant direction in inertial space. This is illustrated in Figure 3.2, which shows the paths traced by quasi-projections (meaning the small angle itself is used rather than its sine, as in a proper projection) of the angular momenta direction vectors (angular momenta vectors normalized to unit length) for orbit, Alpha, and Beta onto the X-Y plane of the inertial reference frame having +Z axis aligned with the total angular momentum vector at the initial time. The relative radii of each pair of circles matches the 75/25 ratio of Alpha angular momentum magnitude to orbit angular momentum magnitude. All of this behavior can be described as a Cassini state for the KW4 system, and follows directly from the conservation of total angular momentum. In particular, the system is in what may be classified as Cassini state 2, but of a non-standard kind in that the primary spin and mutual orbit angular momenta are in matched precession rather than the secondary spin and mutual orbit. The matching precession rates for this mode are some of the main rates that the analysis of Chapter IV seeks to independently recover.

The first three low resolution runs in Table 3.3 were carried out to initially characterize the nature of the longest period mode over very long simulation durations,
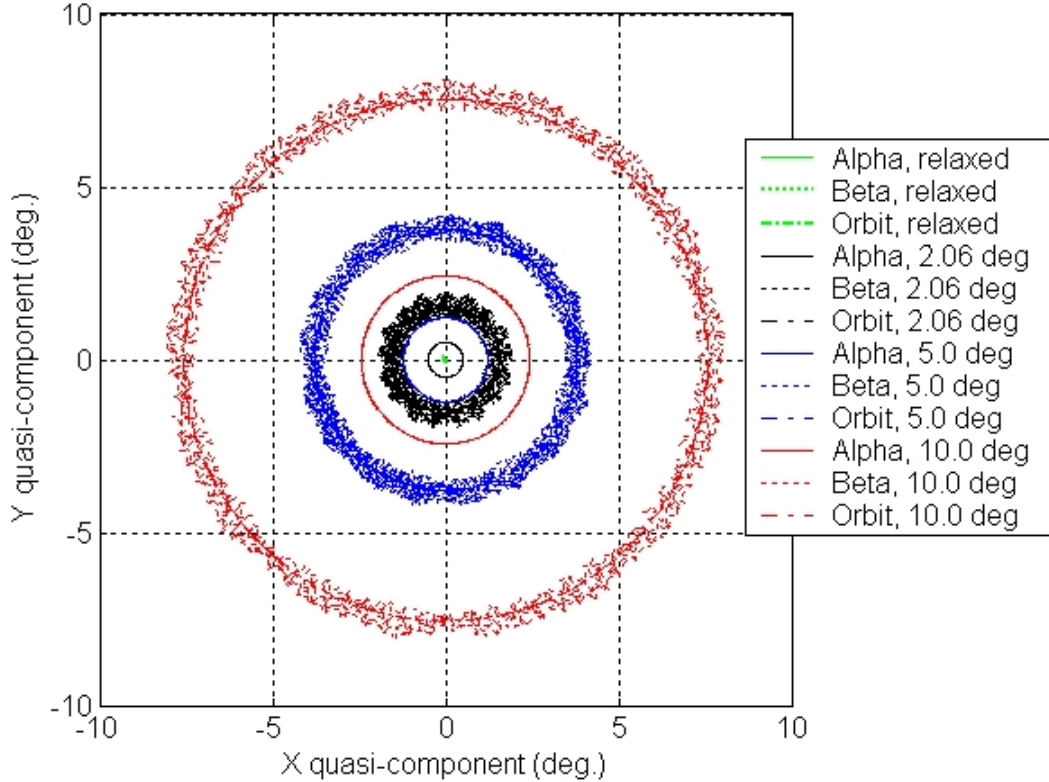
Figure 3.2: Comparison, between simulated cases, of quasi-projections of the orbit, Alpha, and Beta angular momenta direction vectors. These direction vectors are the angular momenta vectors normalized to unit length, and they are quasi-projected onto the X-Y plane of the inertial reference frame having +Z axis aligned with the total angular momentum vector at the initial time.

and the two runs appearing after those plus the first row run were for similar initial exploration of the three faster modes. The rest of the runs in the table, using the high resolution models, eventually end with the most energetically relaxed configuration identified for the full system, in the last row. This has degeneracy of the Cassini state with all three spin poles (of the two components and the orbit) parallel to each other. In addition, Beta has very small libration or rotation away from the line between centers, and all other dynamic motions are small or modest. The initial-time osculating eccentricity value of this most relaxed case is nonzero due to the non-spherical mass distributions of the components, but the orbital path is still almost circular due to

regular oscillation of the true anomaly while the argument of periapsis circulates.

In contrast, the most energetically excited case that a full simulation was carried out for is given in the second to last row of Table 3.3. This excited configuration has a large Cassini state pole offset at the limit of what might plausibly exist for KW4. While this offset is maintained over time the dynamic variations in most all other quantities are large. The oscillation in angular velocity of Beta has amplitude varying from zero to $\approx 2 \times 10^{-5}$, causing beta to librate by several degrees during some orbits and barely librate at all during other orbits only a few days later. Such motion of Beta corresponds to large angular accelerations on it, and such shaking could lead to the estimated larger density for Beta than for Alpha through material redistribution into a less porous structure. Such motion could also make estimation of a single rotation rate variation or libration frequency from the raw data less accurate.

The uncertainty in the determined inertial directions of the estimated Alpha spin pole and mutual orbit normal, along with the fact of the regularity of likely excitation events, suggest that KW4 is not in the most relaxed configuration identified here, with respect to the longest period mode. It is also unlikely to be in the most excited configuration identified here either, and instead may inhabit an intermediate point in the parameter space. With respect to the shorter period modes, sizeable observed offsets of Beta's long axis from the line between centers, varying in magnitude and sign between different epochs in the observation periods, were seen (Steve Ostro, personal communication). These deviations were not fully understood, and hence not reported in Scheeres and Fahnestock et al [66], but they indicate that Beta has libration motion inconsistent with the system being in the most relaxed configuration. The density disparity between Alpha and Beta, and difficulty of estimating Beta's exact rotation state from raw data, also indirectly point to shorter period modes

motion more consistent with the system being in a moderately excited configuration.

Also listed in Table 3.3 are the maximum amplitude of variation in Beta's libration angle (hereafter η) away from the line between centers, the mean total energy of the system, and the maximum tradeoff between potential and kinetic energy over the simulation duration (which is longer than the third mode's period in all cases). These numbers provide a fuller comparison of the most relaxed and most excited configurations identified here, as bounds on what is possible for the real KW4 system. An even more complete comparison is provided by Figures 3.3 through 3.6. Note in Figure 3.3 the nearly constant but different inclinations between the two cases, and the switch between circulation of true anomaly for the excited case and circulation of periapsis for the relaxed case. The latter behavior along with nonzero mean osculating eccentricity indicates mutual orbital motion that is very nearly circular but with a "super-Keplerian" rate according to the system mass and semi-major axis numbers estimated through the Keplerian orbit fitting that was performed with the observation data. This simply indicates that naive reliance on Keplerian orbit fitting may not yield extremely accurate masses for the full-detail system.

3.4   Demonstration of Perihelion Passage Excitation

As discussed earlier, an alternative to starting propagation of the system with different levels of energy excitation is starting it in a relaxed configuration and simulating an excitation event acting upon it. And as mentioned before, the most sensible such excitation event to examine is the binary's gravitational interaction with the sun during one of the binary's perihelion passages. To accomplish simulation of such solar tide effects on the binary requires some modification of the earlier presented F2BP propagation methodology to include the perturbing effects of a distant third body.

(a) Semi-major axis behavior

(b) Eccentricity behavior

(c) Inclination behavior

(d) Longitude of ascending node behavior

(e) Argument of periapsis behavior

(f) True anomaly behavior
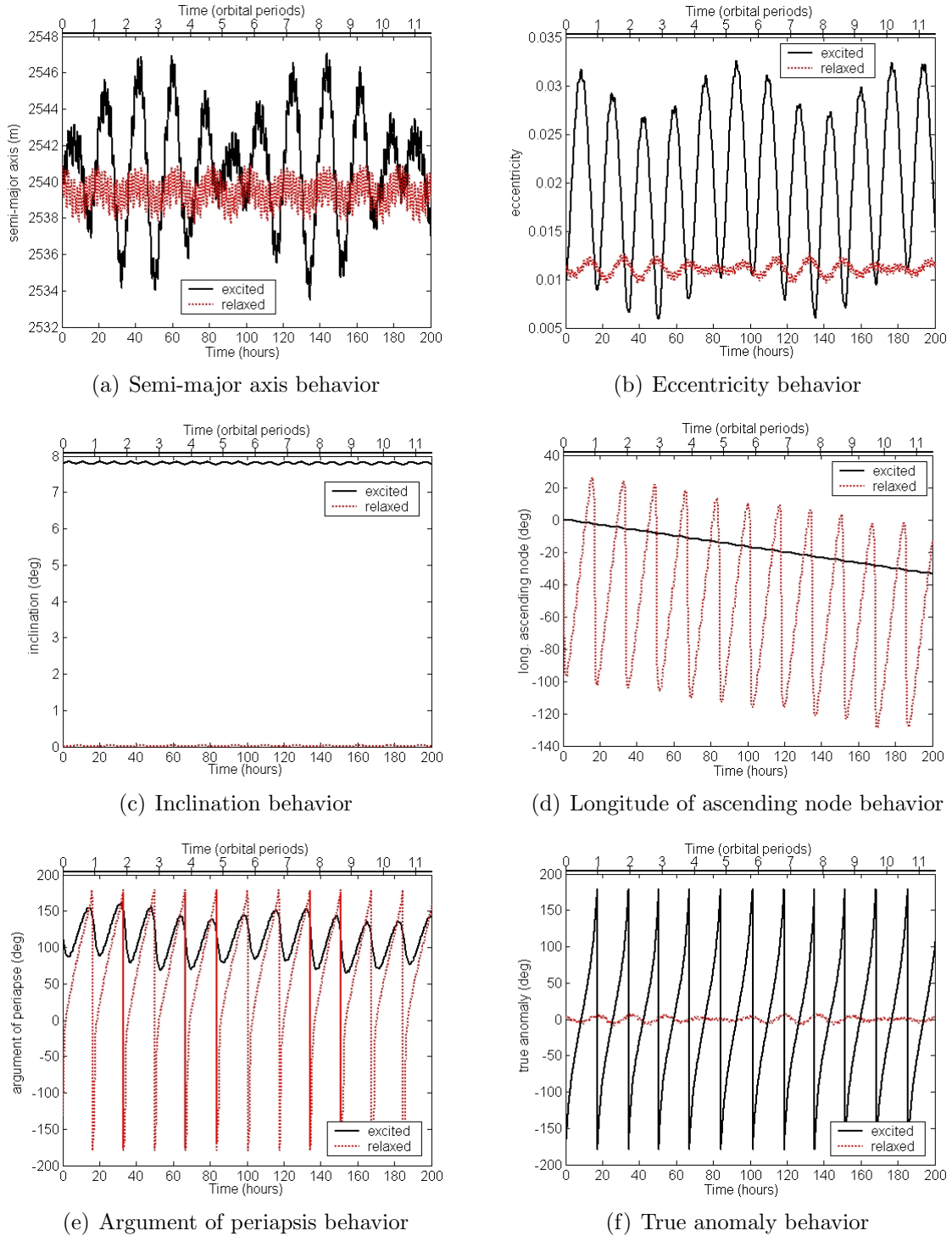
Figure 3.3: Comparison of trajectories of standard osculating orbit elements between the most relaxed and most excited configurations for KW4. The four angular elements are measured relative to the inertial reference frame aligned with the total angular momentum vector at the initial time. These orbit elements are different in nature from the parametric orbit elements fitted to observed system motion under Keplerian assumptions, so no comparison can be made with those quantities.
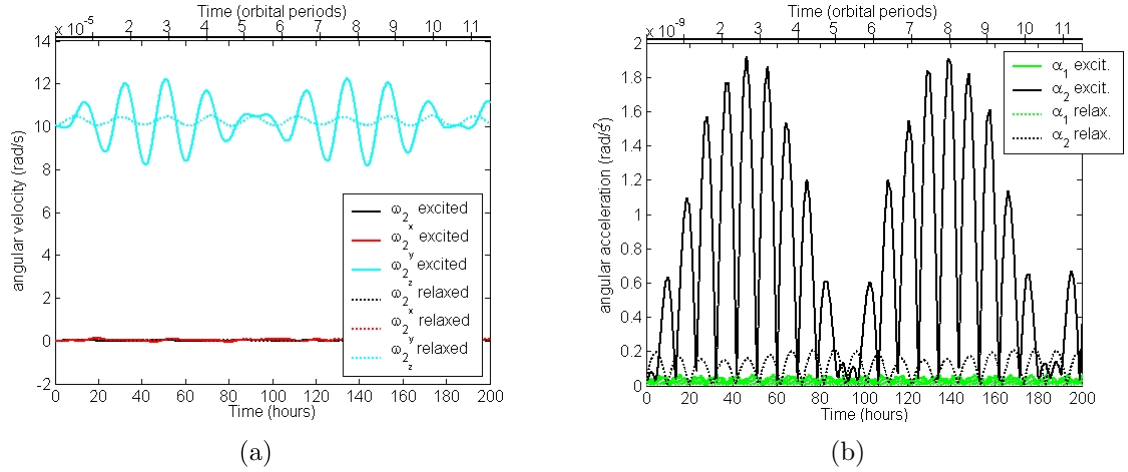
Figure 3.4: Comparison between most relaxed and most excited configurations identified in text, of the components of angular velocity of Beta, in its own frame, and of the magnitudes of angular acceleration acting upon Alpha ($\boldsymbol{\alpha}_1$) and upon Beta ($\boldsymbol{\alpha}_2$).

(a) Vector components   (b) Isometric view
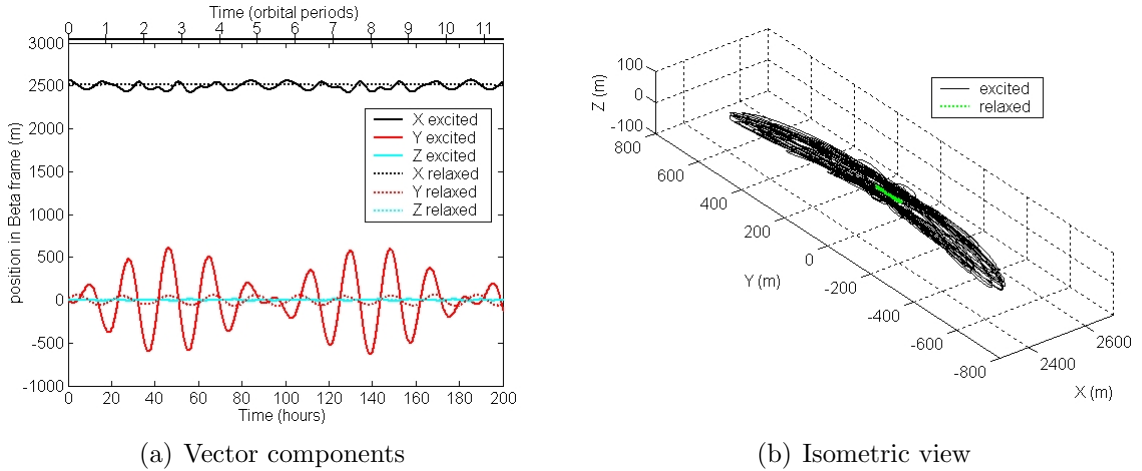
Figure 3.5: Trajectory of center of mass of Alpha in the frame fixed to Beta.

This involves introducing a modification to the relative force term $\partial U\,/\,\partial\mathbf{R}$ within the set of EOM from Section 2.3 that is applicable according to the choice of integration approach. It is assumed that to first order the effects of the third body are adequately captured through additions to the relative force alone, i.e., through the direct effect on the translational dynamics alone. This in turn will transfer into effects on the rotational dynamics via the full coupling of the system. In other words, it is

75
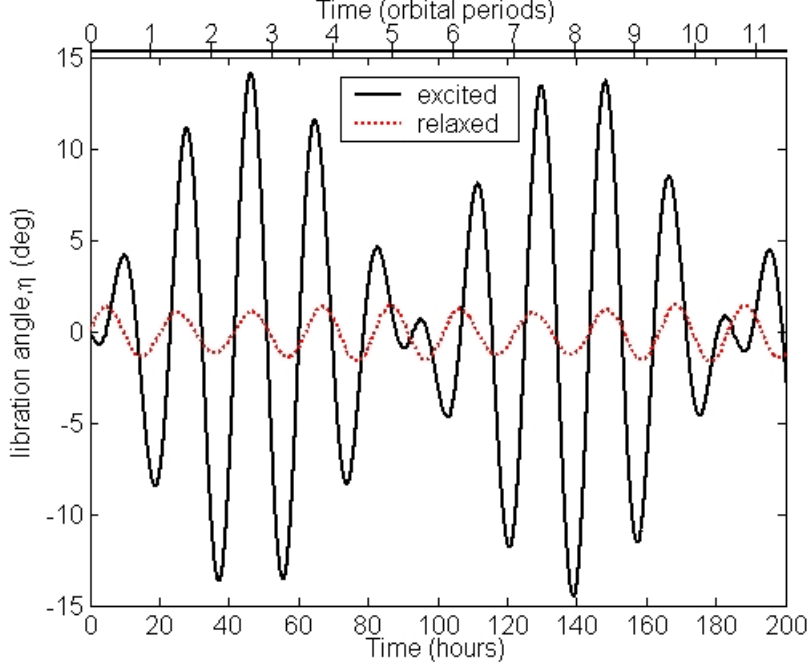
Figure 3.6: Comparison between most relaxed and most excited configurations of Beta libration angle behavior.

assumed that no change is needed to the relative moment $\mathbf{M}$ in the EOM itself, or no direct effects on the rotational dynamics are needed to capture the third body perturbation. Ultimately, one may employ the replacement rule of

$$\frac{\partial U}{\partial \mathbf{r}} \quad \Rightarrow \quad \frac{\partial U}{\partial \mathbf{r}} \; + \; \frac{m_1}{m_1 \; + \; m_2}\mathbf{C}_2 \; - \; \frac{m_2}{m_1 \; + \; m_2}\mathbf{C}_1 \tag{3.1}$$

within either set of EOM presented earlier. One has a choice as to how to obtain the potential gradients denoted by $\mathbf{C}_{(1,2)}$. One can use the partial derivative, with respect to the position vector from the third body to Alpha's centroid, of the polyhedron plus point mass potential formulation [46], using the full-detail shape model of Alpha, and similarly for Beta. Alternatively one can just use the partial derivative, with respect to the same position vector, of the two-point-mass potential approximating both the binary component in question and the distant third body as spheres. It was found that the former approach gives quite erroneous results, unlike the latter one, for any scenario in which the distance from the binary barycenter to the third body is

76

very large compared to the binary system's length scale and the mass of the third body is correspondingly large (e.g. perihelion distance and the mass of the sun). In such a scenario, in the polyhedron plus point mass potential formulation, the true contribution of each edge and each face becomes very small, tending towards zero. Then the very small sum of these small contributions is multiplied by the normalized gravity constant G, density of the binary component, and the very large third body mass. Numerical issues aside, this would in theory still produce the correct number for the $\mathbf{C}_i$ in question. But given very poor numerical scaling in such cases and round-off error at machine precision, the computed contributions of each edge or face as determined through the arctangent and natural log function calls of the formulation (refer to [46] for the calculation of L_e and ω_f within Eq. 2.1) are too large in value, leading to an obviously incorrect (impossibly large) final $\mathbf{C}_i$ value.

This is illustrated with a series of test cases propagating simple 8-face octahedra with total mass and dimensions within a factor of about four of the total mass and dimensions of the KW4 components, from initial conditions for a nearly circular relative orbit with radius very close to the nominal semi-major axis within the KW4 system (see section 3.1). The starting distance of the third body from this test binary's barycenter was 100 km, and the starting mass of the third body was 0.1 times the total mass of the test binary system. Holding all other initial conditions the same, this distance was successively increased by factors of 2, 5, or 10 and the third body mass concurrently increased by the square of that same factor, so that the attraction should in theory retain exactly the same magnitude. Figure 3.7 shows the sum of all face contributions and sum of all edge contributions, within the expression for $\mathbf{C}_1$, vs. increasing third body separation and increasing square root of third body mass.

(a) Sum of face contributions within $\mathbf{C}_1$

(b) Sum of edge contributions within $\mathbf{C}_1$

(c) $\mathbf{C}_{1_{poly}} / \mathbf{C}_{1_{pointmass}}$
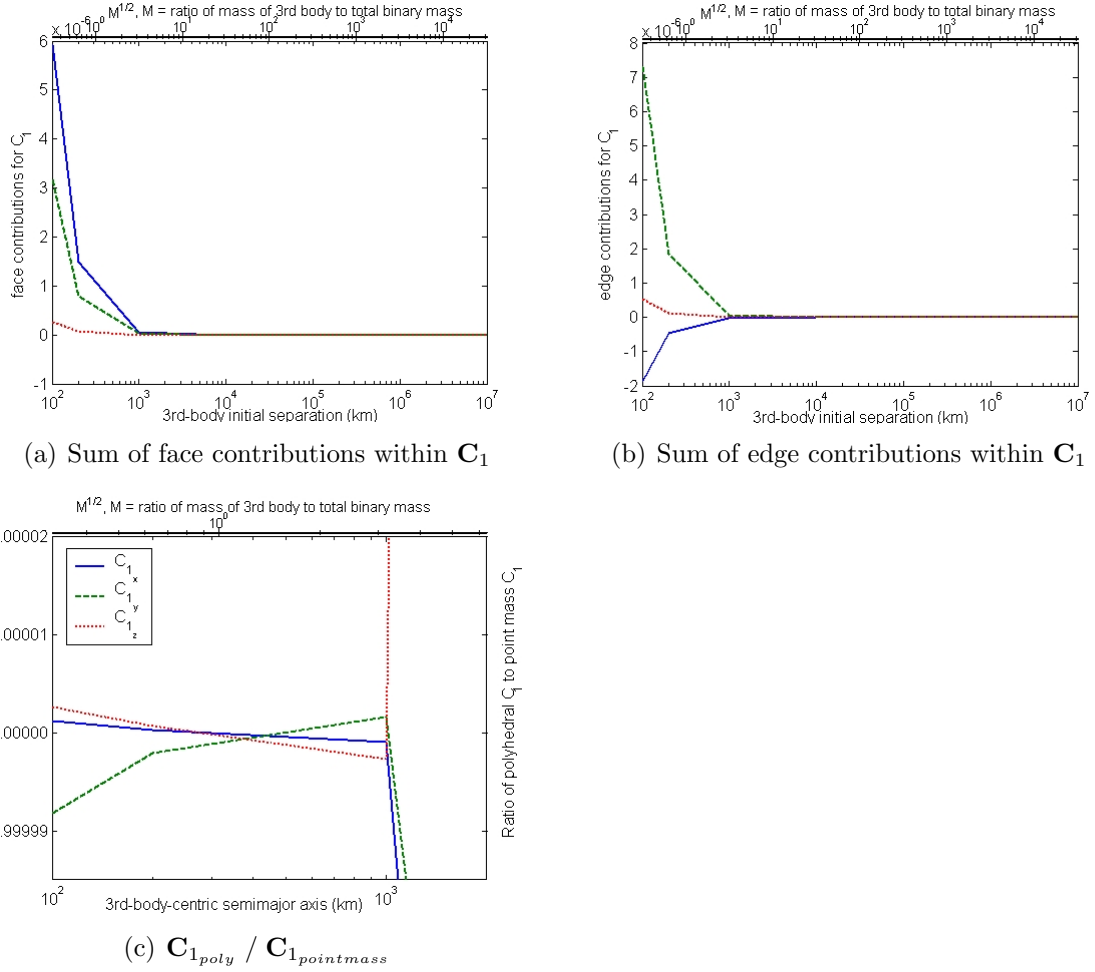
Figure 3.7: Illustration of relative accuracy of polyhedron plus point mass and two-point-mass formulations for mutual potential between a third body and the Alpha component of an octohedral "test" binary system. The sum of contributions of all faces and sum of contributions of all edges toward the mutual potential gradient according to the former formulation is shown at top. At bottom are individual ratios of the components of that gradient determined from the polyhedron plus point mass formulation to the components of that gradient determined from the simple two-point-mass formulation.

These sums are not yet multiplied by G, Alpha's density, and the third body mass, and they become relatively very small regardless of the normalization used. The ratios of the $\mathbf{C}_1$ components calculated for the polyhedron plus point mass formulation to the matching $\mathbf{C}_1$ components calculated for the two-point-mass formulation are plotted vs. distance and root of third body mass in the same figure. In theory these ratios

78

should continue converging toward unity, but it is seen that the breakdown in the polyhedral method, as explained above, sets in at a separation distance between only 300 and 500 km. Beyond that range there is a switch to the polyhedral method severely diverging from the two-point-mass approximation with increasing distance. Note that each octahedral body in the test binary used here has comparatively few face and edge contributions due to its mere 8 faces, and for realistic meshes the size of each of the very many more contributions would be far smaller, making the results even worse. Given these results, the two-point-mass approximation is employed for the realistic scales of all plausible flyby scenarios examined for this work.

With the above modifications for including a perturbing third body in place, a perihelion passage simulation was performed using the initial conditions as tabulated in Table 3.4. The initial conditions for the relative motion and rotation of the binary are seen to match those for the prior "most relaxed case", with the initial binary orbit pole and the initial spin pole of both components all being aligned. Their common direction in inertial space is chosen consistent with the orientation results in Table 1 of Ostro et al [62]. The initial conditions for the heliocentric orbit are taken from Table S2 of the online supplement to the same source. The initial orientation and system setup are illustrated with respect to the ecliptic J2000 reference frame in Figure 3.8.

The simulation covers a duration of approximately 37.05 days, centered on the perihelion epoch, and sweeps out 120 degrees of the orbit on either side. The change in total energy of the binary system across the perihelion passage due to the external forces applied by the sun is clearly visible when total energy is plotted against time. However, it is small in relative terms: there is only an increase of 0.0014 percent from the total energy averaged over the first week of the simulation to that averaged over the last week.

Table 3.4: Initial conditions for simulation of perihelion passage by KW4 *.

Initial condition (units)	Alpha	Beta
ψ (deg)	27.05	0
θ (deg)	0	0
ϕ (deg)	-83.93	180.0
ω_x (deg day^{-1})	0	0
ω_y (deg day^{-1})	0	0
ω_z (deg day^{-1})	3125.4	496.4
a (m)	2540.5	
e	0.01125	
i (deg)	151.8	
Ω (deg)	55.8	
ω (deg)	0	
ν (deg)	0	
a_{sun} (AU)	0.6422962390	
e_{sun}	0.6883867034	
$r_{perihel.}(AU)$	0.200148	
i_{sun} (deg)	38.8905365946	
Ω_{sun} (deg)	244.9330159090	
ω_{sun} (deg)	192.5958593259	
ν_{sun} (deg)	-120.0	

* As before the Euler angles ψ, θ, and ϕ orient each binary component relative to the initial binary orbit frame. The angular velocity components ω_i are in each body-fixed frame. All other angular values and orbit elements are referred to the ecliptic J2000 reference frame.

According to a number of other numerical simulations performed earlier, using simple spheres in mutual orbit with masses equivalent to KW4's components and all propagated through perihelion passage at the current 0.2 AU perihelion distance, it was expected to find shifts in the osculating eccentricity up to 0.002 and shifts in the orbit pole up to 0.5° (Scheeres and Fahnestock et al [66]). Figure 3.9 shows the current simulation's output in eccentricity and in the quasi-projections of the orbit, Alpha, and Beta angular momentum direction vectors onto the common inertial plane perpendicular to the initial total angular momentum vector.
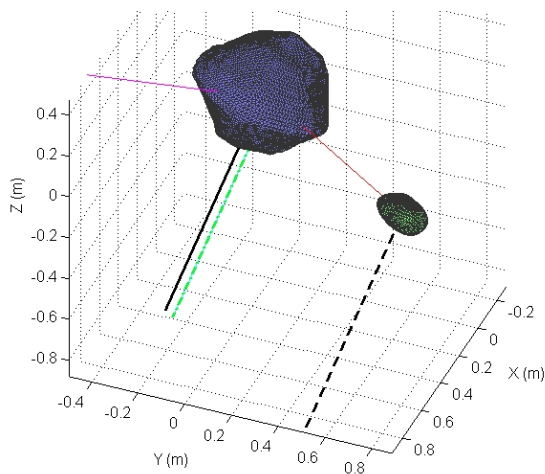
(a) Isometric view
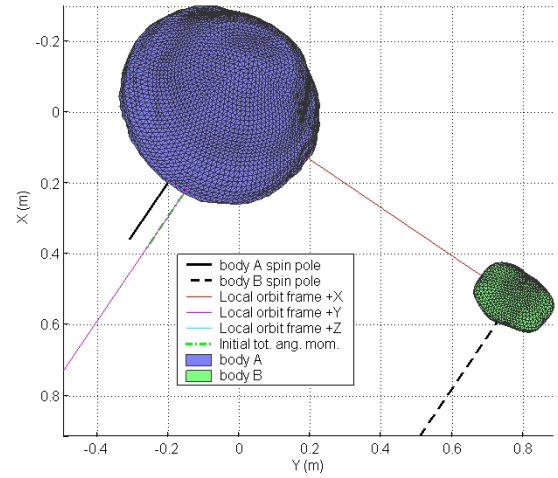
(b) View from +Z
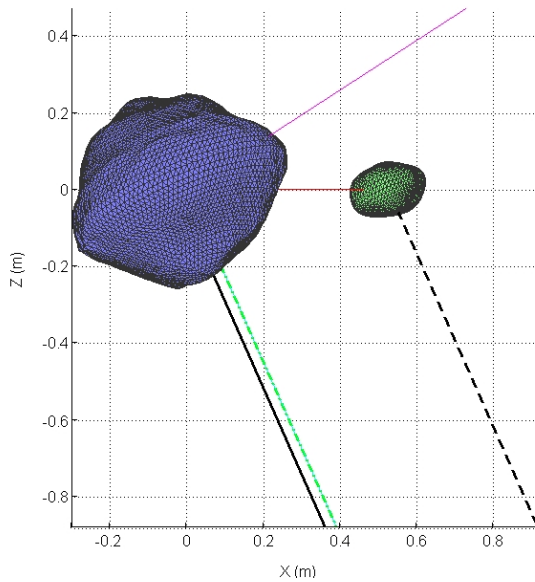
(c) View from -Y
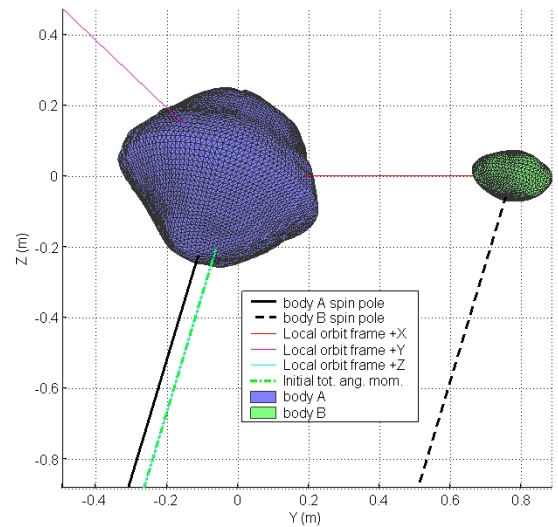
(d) View from +X

Figure 3.8: Initial system configuration for simulation of perihelion passage by KW4.
Is oriented in the ecliptic J2000 reference frame.

It is not possible to discern any net change in eccentricity over the perihelion passage, in part because of the comparatively large noisy oscillation in eccentricity existing before, after, and independent of the passage. This already has maximum amplitude about 1.5 times the predicted limit for the shift in e. As to whether the calculated mean of this oscillation changes, the number found for that is too

small to be significant. The eccentricity clearly varies in the three fastest modes, and the slowest of these is the one with period of ≈188 hr. Computing the mean over averaging windows of twice this period, located at the beginning and end of the simulation duration, gives a difference between the means of only about 1.49×10^{-5}, at least two orders of magnitude smaller than the predicted limit. It is concluded that overall the interaction with the sun during this particular perihelion passage simulation does not excite the 188 hr or shorter period modes very efficiently, for the dynamics of the system.

(a) Osculating eccentricity

(b) Orbit, Alpha, and Beta angular momentum projections
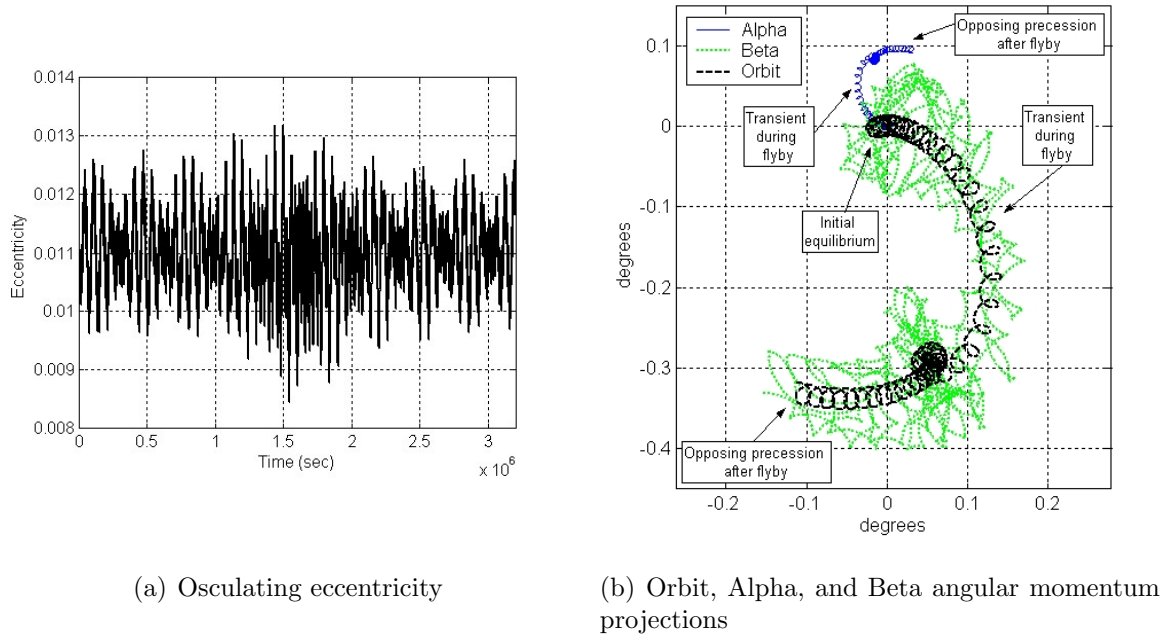
Figure 3.9: Excitation (or lack thereof) of different period dynamic modes of system across simulated perihelion passage. This starts from the most relaxed configuration. The angular momentum direction vector quasi-projections at right are onto the inertial plane normal to the initial total angular momentum vector.

In contrast, the longest period mode is clearly excited in only one perihelion passage, with a shift in the offset angle Δ from nearly $0°$ to approximately $0.45°$. This is seen in the second panel of Figure 3.9. Going into the passage, the quasi-projections

of the angular momenta direction vectors are very close to the origin. Then during a transient phase lasting through the passage itself they undergo a symmetric spiral migration outward from the origin, as the total energy level of the system is raised. After the arresting of this migration at the end of the transient period, the quasi-projections settle into tracing out opposing arcs with a steady precession. This goes on for the rest of the simulation duration and continues until the next perihelion passage. The new distance between the quasi-projections (i.e. new offset angle) is about $0.45°$ in this case, and a random walk is expected in the offset angle over many passages to move the system to its actual intermediate excitation level. Therefore it is demonstrated that at least for the longest period dynamical mode, and possibly in a cumulative fashion for the faster ones as well, gravitational perturbation by the sun is a major excitation source.

CHAPTER IV

Analytical Formulae Describing F2BP Motion of KW4-Like Systems and Estimation of Their Characteristics

This chapter takes somewhat of a departure from the "numerical experiment" focus of the last chapter, in order to develop and present the simplest possible non-trivial analytical theory that can properly describe the motion of a binary asteroid system similar to KW4. Here "properly describing the motion" means that with a straightforward analytical calculation the theory recovers key quantities or parameters for the various dynamical modes profiled earlier, such as periods, rates, and amplitudes, which match the best fits for those quantities or parameters to the full-detail numerical simulation results. Also, here a binary system "similar to KW4" means any member of the class of small asynchronous binaries, as introduced in the motivation at the start of the previous chapter.

The simple analytical theory is developed here in two parts, by pursuing two independent approaches. In the first approach the effects of Alpha's oblateness are examined while ignoring the effects of Beta's triaxiality by assuming Beta remains "locked" into its gravity gradient orientation and perfectly synchronous rotation. Thus Beta's angular momentum is neglected, having no component independent of or not included with the orbit's angular momentum. Note that with the neglect of Beta's

84

angular momentum, the angular momentum vectors of Alpha and the orbit must precess at equal rates due to conservation of angular momentum, and the subsequent derivation separately identifies what the Alpha spin pole and orbit normal precession rates are and independently establishes their equality. This first approach allows for remote estimation of some mass properties of Alpha before entering the very limited gravitational sphere of influence of the system.

In the second approach the effects of Beta's triaxiality are examined while ignoring all abberation of Alpha's shape from that of a perfect sphere. Similarly, with neglect of Alpha's shape, conservation of angular momentum again implies a coupling between Beta's orbital and rotational motion, which is also characterized as an output of this part of the theory. This second approach allows for some remote estimation of mass properties of Beta, also before entering the gravitational influence of the binary system itself.

Before embarking on either approach, however, it is necessary to lay the foundation for the analysis by defining a simple representation for the mutual potential between the binary components that approximates the true mutual potential well enough to still describe all of the major dynamical phenomena to be studied.

4.1 Representation for Mutual Potential to Second Degree and Order

Before proceeding, first note that the mathematical notation used in this chapter is entirely distinct from that used in the prior chapters. Also note that in this chapter, the subscript 1 generally refers to the primary body Alpha, while the subscript 2 generally refers to the secondary, Beta. The mutual potential representation started with is developed in the context of the simple standard two-body problem equation $m\,\ddot{\mathbf{r}} = \partial U/\partial \mathbf{r}$, wherein the mass parameter is $m = (m_1\,m_2)/(m_1 + m_2)$ and $\mathbf{r}$ is

the relative position vector between the body centers of mass (centroids), specifically the vector from Alpha's centroid to Beta's centroid. Also U is the the mutual potential. Let dm_1 and dm_2 be differential mass elements within the body volumes β_1 and β_2, located at positions $\boldsymbol{\rho}_1$ and $\boldsymbol{\rho}_2$ relative to the respective body center of mass:

$$U = \int_{\beta_1} \int_{\beta_2} \frac{G}{||\mathbf{r} + \boldsymbol{\rho}_2 - \boldsymbol{\rho}_1||} \, dm_1 \, dm_2 \qquad (4.1)$$

Defining vector $\Delta\boldsymbol{\rho} = \boldsymbol{\rho}_1 - \boldsymbol{\rho}_2$ and its norm $\Delta\rho$, this mutual potential can then be expressed as

$$U = \int_{\beta_1} \int_{\beta_2} \frac{G}{r \left(1 - \frac{2\mathbf{r}^T \Delta\boldsymbol{\rho}}{r^2} + \frac{\Delta\rho^2}{r^2}\right)^{\frac{1}{2}}} \, dm_1 \, dm_2. \qquad (4.2)$$

Defining the two scalars $\alpha = \Delta\rho/r$ and $q = \left(\mathbf{r}^T \Delta\boldsymbol{\rho}\right) / \left(r\,\Delta\rho\right)$ this potential can be expressed in Legendre series form:

$$U = \int_{\beta_1} \int_{\beta_2} \frac{G}{r} \left[P_o + P_1 \, \alpha + P_2 \, \alpha^2 + \dots \right] dm_1 \, dm_2 \qquad (4.3)$$

where P_i are the Legendre polynomials in q. Assume that it is acceptable to retain the series terms only out to second order in α. Next, substituting α and q back into the first three Legendre polynomials in q and distributing the double integrals gives

$$
\begin{aligned}
U = \frac{G}{r} \Bigg[& \int_{\beta_1} \int_{\beta_2} dm_1 \, dm_2 + \frac{\mathbf{r}^T}{r^2} \int_{\beta_1} \int_{\beta_2} (\boldsymbol{\rho}_1 - \boldsymbol{\rho}_2) \, dm_1 \, dm_2 \\
& + \frac{3\,\mathbf{r}^T}{2\,r^2} \int_{\beta_1} \int_{\beta_2} (\boldsymbol{\rho}_1 - \boldsymbol{\rho}_2)(\boldsymbol{\rho}_1 - \boldsymbol{\rho}_2)^T \, dm_1 dm_2 \, \frac{\mathbf{r}}{r^2} \\
& - \frac{1}{2\,r^2} \int_{\beta_1} \int_{\beta_2} (\boldsymbol{\rho}_1 - \boldsymbol{\rho}_2)^T (\boldsymbol{\rho}_1 - \boldsymbol{\rho}_2) \, dm_1 dm_2 \Bigg].
\end{aligned}
\qquad (4.4)
$$

Using the mass properties of the bodies to partially evaluate the double integrals leads to

$$
\begin{aligned}
U = \frac{G}{r} \Bigg[& m_1 \, m_2 + \frac{3}{2\,r^4} \mathbf{r}^T \left\{ m_2 \int_{\beta_1} \boldsymbol{\rho}_1 \, \boldsymbol{\rho}_1^T \, dm_1 + m_1 \int_{\beta_2} \boldsymbol{\rho}_2 \, \boldsymbol{\rho}_2^T \, dm_2 \right\} \mathbf{r} \\
& - \frac{1}{2\,r^2} \left\{ m_2 \int_{\beta_1} \boldsymbol{\rho}_1^T \, \boldsymbol{\rho}_1 \, dm_1 + m_1 \int_{\beta_2} \boldsymbol{\rho}_2^T \, \boldsymbol{\rho}_2 \, dm_2 \right\} \Bigg].
\end{aligned}
\qquad (4.5)
$$

Next recalling the definition of the standard moment of inertia dyads $\mathbf{I}_i$ (with units of kg-m^2), and using the fact that $\text{tr}[\mathbf{I}_i] = 2 \int_{\beta_i} \boldsymbol{\rho}_i^T \boldsymbol{\rho}_i \, dm_i$, one can incorporate both of the inertia dyads into the mutual potential expression (producing a kind of "mutual" extension of MacCullagh's formula):

$$U = \frac{G}{r} \left[m_1 m_2 + \frac{3}{2\,r^4} \mathbf{r}^T \left(\frac{m_2}{2} \text{tr}[\mathbf{I}_1] \, \mathbf{U} - m_2 \mathbf{I}_1 + \frac{m_1}{2} \text{tr}[\mathbf{I}_2] \, \mathbf{U} - m_1 \mathbf{I}_2 \right) \mathbf{r} \right.$$
$$\left. - \frac{m_2}{4\,r^2} \text{tr}[\mathbf{I}_1] - \frac{m_1}{4\,r^2} \text{tr}[\mathbf{I}_2] \right] \quad (4.6)$$

Here $\mathbf{U}$ is the identity dyad. Normalizing the inertia dyad of each body by its own mass, or in other words using $\tilde{\mathbf{I}}_i = \mathbf{I}_i/m_i$, and defining the unit vector $\hat{\mathbf{r}} = \mathbf{r}/r$, one can obtain a form similar to that presented in Maciejewski [39]:

$$U = \frac{G\,m_1\,m_2}{r} + \frac{G\,m_1\,m_2}{2\,r^3} \left[\text{tr}\left[\tilde{\mathbf{I}}_1\right] + \text{tr}\left[\tilde{\mathbf{I}}_2\right] - 3\,\hat{\mathbf{r}}^T \left(\tilde{\mathbf{I}}_1 + \tilde{\mathbf{I}}_2 \right) \hat{\mathbf{r}} \right] \quad (4.7)$$

Then, dividing the system mass parameter out of both sides of the simple two-body problem equation, one gets

$$\ddot{\mathbf{r}} = \frac{\partial U_o}{\partial \mathbf{r}} + \frac{\partial R}{\partial \mathbf{r}},$$

in which can be identified

$$U_o = \frac{\mu}{r} \quad , \quad R = \frac{\mu}{2\,r^3} \left[\text{tr}\left[\tilde{\mathbf{I}}_1\right] + \text{tr}\left[\tilde{\mathbf{I}}_2\right] - 3\,\hat{\mathbf{r}}^T \left(\tilde{\mathbf{I}}_1 + \tilde{\mathbf{I}}_2 \right) \hat{\mathbf{r}} \right] \quad (4.8)$$

where $\mu = G\,(m_1 + m_2)$. With the correct alignment of the frame in which the mass-normalized moment of inertia dyad $\tilde{\mathbf{I}}_i$ is expressed to the respective body's principal axes, that dyad has only diagonal elements of I_{i_x}, I_{i_y}, I_{i_z}. The above is a simple representation for the mutual potential between the binary components only up to second degree and order, yet it proves sufficient for the analysis below.

4.2 Effect of Primary Oblateness on Mutual Orbit Elements

For the first analytical approach, approximate Alpha as an oblate body with rotational symmetry about the +Z axis of its own body-fixed frame, hence $I_{1_x} =$

$I_{1_y} = I_{eq} < I_{1_z}$. With this, the perturbation part of the simplified mutual potential representation becomes

$$R = \frac{\mu}{2\,r^3}\left[2\,I_{eq} + I_{1_z} + I_{2_x} + I_{2_y} + I_{2_z} - 3\,\hat{\mathbf{r}}^T\tilde{\mathbf{I}}_1\,\hat{\mathbf{r}} - 3\,\hat{\mathbf{r}}^T\tilde{\mathbf{I}}_2\,\hat{\mathbf{r}}\right]. \qquad (4.9)$$

How to model the rightmost part of this expression becomes the next issue. Consider either one of the bodies. Its body frame could be assumed to be aligned with the coordinate frame $(\hat{\mathbf{r}}\ ,\ \hat{\mathbf{r}}_T\ ,\ \hat{\mathbf{h}})$, composed of the previously defined unit vector $\hat{\mathbf{r}}$ pointing from the center of mass of body 1 to the center of mass of body 2, the unit vector $\hat{\mathbf{h}}$ normal to the orbital plane, and unit vector $\hat{\mathbf{r}}_T$ orthogonal to both of the other unit vectors. Or one can assume instead that the body's frame is aligned with the same $(\hat{\mathbf{r}}\ ,\ \hat{\mathbf{r}}_T\ ,\ \hat{\mathbf{h}})$ coordinate frame but then rotated by some additional angle ϕ about the $\hat{\mathbf{h}}$ unit vector of that frame. Or one can assume the more general case of three unit vectors $\hat{\mathbf{x}}$, $\hat{\mathbf{y}}$, and $\hat{\mathbf{z}}$ forming the body's frame expressed in inertial coordinates, $(\hat{\mathbf{x}}\ ,\ \hat{\mathbf{y}}\ ,\ \hat{\mathbf{z}})$. Or one can assume this plus a similar additional rotation by ϕ about the $\hat{\mathbf{z}}$ axis. Which of these four different cases for alignment of the body makes the most sense to use and leads to the cleanest formulation that captures the relevant characteristics of the problem may vary for each body. In the first case, given that the the vector $\hat{\mathbf{r}}$ is also expressed in inertial frame coordinates just like the dyad $\tilde{\mathbf{I}}_i$, then it is easy to see that $\hat{\mathbf{r}}^T\tilde{\mathbf{I}}_i\,\hat{\mathbf{r}} = I_{i_x}$. The same result is obtained for the second alignment case as for the first when 1) the body considered is Alpha under the oblate spheroid assumption and ϕ is any value or 2) the body considered is Beta and ϕ is some multiple of π. There is no simple expression coming from the third or fourth alignment cases above without additional assumptions. However, here too the fourth case gives the same (complicated) result as the third when 1) the body considered is oblate Alpha and ϕ is any value or 2) the body considered is Beta and ϕ is some integer multiple of π.

For later convenience, define the components of $\hat{\mathbf{r}}$ expressed in the inertial frame as functions of the orbital elements $(a, e, i, \Omega, \omega, \nu)$ according to the following:

$$\hat{\mathbf{r}} = \begin{bmatrix} \alpha_1 \\ \alpha_2 \\ \alpha_3 \end{bmatrix} = \begin{bmatrix} c(\Omega)\,c(\nu+\omega) - s(\Omega)\,s(\nu+\omega)\,c(i) \\ s(\Omega)\,c(\nu+\omega) + c(\Omega)\,s(\nu+\omega)\,c(i) \\ s(\nu+\omega)\,s(i) \end{bmatrix} \tag{4.10}$$

This introduces the shorthand notation $cos(\cdot) = c(\cdot)$ and $sin(\cdot) = s(\cdot)$. The above expressions can be obtained from the geometry of the instantaneous orbit frame $(\hat{\mathbf{r}}$, $\hat{\mathbf{r}}_T$, $\hat{\mathbf{h}})$ oriented relative to the inertial frame as illustrated in the left panel of Figure 4.1.

(a) Orientation of mutual orbit frame and relative position vector

(b) Orientation of Alpha spin frame
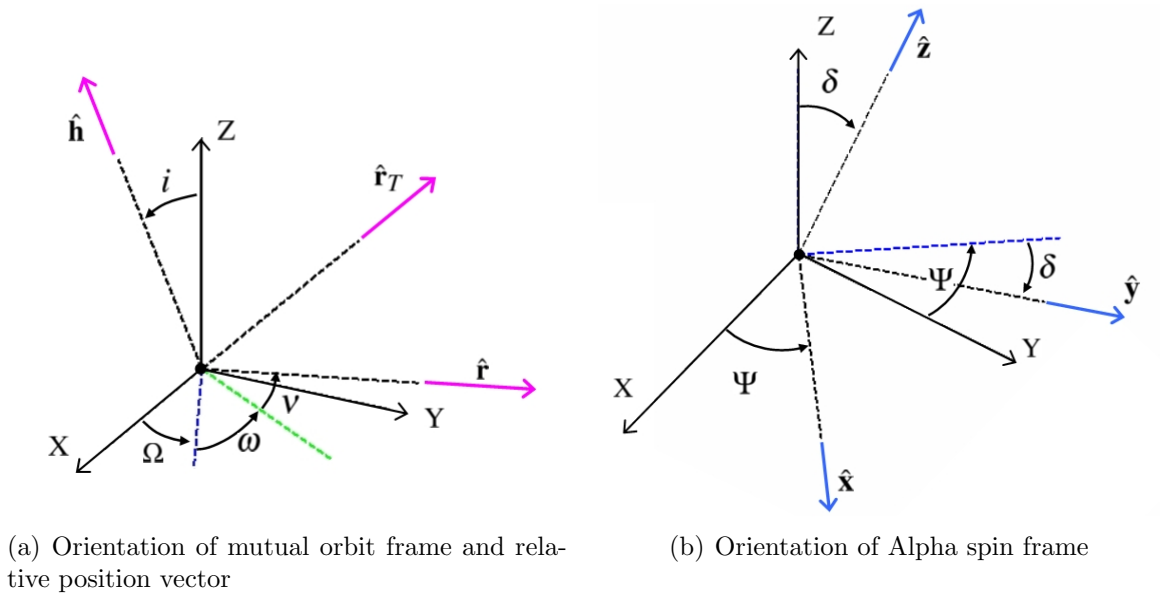
Figure 4.1: Illustration of angles orienting frames involved in analytical formulation for effects of Alpha oblateness.

With this background, one may specify an actual alignment for the bodies for this first analytical approach. Let the larger oblate body 1, Alpha, have a constantly changing angle ϕ as it rotates about its own spin axis, and use the fourth alignment case above with the $(\hat{\mathbf{x}}$, $\hat{\mathbf{y}}$, $\hat{\mathbf{z}})$ frame chosen so that the spin axis $\hat{\mathbf{z}}$ is tilted away from the total angular momentum vector by obliquity angle δ and has a projection in the

inertial frame's X-Y plane located by clock angle Ψ. This geometry is illustrated in the right panel of Figure 4.1. Next assume the smaller triaxial body 2, Beta, remains aligned with the orbit frame but then rotated by $\phi = 180°$, the second alignment case above. This is the assumption of locked synchronous rotation of Beta, which allows one to ignore Beta's triaxiality, because it means that $\hat{\mathbf{r}}^T \tilde{\mathbf{I}}_2 \hat{\mathbf{r}} = I_{2_x}$. Meanwhile the alignment of Alpha means the unit vector $\hat{\mathbf{r}}$ expressed in the frame of body 1 can be written as

$$
\hat{\mathbf{r}} = \begin{bmatrix} k_1\,c(\omega+\nu) + k_2\,s(\omega+\nu) \\ k_3\,c(\omega+\nu) + k_4\,s(\omega+\nu) \\ k_5\,c(\omega+\nu) + k_6\,s(\omega+\nu) \end{bmatrix}
$$

wherein the $k_1 \ldots k_6$ terms, that do not depend on the angles to be averaged over below, are

$$
k_1 = c(\Psi - \Omega) \quad , \quad k_2 = s(\Psi - \Omega)c(i),
$$

$$
k_3 = -s(\Psi - \Omega)c(\delta) \quad , \quad k_4 = c(\Psi - \Omega)c(\delta)c(i) - s(\delta)s(i),
$$

$$
k_5 = -s(\Psi - \Omega)s(\delta) \quad , \quad k_6 = c(\Psi - \Omega)s(\delta)c(i) + c(\delta)s(i).
$$

This allows for writing the perturbation potential for this setup as

$$
R = \frac{\mu}{2r^3}\Bigg[2I_{eq} + I_{1_z} + I_{2_y} + I_{2_z} - 2I_{2_x} - 3\Bigg(\left[(k_1^2 + k_3^2)\,I_{eq} + k_5^2 I_{1_z} \right] c^2(\omega+\nu)
$$

$$
+ \left[(2k_1 k_2 + 2k_3 k_4)\,I_{eq} + 2k_5 k_6 I_{1_z} \right] c(\omega+\nu)s(\omega+\nu)
$$

$$
+ \left[(k_2^2 + k_4^2)\,I_{eq} + k_6^2 I_{1_z} \right] s^2(\omega+\nu) \Bigg) \Bigg]. \tag{4.11}
$$

Next, one performs a "standard" averaging of this perturbation potential over one orbit, or over the interval $[0, 2\pi]$ in mean anomaly M. This involves averaging four collections of quantities which vary going around the orbit, that is four quantities which are powers and products of the sign and cosine of the longitude angle $\omega + \nu$

90

divided by the cube of the relative position vector's magnitude. It is fairly simple to show that the results of averaging these quantities are

$$\frac{1}{2\pi} \int_o^{2\pi} \frac{1}{r^3} \, dM \quad = \quad \frac{1}{a^3 \left(1 - e^2\right)^{\frac{3}{2}}} \tag{4.12}$$

$$\frac{1}{2\pi} \int_o^{2\pi} \frac{c^2(\omega + \nu)}{r^3} \, dM \quad = \quad \frac{1}{2 \, a^3 \left(1 - e^2\right)^{\frac{3}{2}}}, \tag{4.13}$$

$$\frac{1}{2\pi} \int_o^{2\pi} \frac{s^2(\omega + \nu)}{r^3} \, dM \quad = \quad \frac{1}{2 \, a^3 \left(1 - e^2\right)^{\frac{3}{2}}}, \tag{4.14}$$

$$\frac{1}{2\pi} \int_o^{2\pi} \frac{c(\omega + \nu) \, s(\omega + \nu)}{r^3} \, dM \quad = \quad 0. \tag{4.15}$$

It is seen that Eq. 4.11 can be factored such that

$$\overline{R} = \quad D_1 \left(\frac{1}{2\pi} \int_o^{2\pi} \frac{1}{r^3} dM \right) + D_2 \left(\frac{1}{2\pi} \int_o^{2\pi} \frac{c^2(\omega + \nu)}{r^3} dM \right)$$
$$+ D_3 \left(\frac{1}{2\pi} \int_o^{2\pi} \frac{s^2(\omega + \nu)}{r^3} dM \right) + D_4 \left(\frac{1}{2\pi} \int_o^{2\pi} \frac{c(\omega + \nu)s(\omega + \nu)}{r^3} dM \right) \tag{4.16}$$

where

$$D_1 \quad = \quad \frac{\mu}{2} \left(2I_{eq} + I_{1_z} + I_{2_y} + I_{2_z} - 2I_{2_x} \right) \tag{4.17}$$

$$D_2 \quad = \quad -\frac{3\mu}{2} \left[\left\{ k_1^2 + k_3^2 \right\} I_{eq} + k_5^2 I_{1_z} \right] \tag{4.18}$$

$$D_3 \quad = \quad -\frac{3\mu}{2} \left[\left\{ k_2^2 + k_4^2 \right\} I_{eq} + k_6^2 I_{1_z} \right] \tag{4.19}$$

and it is not necessary to be concerned with what D_4 is, because as Eq. 4.15 indicates, its contribution to the averaged $\overline{R}$ will be zero. One should plug back into D_2 and D_3 the full expressions for $k_1 \ldots k_6$ and expand to see where the orbital elements are within the whole $\overline{R}$ for this case, before going on to finding partial derivatives of that $\overline{R}$ with respect to those orbital elements, for use in the Lagrange Planetary Equations (LPEs). Doing this for D_2 first yields, after much simplification:

$$D_2 \quad = \quad -\frac{3\mu}{2} \left[I_{eq} + (I_{1_z} - I_{eq}) \, s^2(\Psi - \Omega) s^2(\delta) \right] \tag{4.20}$$

91

And similarly for D_3:

$$D_3 = -\frac{3\mu}{2}\left[I_{eq} + (I_{1_z} - I_{eq})\left\{s^2(\delta)c^2(i)c^2(\Psi - \Omega)\right.\right.$$

$$\left.\left. + 2c(\delta)s(\delta)c(i)s(i)c(\Psi - \Omega) + c^2(\delta)s^2(i)\right\}\right] \qquad (4.21)$$

Substitution then leads to the averaged perturbation potential in this case being

$$\overline{R} = \frac{2D_1 + D_2 + D_3}{2a^3(1 - e^2)^{\frac{3}{2}}}$$

$$\overline{R} = \frac{\mu}{2a^3(1 - e^2)^{\frac{3}{2}}}\left[(I_{1_z} - I_{eq})\left(1 - \frac{3}{2}\left\{s^2(\Psi - \Omega)s^2(\delta) + s^2(\delta)c^2(i)c^2(\Psi - \Omega)\right.\right.\right.$$

$$\left.\left.\left. + 2c(\delta)s(\delta)c(i)s(i)c(\Psi - \Omega) + c^2(\delta)s^2(i)\right\}\right) + I_{2_y} + I_{2_z} - 2I_{2_x}\right]. \qquad (4.22)$$

It is desired to use averaged perturbation potential within the Lagrange Planetary Equations (LPEs) for averaged time variation of the orbital elements $(a, e, i, \Omega, \omega, M)$ in terms of the perturbing potential. Here the mean motion of the system is $n = \sqrt{\mu/a^3}$, and the LPEs are:

$$\frac{da}{dt} = \frac{2}{n\,a}\left(\frac{\partial R}{\partial M}\right)$$

$$\frac{de}{dt} = \frac{1 - e^2}{n\,a^2\,e}\left(\frac{\partial R}{\partial M}\right) - \frac{\sqrt{1 - e^2}}{n\,a^2\,e}\left(\frac{\partial R}{\partial \omega}\right)$$

$$\frac{di}{dt} = \frac{1}{n\,a^2\,\sqrt{1 - e^2}}\left[cot(i)\left(\frac{\partial R}{\partial \omega}\right) - \frac{1}{s(i)}\left(\frac{\partial R}{\partial \Omega}\right)\right]$$

$$\frac{d\Omega}{dt} = \frac{1}{n\,a^2\,\sqrt{1 - e^2}}\left[\frac{1}{s(i)}\left(\frac{\partial R}{\partial i}\right)\right]$$

$$\frac{d\omega}{dt} = \frac{\sqrt{1 - e^2}}{n\,a^2\,e}\left(\frac{\partial R}{\partial e}\right) - \frac{cot(i)}{n\,a^2\,\sqrt{1 - e^2}}\left(\frac{\partial R}{\partial i}\right)$$

$$\frac{dM}{dt} = n - \frac{1 - e^2}{n\,a^2\,e}\left(\frac{\partial R}{\partial e}\right) - \frac{2}{n\,a}\left(\frac{\partial R}{\partial a}\right)$$

Using $\overline{R}$ within these instead of R should give the desired averaged, or mean, rates of change for the orbital elements. As an intermediate step, first write the partial

derivatives of the $\overline{R}$ of Eq. 4.22 with respect to the orbital elements:

$$\frac{\partial \overline{R}}{\partial a} = \frac{-3\mu}{2a^4(1-e^2)^{\frac{3}{2}}} \left[(I_{1_z} - I_{eq}) \left(1 - \frac{3}{2} \left\{ s^2(\Psi - \Omega)s^2(\delta) + s^2(\delta)c^2(i)c^2(\Psi - \Omega) \right. \right. \right.$$
$$\left. \left. \left. + 2c(\delta)s(\delta)c(i)s(i)c(\Psi - \Omega) + c^2(\delta)s^2(i) \right\} \right) + I_{2_y} + I_{2_z} - 2I_{2_x} \right] \quad (4.23)$$

$$\frac{\partial \overline{R}}{\partial e} = \frac{3\mu e}{2a^3(1-e^2)^{\frac{5}{2}}} \left[(I_{1_z} - I_{eq}) \left(1 - \frac{3}{2} \left\{ s^2(\Psi - \Omega)s^2(\delta) + s^2(\delta)c^2(i)c^2(\Psi - \Omega) \right. \right. \right.$$
$$\left. \left. \left. + 2c(\delta)s(\delta)c(i)s(i)c(\Psi - \Omega) + c^2(\delta)s^2(i) \right\} \right) + I_{2_y} + I_{2_z} - 2I_{2_x} \right] \quad (4.24)$$

$$\frac{\partial \overline{R}}{\partial i} = \frac{-3\mu}{4\,a^3\,(1-e^2)^{\frac{3}{2}}} (I_{1_z} - I_{eq}) \left\{ c(2\delta)s(2i) + s(2\delta)c(2i)c(\Psi - \Omega) \right.$$
$$\left. + s^2(\delta)s(2i)s^2(\Psi - \Omega) \right\} \quad (4.25)$$

$$\frac{\partial \overline{R}}{\partial \Omega} = \frac{-3\mu}{4\,a^3\,(1-e^2)^{\frac{3}{2}}} (I_{1_z} - I_{eq}) \left\{ 2s(\delta)s(i)s(\Psi - \Omega) \left[c(\delta)c(i) - s(i)s(\delta)c(\Psi - \Omega) \right] \right\}$$
$$(4.26)$$

$$\frac{\partial \overline{R}}{\partial \omega} = \frac{\partial \overline{R}}{\partial M} = 0 \quad (4.27)$$

It is also interesting to write the partials of $\overline{R}$ with respect to δ and Ψ:

$$\frac{\partial \overline{R}}{\partial \delta} = \frac{-3\mu}{4\,a^3\,(1-e^2)^{\frac{3}{2}}} (I_{1_z} + I_{eq}) \left\{ c(2i)s(2\delta) + s(2i)c(2\delta)c(\Psi - \Omega) \right.$$
$$\left. + s^2(i)s(2\delta)s^2(\Psi - \Omega) \right\} \quad (4.28)$$

$$\frac{\partial \overline{R}}{\partial \Psi} = \frac{-3\,\mu}{4\,a^3\,(1-e^2)^{\frac{3}{2}}} (I_{1_z} - I_{eq}) \left\{ 2s(\delta)s(i)s(\Psi - \Omega) \left[-c(\delta)c(i) + s(i)s(\delta)c(\Psi - \Omega) \right] \right\}$$
$$= -\frac{\partial \overline{R}}{\partial \Omega} \quad (4.29)$$

Considering Eq. 4.28, one sees that it is the same as the expression for $\partial \overline{R}/\partial i$ but with each instance of δ replaced by i and each instance of i replaced by δ. Whether this fact, and the fact that $\partial \overline{R}/\partial \Psi$ is the negative of $\partial \overline{R}/\partial \Omega$, convert respectively into having the rate in δ and the rate in i being the same except for an opposing sign and having the rate in Ψ and the rate in Ω be identically the same isn't yet obvious by itself. The rate in δ and the rate in i would be equal and opposite if the total offset between orbit normal and body 1 spin pole, $\Delta = i + \delta$, is actually constant.

Putting aside the numerical results presented earlier, this has not yet been suggested by the analysis. In any case, plugging Eqs. 4.23−4.27 into the actual LPEs makes the desired mean rates for the orbital elements come out to be:

$$\frac{\overline{\mathrm{d}a}}{\mathrm{d}t} = \frac{\overline{\mathrm{d}e}}{\mathrm{d}t} = 0 \tag{4.30}$$

$$\frac{\overline{\mathrm{d}i}}{\mathrm{d}t} = \frac{3\sqrt{\mu}}{2a^{\frac{7}{2}}(1-e^2)^2}\left(I_{1_z} - I_{eq}\right)\left\{s(\delta)s(\Psi - \Omega)\left[c(\delta)c(i) - s(i)s(\delta)c(\Psi - \Omega)\right]\right\} \tag{4.31}$$

$$\frac{\overline{\mathrm{d}\Omega}}{\mathrm{d}t} = \frac{-3\sqrt{\mu}}{2a^{\frac{7}{2}}(1-e^2)^2}\left(I_{1_z} - I_{eq}\right)\left\{c(2\delta)c(i)\right.$$
$$\left. + s(2\delta)\frac{c(2i)}{2s(i)}c(\Psi - \Omega) + s^2(\delta)c(i)s^2(\Psi - \Omega)\right\} \tag{4.32}$$

$$\frac{\overline{\mathrm{d}\omega}}{\mathrm{d}t} = \frac{3\sqrt{\mu}}{2a^{\frac{7}{2}}(1-e^2)^2}\left[\left(I_{1_z} - I_{eq}\right)\left\{1 - \frac{3}{2}s^2(\delta)s^2(\Psi - \Omega)\right.\right.$$
$$- \frac{3}{2}\left[s(\delta)c(i)c(\Psi - \Omega) + c(\delta)s(i)\right] + s^2(\delta)c^2(i)s^2(\Psi - \Omega)$$
$$\left.\left. + s(2\delta)c(i)c(\Psi - \Omega)\left(\frac{1}{2s(i)} - s(i)\right) + c(2\delta)c^2(i)\right\} + I_{2_y} + I_{2_z} - 2I_{2_x}\right] \tag{4.33}$$

$$\frac{\overline{\mathrm{d}M}}{\mathrm{d}t} = \sqrt{\frac{\mu}{a^3}} + \frac{3\sqrt{\mu}}{2a^{\frac{7}{2}}(1-e^2)^{\frac{3}{2}}}\left[\left(I_{1_z} - I_{eq}\right)\left(1 - \frac{3}{2}\left\{s^2(\Psi - \Omega)s^2(\delta)\right.\right.\right.$$
$$+ s^2(\delta)c^2(i)c^2(\Psi - \Omega) + 2c(\delta)s(\delta)c(i)s(i)c(\Psi - \Omega)$$
$$\left.\left.\left. + c^2(\delta)s^2(i)\right\}\right) + I_{2_y} + I_{2_z} - 2I_{2_x}\right] \tag{4.34}$$

The mean rate in M is not equal to just n, which implies the need to define a modified "effective" semimajor axis $\bar{a}$ using the mean rates in M and ω averaged over one orbit as above, rather than using osculating a itself at any epoch. So one can evaluate the last two of the above equations, then replace a in the right hand sides of all of the above equations with

$$\bar{a} = a\left(\frac{1}{\dot{\overline{M}}/n + \dot{\bar{\omega}}/n}\right)^{\frac{2}{3}}, \tag{4.35}$$

and then evaluate all of those equations again. Note that in the special case of nearly

94

circular mutual orbit motion ($e \approx 0$) and also the constraints $\Delta = i + \delta$ and $\Psi = \Omega$, the denominator in the above simplifies to

$$1 + \frac{3\left(I_{1_z} - I_{eq}\right)}{4a^2}\left(2c^2(i)c^2(\delta) + 1 + c^2(\delta) + s^2(i) + 2c(2\Delta)\right.$$

$$\left. -3s(\Delta) + s(2\delta)\frac{c^3(i)}{s(i)}\right) + \frac{3}{a^2}\left(I_{2_y} + I_{2_z} - 2I_{2_x}\right). \qquad (4.36)$$

The results obtained by this method agree with the average rates of change $\dot{\overline{\Omega}}$, $\dot{\overline{\omega}}$, and $\dot{\overline{M}}$ fitted to plotted numerical data, for each case having numerical simulation results covering long time periods. This is shown in Figures 4.2 and 4.3, which show the

(a) Right ascension of mutual orbit

(b) Clock angle of Alpha spin pole

(c) Inclination of mutual orbit

(d) Obliquity of Alpha spin pole
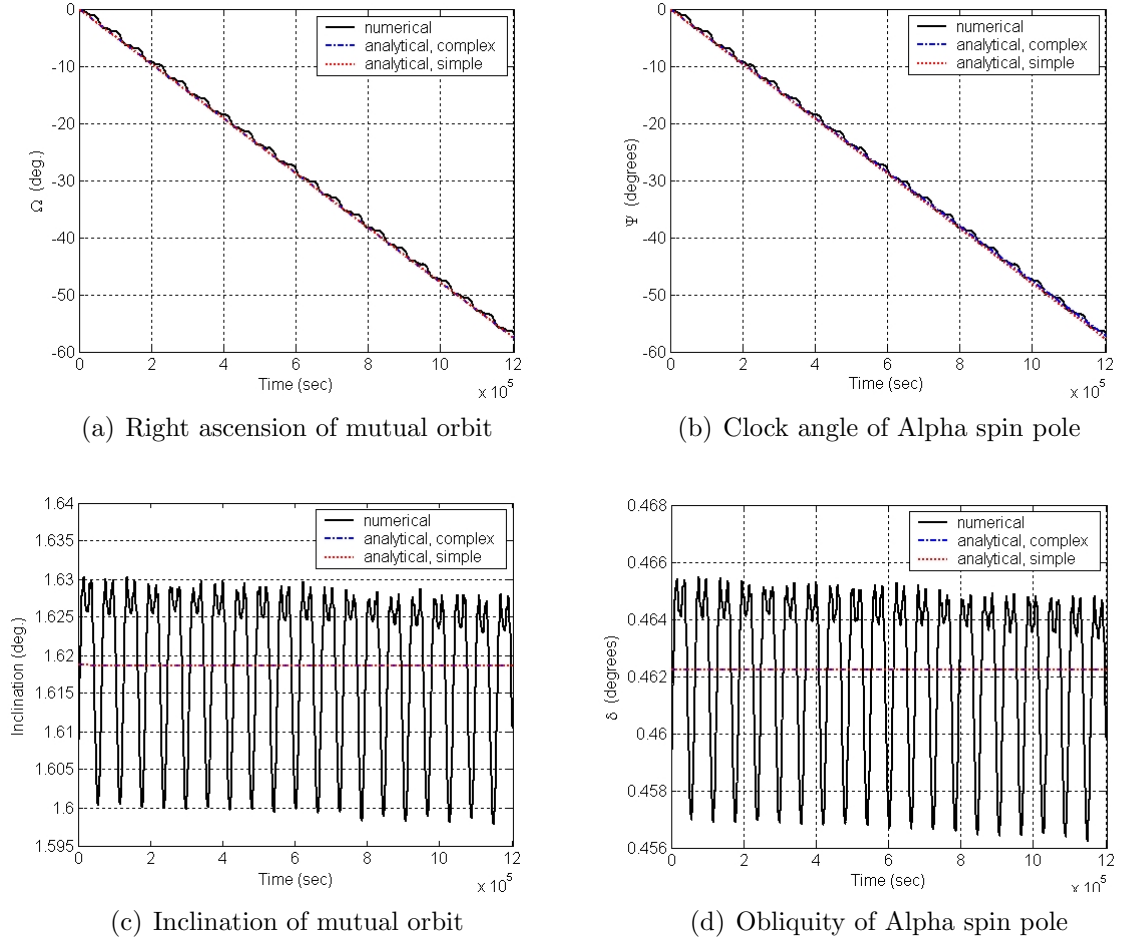
Figure 4.2: Comparison between numerical F2BP simulation output and mean rates of change computed by analytical formulae, most relaxed case. Here we use both the simple and more involved methods detailed at the end of sections 4.2 and 4.3, for case with (Δ_0 =2.06 deg, e_0 =0.0085, ν_0 =0 deg).

95

numerical results for time evolution of inclination and right ascension of ascending node of the orbit with linear curves superimposed that have slopes matching the rates calculated by the above formulae. The two different cases for the two figures vary in the level of energy excitation of the system (i.e. they are for initial conditions sets of $\{\Delta_0 = 2.06 \text{ deg}, e_0 = 0.0085, \nu_0 = 0 \text{ deg}\}$ and $\{\Delta_0 = 10.0 \text{ deg}, e_0 = 0.01, \nu_0 = 180 \text{ deg}\}$ respectively).
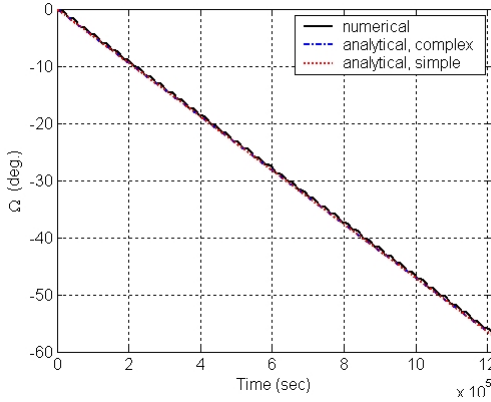
(a) Right ascension of mutual orbit
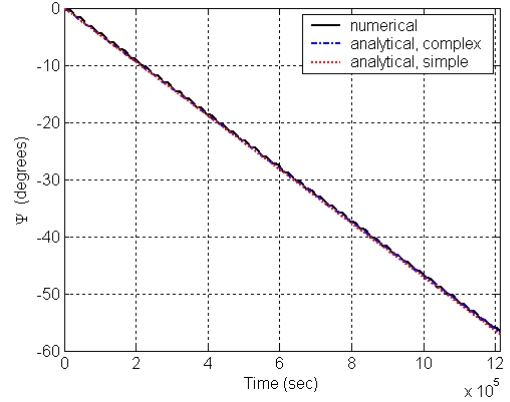
(b) Clock angle of Alpha spin pole
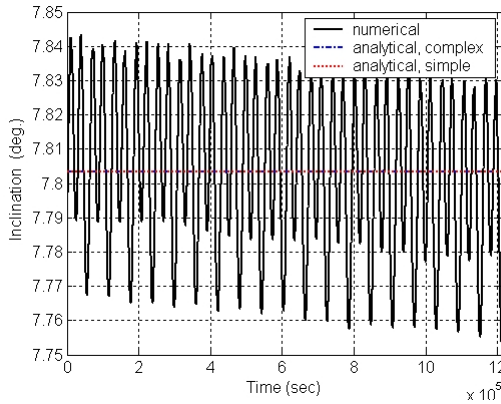
(c) Inclination of mutual orbit
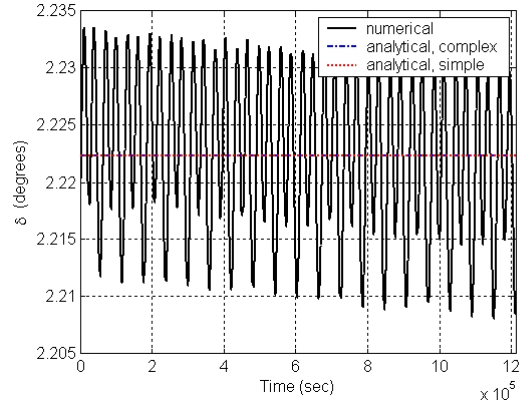
(d) Obliquity of Alpha spin pole

Figure 4.3: Comparison between numerical F2BP simulation output and mean rates of change computed by analytical formulae, most excited case. Here we use both the simple and more involved methods detailed at the end of sections 4.2 and 4.3, for case with ($\Delta_0 = 10.0$ deg, $e_0 = 0.01$, $\nu_0 = 180$ deg).

4.3 Effect of Primary Oblateness on Primary Spin Axis Orientation

Next turn to the analogous calculation of mean rates of change for the angles δ and Ψ defining the orientation of the spin axis of Alpha. The rate $\dot{\Psi}$ will represent a precession of Alpha's spin pole, and it is assumed at first that this is entirely independent of any precession of the orbit pole, notwithstanding the numerical results observed earlier and a general understanding of Cassini states. Thus any agreement that might eventually be obtained between the analytical formulae for the two precession rates will be an independent result.

The most basic equation to start with here is $\dot{\mathbf{H}}_1 = \mathbf{M}_1$ with $\mathbf{H}_1$ being the angular momentum vector of body 1, and $\mathbf{M}_1$ being the moment acting on body 1. Which frame this equation is written out with respect to makes a difference in the complexity of the result. If the inertial frame is used, then $\mathbf{M}_1 = [M_X \ \ M_Y \ \ M_Z]^T$. If the frame used is the frame fixed to body 1, then $\mathbf{M}_1 = [M_x \ \ M_y \ \ M_z]^T$. If the frame used is the precessing "spin" frame about whose third axis the body 1 spins with rate $\dot{\phi}$, then $\mathbf{M}_1 = [M_{x'} \ \ M_{y'} \ \ M_{z'}]^T$. The left hand side is simplest with the latter, for which

$$\mathbf{I}_1\dot{\boldsymbol{\omega}}_1 + \left(\boldsymbol{\omega}_1 - \begin{bmatrix} 0 & 0 & \dot{\phi} \end{bmatrix}^T\right) \times (\mathbf{I}_1\boldsymbol{\omega}_1) = \mathbf{M}_1. \tag{4.37}$$

Here

$$\boldsymbol{\omega}_1 = \begin{bmatrix} -\dot{\delta} \\ -\dot{\Psi}s(\delta) \\ \dot{\phi} + \dot{\Psi}c(\delta) \end{bmatrix}, \qquad \left(\boldsymbol{\omega}_1 - \begin{bmatrix} 0 & 0 & \dot{\phi} \end{bmatrix}^T\right) = \begin{bmatrix} -\dot{\delta} \\ -\dot{\Psi}s(\delta) \\ \dot{\Psi}c(\delta) \end{bmatrix}$$

are the angular velocity vector of body 1 relative to the inertial frame expressed in the spin frame and the angular velocity of the spin frame relative to the inertial frame expressed in the spin frame, respectively. (This is not to be confused with

the argument of periapsis ω). Recall that $\mathbf{I}_1 = m_1\tilde{\mathbf{I}}_1$ is the same in both the spin frame and body 1 frame due to the principal axes and oblate Alpha assumptions. Expanded, equation 4.37 is:

$$
\begin{aligned}
I_{eq}\left(-\ddot{\delta}\right) - \left(I_{1_z} - I_{eq}\right)\dot{\Psi}^2 c(\delta)s(\delta) - I_{1_z}\dot{\phi}\dot{\Psi}s(\delta) &= \frac{M_{x'}}{m_1} \\
I_{eq}\left(-\ddot{\Psi}s(\delta) - \dot{\delta}\dot{\Psi}c(\delta)\right) + \left(I_{1_z} - I_{eq}\right)\dot{\delta}\dot{\Psi}c(\delta) + I_{1_z}\dot{\delta}\dot{\phi} &= \frac{M_{y'}}{m_1} \qquad (4.38) \\
I_{1_z}\left(\ddot{\Psi}c(\delta) - \dot{\delta}\dot{\Psi}s(\delta) + \ddot{\phi}\right) &= \frac{M_{z'}}{m_1}
\end{aligned}
$$

If needed, one can use for the right hand side of the above either of

$$
\begin{bmatrix} \frac{M_{x'}}{m_1} \\[2mm] \frac{M_{y'}}{m_1} \\[2mm] \frac{M_{z'}}{m_1} \end{bmatrix} = \begin{bmatrix} \frac{M_x}{m_1}c(\phi) - \frac{M_y}{m_1}s(\phi) \\[2mm] \frac{M_x}{m_1}s(\phi) + \frac{M_y}{m_1}c(\phi) \\[2mm] \frac{M_z}{m_1} \end{bmatrix} ,
$$

$$
\begin{bmatrix} \frac{M_{x'}}{m_1} \\[2mm] \frac{M_{y'}}{m_1} \\[2mm] \frac{M_{z'}}{m_1} \end{bmatrix} = \begin{bmatrix} \frac{M_X}{m_1}c(\Psi) + \frac{M_Y}{m_1}s(\Psi) \\[2mm] -\frac{M_X}{m_1}c(\delta)s(\Psi) + \frac{M_Y}{m_1}c(\delta)c(\Psi) - \frac{M_Z}{m_1}s(\delta) \\[2mm] -\frac{M_X}{m_1}s(\delta)s(\Psi) + \frac{M_Y}{m_1}s(\delta)c(\Psi) + \frac{M_Z}{m_1}c(\delta) \end{bmatrix} .
$$

$$(4.39)$$

Now one has a choice about which frame to find and express the moment on body 1 with respect to and how to find that moment. Trying to obtain it, in analytically closed form, from the gradient of the second degree and order mutual potential as in Eq. 2.39 is not feasible especially once introducing the full expressions for the relative attitude matrix $\mathbf{T}$'s elements in terms of the angles involved in the geometric setup. Likewise infeasible is trying to obtain the moment on body 1 from time differentiation of both sides of the equation for total angular momentum of the system as expressed in the inertial frame. The latter produces moment expressions involving second time derivatives of the orbit angular motion variable $\lambda = \omega + \nu$, which makes the full equations obtained by substitution of the moment expressions through 4.39 into 4.38

not amenable to the usual method of averaging over λ.

A different approach is to go directly back to $\dot{\mathbf{H}}_1 = \mathbf{M}_1$ and to start over with a coordinate-independent formulation instead, recognizing that the derivative of the angular momentum vector of body 1 can be resolved into three orthogonal components. These components have magnitudes equal to the magnitude change of the angular momentum vector and the scaled $\dot{\Psi}$ and $\dot{\delta}$ rates being sought after, respectively. Also, at the beginning one may make the approximation of including in the analytical model herein only the portion of $\mathbf{M}_1$ due to gradients of mutual potential with respect to relative position, and not any portion of $\mathbf{M}_1$ due to gradients of mutual potential with respect to relative attitude. Thus one ignores the relative moment $\mathbf{M}$ of Eq. 2.40 and then according to Eq. 2.39 (accounting for the change of notation) $\mu_A \Leftrightarrow \mathbf{M}_1$ truncates to just

$$\mathbf{M}_1 = -\mathbf{r} \times \frac{\partial U}{\partial \mathbf{r}}. \tag{4.40}$$

So far in this chapter, expressions for the derivative of the mutual potential with respect to relative position, up to 2nd degree and order consistent with earlier assumptions of this analytical development, have not actually been directly written out. To do that, one starts with the mutual potential from Eq. 4.7,

$$
\begin{aligned}
U &= \frac{G\,m_1\,m_2}{r} + \frac{G\,m_1\,m_2}{2\,r^3}\left[\mathrm{tr}\!\left[\tilde{\mathbf{I}}_1\right] + \mathrm{tr}\!\left[\tilde{\mathbf{I}}_2\right] - 3\,\hat{\mathbf{r}}^T\left(\tilde{\mathbf{I}}_1 + \tilde{\mathbf{I}}_2\right)\hat{\mathbf{r}}\right] \\
&= \frac{G\,m_1\,m_2}{r} + \frac{G\,m_1\,m_2}{2\,r^3}\,J_2(\mathbf{r}).
\end{aligned}
\tag{4.41}
$$

This leads to

$$
\begin{aligned}
\mathbf{M}_1 &= \mathbf{r} \times -\frac{\partial}{\partial \mathbf{r}}\left(\frac{G\,m_1\,m_2}{r} + \frac{G\,m_1\,m_2}{2\,r^3}\,J_2\right) \\
&= -\mathbf{r} \times \left(\frac{-G\,m_1\,m_2}{r^3}\mathbf{r} - \frac{3\,G\,m_1\,m_2}{2\,r^5}\mathbf{r}\,J_2(\mathbf{r}) + \frac{G\,m_1\,m_2}{2\,r^3}\frac{\partial J_2(\mathbf{r})}{\partial \mathbf{r}}\right) \\
&= \frac{-G\,m_1\,m_2}{2\,r^3}\left(\mathbf{r} \times \frac{\partial J_2(\mathbf{r})}{\partial \mathbf{r}}\right)
\end{aligned}
$$

99

$$= \frac{-G\,m_1\,m_2}{2\,r^3} \left(\mathbf{r} \times \frac{\partial}{\partial \mathbf{r}} \left[\operatorname{tr}\!\left[\tilde{\mathbf{I}}_1\right] + \operatorname{tr}\!\left[\tilde{\mathbf{I}}_2\right] - 3\,\hat{\mathbf{r}}^T \left(\tilde{\mathbf{I}}_1 + \tilde{\mathbf{I}}_2 \right) \hat{\mathbf{r}} \right] \right)$$

$$= \frac{3\,G\,m_1\,m_2}{2\,r^3} \left(r\,\hat{\mathbf{r}} \times \frac{1}{r}\frac{\partial}{\partial \hat{\mathbf{r}}} \left(\hat{\mathbf{r}}^T \left(\tilde{\mathbf{I}}_1 + \tilde{\mathbf{I}}_2 \right) \hat{\mathbf{r}} \right) \right)$$

$$= \frac{3\,G\,m_1\,m_2}{r^3} \left(\hat{\mathbf{r}} \times \left(\tilde{\mathbf{I}}_1 + \tilde{\mathbf{I}}_2 \right) \hat{\mathbf{r}} \right). \tag{4.42}$$

For the left side of $\dot{\mathbf{H}}_1 = \mathbf{M}_1$, note that the derivative of the angular momentum vector of body 1 can be resolved as:

$$\dot{\mathbf{H}}_1 = \dot{H}_1\,\hat{\mathbf{H}}_1 + H_1\,\dot{\hat{\mathbf{H}}}_1 = \dot{H}_1\,\hat{\mathbf{H}}_1 + H_1\,s(\delta)\,\dot{\Psi}\,\mathbf{X} + H_1\,\dot{\delta}\,\mathbf{Y}. \tag{4.43}$$

Herein the unit vectors $\hat{\mathbf{H}}_1$, $\mathbf{X}$, and $\mathbf{Y}$ are all mutually orthogonal, and one can dot product both sides of $\dot{\mathbf{H}}_1 = \mathbf{M}_1$ with each one of these unit vectors to obtain

$$\dot{H}_1 = \hat{\mathbf{H}}_1 \cdot \mathbf{M}_1 \quad , \quad \dot{\Psi} = \frac{1}{s(\delta)\,H_1}\,\mathbf{X} \cdot \mathbf{M}_1 \quad , \quad \dot{\delta} = \frac{1}{H_1}\,\mathbf{Y} \cdot \mathbf{M}_1. \tag{4.44}$$

So far this has all been coordinate free or frame independent. Now when one must choose a frame to work in, it is simplest at the highest level to express the unit vectors with respect to the inertial frame, hence

$$\hat{\mathbf{H}}_1 = \begin{bmatrix} -s(\delta)s(\Psi) \\ s(\delta)c(\Psi) \\ c(\delta) \end{bmatrix}, \quad \mathbf{X} = \begin{bmatrix} -c(\Psi) \\ -s(\Psi) \\ 0 \end{bmatrix}, \quad \mathbf{Y} = \begin{bmatrix} -c(\delta)s(\Psi) \\ c(\delta)c(\Psi) \\ -s(\delta) \end{bmatrix}. \tag{4.45}$$

This can be seen graphically from the leftmost illustration in Figure 4.4. One must also express $\mathbf{M}_1$ in the inertial frame, so recalling all of the body alignment assumptions, from Eq. 4.42 one has

$$\mathbf{M}_1 = \frac{3\,G\,m_1\,m_2}{r^3} \begin{bmatrix} \alpha_1 \\ \alpha_2 \\ \alpha_3 \end{bmatrix} \times \left\{ \begin{bmatrix} c(\Psi) & -c(\delta)s(\Psi) & -s(\delta)s(\Psi) \\ s(\Psi) & c(\delta)c(\Psi) & s(\delta)c(\Psi) \\ 0 & -s(\delta) & c(\delta) \end{bmatrix} \begin{bmatrix} I_{eq} & 0 & 0 \\ 0 & I_{eq} & 0 \\ 0 & 0 & I_{1_z} \end{bmatrix} \right.$$

$$\cdot \begin{bmatrix} c(\Psi) & s(\Psi) & 0 \\ -c(\delta)s(\Psi) & c(\delta)c(\Psi) & -s(\delta) \\ -s(\delta)s(\Psi) & s(\delta)c(\Psi) & c(\delta) \end{bmatrix} \begin{bmatrix} \alpha_1 \\ \alpha_2 \\ \alpha_3 \end{bmatrix}$$

$$+ \begin{bmatrix} -\hat{\mathbf{r}} & -\hat{\mathbf{r}}_T & \hat{\mathbf{h}} \end{bmatrix} \begin{bmatrix} I_{2_x} & 0 & 0 \\ 0 & I_{2_y} & 0 \\ 0 & 0 & I_{2_z} \end{bmatrix} \begin{bmatrix} -\hat{\mathbf{r}}^T \\ -\hat{\mathbf{r}}_T^T \\ \hat{\mathbf{h}}^T \end{bmatrix} \hat{\mathbf{r}} \Bigg\},$$

$$\mathbf{M}_1 = \frac{3\,G\,m_1\,m_2}{r^3} \begin{bmatrix} \alpha_1 \\ \alpha_2 \\ \alpha_3 \end{bmatrix} \times \Bigg\{ \begin{bmatrix} c(\Psi) & -c(\delta)s(\Psi) & -s(\delta)s(\Psi) \\ s(\Psi) & c(\delta)c(\Psi) & s(\delta)c(\Psi) \\ 0 & -s(\delta) & c(\delta) \end{bmatrix}$$

$$\cdot \begin{bmatrix} I_{eq}\left(\alpha_1 c(\Psi) + \alpha_2 s(\Psi)\right) \\ I_{eq}\left(-\alpha_1 c(\delta)s(\Psi) + \alpha_2 c(\delta)c(\Psi) - \alpha_3 s(\delta)\right) \\ I_{1_z}\left(-\alpha_1 s(\delta)s(\Psi) + \alpha_2 s(\delta)c(\Psi) + \alpha_3 c(\delta)\right) \end{bmatrix} + \begin{bmatrix} \alpha_1 \\ \alpha_2 \\ \alpha_3 \end{bmatrix} I_{2_x} \Bigg\},$$

$$\mathbf{M}_1 = \frac{3\,G\,m_1\,m_2}{r^3}$$

$$\begin{bmatrix} \alpha_1 \\ \alpha_2 \\ \alpha_3 \end{bmatrix} \times \begin{bmatrix} (I_{eq}-I_{1_z})\left\{\alpha_1 c^2(\Psi) + \alpha_1 c^2(\delta)s^2(\Psi) + \alpha_2 s^2(\delta)c(\Psi)s(\Psi) + \alpha_3 c(\delta)s(\delta)s(\Psi)\right\} + I_{1_z}\alpha_1 \\ (I_{eq}-I_{1_z})\left\{\alpha_2 s^2(\Psi) + \alpha_2 c^2(\delta)c^2(\Psi) + \alpha_1 s^2(\delta)c(\Psi)s(\Psi) - \alpha_3 c(\delta)s(\delta)c(\Psi)\right\} + I_{1_z}\alpha_2 \\ (I_{eq}-I_{1_z})\left\{\alpha_3 s^2(\delta) + \alpha_1 c(\delta)s(\delta)s(\Psi) - \alpha_2 c(\delta)s(\delta)c(\Psi)\right\} + I_{1_z}\alpha_3 \end{bmatrix},$$

$$\mathbf{M}_1 = \frac{3\,G\,m_1\,m_2\,(I_{eq}-I_{1_z})}{r^3}$$

$$\begin{bmatrix} \left(\alpha_3^2-\alpha_2^2\right)c(\delta)s(\delta)c(\Psi) - \alpha_1\alpha_3 s^2(\delta)c(\Psi)s(\Psi) + \alpha_1\alpha_2 c(\delta)s(\delta)s(\Psi) + \alpha_2\alpha_3\left(s^2(\delta)c^2(\Psi) - c^2(\delta)\right) \\ \left(\alpha_3^2-\alpha_1^2\right)c(\delta)s(\delta)s(\Psi) + \alpha_1\alpha_3\left(c^2(\delta) - s^2(\delta)s^2(\Psi)\right) + \alpha_1\alpha_2 c(\delta)s(\delta)c(\Psi) + \alpha_2\alpha_3 s^2(\delta)c(\Psi)s(\Psi) \\ \frac{1}{2}\left(\alpha_1^2-\alpha_2^2\right)s^2(\delta)s(2\Psi) - \alpha_1\alpha_2 s^2(\delta)c(2\Psi) - \alpha_1\alpha_3 c(\delta)s(\delta)c(\Psi) - \alpha_2\alpha_3 c(\delta)s(\delta)s(\Psi) \end{bmatrix}. \quad (4.46)$$

Substituting this and the unit vector definitions of 4.45 into equations 4.44 yields a consistent set of equations $\dot{\mathbf{W}} = f(\mathbf{W}, \mathbf{Q})$, with "states" vector $\mathbf{W} = [\, H_1, \, \Psi, \, \delta\,]$ and "parameters" vector $\mathbf{Q} = [\, m_1, \, m_2, \, I_{1_z}, \, I_{eq}, \, r, \, \alpha_1, \, \alpha_2, \, \alpha_3 \,]$. It is the last four of these parameters that are expressions of the orbit elements.
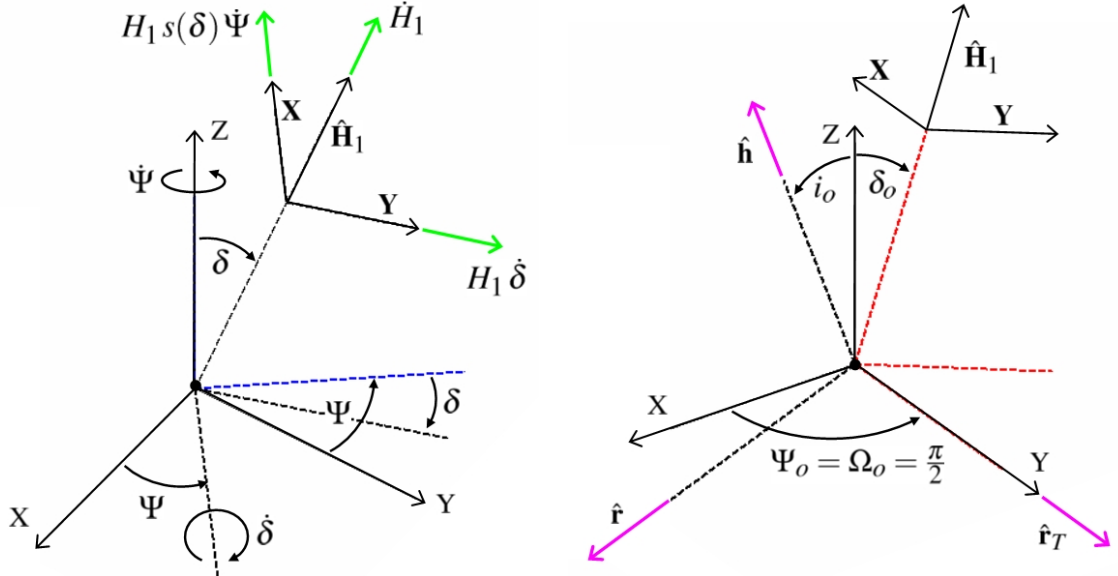
(a) Unit vectors and components of time rate of change of Alpha angular momentum vector $\mathbf{H}_1$

(b) Special alignment at one time instant for simple approach

Figure 4.4: Illustration of geometric setups for obtaining mean rates of the angles orienting Alpha's spin axis.

Just as in the last section, one can perform a standard averaging of these consistent equations over one orbital period of the system's motion. At the deepest level, this comes down to averaging the squares and products of the α_i's (components of $\hat{\mathbf{r}}$) divided by the cube of relative position magnitude, since that is the only part of these equations where the orbit elements appear. Recalling Eq. 4.10 and Eqs. 4.12$-$4.15, the results of this averaging process are:

$$\frac{1}{2\pi} \int_0^{2\pi} \frac{\alpha_1^2}{r^3} dM = \frac{c^2(\Omega) + c^2(i)s^2(\Omega)}{2\, a^3 \left(1 - e^2\right)^{\frac{3}{2}}} \tag{4.47}$$

$$\frac{1}{2\pi} \int_0^{2\pi} \frac{\alpha_2^2}{r^3} dM = \frac{s^2(\Omega) + c^2(i)c^2(\Omega)}{2\, a^3 \left(1 - e^2\right)^{\frac{3}{2}}} \tag{4.48}$$

102

$$\frac{1}{2\pi}\int_0^{2\pi}\frac{\alpha_3^2}{r^3}dM \;=\; \frac{s^2(i)}{2\,a^3\,(1-e^2)^{\frac{3}{2}}} \tag{4.49}$$

$$\frac{1}{2\pi}\int_0^{2\pi}\frac{\alpha_1\alpha_2}{r^3}dM \;=\; \frac{s^2(i)c(\Omega)s(\Omega)}{2\,a^3\,(1-e^2)^{\frac{3}{2}}} \tag{4.50}$$

$$\frac{1}{2\pi}\int_0^{2\pi}\frac{\alpha_1\alpha_3}{r^3}dM \;=\; \frac{-c(i)s(i)s(\Omega)}{2\,a^3\,(1-e^2)^{\frac{3}{2}}} \tag{4.51}$$

$$\frac{1}{2\pi}\int_0^{2\pi}\frac{\alpha_2\alpha_3}{r^3}dM \;=\; \frac{c(i)s(i)c(\Omega)}{2\,a^3\,(1-e^2)^{\frac{3}{2}}} \tag{4.52}$$

Substitution of these into equation 4.46 and use of that with 4.45 in the first of equations 4.44 yields, after significant simplification:

$$\dot{H}_1 = 0 \implies H_1 = \text{constant} \tag{4.53}$$

Then from the second two of Eqs. 4.44, treating the Alpha angular momentum magnitude as a constant,

$$\dot{\bar{\Psi}} \;=\; \frac{3\,G\,m_1\,m_2\,(I_{eq}-I_{1_z})}{2\,a^3\,(1-e^2)^{\frac{3}{2}}\,H_1}\Big\{c(\delta)\left[c^2(i)-s^2(i)c^2(\Omega)\right]$$
$$+\,c(\delta)s(\Psi)s^2(i)s(\Psi-2\Omega)\,+\,c(2\delta)c(i)s(i)c(\Psi-\Omega)/s(\delta)\Big\}, \tag{4.54}$$

$$\dot{\bar{\delta}} \;=\; \frac{3\,G\,m_1\,m_2\,(I_{eq}-I_{1_z})}{2\,a^3\,(1-e^2)^{\frac{3}{2}}\,H_1}\Big\{-s(\delta)s^2(i)c(\Psi-\Omega)s(\Psi-\Omega)+c(\delta)c(i)s(i)s(\Psi-\Omega)\Big\}. \tag{4.55}$$

These two already averaged equations can then be solved together once nominal values for all orbital elements, angles, Alpha inertia dyad diagonal elements, and other mass properties are inserted. In particular, one can use an iterative method leveraging the contraction mapping principle. First take initial guesses for what $\dot{\bar{\delta}}$ and $\dot{\bar{\Psi}}$ are and use those to get an initial guess value for the constant scalar H_1 using the expression for that within the body 1 frame:

$$H_1 \;=\; \left(\mathbf{H}_1^T\mathbf{H}_1\right)^{\frac{1}{2}} \;=\; \left(m_1^2 I_{eq}^2\dot{\delta}^2 + m_1^2 I_{eq}^2\dot{\Psi}^2 s^2(\delta) + m_1^2 I_{1_z}^2\left[\dot{\phi}^2 + 2\,\dot{\phi}\dot{\Psi}c(\delta) + \dot{\Psi}^2 c^2(\delta)\right]\right)^{\frac{1}{2}} \tag{4.56}$$

Then one evaluates Eqs. 4.54, 4.55 again and repeats with the new $\dot{\bar{\delta}}$ and $\dot{\bar{\Psi}}$, and so on until the mean angular rates stop changing from iteration to iteration.

Doing this for each case having numerical simulation results covering long time periods, and comparing the results against the average rates of change $\dot{\bar{\delta}}$ and $\dot{\bar{\Psi}}$ fitted to the plotted numerical data, one can see that the formulation of this section, together with the final equations of section 4.2, finally produces most of the expected agreements. That is, the inclination and δ (alpha obliquity angle) mean rates are both nearly zero or five to six orders of magnitude less than any other rates, within both the numerical and analytical results. And the mean rates in Ω and Ψ are just about equal, within the numerical results, within the analytical results, and also between the analytical and numerical results.

As a much simpler alternative to the above, one can make an adaptation to the previous method by examining the system just at one particular instant in time, at which a special alignment occurs, but without any loss of generality for the results. Stated more formally, one can assume that the mean rates of all orbit elements and of the body 1 spin pole orientation angles at this one time are the same mean rates that hold at all other times. The instant in question is the moment when both the line between the centers of mass for the two bodies (the line of syzygy) and the tilted orbit normal vector lie in the X-Z plane of the inertial reference frame having its +Z axis parallel to the total angular momentum. **NO** restriction of the angular momentum vector of body 1 (or Alpha's spin pole) to also lie in the X-Z plane, tilted opposite the orbit normal, is being made yet. Instead, this is just evaluating the "$\mathbf{r}$ crossed with force term" expression for $\mathbf{M}_1$ on the right hand side of the $\dot{\mathbf{H}}_1 = \mathbf{M}_1$ equation at this particular instant in time, and that is acceptable because there are no dynamics in that force evaluation. At this instant, $\Omega = \pi/2$ and $\omega + \nu = -\pi/2$, and one can

obtain from Eq. 4.10 (or observe directly from the geometry shown in the rightmost illustration in Figure 4.4) that $\hat{\mathbf{r}} = [\alpha_1 , \alpha_2 , \alpha_3]^T = [c(i) , 0 , -s(i)]^T$, so with this the un-averaged equation 4.46 simplifies to

$$\mathbf{M}_1 = \frac{3\,G\,m_1\,m_2\,(I_{eq} - I_{1_z})}{r^3} \begin{bmatrix} s(i)^2 c(\delta)s(\delta)c(\Psi)+c(i)s(i)s^2(\delta)c(\Psi)s(\Psi) \\ \\ \left(s(i)^2-c(i)^2\right)c(\delta)s(\delta)s(\Psi)-c(i)s(i)\left(c^2(\delta)-s^2(\delta)s^2(\Psi)\right) \\ \\ c(i)^2 s^2(\delta)c(\Psi)s(\Psi)+c(i)s(i)c(\delta)s(\delta)c(\Psi) \end{bmatrix} \quad (4.57)$$

Now assume that at this time instant, it is also true that the angle $\Psi = \pi/2$. This means that the orbit normal and body 1 spin axis are coplanar with the total angular momentum vector, but just at this one instant (no results of dynamics are incorporated into this yet). The above then simplifies to

$$\mathbf{M}_1 = \frac{3\,G\,m_1\,m_2\,(I_{1_z} - I_{eq})}{r^3} \begin{bmatrix} 0 \\ \\ c(\delta + i)s(\delta + i) \\ \\ 0 \end{bmatrix} \quad (4.58)$$

and it seems that there is only a Y-component (in the inertial reference frame) for this moment on Alpha. With the current special alignment at just this one instant in time, the unit vectors are

$$\hat{\mathbf{H}}_1 = \begin{bmatrix} -s(\delta) \\ \\ 0 \\ \\ c(\delta) \end{bmatrix}, \quad \mathbf{X} = \begin{bmatrix} 0 \\ \\ -1 \\ \\ 0 \end{bmatrix}, \quad \mathbf{Y} = \begin{bmatrix} -c(\delta) \\ \\ 0 \\ \\ -s(\delta) \end{bmatrix} \quad (4.59)$$

and taking the dot products of these with the above moment on body 1 as in Eqs. 4.44, and then doing the averaging over the orbital period gives

$$\dot{\bar{H}}_1 = 0, \quad \dot{\bar{\delta}} = 0, \quad \dot{\bar{\Psi}} = \frac{-\,3\,G\,m_1\,m_2\,(I_{1_z} - I_{eq})\,c(\delta + i)s(\delta + i)}{2\,a^3\,(1 - e^2)^{\frac{3}{2}}\,H_1\,s(\delta)}. \quad (4.60)$$

According to the earlier stipulations that angle $\Psi = \pi/2$, and that the orbit normal and spin vector are tilted in opposite directions from the inertial +Z-axis, in the same

plane, at just that particular moment in time, one has that

$$H_1\, s(\delta) \;=\; m\,\sqrt{\mu\,p}\; s(i)$$

$$H_1 \;=\; \frac{m\,\sqrt{\mu}a^{\frac{1}{2}}\,(1-e^2)^{\frac{1}{2}}\,s(i)}{s(\delta)} \qquad\qquad (4.61)$$

such that

$$\dot{\overline{\Psi}} \;=\; -\frac{3\sqrt{\mu}}{2\,a^{\frac{7}{2}}\,(1-e^2)^2}\,(I_{1_z}-I_{eq})\,\frac{c(\delta+i)s(\delta+i)}{s(i)} \qquad\qquad (4.62)$$

It is seen that this matches up perfectly with the final equation for $\mathrm{d}\Omega\,/\,\mathrm{d}t$ at the end

of section 4.2, after the same alignment stipulation of $\Psi = \Omega$ is taken into account

within that. The interpretation of all of this is that **if** one happens to have the

alignment specified here in this section, with coplanar momenta vectors and relative

position vector, at some initial time, then that alignment of coplanar momenta vectors

is preserved over all times due to the identical angular mean rates. Likewise if there

is a poles offset at the initial time, Δ, this remains the same for all times thereafter.

Looking at all average rates of change as fitted to the plotted numerical data for

each case having numerical simulation results covering a long enough time-span, it

is seen that the much simpler method here, as opposed to the prior iterative solu-

tion scheme, also gives us most of the expected agreements together with the final

equations of section 4.2. That is, the inclination and δ (alpha obliquity angle) mean

rates are again nearly zero or several orders of magnitude less than any other rates

within both the numerical and analytical results. And the mean rates in Ω and Ψ

are approximately equal in the numerical results, also matching each way with the

identically equal analytical result for those mean rates. This agreement is also shown,

for using both the complex and simpler analytical methods of this section, in Figures

4.2 and 4.3 for relaxed and excited cases, respectively. These show numerical results

for time evolution of obliquity and Alpha spin pole clock angle (Ψ) with linear curves

superimposed that have slopes matching the rates calculated by the above formulae, using both of the methods. These plots demonstrate that the analytical formulae developed in this and the last section recover accurately the longest period mode of motion for this general class of binary asteroid systems, as it was revealed through the detailed F2BP simulation.

As a few final notes here, the results of this and the last section analytically verify the existence of, and analytically give the co-precession rate for, the numerically observed generalized Cassini state 2 occupied by the real system. This Cassini state 2 is different from that considered in most all previously published treatments of Cassini states in that it involves co-precession of the larger primary's spin and the mutual orbit rather than co-precession of the smaller satellite's spin and that satellite's orbit about the primary. Also unlike other treatments, in the development above one does not eliminate at the start the shape effects of the body whose spin is not involved in the Cassini state being examined (here this is Beta, in other treatments Alpha) by dropping out the matching half of the original mutual potential expression of Eq. 4.6. Instead Beta is simply locked to alignment with the mutual orbit, and that results in elimination of any Beta inertia elements through the steps to reach Eq. 4.46. In this sense, the treatment herein can be considered more general. Looking at the final precession rate result, it is seen that it can be rewritten as

$$\dot{\Omega} \; = \; \dot{\Psi} \; = \; -\frac{3}{2} \frac{n^2 \; (I_{1_z} - I_{eq}) \; c(\Delta)s(\Delta)}{n \, p^2 \; s(i)} \tag{4.63}$$

where p here is the semi-latus rectum of the orbit. Note that this rate is essentially a torque proportional to the inertia difference $(I_{1_z} - I_{eq})$, which captures the primary oblateness, divided by $n \, p^2 \, s(i)$, which is the projection of the **orbit's** angular momentum onto the invariant plane normal to the total angular momentum vector, and can be viewed as resistance to that torque. Almost all other treatments treat the Cassini

107

state (involving the satellite and orbit instead) as a similar torque proportional to the inertia difference representing **satellite** oblateness, divided by the projection of the **satellite's** spin-axis angular momentum component onto the same invariant plane. Thus the other treatments' rate expressions involve $(I_{2_z} - I_{2\ eq})/I_{2_z}$ instead. It is clear from balancing of angular momentum projections in the invariant plane that in the present ideal case $\dot{\phi}\,I_{1_z}\,sin(\delta) \approx n\,p^2\,s(i)$, and by substitution into Eq. 4.63 the other treatments can be reconciled with ours, allowing for the fact that herein Alpha's and not Beta's spin is in co-precession with the orbit. Alternatively writing Eq. 4.63 as

$$\dot{\Omega} = \dot{\Psi} = -\gamma\frac{c(\Delta)s(\Delta)}{s(i)} \quad \text{with} \quad \gamma = \frac{3}{2}\left(\frac{\sqrt{\mu}}{a^{\frac{7}{2}}\left(1-e^2\right)^2}\right)\left(I_{1_z} - I_{eq}\right), \quad (4.64)$$

it is seen that collection γ would be a constant precession factor of the familiar sort only if the orbit is constant. The period for the precession motion, which is in turn the longest period evident in the system's different dynamical modes, is extremely short compared to the tidal evolution timescale, so that one could neglect all changes to the orbit due to tidal evolution. However, in general the orbit is not constant. As a final note, it is found that at least for the KW4 system the parameter $|\dot{\Omega}|/\gamma$ has a value sufficiently high that, by comparison with a treatment such as Gladman et al [67], the variant of the Cassini state 2 that the system is currently in is expected to be stable under long-term tidal evolution. However, a rigorous analysis of this has yet to be performed.

4.4 Effect of Secondary Triaxiality on Librational Dynamics of the Secondary

For the second major analytical approach of this chapter, the effects of Beta's triaxiality on the shorter period modes of motion for the binary system are exam-

ined, while ignoring Alpha's aspherical shape. One starts by considering a co-orbiting relative equilibrium corresponding to an idealized case with all shape information of Alpha suppressed and perfect synchronous rotation of Beta, itself exhibiting shape and mass concentration symmetry about at least two Beta principle axis planes. This relative equilibrium is a much more relaxed configuration than any possible configuration still consistent with the true system's full shape detail. But about this relative equilibrium, one can use variations to obtain an approximate linear time-invariant perturbation dynamics system with nine states (deviations in relative position, relative velocity, and Beta angular velocity vectors). Next one allows Beta to not have perfect synchronous rotation and deviate from this aligned equilibrium such that its triaxial shape does have an effect, but assumes such divergence is small so that the dynamics of the ensuing motion are adequately described by the linear perturbation dynamics system. The dimension of this system can be reduced by one through application of the conservation of total angular momentum, and for the eight states left, there are four oscillatory modes of motion manifested by the system, with frequencies denoted ω_i, $i \in \{a, b, c, d\}$. It is desired to develop analytic expressions for these mode frequencies.

For a first cut analysis, one can use the simplest model which may still include the pertinent features that need to be exploited, i.e. one can merely model Alpha as a sphere and Beta with a second degree-and-order gravity field. Hence, from the earlier mutual potential expression of Eq. 4.7, assuming $I_{1_x} = I_{1_y} = I_{1_z} = I_{\mathrm{sph}}$:

$$U = \frac{G\,m_1\,m_2}{r} + \frac{G\,m_1\,m_2}{2\,r^3} \left[\mathrm{tr}\!\left[\tilde{\mathbf{I}}_2 \right] - 3\,\hat{\mathbf{r}}^T\,\tilde{\mathbf{I}}_2\,\hat{\mathbf{r}} \right] \tag{4.65}$$

Due to the symmetry of the Beta model here it is found that, with virtually no modification, one can apply the formulation presented in Fahnestock and Scheeres [68] and refined in Fahnestock and Scheeres [6] for the case of a large spacecraft secondary and

an asteroidal primary in a hybrid natural/artificial binary system. This formulation starts from equations of motion for the relative position, relative velocity, and Beta angular velocity vectors that are written in the frame of Beta, i.e.

$$\mathbf{r}'' + \boldsymbol{\omega}_2' \times \mathbf{r} + 2\boldsymbol{\omega}_2 \times \mathbf{r}' + \boldsymbol{\omega}_2 \times \boldsymbol{\omega_2} \times \mathbf{r} = \partial u/\partial \mathbf{r} \tag{4.66}$$

$$\tilde{\mathbf{I}}_2 \boldsymbol{\omega_2'} + \boldsymbol{\omega_2} \times \tilde{\mathbf{I}}_2 \boldsymbol{\omega_2} = \zeta \mathbf{r} \times (-\partial u/\partial \mathbf{r}), \tag{4.67}$$

in which the relative position vector $\mathbf{r}$ with direction $\hat{\mathbf{r}}$ and magnitude r is henceforth switched to being from the centroid of Beta to the centroid of Alpha. These equations are fully normalized, using the length scale R_o and the time scale $\sqrt{G(m_1 + m_2)/R_o^3}$, so that $'$ denotes differentiation in the new time scale and the normalized potential u in the above is, for the case being addressed here,

$$u = \frac{1}{r} + \frac{1}{2\,r^3}\left[I_{2_x} + I_{2_y} + I_{2_z} - 3\,\hat{\mathbf{r}}^T\,\tilde{\mathbf{I}}_2\,\hat{\mathbf{r}}\right] \tag{4.68}$$

The previous values for the I_{2_i} inertia elements have been divided by R_o^2 to get the new values for the I_{2_i}'s used in Eq. 4.68 and hereafter. Let the unit vectors $(\hat{\mathbf{i}}, \hat{\mathbf{j}}, \hat{\mathbf{k}})$ form the Beta-fixed frame so that $\hat{\mathbf{i}}$ points from Beta's centroid in the outward direction along the Beta principle axis closest to parallel with the instantaneous orbital radius vector. Due to the symmetry of Beta, in this frame and at the relative equilibrium the vectors $\mathbf{r}$ and $\partial u/\partial \mathbf{r}$ both have components only in the $\hat{\mathbf{i}}$ direction, denoted x and u_x respectively. Likewise, due to the assumed symmetry of Beta about the X-Y and X-Z planes, at the relative equilibrium currently being addressed the matrix $\partial^2 u/\partial \mathbf{r}^2$ has nonzero elements only on its diagonal, denoted u_{xx}, u_{yy}, and u_{zz} respectively. Further, $\boldsymbol{\omega}_2$ becomes the constant rate of orbital mean motion about $\hat{\mathbf{k}}$, equal to unity with proper choice of R_o for the normalization. Thus the five scalars needed along with the inertia elements and the mass fraction $\zeta = m_1/(m_1 + m_2)$ to completely describe

110

the perturbation dynamics system are

$$x = -1 \quad , \quad u_x = 1 - 3I_{2_x} + \frac{3}{2}I_{2_y} + \frac{3}{2}I_{2_z} \quad , \quad u_{xx} = 2 - 12I_{2_x} + 6I_{2_y} + 6I_{2_z}$$

(4.69)

$$u_{yy} = -1 + \frac{3}{2}\left[4I_{2_x} - 3I_{2_y} - I_{2_z}\right] \quad , \quad u_{zz} = -1 + \frac{3}{2}\left[4I_{2_x} - I_{2_y} - 3I_{2_z}\right].$$

(4.70)

The plant matrix of that linear system is itself [68, 6]:

$$
\left[
\begin{array}{ccc|ccc|ccc}
\multicolumn{3}{c|}{\mathbf{0}_{3\times3}} & \multicolumn{3}{c|}{\mathbf{U}_{3\times3}} & \multicolumn{3}{c}{\mathbf{0}_{3\times3}} \\
\hline
1 + u_{xx} & 0 & 0 & 0 & 2 & 0 & 0 & 0 & 2\,x \\
0 & 1 + u_{yy} - \frac{\zeta\,x}{I_{2_z}}\left(u_x - x\,u_{yy}\right) & 0 & -2 & 0 & 0 & 0 & 0 & 0 \\
0 & 0 & u_{zz} - \frac{\zeta\,x}{I_{2_y}}\left(u_x - x\,u_{zz}\right) & 0 & 0 & 0 & -x + \frac{x(I_{2_z}-I_{2_x})}{I_{2_y}} & 0 & 0 \\
\hline
0 & 0 & 0 & & & & 0 & \frac{\left(I_{2_y}-I_{2_z}\right)}{I_{2_x}} & 0 \\
0 & 0 & -\frac{\zeta}{I_{2_y}}\left(u_x - x\,u_{zz}\right) & \multicolumn{3}{c|}{\mathbf{0}_{3\times3}} & \frac{(I_{2_z}-I_{2_x})}{I_{2_y}} & 0 & 0 \\
0 & \frac{\zeta}{I_{2_z}}\left(u_x - x\,u_{yy}\right) & 0 & & & & 0 & 0 & 0 \\
\end{array}
\right]
$$

(4.71)

in which $\boldsymbol{\omega}_2 = 1\hat{\mathbf{k}}$ has already been used. Here $\mathbf{U}_{3\times3}$ and $\mathbf{0}_{3\times3}$ are the identity dyad and zeros matrix, respectively. This plant matrix has one zero eigenvalue for the state to be eliminated, and for the eight eigenvalues of the eight remaining states, the frequencies of the four pure oscillatory modes are given by:

$$
\begin{aligned}
\omega_a^2, \omega_b^2 &= -\frac{1}{2}\left[2 - u_{xx} - u_{yy} + \frac{\zeta\,x}{I_{2_z}}\left(u_x - x\,u_{yy}\right)\right] \\
&\quad \pm \frac{1}{2}\left\{\left[2 - u_{xx} - u_{yy} + \frac{\zeta\,x}{I_{2_z}}\left(u_x - x\,u_{yy}\right)\right]^2 \right. \\
&\quad \left. -4\left[\frac{4\zeta x}{I_{2_z}}\left(u_x - x\,u_{yy}\right) + \left(1 + u_{yy} - \frac{\zeta\,x}{I_{2_z}}\left(u_x - x\,u_{yy}\right)\right)\left(1 + u_{xx}\right)\right]\right\}^{\frac{1}{2}},
\end{aligned}
$$

(4.72)

111

$$\omega_c^2, \omega_d^2 = -\frac{1}{2}\left[-\frac{\left(I_{2_y} - I_{2_z}\right)\left(I_{2_z} - I_{2_x}\right)}{I_{2_x}I_{2_y}} - u_{zz} + \frac{\zeta\,x}{I_{2_y}}\left(u_x - x\,u_{zz}\right)\right]$$

$$\pm \frac{1}{2}\left\{\left[-\frac{\left(I_{2_y} - I_{2_z}\right)\left(I_{2_z} - I_{2_x}\right)}{I_{2_x}I_{2_y}} - u_{zz} + \frac{\zeta\,x}{I_{2_y}}\left(u_x - x\,u_{zz}\right)\right]^2\right.$$

$$-4\left[\frac{\left(I_{2_y} - I_{2_z}\right)\left(I_{2_z} - I_{2_x}\right)}{I_{2_x}I_{2_y}}\left(u_{zz} - \frac{\zeta\,x}{I_{2_y}}\left(u_x - x\,u_{zz}\right)\right)\right.$$

$$\left.\left.-\frac{\left(I_{2_y} - I_{2_z} + I_{2_x}\right)\left(I_{2_y} - I_{2_z}\right)\zeta\,x}{I_{2_y}^2 I_{2_x}}\left(u_x - x\,u_{zz}\right)\right]\right\}^{\frac{1}{2}}. \qquad (4.73)$$

Next one can define three constants for the system as three rational combinations of the inertia dyad elements related to one another through a nice permutation relationship, as follows:

$$\kappa_1 = \frac{I_{2_x} - I_{2_z}}{I_{2_y}} \qquad , \qquad \kappa_2 = \frac{I_{2_y} - I_{2_x}}{I_{2_z}} \qquad , \qquad \kappa_3 = \frac{I_{2_z} - I_{2_y}}{I_{2_x}} \qquad (4.74)$$

Then after working through the algebra following substitution of 4.69-4.70 into Eq. 4.72 and 4.73, the four mode frequencies are for this current scenario:

$$\omega_a^2, \omega_b^2 = \left[\frac{-12I_{2_x} + 3I_{2_y} + 9I_{2_z}}{4} - \frac{1}{2} - \frac{3}{2}\zeta\kappa_2\right] \pm \left[\frac{9}{4}\left(\frac{12I_{2_x} - 7I_{2_y} - 5I_{2_z}}{2} - \zeta\kappa_2\right)^2\right.$$

$$\left.+\frac{3}{4}\left(-20I_{2_x} + 17I_{2_y} + 3I_{2_z}\right) - \frac{3}{2}\zeta\kappa_2 + \frac{1}{4}\right]^{\frac{1}{2}} \qquad (4.75)$$

$$\omega_c^2, \omega_d^2 = \left[\frac{12I_{2_x} - 3I_{2_y} - 9I_{2_z}}{4} - \frac{1}{2} + \frac{\kappa_1\kappa_2}{2} + \frac{3}{2}\zeta\kappa_1\right]$$

$$\mp \left[\left(\frac{-12I_{2_x} + 3I_{2_y} + 9I_{2_z}}{4} + \frac{1}{2} + \frac{\kappa_1\kappa_3}{2} - \frac{3}{2}\zeta\kappa_1\right)^2 + 3\zeta(1 + \kappa_1)\kappa_1\kappa_3\right]^{\frac{1}{2}} \qquad (4.76)$$

For validation purposes one may substitute into these expressions the inertia dyad elements and mass fraction corresponding to the high resolution shape models of KW4. It is helpful to normalize everything using the component centroids separation, averaged over one of the high resolution simulations presented in the last chapter,

as the normalizing length scale. Along with that one should normalize everything using the matching mean motion. This yields, for that particular high resolution simulation example case, periods of $2\pi/\omega_a = 20.80$, $2\pi/\omega_b = 16.38$, $2\pi/\omega_c = 36.67$, and $2\pi/\omega_d = 11.16$, all in hours. There are many factors working against good agreement between these periods and those extracted from the power spectral density plots of quantities from the high resolution simulation output for the same case. First is the major approximation in the above formulation of ignoring all true shape information for Alpha. But note that two of the periods above (those from ω_d, ω_b) are quite close to four and six times the spin period of Alpha. In general, inclusion of the equatorial ellipticity and other Alpha shape information as in the full-detail system may amount to excitation and slight frequency shifting of these modes through a driving frequency (the spin frequency of Alpha) approaching higher-order resonances with them. Further, the oscillations of the real system may be large enough to go beyond the region of the phase space where the linear perturbation dynamics system is valid in the first place, and into a nonlinear regime. In light of these considerations, when the position and velocity of Alpha's centroid in the frame fixed to Beta and Beta's angular velocity in its own frame are resolved from the raw simulation output, those quantities show periods with excellent agreement with the analytical results (20.4 hr, 16.0-16.8 hr, 36.3 hr, 11.2 hr). Other dominant periods observed in the time responses of different quantities such as Beta's libration angle and the mutual orbit elements do not agree as well, being more commensurate with the 17.268 hr Alpha spin free precession period and the true orbital period adjusted to match the average centroid separation (in turn usually reduced from average semimajor axis due to small average eccentricity with circulating periapsis and librating true anomaly). The same picture as above in periods comparison also holds for the other simulation cases.

4.5 Utility of Analytical Formulae for Mass Property Measurement

Remote observation, primarily from Earth's vicinity and particularly with planetary radar, can already yield various items of information for a binary asteroid, which are unavailable for a solitary asteroid body. These include accurate estimation of the total system mass $m_1 + m_2$ from measurement of a binary system's orbital period. In addition, one can estimate the mass fraction ζ from measurement of the motion of each component relative to the system barycenter's apparent position, as best fitted to the binary system's heliocentric orbit (see, for example, [62]). Together with the total system mass and body shapes/volumes, this mass fraction yields the component densities as well. However, with the above analytical theory describing the effects of Alpha oblateness and Beta triaxiality, one can go beyond obtaining these pieces of information, using further high quality remote observation data.

Particularly in the context of a spacecraft on a rendezvous mission to a binary system that is still at a large distance from its target (though in the far term extremely advanced space telescope facilities in Earth's proximity may provide similar imaging capability), the long term precession and coupled Beta libration and orbit motion can be captured in imaging of the binary. From the time history of images the precession period can be measured, and with that one can use the concurrent solution of Eqs. 4.54 and 4.55, or simply use Eq. 4.62, to estimate $I_{1_z} - I_{eq}$. This excess of Alpha's moment of inertia about its spin axis above its average moment of inertia about a transverse axis is essentially the J_2 term for Alpha. In addition, after the observed motion of the coupled Beta libration and orbit dynamics is processed into the quantities serving as states of the linearized system about the hypothetical relative equilibrium of the last section, the frequencies or corresponding periods for those quantities can be extracted. Since these frequencies are expressed in Eqs. 4.75

and 4.76 as a function of the elements of the inertia dyad of Beta, that relationship can be inverted. Note that only two of the κ parameters are independent, the third being determined from the other two according to the constraint relationship $\kappa_1 \kappa_2 \kappa_3 + \kappa_1 + \kappa_2 + \kappa_3 = 0$. One can also turn all groupings of inertia elements themselves appearing in the frequency expressions of Eqs. 4.75 and 4.76 into linear combinations of the differences $\left(I_{2_y} - I_{2_x}\right)$ and $(I_{2_z} - I_{2_x})$. Then these two differences plus any two of the three κ_i's are four values that can be solved for from the four frequencies obtained from observation. The unknown inertia elements I_{2_x}, I_{2_y}, I_{2_z} can themselves be determined from those four values, completing estimation of Beta's mass parameters from measurements of system motion. As imaging data that is good enough to allow for measuring the above system motion will also be good enough for detailed shape model determination, it is likely that such body shapes will also be available. Then an independent calculation of inertia can be made from the shapes, assuming homogenous density. A comparison of the two sets of inertia numbers, from the shape and from the inversion of the observed behavior using the above analytical formulae, will reveal the degree of error in the homogeneity assumption and yield a first-cut quantification of density variation inside the bodies. This in turn can constrain understanding of the macro-porosity and internal structure of the bodies.

Since all observation data mentioned here can be taken from afar through standoff observation by the spacecraft, the methods outlined in this chapter provide a mechanism for remotely analyzing the preliminary mass distribution properties before the spacecraft enters the sphere of influence of the system itself. In addition to being scientifically interesting in all the ways mentioned above, this may be extremely useful for reducing risk and improving chances for success for future rendezvous missions to binary asteroids.

CHAPTER V

Simulation and Analysis of Particle Motion within Binary Asteroids

Here a different approach is taken to studying the same general class of small asynchronous binaries for which the formulae in the last chapter were derived. In particular, that prior analysis centered on the relationship between the mass distribution properties of the binary components and observable binary motions consistent with the system's dynamic modes (having varying timescales or periods). But is also of interest to explore what happens with such systems over very long timescales. Here "long timescales" means on the order of 10^4 years up to the average dynamical lifetime of a typical NEA (the average duration for which it exists in the inner solar system before solar or planetary impact or ejection from that region, $\approx 10^7$ years per [69]). These are long enough timescales that the previously detailed periods for the angular momenta precession, libration, and other dynamic modes of the system can be viewed as transpiring nearly instantaneously.

To understand various processes that may govern the long timescale behavior and evolution of binary asteroid systems of this class from their formation through their current configuration to their final fates, it turns out to be useful to study the cumulative effects of particle motion within these systems. Here particle motion means the propagated motion of pieces of material that are nearly massless in comparison

to the binary components, but not necessarily small or low in mass in absolute terms. In other words, the particles herein may range from pebbles to large boulders or spacecraft, and are not of microscopic size.

In the process of completing the research work for this dissertation, however, exploration of such particle motion was not begun solely with the aim of studying the cumulative effect of that motion as it relates to long timescale evolution of binary asteroids. It was also (first) desired to study the behavior of ejecta from the surfaces of both components of a binary, after the fashion of previous ejecta studies for a solitary asteroidal body (e.g. Scheeres et al [70],[71]). It was also desired to characterize important features of trajectories that spacecraft or debris in a debris ring may evolve along within a binary system. To some extent, studying all of these problems of interest has utilized a common approach, presented below first. Then each of the major problem types are addressed in turn.

5.1 Methodology for Precise Dynamic Simulation of Test Particles within F2BP

The motion of particles within the complex time-varying gravity field of the full-detail system, itself evolving according to the F2BP dynamics, may be assumed not to impact those F2BP dynamics at all, **if** each particle is truly a test particle (i.e. is assumed to be comparatively nearly massless). This defines what will henceforth be called the Restricted but Full Three-Body-Problem (RF3BP): "restricted" because of the assumption of neglecting the particle mass yet "full" in detail because of no simplifications for the underlying F2BP. This is another principal problem type for astrodynamics which actually is the emphasis for this chapter. Of course this RF3BP is only an approximation, and the particles that evolve according to the equations of motion (EOM) for it must be given mass later on, to accurately represent the flows

of mass and linear and angular momentum that occur with such particle motion, as relevant for the binary's dynamical evolution.

Below are presented the EOM that give the motion of particles themselves according to the RF3BP. The notation here follows after that in the previous chapter. Generally denote $\boldsymbol{\rho}$ (no subscript) as the position vector of a particle. One can write the particle's EOM with respect to, and coordinate $\boldsymbol{\rho}$ within, any one of several coordinate frames. In order to match with the usual formulation of the standard restricted three body problem (hereafter R3BP) in which both Alpha and Beta are approximated as point masses in circular orbits about the barycenter, it is helpful to define an "osculating orbit frame" with origin at the system barycenter, i.e. a rotating barycentric frame. At every instant in time this frame has its +X axis fixed to the line of syzygy connecting the component centers of mass, and pointing from Alpha toward Beta. The frame's +Z axis remains aligned to the pole of the binary mutual orbit, and its +Y axis is given by the right hand rule from the +X and +Z axes. Note that when **not** treating the R3BP system or a similar approximation to the real system, for which the dynamics have no explicit dependence on time, the +Z axis of the rotating barycentric frame and its angular velocity $\boldsymbol{\omega}_{\mathrm{orb}}$ are no longer inertially fixed and constant, respectively.

Assume a normalization of the EOM using a characteristic length scale, mass, and time scale. For the characteristic length scale L one may choose the initial semi-major axis (or for 1999 KW4, roughly 2540.5 meters), for the characteristic mass one may choose the total system mass $m_T = m_1 + m_2$ (or for 1999 KW4, about 2.47×10^{12} kg), and for the characteristic time scale one may use the mean motion from the above two numbers, i.e. $\sqrt{G(m_1 + m_2)/L^3}$. Then the fully normalized EOM for a particle

in the binary, written with respect to the rotating barycentric frame, are:

$$\ddot{\boldsymbol{\rho}} + \widetilde{\dot{\boldsymbol{\omega}}_{\text{orb}}}\boldsymbol{\rho} + 2\widetilde{\boldsymbol{\omega}_{\text{orb}}}\dot{\boldsymbol{\rho}} + \widetilde{\boldsymbol{\omega}_{\text{orb}}}\widetilde{\boldsymbol{\omega}_{\text{orb}}}\boldsymbol{\rho} = \frac{\partial U_{1,2}}{\partial \boldsymbol{\rho}} \tag{5.1}$$

Here the notation $\widetilde{\mathbf{a}}$ is introduced, which represents the skew-symmetric matrix result of the cross product operator acting on vector $\mathbf{a}$, i.e. $\widetilde{(\cdot)} : \Re^3 \mapsto \mathfrak{so}(3)$ is an isomorphism between $\Re^3$ and skew-symmetric matrices defined such that $\widetilde{\mathbf{x}}\mathbf{y} = \mathbf{x} \times \mathbf{y}$ for any $\mathbf{x}, \mathbf{y} \in \Re^3$. The normalized EOM instead written with respect to the Alpha-fixed frame (as may be useful for treating close orbits about Alpha) are:

$$\ddot{\boldsymbol{\rho}} + \widetilde{\dot{\boldsymbol{\omega}}_1}\boldsymbol{\rho} + 2\widetilde{\boldsymbol{\omega}_1}\dot{\boldsymbol{\rho}} + \widetilde{\boldsymbol{\omega}_1}\widetilde{\boldsymbol{\omega}_1}\boldsymbol{\rho} + \ddot{\mathbf{r}}_l = \frac{\partial U_{1,2}}{\partial \boldsymbol{\rho}} \tag{5.2}$$

And similarly, for completeness, the normalized EOM written with respect to the Beta-fixed frame are:

$$\ddot{\boldsymbol{\rho}} + \widetilde{\dot{\boldsymbol{\omega}}_2}\boldsymbol{\rho} + 2\widetilde{\boldsymbol{\omega}_2}\dot{\boldsymbol{\rho}} + \widetilde{\boldsymbol{\omega}_2}\widetilde{\boldsymbol{\omega}_2}\boldsymbol{\rho} + \ddot{\mathbf{r}}_2 = \frac{\partial U_{1,2}}{\partial \boldsymbol{\rho}} \tag{5.3}$$

Here the $\ddot{\mathbf{r}}_1$ denotes the inertial acceleration of the centroid of Alpha and similarly for Beta. Finally, and most simply, there are the normalized EOM in the inertial barycentric frame:

$$\ddot{\boldsymbol{\rho}} = \frac{\partial U_{1,2}}{\partial \boldsymbol{\rho}} \tag{5.4}$$

In each case, the position vector $\boldsymbol{\rho}$ is coordinated in the appropriate frame of the EOM.

Throughout the above equations, $U_{1,2}$ is the total normalized force potential at a field point due to the mass distributions of both Alpha and Beta. Depending on the model of the system used, $U_{1,2}$ may become simpler or more complicated, just as it does with the choice of different frames and hence different EOM. The forms of $U_{1,2}$ are presented here only for those cases of greatest relevance. For the R3BP case (in

which both Alpha and Beta are approximated as perfect spheres), this force potential for the rotating barycentric frame EOM is

$$U_{1,2} = (1-\nu)\,\frac{1}{\sqrt{(x+\nu)^2 + y^2 + z^2}} + \nu\,\frac{1}{\sqrt{(x-(1-\nu))^2 + y^2 + z^2}}. \tag{5.5}$$

where $\nu = m_2/(m_1 + m_2) \le 0.5$. Of course $\{x, y, z\}$ are the components of $\boldsymbol{\rho}$ in the rotating barycentric frame. If Alpha is approximated as a sphere but Beta is instead approximated as a triaxial ellipsoid with longest semi-axis locked to the line of syzygy at all times, so that Beta's rotation is synchronous with the mutual orbit, then one has what may be called the RSE3BP (restricted sphere+ellipsoid three body problem). In this case, the force potential for the rotating barycentric frame EOM is

$$U_{1,2} = (1-\nu)\,\frac{1}{\sqrt{(x+\nu)^2 + y^2 + z^2}} + \nu\,U_{\text{ellip}}(x-(1-\nu), y, z) \tag{5.6}$$

where U_{ellip} is the standard ellipsoid potential result, calculated in the fashion indicated in equations 11-13 of Bellerose and Scheeres [72], but with the normalization length scale of L rather than of the largest semi-axis, and hence the normalized largest semi-axis no longer equal to one. These expressions are, assuming normalized ellipsoid semi-axes of $a > b > c$ and the +X axis of the Beta-fixed frame aligned with the largest semi-axis a:

$$U_{\text{ellip}} = \frac{3}{4} \int_\lambda^\infty \left(1 - \frac{(x-1+\nu)^2}{a^2+p} - \frac{y^2}{b^2+p} - \frac{z^2}{c^2+p}\right) \frac{dp}{\Delta(p)} \tag{5.7}$$

Here p is just the constant of integration for the elliptic integrals, and

$$\Delta(p) \triangleq \sqrt{(a^2+p)\,(b^2+p)\,(c^2+p)}, \tag{5.8}$$

and similarly for $\Delta(\lambda)$. The bound λ for the integration is given by the single positive root of

$$\Phi(\lambda) \triangleq \frac{(x-1+\nu)^2}{a^2+\lambda} + \frac{y^2}{b^2+\lambda} + \frac{z^2}{c^2+\lambda} - 1 = 0. \tag{5.9}$$

Finally, if instead each binary component is represented as a full polyhedral mesh with almost arbitrary shape, one has the proper RF3BP and for any set of EOM, as written above, the force potential is:

$$
\begin{aligned}
U_{1,2} &= -G\,\rho_1 \left(-\frac{1}{2} \sum_{e \in Alpha\ edges} \mathbf{r}_{e_1} \cdot \mathrm{E}_{e_1} \cdot \mathbf{r}_{e_1}\, L_{e_1} + \frac{1}{2} \sum_{f \in Alpha\ faces} \mathbf{r}_{f_1} \cdot \mathrm{F}_{f_1} \cdot \mathbf{r}_{f_1}\, \omega_{f_1} \right) \\
&\quad -G\,\rho_2 \left(-\frac{1}{2} \sum_{e \in Beta\ edges} \mathbf{r}_{e_2} \cdot \mathrm{E}_{e_2} \cdot \mathbf{r}_{e_2}\, L_{e_2} + \frac{1}{2} \sum_{f \in Beta\ faces} \mathbf{r}_{f_2} \cdot \mathrm{F}_{f_2} \cdot \mathbf{r}_{f_2}\, \omega_{f_2} \right)
\end{aligned}
\tag{5.10}
$$

Here G is the normalized gravity constant (and for this current problem's normalization, unity), and likewise the assumed constant scalar body densities ρ_1 and ρ_2 are also normalized. The edge- and face-specific dyads are given respectively by (from [46])

$$
\mathrm{E}_e = \mathbf{n}_i (\mathbf{n}_e^i)^T + \mathbf{n}_j (\mathbf{n}_e^j)^T \quad , \quad \mathrm{F}_f = \mathbf{n}_f (\mathbf{n}_f)^T
\tag{5.11}
$$

where $\mathbf{n}_f$ is the unit vector normal to the face indexed by f, and the face indices i and j here refer to the faces on each side of the edge indexed by e, and also $\mathbf{n}_e^{\{i,j\}}$ is the outward-pointing unit vector normal to both the edge indexed by e and the unit vector normal to the face indexed by $\{i,j\}$. Neither of these dyads depend on the relative position vector of the particle, but that comes into the vector $\mathbf{r}_f$ from the field point at which the potential is being evaluated to any fixed point in the plane of the face denoted by f, and the vector $\mathbf{r}_e$ from the same field point to any point along the edge denoted by e. It also comes into the vectors $\mathbf{r}_k, \mathbf{r}_l, \mathbf{r}_m$ from that field point to the vertices denoted k, l, m at the corners of a given face or at the endpoints of a given edge. And those vectors or their lengths $r_k = \|\mathbf{r}_k\|\,,\, r_l = \|\mathbf{r}_l\|\,,\, r_m = \|\mathbf{r}_m\|$ are in turn used to calculate the scalar quantities (also from [46]):

$$
L_e = \log \frac{r_k + r_l + \|e\|}{r_k + r_l - \|e\|}
\tag{5.12}
$$

$$
\omega_f = 2 \arctan \frac{\mathbf{r}_k \cdot (\widetilde{\mathbf{r}}_l \mathbf{r}_m)}{r_k r_l r_m + r_k (\mathbf{r}_l \cdot \mathbf{r}_m) + r_l (\mathbf{r}_m \cdot \mathbf{r}_k) + r_m (\mathbf{r}_k \cdot \mathbf{r}_l)}
\tag{5.13}
$$

121

Here $\|e\|$ is the length of the edge in question. It is important to note that the relative position vector required within the quantities $\mathbf{r}_e$, $\mathbf{r}_f$, L_e and ω_f of the particle must be **expressed in the frame fixed to the respective body**. Hence one must use the transpose of attitude rotation matrices R_1 and R_2, which map from the frame of Alpha to the frame of the EOM and from the frame of Beta to the frame of the EOM, respectively, to convert the position vector $\boldsymbol{\rho}$ within the EOM into each body frame. These rotation matrices then show up in the partial derivatives of the potential with respect to $\boldsymbol{\rho}$. For the force on the particle, the first partial is:

$$
\frac{\partial U_{1,2}}{\partial \boldsymbol{\rho}} = -G\,\rho_1\,R_1 \left(\sum_{e \in Alpha\ edges} \mathrm{E}_{e_1} \cdot \mathbf{r}_{e_1}\, L_{e_1} - \sum_{f \in Alpha\ faces} \mathrm{F}_{f_1} \cdot \mathbf{r}_{f_1}\, \omega_{f_1} \right)
$$
$$
-G\,\rho_2\,R_2 \left(\sum_{e \in Beta\ edges} \mathrm{E}_{e_2} \cdot \mathbf{r}_{e_2}\, L_{e_2} - \sum_{f \in Beta\ faces} \mathrm{F}_{f_2} \cdot \mathbf{r}_{f_2}\, \omega_{f_2} \right) \quad (5.14)
$$

And for the gravity gradient matrix, or the second partial:

$$
\frac{\partial^2 U_{1,2}}{\partial \boldsymbol{\rho}^2} = -G\,\rho_1\,R_1 \left(\sum_{e \in Alpha\ edges} \mathrm{E}_{e_1}\, L_{e_1} - \sum_{f \in Alpha\ faces} \mathrm{F}_{f_1}\, \omega_{f_1} \right) R_1^T
$$
$$
-G\,\rho_2\,R_2 \left(\sum_{e \in Beta\ edges} \mathrm{E}_{e_2}\, L_{e_2} - \sum_{f \in Beta\ faces} \mathrm{F}_{f_2}\, \omega_{f_2} \right) R_2^T \quad (5.15)
$$

Also, it should be noted again that the Laplacian of the potential from each body individually is given by

$$
\nabla^2 U_i = -G\,\rho_i \sum_{f \in faces\ in\ body\ i} \omega_{f_i}\ , \quad i \in (1,2) \quad (5.16)
$$

and switches value from zero at particle positions outside the body polyhedron to -4π at particle positions interior to that polyhedron.

The general simulation package implemented for particle propagation makes use of the RF3BP formulation, while the R3BP and RSE3BP formulations limited to just the rotating barycentric frame EOM are useful for some analytical purposes (see below). It was originally intended for the single-processor C++ implementation of

the RF3BP formulation to be flexible enough to propagate any of the four sets of particle EOM for the four frames. However, only the barycentric inertial frame EOM were propagated for the results herein. It was also intended to have options in the code for driving the motions of Alpha and Beta in several ways: 1) by interpolating the raw state data files output from prior full-detail F2BP simulation of KW4; 2) by moving the components according to periodic functions tuned to the frequencies of the four dynamic modes, as measured from looking at prior full-detail F2BP simulation of KW4; 3) by propagating concurrently with the particle EOM other equations of motion for the binary itself using approximate (but fast to compute) 2nd-degree-and-order gravity representations of each component. Only the first of these methods (having the highest fidelity) is used for the particle motion results herein. Finally, it should be noted that impact detection is implemented using the Laplacian for each body.

5.2 Analysis of RF3BP Particle Trajectory Results

The trajectory results of any particles propagated with the above may be sorted according to the final outcome or disposition of the trajectories (from among the four possibilities of impact onto Alpha, impact onto Beta, escape from the system, or lingering in "orbit" at the maximum simulation duration). Those particles with each disposition may be further sorted according to whether that outcome matches the expected outcome based on the initial energy of the particle's trajectory. The Jacobi energy function J for a trajectory is time-varying in the full system. However for the earlier-mentioned R3BP and RSE3BP approximate systems, the potential through which a particle moves is time-invariant in the uniformly rotating barycentric frame, and hence the Jacobi function for a trajectory becomes a Jacobi integral. One can

compute the integral's value at the L1 point for the R3BP, or at the analogue to the L1 point for the RSE3BP found in the rotating barycentric frame at the location $y = z = 0$ and x equal to the root of

$$0 = x - \frac{1-\nu}{(x+\nu)^2} - \nu\,(x-(1-\nu))\frac{3}{2}\int_\lambda^\infty \frac{dp}{(p+a^2)\Delta(p)}. \tag{5.17}$$

Here $\nu = m_1/(m_1+m_2)$ again, and $\lambda = (x-(1-\nu))^2 - a^2$ with a being the longest semi-axis of the Beta triaxial ellipsoid, and Δ is as defined for this standard elliptic integral by Eq. 5.8. Specifically, the Jacobi integral value for the RSE3BP when stationary at this RSE3BP L1-analogue point is

$$J_{\mathrm{RSE3BP_{L1}}} = -\frac{1}{2}x_{\mathrm{L1}}^2 - \frac{1-\nu}{|x_{\mathrm{L1}}+\nu|} - \nu\frac{3}{4}\int_\lambda^\infty \left(\frac{1}{\Delta(p)} - \frac{(x-(1-\nu))^2}{(p+a^2)\Delta(p)}\right)dp. \tag{5.18}$$

For each regolith particle propagated one may compute from its initial conditions the initial RF3BP Jacobi function value using the following equation, with all variables with respect to the rotating barycentric frame:

$$J_{\mathrm{RF3BP_o}} = \frac{1}{2}\dot{\boldsymbol{\rho}}\cdot\dot{\boldsymbol{\rho}} - \frac{1}{2}\left[\widetilde{\boldsymbol{\omega}_{\mathrm{orb}}}\boldsymbol{\rho}\right]\cdot\left[\widetilde{\boldsymbol{\omega}_{\mathrm{orb}}}\boldsymbol{\rho}\right] - U_{1,2} \tag{5.19}$$

Herein the $U_{1,2}$ is evaluated with Eq. 5.10. Comparison between the $J_{\mathrm{RF3BP_o}}$ value and the $J_{\mathrm{R3BP_{L1}}}$ or $J_{\mathrm{RSE3BP_{L1}}}$ value for the approximate model equilibrium points gives an expected trajectory outcome. In particular, if the value of $J_{\mathrm{RF3BP_o}}$ is smaller than the value of $J_{\mathrm{R3BP_{L1}}}$ or $J_{\mathrm{RSE3BP_{L1}}}$, then a return impact back onto the body from which the particle originated is expected (though not guaranteed for the full system). If that inequality is reversed but $J_{\mathrm{RF3BP_o}}$ is less than zero, then return impact or transfer impact or lingering in orbit are all outcomes with no expectation either way. Instead only the escape outcome is not expected (though not strictly excluded for the full system). If $J_{\mathrm{RF3BP_o}}$ is greater than zero, then one might expect the escape outcome, although strictly speaking many trajectories such as retrograde

ones may have a positive $J_{\mathrm{RF3BP_O}}$ value and never come close to escaping. One can compare the actual propagated outcome against the expected ones to then do further sorting, which characterizes the degree to which the time-varying nature of the full system's potential in the rotating barycentric frame (what sets the full system apart from the R3BP or RSE3BP approximations) is important.

5.3   Investigation of Ejecta from Binary Components

This section presents the results of using the prior approach in studying the motion of ejecta particles originating from both binary component surfaces with substantial initial surface-relative velocity. The specific system for which this is studied is again the 1999 KW4 system, as it typifies the small asynchronous binaries class and is likely the best characterized member of that class at the time of this writing, from the studies in previous chapters.

Specifically, the F2BP motion results set for KW4 used as underlying binary motion for dynamic simulation of ejecta particles here is that matching the lowest excitation level identified for the KW4 system. This gives the cleanest picture of the dispersion of the ejecta particle batches possible. In this configuration the initial spin-orbit pole offset angle for the system's Cassini state is 0° and the initial osculating eccentricity and mean anomaly are 0.01125 and 0° (see section 3.3). The state of the binary system itself is interpolated from this "most-relaxed" case's binary system propagation output files, whenever required for computation of the net force acting on each test particle. That net force is determined as the sum of the forces due to the gravitational interaction of each polyhedral body model with the test particle.

5.3.1 Setup for simulating batches of ejecta particles

Batches of ejecta particles are propagated from several locations on the component surfaces. Particularly, it is desired to explore the behavior of ejecta launched approximately in several discrete directions in the X-Y plane of the rotating barycentric frame for the system. The directions from Beta are along the +X and -X axes of the on-average synchronously locked Beta (i.e. toward Alpha and opposite Alpha, respectively), and also along the +Y and -Y axes of the synchronous Beta (opposite the direction of Beta's orbital travel and with Beta's orbital travel, respectively). In addition, the discrete directions from Alpha are along the line of syzygy from Alpha's center of mass toward Beta's center of mass, and then rotated by a phase angle ϕ about the (north) spin pole of Alpha in 45° increments, hence $\phi \in \{0°, 45°, 90°, 135°, 180°\}$. The approach taken is to pick the facet that has a normal vector as close to each desired discrete direction vector as possible, both in orientation and in the proximity of the normal vector's base to where the direction vector intersects the body mesh. Then a batch of particles is propagated from a point just slightly displaced outward (by only 0.001% of the applicable mean body radius) above the center of each of those chosen launch facets. For Alpha, only one such launch facet is selected, for the $\phi = 0°$ direction towards Beta and using the initial attitude of Alpha in the prior most-relaxed scenario. Then for the other directions from Alpha, the starting time for the particle propagation (from the same launch facet) is adjusted later within the underlying F2BP output's time span, in order to match that time when the relative phase of the launch facet with respect to the plane of syzygy has reached the nonzero value of ϕ desired.

For each of these nine body and facet or body and relative attitude phase angle combinations, the initial velocity vector, relative to the body-fixed frame and to the

body's surface, that is given to each particle in the batch of particles simulated is determined by a fixed magnitude v_o, and random direction. The direction is specified with a random variable clock angle ψ from the direction of the edge connecting the first and second vertices for the launch facet (using uniform distribution between 0 and 2π) and a random variable cone angle ϑ away from the face normal vector (using gaussian distribution centered on zero mean with $\sigma = 0.75$ radians). To prevent the surface-relative initial velocity vector from ever pointing down into the surface, any random draw value of ϑ larger than $\pi/2 - 0.00001$ is rotated back to $\vartheta = 0.00001$ while keeping the same clock angle.

The magnitude of the surface-relative launch velocity, v_o, remains fixed within each batch of particles propagated, but is varied with discrete values between different batches. These values are in turn chosen just higher and lower than the so-called "guaranteed return speed", v_{return}, just higher and lower than the so-called "guaranteed escape speed", v_{escape}, and near the average of the guaranteed return speed and guaranteed escape speed, all for two different assumptions about the direction of the velocity vector in the calculation of those speeds. Therefore there are five discrete velocity values chosen for each assumption, for ten velocity values in all.

The "guaranteed return speed" here is defined as the minimum, across the full time history of F2BP propagation states captured, of the launch velocity that gives the particle an RF3BP Jacobi value at launch at that time, J_{RF3BP_t}, equal to the value of $J_{\text{RSE3BP}_{\text{L1}}}$ computed according to Eq. 5.18. This of course is not an upper bound on launch velocity which truly guarantees return of a particle to its source body within the full-detail system, but only an approximation to that. Hence "guaranteed return speed" is only a label for the quantity. Also, because computational limits preclude calculation of the launch velocity required to make $J_{\text{RF3BP}_t} = J_{\text{RSE3BP}_{\text{L1}}}$ at **every**

instant in the time history of F2BP states, only a finite set τ of times within that output history are used. For notation, here let a first-level right subscript indicate the body or the point that a quantity applies to, a second-level right subscript indicate a step or instant in time, a left subscript indicate the frame a quantity is coordinated or expressed in, and a left superscript denote the frame the quantity (such as velocity) is relative to. Any of these are omitted when not relevant or when the relationship holds independent of frame, etc. Also $_I$ indicates the inertial barycentric frame, $_B$ indicates the rotating barycentric frame, $_1$ indicates the Alpha-fixed frame or the Alpha body itself, $_2$ indicates the Beta-fixed frame or the Beta body itself, and $_f$ refers to the chosen launch facet, or more particularly the center point of that chosen launch facet. If the assumption about the direction of the launch velocity vector is that it is aligned with the normal to the launch face, then the following equations give this guaranteed return speed for a particle launched from Alpha:

$$
v_{\text{return}} \;=\; \min_{t \in \tau}\left(\frac{-B_t + \sqrt{B_t^2 - 4\,A_t\,C_t}}{2\,A_t} \right), \tag{5.20}
$$

where

$$
A_t \;=\; {_I}\boldsymbol{\kappa}_t \cdot {_I}\boldsymbol{\kappa}_t, \quad B_t \;=\; 2{_I}\boldsymbol{\kappa}_t \cdot {_I}\boldsymbol{\chi}_t, \quad C_t \;=\; {_I}\boldsymbol{\chi}_t \cdot {_I}\boldsymbol{\chi}_t - {_I^B}\dot{\boldsymbol{\rho}}_{f_t} \cdot {_I^B}\dot{\boldsymbol{\rho}}_{f_t}, \tag{5.21}
$$

$$
{_I}\boldsymbol{\kappa}_t \;=\; {_I}\mathrm{R}_{1_t}\, {_1}\mathbf{n}_f \quad , \quad {_I}\boldsymbol{\chi}_t \;=\; {_I^I}\mathbf{v}_{1_t} + {_I}\mathrm{R}_{1_t}\, \widetilde{{_1}\boldsymbol{\omega}_{1_t}}\, {_1}\boldsymbol{\rho}_f - {_I}\mathrm{R}_{B_t}\, \widetilde{{_B}\boldsymbol{\omega}_{\text{orb}_t}}\, {_B}\boldsymbol{\rho}_{f_t}, \tag{5.22}
$$

$$
{_B}\dot{\boldsymbol{\rho}}_{f_t} \cdot {_B}\dot{\boldsymbol{\rho}}_{f_t} \;=\; 2\left[J_{\text{RF3BP}_t} + \frac{1}{2}\left[\widetilde{\boldsymbol{\omega}_{\text{orb}_t}}\boldsymbol{\rho}_{f_t} \right] \cdot \left[\widetilde{\boldsymbol{\omega}_{\text{orb}_t}}\boldsymbol{\rho}_{f_t} \right] + U_{1,2_t} \right]. \tag{5.23}
$$

For a particle launched from Beta rather than Alpha, the same equations above apply with $_1$ replaced by $_2$ throughout. An alternate assumption about the direction of the launch velocity vector is that it is pointed in whatever direction makes the greatest

addition to the squared magnitude of the velocity, relative to the rotating barycentric frame, of the launched particle. This is most likely to increase the Jacobi function's value, so it is the preferred assumption. With it, one should redefine $_I\boldsymbol{\kappa}_t$ as

$$_I\boldsymbol{\kappa}_t \;=\; \frac{_I\boldsymbol{\chi}_t}{\|_I\boldsymbol{\chi}_t\|}. \tag{5.24}$$

This alignment of $_I\boldsymbol{\kappa}_t$ and $_I\boldsymbol{\chi}_t$ is the most likely to increase the Jacobi function (tending to make it less negative) so that v_{return} must be smaller to bring the Jacobi function down to the desired sphere plus ellipsoid system's L1 equivalent point Jacobi integral value. The smaller upper bound which results is more conservative.

The "guaranteed escape speed" is instead the maximum, across the full time history of F2BP propagation states, of the launch velocity that gives the particle an RF3BP Jacobi value at launch at that time, J_{RF3BP_t}, equal to zero. This of course is not a lower bound on launch velocity that actually guarantees the escape of a particle subject to the dynamics of the full-detail system, but rather an approximation to such a lower bound. Yet as before, "guaranteed escape speed" makes a useful label for this value. The same set of Eqs. 5.20-5.23 apply for calculation of this guaranteed escape speed using the first assumption of face-normal-aligned launch direction, with the simple modifications of a) "max" instead of "min" used and b) J_{RF3BP_t} replaced by 0. With the other assumption of the launch velocity vector being pointed in the optimal direction, i.e. in whatever direction makes the greatest subtraction to the squared magnitude of the launched particle's initial velocity with respect to the rotating barycentric frame, the sign on the right hand side of Eq. 5.24 must be reversed. This anti-alignment is the most likely to reduce the Jacobi function (tending to make it more negative) so that v_{escape} must be larger to bring the Jacobi function up to zero. The larger lower bound which results is more conservative.

Note that all of these calculations to determine the guaranteed return and escape

speeds are performed independently for each chosen launch facet, to use in determining the discrete values of v_o used for generation of the initial velocity vectors for particles launched from that facet. Doing the same calculations (under the first assumption of a facet normal launch direction) for not just these chosen facets but every facet on each body model yields the interesting maps of expected return and escape velocity bounds at all latitudes and longitudes, presented as a side note in Appendix B.

In addition to post-processing the batches of ejecta particles for each particle's final disposition (return impact, transfer impact, escape, or lingering in "orbit") and the expectation regarding that disposition, the particle-mass-specific changes to the angular momenta of the system caused by each particle moving along its trajectory is calculated. These are accumulated across all particles in a batch, and further averaged over all batches launched from a given location (body and facet or body and relative attitude phase angle ϕ combination). The angular momenta changed are those of Alpha, of Beta, of the mutual orbit, and of Beta and the mutual orbit together. The method for calculation of such changes are dealt with in section 5.4 in more detail.

5.3.2 Ejecta particle dispositions and binary component angular momentum changes

The disposition results for the ≈45,000 total ejecta particles simulated are shown in Figure 5.1 for the 50 batches of 500 particles each originating from Alpha, and in Figure 5.2 for the 40 batches of 500 particles each originating from Beta. Each panel in the figures shows results for launching from a different body and facet or body and relative attitude phase angle combination, and in each panel the dispositions for the ten batches specific to that combination are plotted against the full range of the ten velocity values used, on the horizontal axis. In these plots, green shows particles

130
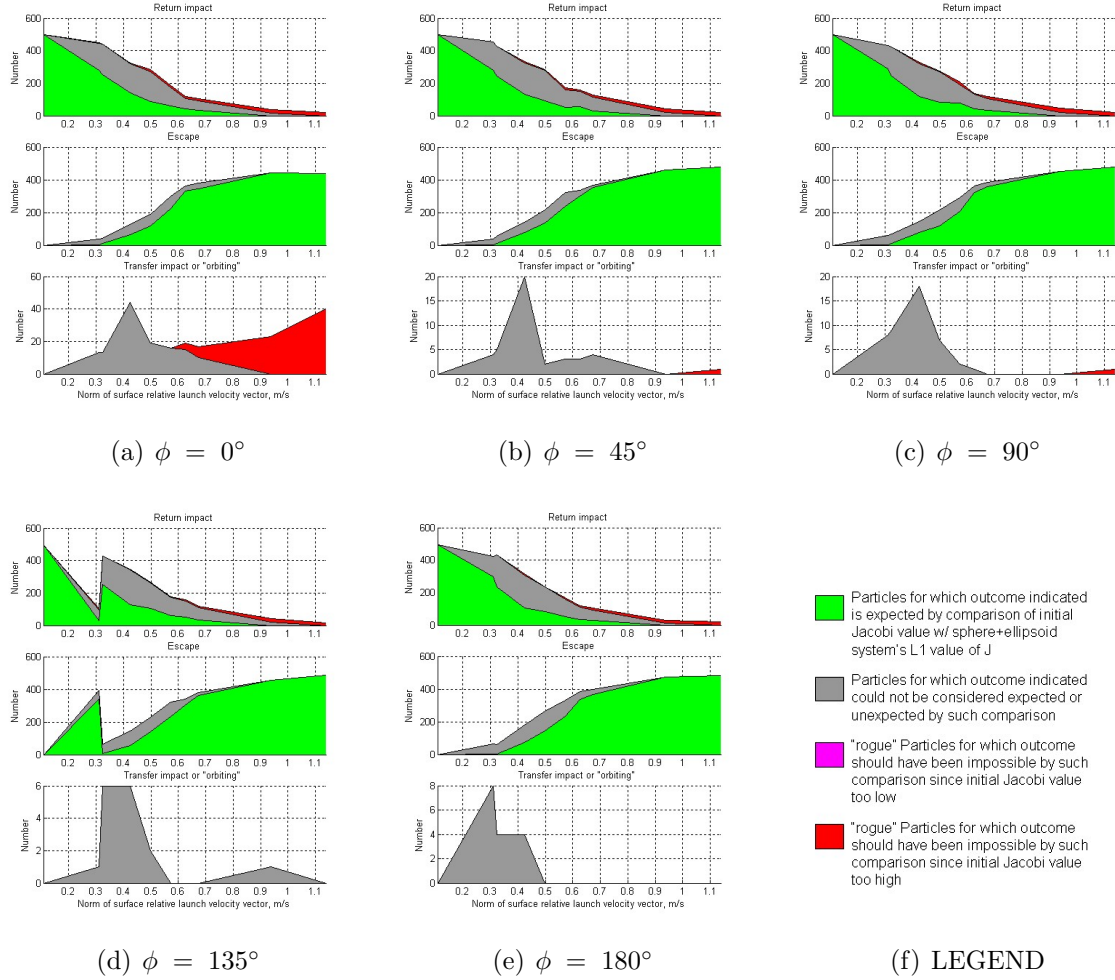
Figure 5.1: Disposition results for ejecta particles launched from equatorial region of Alpha, at differing phase angle ϕ counterclockwise from plane of syzygy on the side facing Beta.

for which the outcome indicated was expected according to comparison of their own particle-specific initial-time Jacobi values with the $J_{\mathrm{RSE3BP_{L1}}}$ value of -0.1119978 (with dimensions $\mathrm{m^2/s^2}$) or zero. Red or magenta shows "rogue" particles for which the outcome indicated was not expected according to such comparison. Gray shows particles for which the outcome indicated was neither expected nor unexpected by such comparison. Note the distinction between magenta and red: magenta means the outcome was unexpected because the particle's initial Jacobi value was too low (it should have return impacted instead), while red in this panel means the outcome
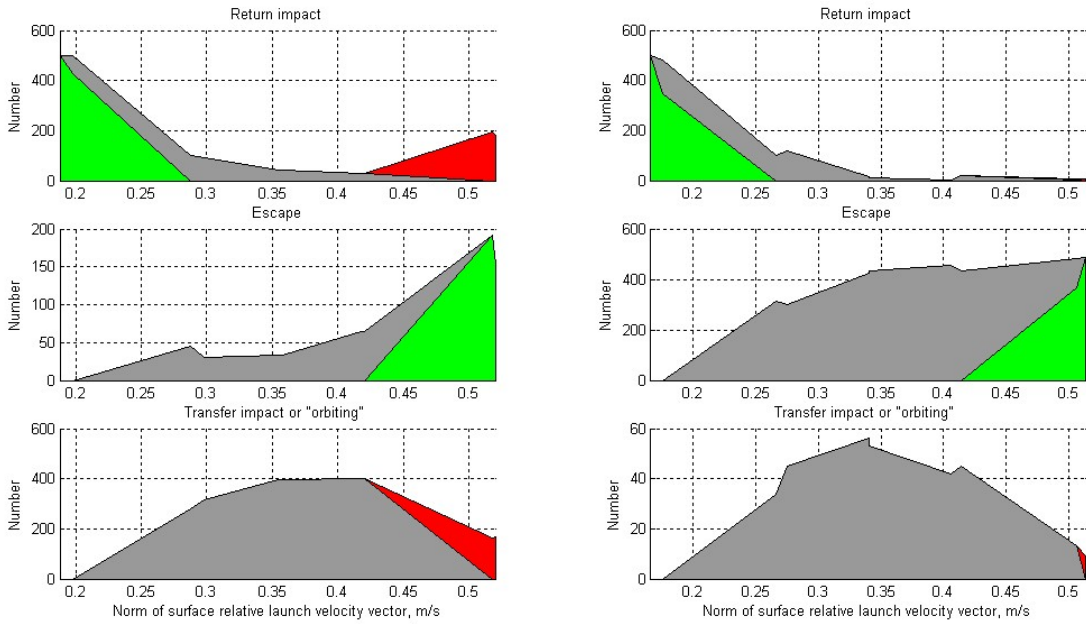
(a) Launch in Beta +Y Direction

(b) Launch in Beta -X Direction
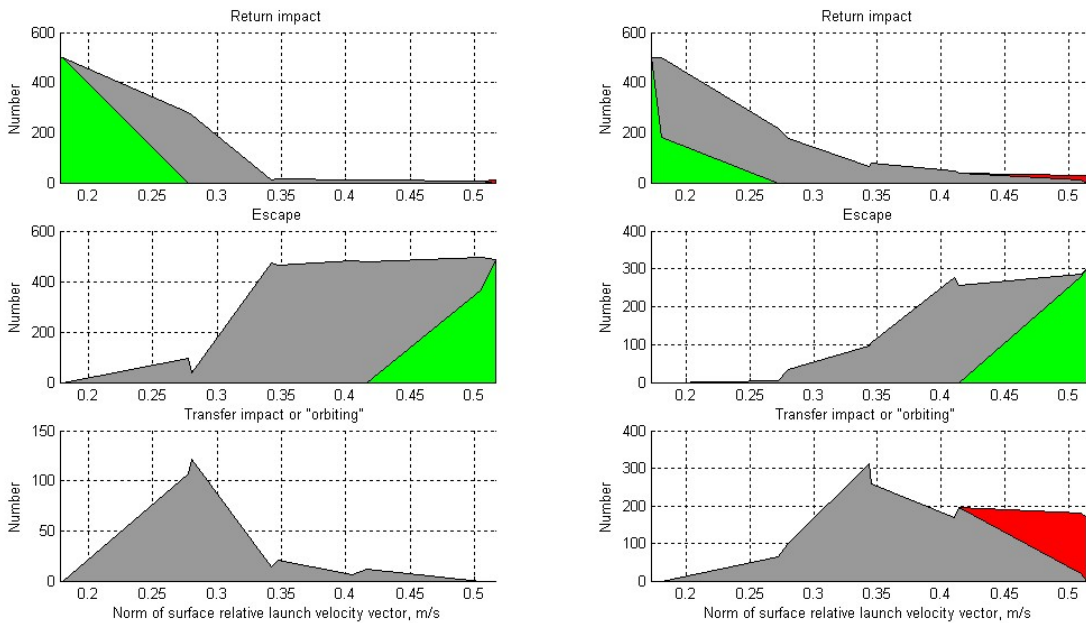
(c) Launch in Beta -Y Direction

(d) Launch in Beta +X Direction

Figure 5.2: Disposition results for ejecta particles launched from equatorial region of Beta, in directions approximately aligned with the positive and negative X and Y principal axes of Beta. This is assuming Beta is in a synchronously locked orientation.

was unexpected because the initial Jacobi value was too high (it should have escaped instead).

Only the Z-axis components, in the inertial barycentric frame, of the averaged particle-mass-specific changes to system angular momenta are summarized in Table 5.1 for particles originating from Alpha and Table 5.2 for particles originating from Beta. All such changes to the system angular momenta are vector quantities, but the largest or dominant component of those is this Z-axis component. Again, for every number in these tables, averaging was performed over all of the batches launched from a given location with different launch velocity magnitudes. Each column can be viewed as representing the net effect on the system angular momenta of excavating a fountain of debris having a spectrum of ejection velocities. Note here it is NOT expected that the numbers for the change in Z-component of Alpha's angular momentum and the change in Z-component of the combined Beta and orbit angular momentum balance each other. Note also that these are mass-specific results: the absolute angular momenta changes are given by multiplying these numbers with the

Table 5.1: Velocity-averaged particle-mass-specific changes to angular momenta of binary system components, as a result of the ejecta particle motion, for ejection from Alpha's surface. The inertial barycentric angular momenta changes of all ejecta particles reaching each outcome (taken together as a set) are also given here.

ΔH_z of item (m^2/s)	$\phi =$ 0°	$\phi =$ 45°	$\phi =$ 90°	$\phi =$ 135°	$\phi =$ 180°
① return particles	9.4314	38.6310	57.5020	43.7641	13.9257
② transfer particles	-119.3020	-146.7850	-87.3798	-78.2972	-31.9719
③ orbiting particles	42.3234	61.8396	73.7058	56.0223	46.2943
④ escaping particles	-12.9736	27.3207	41.3934	32.7812	11.2132
⑤ mutual orbit	368.2942	244.3661	151.4244	70.1776	39.4412
⑥ Alpha spin state	-667.0662	-560.3487	-535.9336	-453.5003	-508.2617
⑦ Beta spin state	-15.3761	-10.7878	-0.9460	4.5388	-1.3406
⑧ sum of ⑤ and ⑦	352.9182	233.5783	150.4784	74.7165	38.1006

Table 5.2: Velocity-averaged particle-mass-specific changes to angular momenta of binary system components, as a result of the ejecta particle motion, for ejection from Beta's surface. The inertial barycentric angular momenta changes of all ejecta particles reaching each outcome (taken together as a set) are also given here.

ΔH_z m^2/s	+Y axis launch	-X axis launch	-Y axis launch	+X axis launch
① return particles	219.7794	21.8366	-219.2214	-16.5369
② transfer particles	186.6390	19.5891	-220.3012	1.3410
③ orbiting particles	284.2133	89.9026	-140.3660	75.0153
④ escaping particles	290.9639	-3.4489	-133.2158	48.5031
⑤ mutual orbit	-601.6618	-1368.9069	-2064.9165	-931.5915
⑥ Alpha spin state	20.5225	83.8435	155.5261	195.8350
⑦ Beta spin state	-50.5025	36.9662	35.4229	-27.9189
⑧ sum of ⑤ and ⑦	-652.1643	-1331.9407	-2029.4935	-959.5103

amount (mass) of ejected material, which like the ejection velocities in turn depends on the energy level of the impact or explosion which releases that material. In this work no attempt is made at quantifying these details of impact or explosion mechanics and cratering.

In the case of launch from Alpha with $\phi = 0°$, at the highest launch speeds everything escapes except for what smacks into Beta (mainly along the leading face of Beta in the sense of its orbital motion) plus a few strange cases of return to Alpha almost immediately, at points extremely close to the launch point. The latter cases are best explained in terms of very fast ejecta traveling almost horizontally with respect to the launch facet and then hitting adjacent facets as they rotate into the flight path, before the Alpha body can rotate further "out of the way". In the same launch from Alpha case with $\phi = 0°$, at the very lowest launch speeds everything returns to Alpha (without even a single rogue particle) and the smear of return landing points tends to be strongly skewed toward negative longitudes, with little latitude spread. For this same launch from Alpha case there appears to be a trend of having particles

transfer impact or remain in orbit when they should escape more than having particles transfer impact or remain in orbit when they should have return impacted. However, this appears to have more to do with the geometry and obstruction of flight paths by Beta and local surface topography on Alpha, as opposed to being a genuine bias. Finally for the same case and all other cases of launch from Alpha, there seems to be a clearly larger depression of angular momentum of Alpha than boost to angular momentum of the mutual orbit.

For the launch of ejecta from Alpha with $\phi = 45°$ phase of the launch location from the sub-Beta point at the time of launch, as the launch speed increases, transfer particle outcomes suddenly become more frequent, but then just as rapidly become very small in number. This "peak" in transferring particles seems to match with the velocity magnitude that will move the launched particles out to the approximate distance of Beta's orbit in the same amount of time that it takes Beta to progress around its orbit and pass into the cone of ejecta. At lower launch speeds than that of this peak, the particles fly through Beta's mean orbital radius in a flyby of Beta behind it, while at higher launch speeds the particles pass through that radius in a flyby of Beta in front of it, as opposed to colliding with Beta while outbound. At the very highest launch speed, only very few of the 500 particles get caught into Alpha's rotating surface (having been launched nearly horizontally) and everything else except one transferring particle (which likely went far out, then came back in and struck Beta on approach to periapsis) escapes the system.

For the case of launch from Alpha with $\phi = 90°$ phase of the launch location from the initial sub-Beta point at the time of launch, as the launch speed increases, having everything impact as expected with a definite smear of return landing points in the direction of negative longitude and very little latitude spread gives way to

a few transfers and an even smear of the return landing points all the way around Alpha, but still little latitude spread. Then the latitude spread of return impact points grows, and an increasing fraction of particles go to escaping as expected. At the very highest launch speed, only a bunch of very fast nearly horizontal particles get caught into Alpha's rotating surface as before, and all else escapes as expected. This same progression is observed in the cases of launch from Alpha with $\phi = 135°$ and $\phi = 180°$ as well. But moving from the $\phi = 45°$ to $\phi = 90°$ to $\phi = 135°$ to $\phi = 180°$ cases, the peak in particle transfers broadens and becomes lower, and also moves to the left (to lower launch velocities). This makes sense for the timing for collision with Beta while moving toward apoapsis, or while just moving in an outbound direction. One last notable feature particular to the $\phi = 135°$ case only is a sudden plummet in the number of return impacting particles, and corresponding spike in the number of escaping particles at a launch velocity of $\approx$0.3 m/s, which remains difficult to explain.

Next for launch from Beta in Beta's +Y direction (from facet 1056 of the Beta mesh in this setup), which points away from the trailing face in the context of Beta's orbit. As the launch speed increases more and more of the particles make the transfer onto Alpha, and the vast majority of the transferring particles are at first biased toward higher amounts of angular momentum transported to Alpha (i.e. there are only a few outlying particles that impart much less angular momentum to Alpha than the rest of the transferring particles). However the latter bias/outlier effect goes away once the launch speed is raised even further. Most curiously, with further increasing launch speed the growing number of transfers then gives way to a surge of return impactors at the very highest launch speeds and corresponding reduction of the number of transfers at those speeds. The explanation for this strange change seems to be that because launch is from the +Y face, particles are being launched

backward against the orbit of Beta. So as launch speed increases, these particles go from still orbiting mostly along with Beta, to moving slowly at apoapsis of new orbits around Alpha that carry the particles down into Alpha's surface at periapsis, to moving slowly in such plunging orbits in the retrograde direction, to moving in larger semi-major axis orbits in the retrograde direction (meaning fewer particles plunge in far enough to hit Alpha and more stay out in orbits that may collide with Beta moving in the direction opposed to Beta's orbital motion). The final scenario is flagged as a return impact despite its high energy launch condition.

For launch from Beta in Beta's -X direction (from facet 1086 of the Beta mesh), which points away from Alpha along line of syzygy, the following is observed as launch speed increases: At the very lowest speed, all of the particles come right back without moving around Beta's surface much in either latitude or longitude. But then with increasing launch speed the spread over Beta of return impact locations grows, and a growing fraction of particles transfer, that then being replaced by a growing fraction of particles escaping. This looks similar to the case of launch in Beta's -Y direction (from facet 1116 of the Beta mesh), which points out from the leading face in the context of Beta's orbital motion. As launch speed goes up, at first everything returns close to the point of origin with a few outlying particles losing much more angular momentum than most all the rest, and then there is a spread in landing locations around Beta skewed a bit more toward the side away from Alpha. And there is eventual transition to most all escaping particles, with most of the escapees being uncertain at one launch speed, then suddenly transitioning to being expected at the very highest launch speed.

Lastly, for the case of launch from Beta's +X face (facet 1146 in particular), in the direction pointing toward Alpha along the line of syzygy. Progressively raising

the launch speed shows that particles begin reaching Alpha and such transferring and orbiting particles (mainly comprised, as a category, of the former) build up in number before escaping particles also accumulate. At the very highest launch speeds the fraction of rogues in each of the non-return-impacting dispositions remains nonexistant for the escapees and goes way up (in the too high Jacobi function value type of rogue) for the transfers and orbiters. In fact at the highest launch speed, all transfers and orbiters are this type of rogue result. Simply put, Alpha is just in the way of the fountain of fast-moving ejecta coming off of Beta towards it. Most all of the behavior for this and each of the above cases makes sense in keeping with the relative orientation of the launched distribution of ejecta, Alpha and Beta's placement, and the sense of the system's orbital motion.

5.4 Investigation of Primary Equator Regolith Lofting and Hypothesized Binary Evolution Mechanism

In contrast with the last section's examination of motion of particles originating from both body surfaces at high initial surface-relative velocity, here the motion of particles from only one component (Alpha) and only one region of its surface (that near the equator) is examined with **zero** initial surface-relative velocity. The only way in which motion of particles still results without such relative velocity is through making the dynamical state of the binary include a primary rotation rate which exceeds the "disruption spin rate" for which loose material at some point on the primary surface will be spun off. In other words, through setting the initial condition for primary spin fast enough that the surface-normal component of centrifugal acceleration felt by loose material somewhere on the surface is slightly larger in magnitude than the surface-normal component of gravitational acceleration felt by that material, so that the net acceleration in the surface normal direction is outward and the material

138

cannot be maintained on the surface.

This is not merely a hypothetical setup, but is suggested by the earlier mentioned fact that the highest points on the raised equatorial band of KW4 Alpha are only several meters below the altitude above the spin axis at which, with the same currently measured rapid spin rate, this outward net acceleration and levitation of material would arise. Note that this several meters is within the vertical uncertainty, or vertical resolution, in the detailed radar-derived primary shape model for that KW4 system, which is on the order of a few times less than the mean edge length for that mesh model [Lance Benner, personal communication], about 39 meters for KW4's case. So KW4 may actually have points at an altitude sufficient for current spin rate material levitation. Furthermore, this feature is not unique to KW4. Observational results for several binary primaries show them to be to be spinning at or near their individual "disruption spin rates" (see for example [73, 74, 75, 76, 77]). Pravec et al also find in their photometric survey of binary NEAs [14], and in their survey of binary asteroid angular momentum content [63], that this feature is not uncommon but frequent enough to possibly be considered a defining characteristic of the class of small asynchronous binaries being primarily focused on in this dissertation. Given the frequency with which binary asteroid primaries are found at or near their disruption spin rates, it is natural to consider what dynamical implications there are for material being levitated from their equatorial regions , hereafter referred to as regolith lofting.

In particular, it is interesting to consider whether the regolith lofting persists over time, and if so whether it is episodic or continuously occurring. Further, as every regolith particle has mass it will carry linear and angular momentum with it, and may transfer some of that linear or angular momentum between the binary system's components and the binary's mutual orbit. This suggests in turn that the regolith

lofting, if persistent over time, may have a role to play in the long timescale evolution of binary asteroid systems.

Mechanisms for such evolution have been studied previously. The usual solid-body tides driven evolution should be present, though the key parameters for it are highly uncertain for rubble-pile bodies like the primary and secondary probably are. The proposal and study of the BYORP mechanism by Cuk et al [35, 36], a process involving a net effective torque on the binary's mutual orbit due to solar flux reflection, absorption and re-radiation acting on the secondary body, was previously mentioned in the introduction. Here a different mechanism is described for similar binary orbit growth, that of continued YORP spin-up of the primary leading directly to orbit expansion by transfer of angular momentum through persistent regolith lofting motion. Note the BYORP theory does not include detailed modelling of particle motion or angular momentum transfer between parts of the system. Note for comparison that the mechanism described here, which fits well with the available observational results, also predicts orbit expansion times several times faster than those predicted by tidal dissipation effects alone, yet much slower than the orbit expansion claimed to be produced by BYORP.

The hypothesized mechanism is simple: Continued YORP angular acceleration of the primary can cause it to spin at rates where loose material on the equator can lift off into orbit. The presence of the secondary, or more properly gravitational interaction between the particles and the secondary, causes these particles to lose angular momentum and then re-impact onto the surface of the primary, in this way transferring angular momentum through the gravitational interaction into the binary orbit and causing it to grow. On average, it is expected that all angular momentum deposited by YORP into the primary's spin state which pushes the primary surface

beyond the surface disruption limit will eventually be transferred into the orbit. Thus, in a steady-state approximation, the orbit angular momentum will grow at a rate equal to the rate that YORP causes the primary's angular momentum to grow. This effect should act as a rotational speed limit on the primary, keeping it rotating at or near its surface disruption limit, as observational evidence supports.

While the hypothesis is simple, there are many assumptions implicit in it that must be verified. This section presents work to flesh out the details of this mechanism and to confirm, with rigorous simulations, that the mechanism works as proposed. For carrying out this confirmation, the specific example binary system of 1999 KW4 from before is used again, as it typifies the small asynchronous binaries class and is at the time of writing the best characterized member of it.

5.4.1 Precise dynamic simulation results

Several F2BP motion results sets for KW4 specifically are used as underlying binary motion for dynamic simulation of lofted particles through the system. These results sets match with 0.0°, 2.5°, and 5.0° of initial pole offset angle and with 0° and 180° of initial phase of the chosen lofting facet (see below) w.r.t. the syzygy plane (the plane formed by the Alpha spin pole and line of syzygy), measured counterclockwise from the Beta side of Alpha. While all of these results sets are generated using an initial Alpha spin rate of 0.000651444 rad/s, the set for 2.5° pole offset and 180° phase (for lofting from the side opposite Beta) is also generated a second time with the initial Alpha spin rate of 0.000641444 rad/s, while that for 2.5° offset but 0° phase (for lofting from the same side as Beta) is also regenerated with the initial Alpha spin rate of 0.000640444 rad/s.

An explanation is in order for this choice of parameters and for why the initial Alpha angular velocity, aligned to the Alpha $+Z$ axis, is given these magnitudes, rather

than the best estimated observation-derived spin rate for KW4 Alpha (0.000631343 rad/s, per [62]). The parameters come from an effort to identify the exact location on Alpha's surface and exact binary system conditions at which lofting would most likely first occur under YORP-driven primary spin-up. Here "binary system conditions" includes Alpha spin rate, mutual orbit elements, Alpha spin and orbit pole offset angle, Beta libration angle, and initial relative pose (in phase angle from the syzygy plane) of the above lofting location on Alpha's surface, and so forth.

First looking at the uniformly spinning Alpha model by itself, one may calculate for every face the angular velocity at which lofting will first occur (as angular velocity is slowly increased) at **any** point on that face, and the angular velocity at which lofting should first be guaranteed to occur at **every** point on that face. This is plotted in Figure 5.3, for most all facets not lying at extreme latitudes (i.e. near the north pole, and thus having very low face ID #'s, or near the south pole, and thus having very high face ID #'s approaching the total Alpha face count of 9168). As seen in the zoomed in panel, near equatorial face # 4113 had the lowest guaranteed-everywhere-lofting spin rate, equal to 0.000651444 rad/s (about 3.18% higher than the observation-derived spin rate). Simultaneously, the same face # 4113's first-lofting spin rate **is almost exactly** the observation-derived spin rate. Thus this face is adopted as the chosen lofting facet, and it is determined that suitable threshold rates at which lofting might be considered to "turn on" there, for purposes of the model of the next subsection, should be chosen about halfway between the first-lofting and guaranteed-everywhere-lofting spin rates for this face, or about 0.000641444 rad/s.

Next, one proceeds from the model of uniformly spinning Alpha by itself to a toy model for the full binary system, having both full-detail body meshes but keeping both centroids locked to an assumed perfect circular Keplerian orbit and keeping Beta's

142
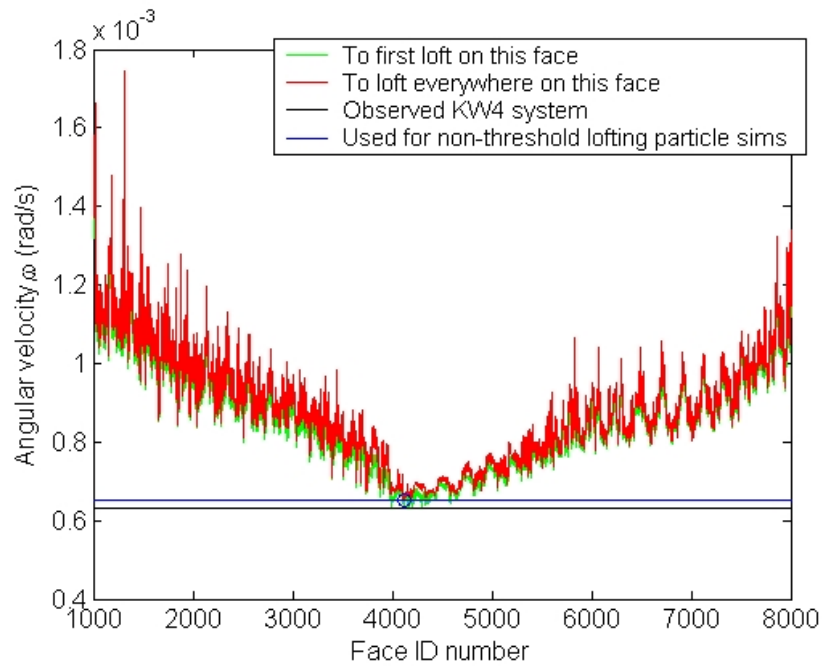
(a) Across large range of lattitudes
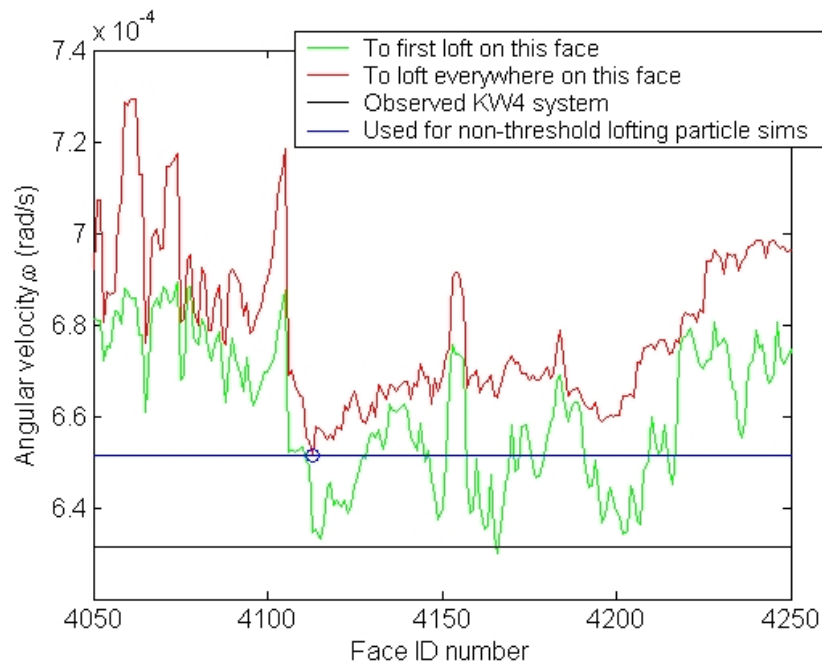
(b) Zoomed in on facets near the equator

Figure 5.3: Spin rates computed for lofting on each facet vs. facet ID # on KW4 Alpha. This is computed for the uniformly spinning Alpha body mesh by itself, balancing surface-normal components of centripetal acceleration and gravitational acceleration.
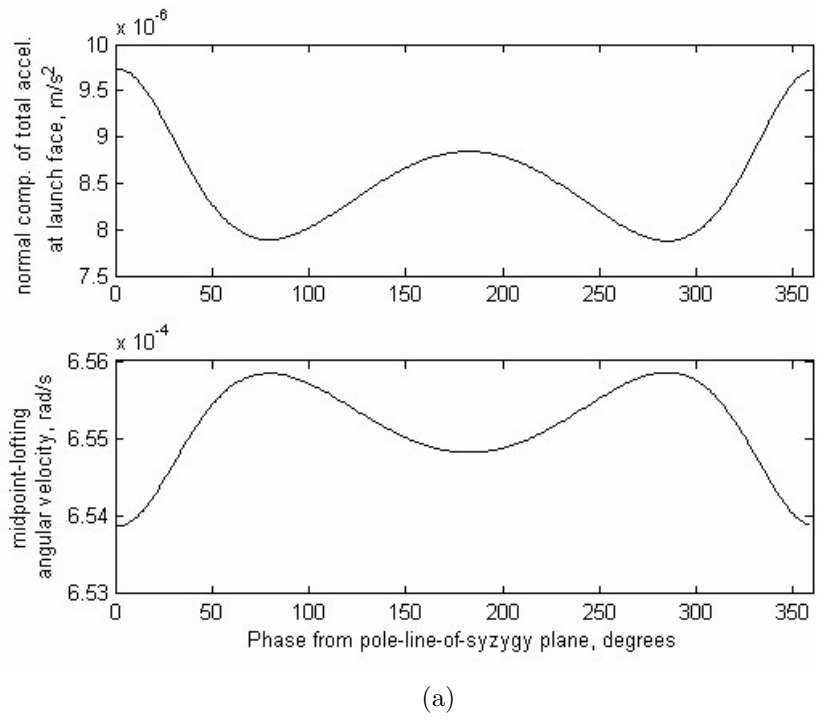
(a)
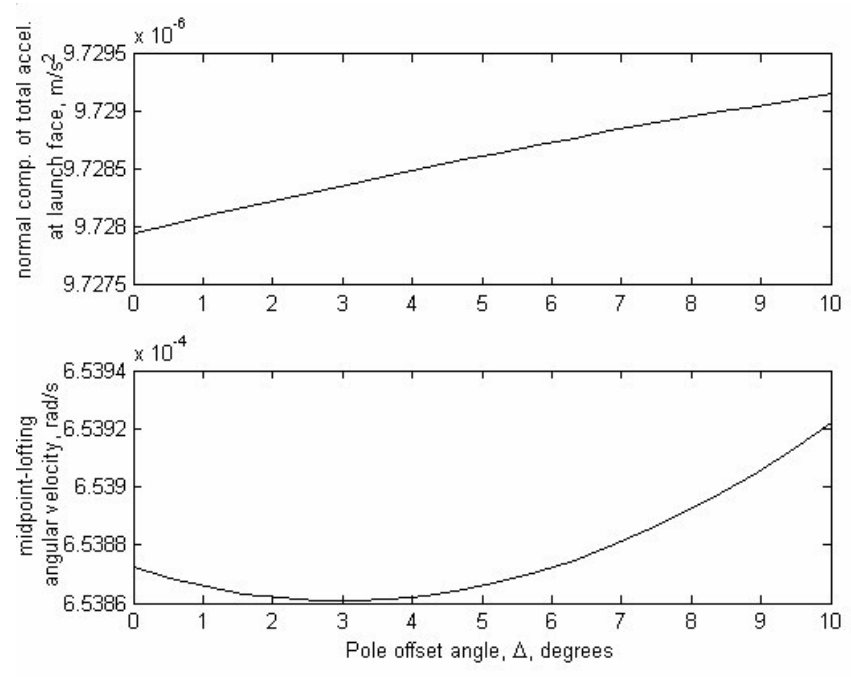
(b)

Figure 5.4: Spin rate computed to guarantee lofting everywhere on a facet vs. initial
facet phase and vs. pole offset angle Δ. (The facet considered is # 4166,
very near the selected lofting facet.)

144

longest axis locked to the line of syzygy. This gives a static setup in which to test the guaranteed-everywhere-lofting spin rate on the chosen face # 4113 or some other very nearby face, at different phases of that face from the syzygy plane. As expected from intuition about the radial component of tidal acceleration, two minima in this spin rate occur at 0° and 180° of phase. Refer to Figure 5.4, panel (a). The minima are separated by about 1×10^{-6} rad/s in value, the 0° phase number being lower. This is as expected, given the asymmetry of tidal acceleration in such a system for which the ratio of mean primary radius to orbit size is **not** $\ll 1$. Hence the threshold for same side lofting is chosen to be 1×10^{-6} rad/s lower than the 0.000641444 rad/s threshold chosen by the last paragraph for opposite side lofting. Fixing 0° phase, the guaranteed-everywhere-lofting spin rate on face # 4113 or some other nearby face is also found to have a minimum at $\approx$2-3° along the pole offset angle coordinate of parameter space (see Figure 5.4, panel (b)). Varying Beta libration angle and slightly varying the in-plane orbit elements both have minimal effect on first-lofting or guaranteed-everywhere-lofting spin rates.

All of this information is used to guide the choice of initial configuration conditions for simulation of the F2BP binary motion, and corresponding simulation of particle trajectories within the binary (as the binary follows that motion) starting from Alpha's surface, on the chosen lofting facet. For the latter simulation by the methods of section 5.1, at the initial time particles are placed in a triangular grid over the triangular facet, with zero velocity relative to the moving surface below. The particles are displaced by a very small distance ($\approx$0.25 m) outward along the face normal direction, to avoid intersection with the body polyhedral mesh and erroneous immediate detection of a collision at the initial time. The particles are not given any physical size, and while a very small normalized mass is assigned to them

within the RF3BP code, they essentially act as massless test particles as intended.

The results of batches of regolith particles thus propagated are sorted according to their final dispositions, and further sorted by the expectation about those dispositions if applicable. Lofted particles are observed going to the outcomes of transfer impact onto Beta, "orbit", and escape in small numbers only for the cases with the higher initial Alpha spin rate of 0.000651444 rad/s, so such sorting is only relevant to those cases. When some particles go to dispositions other than return impact onto Alpha like this, it causes a problem with eventual draining of particles from the surface of Alpha in the probability-based simulation of the next subsection. It would also imply continuous erosion of material from the primary in the real binary system, which doesn't seem realistic at this stage in the system's evolution. Thus the next subsection's methodology is employed only with inputs derived from the results sets, for dynamic simulation of lofting particles on top of F2BP motion, matching the two cases with initial Alpha spin rate at the threshold spin rate values.

These inputs, passed to the probability-based propagation, are two key probability matrices (one for lofting from each side) and the means and standard deviations for velocities accompanying non-zero elements of those matrices. The $X-Y$ plane (orbit plane) of the barycentric rotating frame is divided into 36 angular sectors, each $10°$ wide, converging at the location in that frame of the centroid of Alpha. These are numbered 1-36 counterclockwise, starting with the centerline of sector 1 lying on the line of syzygy opposite from Beta. The same type of "bins" in longitude relative to the rotating barycentric frame, aligned the same way but centered on Beta's centroid, are also created and similarly numbered 37-72. In post-processing the output trajectories for a large ensemble of particles propagated using precise dynamic simulation, the longitude in the rotating barycentric frame of the plane projection of the impact

point of each particle trajectory is found. Which longitude bin that impact longitude falls within, for the appropriate body impacted, is then determined. The total time of flight, $t_E - t_S$, for each trajectory is also used to obtain a time bin designation for that particle as

$$\lfloor 18 \ (\|\boldsymbol{\omega}_1\| - \|\boldsymbol{\omega}_{\mathrm{orb}}\|) \ (t_E - t_S)/\pi \rfloor + 1 \,. \tag{5.25}$$

For each particle, given its impact longitude bin and time bin designations, the element of the probability matrix in the row matching the longitude bin number and column matching the time bin number is incremented by one. All particles impacting neither body, but instead escaping or orbiting at the maximum duration, are considered released to those final dispositions instantly. So these cases are all similarly counted up in the first column, in the last rows (with zeros to their right). The entire matrix is divided by the ensemble's size to give probabilities of reaching each location in space and time, or for each discretized possible outcome. For each impacting particle the velocity with respect to, and coordinated in, a local "bin-fixed" frame with $+X$ pointing outward along the bin of impact's centerline, $+Z$ aligned to the barycentric rotating frame's $+Z$ axis, and origin at the point of impact is also found. All such impacting velocity vectors for particles reaching a given bin are accumulated, and the mean and standard deviation is stored along with the matrix for use in the algorithm described below. If applicable, for each escaping/orbiting particle the mass-specific change to the particle's barycentric angular momentum between endpoints of its flight is computed, averaged over all particles escaping/orbiting, and passed on as well.

5.4.2 Novel probabilistic mapping approach

The preceding subsection's precise dynamic simulation of test particles treats those particles as not exerting any influence on the translational or rotational motion of

147

the binary components themselves, nor exerting any influence on each other's motion. This is justified by the fact that particles of realistic size and mass will generate forces and torques on the binary components that are so small compared to the forces and torques exerted by the binary components on each other as to be indistinguishable from numerical noise if included in the dynamic simulation. In other words the relative scaling of the effects of the particles on the components and the effects of the components on each other advocates against the approach of directly including the former effects in the precise dynamic simulation. In addition, the accumulation of the binary components' responses to individual particle motions takes very long times to build up to observable changes, and simulation of the F2BP dynamics for such long times is prohibitively computationally expensive. Even if such computation were free, and despite the excellent symplectic and mean-error-reducing properties of the integration algorithm used, dynamic propagation to such long durations would entail eventual accumulation of numerical error which could confuse or overwhelm the accumulating particle motion effects on the binary itself.

So in order to detail the hypothesized mechanism for slow time evolution of the binary system in response to the shed particles, rather than the fast particle trajectories themselves, a probability-based method is developed here for propagating a simplified model of the binary system plus a collection of primary regolith particles. This model can be run forward for very long durations and much larger particle populations at a comparatively very low computational cost. Yet, as it uses the probability matrices and accompanying random variable parameters derived as above from the output of precise dynamic simulation, this probability-based propagation is grounded in the true full-detail dynamics of the system while computationally independent from them.

First, one defines a particle state vector $\mathbf{x}$ to have one element for each particle, the integer value of which indicates, along with some appropriate buffer variables, the particle's location in space and/or time or else that particle's final disposition reached. Admissible values for elements of $\mathbf{x}$ and their meanings are detailed in Table 5.3. At the initial time, $\mathbf{x}$ is set to uniformly distributed random integers in the range of 1-36, effectively spreading the equal-mass particles evenly around Alpha's equatorial longitude.

Table 5.3: Meaning of values for particle state vector ($\mathbf{x}$) elements

Integer value	Meaning
1 - 36	Particle is lying on surface of Alpha, in 10°-wide sector of longitude on Alpha w.r.t. rotating barycentric frame denoted by value. Such sectors are numbered counterclockwise viewed from north pole of Alpha, 1 being centered on line of syzygy on opposite side from Beta.
37 - 72	Particle has previously or just impacted onto Beta, in 10°-wide sector of longitude on Beta w.r.t. rotating barycentric frame denoted by value. Such sectors are numbered counterclockwise viewed from north pole of Beta, 1 being centered on line of syzygy on the same side as Alpha.
73	Particle has begun a trajectory that will carry it to escape from the system.
74	Particle has begun a trajectory that will leave it still lingering in "orbit" after very long time.
100 - 9999	Particle will later impact into a sector of longitude on Alpha or on Beta, as defined above and given by buffered value, but is currently in flight, with $10000-n$ time intervals past the current time left until impact occurs (n being the current value).
10000	Particle is impacting at this current time step, at sector of longitude given by buffered value.

Note that here the same notation conventions as before (vectors in bold, dyads and matrices in uppercase roman, $\widetilde{(\cdot)}$ for the cross product matrix form) are used again. But also, a first-level right subscript indicates the body the quantity applies to, a second-level right subscript indicates a step or instant in time, a left subscript

indicates the frame a quantity is coordinated in, and a left superscript denotes the frame the quantity (such as velocity) is relative to. Any of these are omitted when not relevant or when the relationship holds independent of frame, etc. Also $_I$ indicates the inertial barycentric frame, $_B$ indicates the rotating barycentric frame, $_1$ indicates the Alpha-fixed frame or the Alpha body itself, $_2$ indicates the Beta-fixed frame or the Beta body itself, and $_i$ indicates the i'th particle.

Aside from the particle states, a set of binary states describing the system at any given time is set to initial values matching the binary models simulated in the previous subsection. This set of states consists of the following: the mass of each component, m_{1_t} and m_{2_t}, the inertia dyad of each component, $_1I_{1_t}$ and $_2I_{2_t}$, the angular velocity vector of each component, $_1\boldsymbol{\omega}_{1_t}$ and $_2\boldsymbol{\omega}_{2_t}$, the attitude rotation matrix mapping from the frame of each component to the inertial frame, $_IR_{1_t}$ and $_IR_{2_t}$, and the barycentric position and velocity of each component center of mass, i.e. $_I\mathbf{r}_{1_t}$, $_I^I\mathbf{v}_{1_t}$, $_I\mathbf{r}_{2_t}$, and $_I^I\mathbf{v}_{2_t}$. In addition, the mean equatorial radius of Alpha, d_{1_t}, is made variable to account for mass loss/addition from/to Alpha's equatorial region making Alpha slightly smaller/larger in size. The time since the propagation's start at discrete time step $_t$ is denoted as t_t. The interval between discrete time steps is determined as the time needed for a point stationary on Alpha's surface to advance from one sector of longitude relative to the rotating barycentric frame, or one "longitude bin", to the next, that is

$$t_{t+1} - t_t \;=\; \frac{\pi}{18 \left(\|\boldsymbol{\omega}_{1_t}\| - \|\widetilde{_I\mathbf{r}_t}\,_I^I\mathbf{v}_t\| \,/\, \|_I\mathbf{r}_t\|^2 \right)}, \qquad _I\mathbf{r}_t =_I \mathbf{r}_{2_t} -_I \mathbf{r}_{1_t}, \qquad _I^I\mathbf{v}_t =_I^I \mathbf{v}_{2_t} -_I^I \mathbf{v}_{1_t}.$$

(5.26)

This can be calculated at any time step, and likewise the angular momenta of the

150

system components can be found at any step from the binary states:

$$I\mathbf{H}_{1_t} = {}_I R_{1_t} \, {}_1 I_{1_t} \, {}_1 \boldsymbol{\omega}_{1_t}, \qquad {}_I \mathbf{H}_{2_t} = {}_I R_{2_t} \, {}_2 I_{2_t} \, {}_2 \boldsymbol{\omega}_{2_t}$$

$$_I\mathbf{H}_{\mathrm{orb}_t} = m_{1_t} \, \widetilde{_I\mathbf{r}_{1_t}} \, {}_I^I \mathbf{v}_{1_t} + m_{2_t} \, \widetilde{_I\mathbf{r}_{2_t}} \, {}_I^I \mathbf{v}_{2_t}, \qquad {}_I\mathbf{H}_{2+\mathrm{orb}_t} = {}_I\mathbf{H}_{2_t} + {}_I\mathbf{H}_{\mathrm{orb}_t} \qquad (5.27)$$

Before discussing the algorithm logic used to propagate from one time step to the next, the changes to the binary states caused by lofting, gravitational interaction during flight, and then impact of a single particle of mass m_i by itself are detailed. First for lofting: Since the particle is released with no initial velocity relative to Alpha's surface, no reaction between the particle and that surface takes place. The rotational state of Alpha (both attitude matrix and angular velocity vector) is preserved from just before lofting ("instant $_-$") to just after lofting ("instant $_+$"). However, Alpha's total mass is reduced by m_i and the inertia dyad of Alpha is also changed, not only directly but by the re-shifting of the Alpha center of mass to account for the new body mass distribution. That centroid shift also slightly adjusts the barycentric position and velocity of the centroid. The following relations result:

$$_1\boldsymbol{\omega}_{1_+} = {}_1\boldsymbol{\omega}_{1_-} \qquad\qquad (5.28)$$

$$_I R_{1_+} = {}_I R_{1_-} \qquad\qquad (5.29)$$

$$m_{1_+} = m_{1_-} - m_i \qquad\qquad (5.30)$$

$$_1 I_{1_+} = {}_1 I_{1_-} + \left(\frac{m_{1_-} \, m_i}{m_{1_-} - m_i} \right) \widetilde{_1\boldsymbol{\rho}_{i_-}} \, \widetilde{_1\boldsymbol{\rho}_{i_-}} \qquad\qquad (5.31)$$

$$_I\mathbf{r}_{1_+} = {}_I\mathbf{r}_{1_-} - \left(\frac{m_i}{m_{1_-} - m_i} \right) {}_I R_{1_-} \, {}_1\boldsymbol{\rho}_{i_-} \qquad\qquad (5.32)$$

$$_I^I\mathbf{v}_{1_+} = {}_I^I\mathbf{v}_{1_-} - \left(\frac{m_i}{m_{1_-} - m_i} \right) {}_I R_{1_-} \, \widetilde{_1\boldsymbol{\omega}_{1_-}} \, {}_1\boldsymbol{\rho}_{i_-} \qquad\qquad (5.33)$$

Here the quantity ${}_1\boldsymbol{\rho}_{i_-}$ is the relative position vector from the centroid of Alpha to the position of the particle i at the instant before lofting, expressed in the Alpha frame at the instant before lofting, prior to the centroid shift involved. The location

on Alpha's equator where the lofting is determined to occur gives this vector. In the present model, this equatorial location is chosen to be either the center of the rotating-barycentric-frame-relative longitude bin 1 (i.e. on the line of syzygy opposite from Beta, or at the anti-Beta point on Alpha) or else the center of the similar longitude bin 19 (on the line of syzygy on the same side as Beta, or at the sub-Beta point on Alpha). Note, for later use in defining the starting point of the trajectory followed by each lofted particle,

$$_I\mathbf{r}_{i_+} = {}_I\mathbf{r}_{1_-} + {}_I\mathrm{R}_{1_-} {}_1\boldsymbol{\rho}_{i_-} \tag{5.34}$$

$$_I^I\mathbf{v}_{i_+} = {}_I^I\mathbf{v}_{1_-} + {}_I\mathrm{R}_{1_-} \widetilde{{}_1\boldsymbol{\omega}_{1_-}} {}_1\boldsymbol{\rho}_{i_-}. \tag{5.35}$$

Next for the set of changes in the binary states that occur from just before to just after impact of the single particle onto either body. Here the relations are shown for a return impact back onto Alpha rather than a transfer impact onto Beta. However, all of the relations are identical in the latter case except for replacing the subscripts $_1$ with $_2$, and using the new quantities thus denoted for Beta. Upon particle impact, the particle mass is added onto the target body with an accompanying direct change to the body inertia dyad plus an indirect change to the same due to body centroid re-shifting. Again, such a centroid shift adjusts the barycentric position and velocity of the centroid. The instantaneous attitude of the body may be assumed unchanged across the impact, but because the incoming particle has velocity relative to the surface just before impact, the body reacts to that with a change in angular velocity (and an extra additive change in inertial barycentric velocity of the body centroid too). Assume for now that the other, final endpoint of the trajectory followed by each lofted but then impacting particle is well-defined as $_I\mathbf{r}_{i_-}$ and $_I^I\mathbf{v}_{i_-}$. Then

$$_1\boldsymbol{\rho}_{i_-} = {}_I\mathrm{R}_{1_-}^T \left({}_I\mathbf{r}_{i_-} - {}_I\mathbf{r}_{1_-} \right) \tag{5.36}$$

152

Then the following relations for the binary state changes across an impact result:

$$_I R_{1+} = {}_I R_{1-} \tag{5.37}$$

$$m_{1+} = m_{1-} + m_i \tag{5.38}$$

$$_1 I_{1+} = {}_1 I_{1-} - \left(\frac{m_{1-} \, m_i}{m_{1-} + m_i} \right) \widetilde{{}_1 \boldsymbol{\rho}_{i-}} \, \widetilde{{}_1 \boldsymbol{\rho}_{i-}} \tag{5.39}$$

$$_I \mathbf{r}_{1+} = {}_I \mathbf{r}_{1-} + \left(\frac{m_i}{m_{1-} + m_i} \right) {}_I R_{1-} \, {}_1 \boldsymbol{\rho}_{i-} \tag{5.40}$$

$$_I^I \mathbf{v}_{1+} = \left(\frac{m_{1-}}{m_{1-} + m_i} \right) {}_I^I \mathbf{v}_{1-} + \left(\frac{m_i}{m_{1-} + m_i} \right) {}_I^I \mathbf{v}_{i-} \tag{5.41}$$

$$_1 \boldsymbol{\omega}_{1+} = \left[{}_1 I_{1-} - \left(\frac{m_{1-} \, m_i}{m_{1-} + m_i} \right) \widetilde{{}_1 \boldsymbol{\rho}_{i-}} \, \widetilde{{}_1 \boldsymbol{\rho}_{i-}} \right]^{-1} \cdot$$
$$\left({}_1 I_{1-} \, {}_1 \boldsymbol{\omega}_{1-} + \left(\frac{m_{1-} \, m_i}{m_{1-} + m_i} \right) {}_I R_{1-}^T \left[{}_I \mathbf{r}_{i-} \, \widetilde{ } \, - {}_I \mathbf{r}_{1-} \right] \left[{}_I^I \mathbf{v}_{i-} - {}_I^I \mathbf{v}_{1-} \right] \right) \tag{5.42}$$

There are also small changes to the binary states that stem from the binary system's reaction opposite the modification of each particle's inertial barycentric angular momentum while it is in flight. This angular momentum change for the particle occurs due to gravitational interaction between the particle and the full mass distributions of the binary components. Again let the particle's trajectory be defined, with starting point denoted here as $\{ {}_I \mathbf{r}_{i_S} , {}_I^I \mathbf{v}_{i_S} \}$ and ending point denoted here as $\{ {}_I \mathbf{r}_{i_E} , {}_I^I \mathbf{v}_{i_E} \}$. Then across the bit of interaction during each of the p discrete time intervals (assumed roughly equal in length) covered by the particle's trajectory, one has that

$$_I \mathbf{H}_{\text{orb}_-} = \left(\frac{m_1 \, m_2}{m_1 + m_2} \right) \widetilde{{}_I \mathbf{r}_-} \, {}_I^I \mathbf{v}_-, \qquad {}_I \mathbf{r}_- = {}_I \mathbf{r}_{2-} - {}_I \mathbf{r}_{1-} , \; {}_I^I \mathbf{v}_- = {}_I^I \mathbf{v}_{2-} - {}_I^I \mathbf{v}_{1-} \tag{5.43}$$

$$_I \mathbf{H}_{\text{orb}_+} = {}_I \mathbf{H}_{\text{orb}_-} - \frac{m_i}{p} \left(\widetilde{{}_I \mathbf{r}_{i_E}} \, {}_I^I \mathbf{v}_{i_E} - \widetilde{{}_I \mathbf{r}_{i_S}} \, {}_I^I \mathbf{v}_{i_S} \right) \tag{5.44}$$

$$e = \left(\widetilde{{}_I \mathbf{H}_{\text{orb}_-}} \, {}_I \mathbf{H}_{\text{orb}_+} \right) / \left\| \widetilde{{}_I \mathbf{H}_{\text{orb}_-}} \, {}_I \mathbf{H}_{\text{orb}_+} \right\| \tag{5.45}$$

$$\theta = \text{acos} \left(\frac{{}_I \mathbf{H}_{\text{orb}_-}}{\left\| {}_I \mathbf{H}_{\text{orb}_-} \right\|} \cdot \frac{{}_I \mathbf{H}_{\text{orb}_+}}{\left\| {}_I \mathbf{H}_{\text{orb}_+} \right\|} \right) \tag{5.46}$$

$$R = \text{expm} \left[\tilde{e} \, \theta \right] \tag{5.47}$$

$$k = \begin{bmatrix} 0 & 0 & 1 \end{bmatrix}^T \cdot \frac{{}_I \mathbf{H}_{\text{orb}_+}}{R \, {}_I \mathbf{H}_{\text{orb}_-} + \delta} \tag{5.48}$$

$$
{}_I\mathbf{r}_{1_+} = \left(\frac{-m_2}{m_1 + m_2}\right) k^2 R \, {}_I\mathbf{r}_- \qquad {}_I\mathbf{r}_{2_+} = \left(\frac{m_1}{m_1 + m_2}\right) k^2 R \, {}_I\mathbf{r}_- \qquad (5.49)
$$

$$
{}_I\mathbf{v}_{1_+} = \left(\frac{-m_2}{m_1 + m_2}\right) \frac{1}{k} R \, {}_I^I\mathbf{v}_- \qquad {}_I\mathbf{v}_{2_+} = \left(\frac{m_1}{m_1 + m_2}\right) \frac{1}{k} R \, {}_I^I\mathbf{v}_- \qquad (5.50)
$$

Herein δ is a very small constant close to machine precision to prevent singularity, expm $[\cdot]$ is the matrix exponential operation, and there are no time subscripts on the component masses because they do not change across this time-step's bit of the interaction. Note that large p for longer flight times can be problematic in that very large p spreads out the change across many time steps until the change improperly numerically disappears given an override needed to avoid numerical error. When the orbit angular momentum change of Eq. 5.44 is segmented into many equal portions applied during each of the time steps for which the particle is in the "in-flight" state, each portion may be too small, such that ${}_I\mathbf{H}_{\mathrm{orb}-}$ and ${}_I\mathbf{H}_{\mathrm{orb}+}$ are so close in direction that the dot product inside of the acos in Eq. 5.46 is nearly unity. In fact, numerical error may result in the dot product being slightly greater than unity, producing imaginary numbers which break the propagation. Therefore an override is introduced to force the dot product to be ≤ 1, and thus $\theta = 0$, in such rare cases.

As for the determination of the final endpoint of a particle's trajectory, and how much later in time that comes than the initial endpoint of the trajectory, that information is derived from the probability matrices from the earlier post-processing of the particle precise dynamic simulation output. Recall that each matrix has rows corresponding to the particle state values 1-74, i.e. corresponding to bins of longitude on Alpha, then bins of longitude on Beta, then the escaping and lingering in orbit final dispositions (see Table 5.3). Also recall the columns correspond to the number of intervals in time covered by the trajectory. The location in time, body reached, and equatorial position on that body (centerlines of longitude bins are used) of a trajec-

tory's final endpoint is randomly selected in roulette wheel fashion using the nonzero probabilities in the probability matrix. This gives the needed inertial position vector $_I\mathbf{r}_E = {_I}\mathbf{r}_{i_-}$ (the latter with respect to the impact equations), computed at point where it must be used given then-current binary state values. Then the particle's velocity in the bin-fixed frame attached to the longitude bin reached by the particle is generated from a normal random variable draw, using the mean and standard deviation corresponding to that bin, as read in along with the matrices. This velocity is converted into the needed inertial particle velocity $_I^I\mathbf{v}_{i_E} = {_I^I}\mathbf{v}_{i_-}$ (the latter with respect to the impact equations). The conversion is made at the point of use for the inertial velocity, given then-current binary state values.

Finally note that the progression of time from one step to the next itself also requires an update of the binary states. Since the mutual orbit is nearly circular, one can approximate the update for the orbit states with a simple rotation about the orbit normal. The updates for the body attitudes may also be approximated with simple rotations about each body's instantaneous angular velocity direction. For Alpha, this simple rotation must also account for any small, constant angular acceleration of Alpha, $\boldsymbol{\alpha}_1$, included in the model to represent YORP or torque from any source external to the binary itself. Assuming alignment between the angular acceleration and the spin vector in the Alpha-fixed frame gives

$$_I\mathrm{R}_{1_{t+1}} = {_I}\mathrm{R}_{1_t} \operatorname{expm} \left[\widetilde{_1\boldsymbol{\omega}_{1_t}} \frac{\|\boldsymbol{\alpha}_1\| \left(t_{t+1} - t_t\right)^2}{2 \|\boldsymbol{\omega}_{1_t}\|} + \widetilde{_1\boldsymbol{\omega}_{1_t}} \left(t_{t+1} - t_t\right) \right]^T \tag{5.51}$$

$$_I\mathrm{R}_{2_{t+1}} = {_I}\mathrm{R}_{2_t} \operatorname{expm} \left[\widetilde{_2\boldsymbol{\omega}_{2_t}} \left(t_{t+1} - t_t\right) \right]^T \tag{5.52}$$

$$_1\boldsymbol{\omega}_{1_{t+1}} = {_1}\boldsymbol{\omega}_{1_t} \left(1 + \frac{\|\mathbf{1}_1\|}{\|\boldsymbol{\omega}_{1_t}\|} \left(t_{t+1} - t_t\right) \right) \tag{5.53}$$

$$R_{\text{orb}} = \operatorname{expm} \left[\frac{\widetilde{_I\mathbf{r}_t\, {_I^I}\mathbf{v}_t}}{\|\widetilde{_I\mathbf{r}_t\, {_I^I}\mathbf{v}_t}\|} \sqrt{G(m_{1_t} + m_{2_t})/\|_I\mathbf{r}_t\|^3} \left(t_{t+1} - t_t\right) \right] \tag{5.54}$$

$$_I\mathbf{r}_{1_{t+1}} = R_{\text{orb}}\,_I\mathbf{r}_{1_t}, \qquad _I\mathbf{r}_{2_{t+1}} = R_{\text{orb}}\,_I\mathbf{r}_{2_t}, \qquad (5.55)$$

$$_I^I\mathbf{v}_{1_{t+1}} = R_{\text{orb}}\,_I^I\mathbf{v}_{1_t}, \qquad _I^I\mathbf{v}_{2_{t+1}} = R_{\text{orb}}\,_I^I\mathbf{v}_{2_t} \qquad (5.56)$$

Having detailed all of the building blocks for the algorithm, the algorithm logic used to propagate from one time step to the next is as follows. Recall that initially all particle states $\mathbf{x}_i$ have values between 1 and 36 representing the particle lying on Alpha's surface in the corresponding longitude bin. First the binary states at a new time step $_{t+1}$ are set equal to those at the previous step $_t$. Then all particles are looped through to determine any motion/changes for each particle, one by one, and the accompanying changes to the new time step's binary states based on what happens to that particle.

If $1 < \mathbf{x}_{i_t} < 19$ or $19 < \mathbf{x}_{i_t} < 37$ then the particle was not previously at a lofting location on Alpha's surface, and remains on the surface but is carried around to the next longitude bin (going counterclockwise) by Alpha's rotation relative to the rotating barycentric frame. So $\mathbf{x}_{i_{t+1}} = \mathbf{x}_{i_t} + 1$, or in the case of $\mathbf{x}_{i_t} = 36$, the state value wraps back to $\mathbf{x}_{i_{t+1}} = 1$. If however $\mathbf{x}_{i_t} = \{1, 19\}$ then the particle was previously at a lofting location and so $\|\boldsymbol{\omega}_{1_t}\|$ is compared with the appropriate threshold rate below which lofting on the opposite or same side from Beta turns off, and the value of d_{1_t} is compared with the threshold mean Alpha radius below which lofting turns off everywhere. If either quantity is too small, $\mathbf{x}_i$ is again incremented by 1 to represent remaining on the rotating surface, but if both quantities are sufficiently large the particle lofts. In the latter case the corresponding probability matrix is used to randomly assign the particle to go to a bin in the "space" of longitude vs. flight-time.

If the column designation y of the bin in longitude vs. flight-time space is 1, the particle is considered to go to the specified impact location immediately or start it's

escape or orbiting path immediately, so $\mathbf{x}_{i_{t+1}}$ is assigned the value of the row of the bin in longitude vs. flight-time space. If this value is between 1 and 36 inclusive, then changes to the current (indexed by $_{t+1}$) binary system states are made matching lofting (Eqs. 5.28-5.33), flight which covers only one time interval (Eqs. 5.43-5.50 with $p = 1$), and return impact onto Alpha (Eqs. 5.36-5.42). If the value is between 37 and 72 inclusive, then changes to the current binary states are made matching lofting, one time interval of flight, and impact onto Beta (using the same equations, respectively). If the value is 73 for escape or 74 for orbiting, changes to current binary states are made just for lofting (Eqs. 5.28-5.33) and for the entire escape or orbiting path at once (Eqs. 5.43-5.50 but replacing Eq. 5.44 with $_I\mathbf{H}_{\mathrm{orb}_+} = {}_I\mathbf{H}_{\mathrm{orb}_-} - m_i \,{}_I\Delta\mathbf{H}_i$ where $_I\Delta\mathbf{H}_i$ is the average mass-specific angular momentum change to an escaping/orbiting particle, from the precise dynamic simulation).

If the column designation y of the bin in longitude vs. flight-time space that the particle is assigned to after lofting is instead > 1, then $\mathbf{x}_{i_{t+1}} = 10000 - y + 1$. Thus this particle state is set to be 10000 minus the number of time intervals of flight-time left to be passed beyond step $_{t+1}$ before the particle ends up at the specified impact location matching the row of the bin in the longitude vs. flight-time space. The row designation x of the bin is placed in a buffer variable for retrieval later when the impact time arrives, and y is also so buffered. In the present time step, changes are made to the current $_{t+1}$ binary states for lofting (Eqs. 5.28-5.33) and for just the first segmented portion of the interaction along the trajectory (Eqs. 5.43-5.50 with p equal to the buffered y).

At the previous higher level of testing the particle state's previous value $\mathbf{x}_{i_t}$, if $74 < \mathbf{x}_{i_t} < 10000$ then the particle was previously lofted and was awaiting impact as of step $_t$. To move the particle toward impact in time, $\mathbf{x}_{i_{t+1}} = \mathbf{x}_{i_t} + 1$ is used, and

changes to the binary states are made for another segmented portion of the particle's interaction along the trajectory (Eqs. 5.43-5.50 with p equal to the y buffered for this particle). If after so incrementing $\mathbf{x}_i$ it becomes true that $\mathbf{x}_{i_{t+1}} = 10000$, then the particle has moved to impact in covering the current time interval to reach step $_{t+1}$. Thus the reassignment $\mathbf{x}_{i_{t+1}} = x$ is made (x having been buffered for this particle) to indicate where the particle impacts, and additionally the changes to binary states matching the impact are made (Eqs. 5.36-5.42).

If $36 < \mathbf{x}_{i_t} < 75$ then the the particle state value is kept the same, i.e. $\mathbf{x}_{i_{t+1}} = \mathbf{x}_{i_t}$, because no further details of motion are included in the present modelling of the system for particles that have already transfer impacted onto Beta or have already embarked upon escaping or orbiting paths.

Once completing the loop through all particle states to determine changes to particle disposition and matching binary state changes, the time t is increased by one interval to get t_{t+1} and the regular updates to the current binary states for time evolution of the binary by itself are applied (Eqs. 5.51-5.56, reconsidering the binary states before use of these equations as if being for the previous time index $_t$). Also, $d_{1_{t+1}}$ is found anew from $m_{1_{t+1}}$. Then all of the above may be iterated for the next time step.

Before doing so, however, a few additional tasks are optionally performed for better fidelity and improved running time. First, because the spin rate of Alpha may have changed over the last time step in response to accumulated effects of particles return impacting onto Alpha, and because the mutual orbit rate will have changed as well, the length of a time interval according to the definition of Eq. 5.26 may have increased or decreased. This time interval re-scaling may require shifting of the value of any particle state with value, at this point in the algorithm, in the range of

$100 < \mathbf{x}_i < 9999$. This shift may be either higher (for increasing interval length) or lower (for decreasing interval length). Recall that $10000 - \mathbf{x}_i$, for $\mathbf{x}_i$ in this range, represents the number of time intervals past the current time yet to pass before the particle will impact. Multiplying the ratio of the old interval length to the new one by this $10000 - \mathbf{x}_i$ and taking the fractional remainder thereof gives a value for a uniform random draw in the interval $0, 1$ to be compared with to determine any incrementing/decrementing of $\mathbf{x}_i$.

Finally, it is found that lofting, flight, and return impact often occur in rapid succession in short transient lofting episodes, separated by long time spans during which the primary is slowly spun back up by the small YORP angular acceleration applied to it. Eventually the lower of the lofting spin rate thresholds is encountered again, and the cycle is repeated. Progressing through natural time steps by all of the above algorithm during the long spin-up periods would be computationally wasteful, as it would explode simulation run time for long durations without revealing further dynamically interesting behavior. Thus, at the point just before looping back to go through all operations for the next natural time step, if a detection buffer indicates that for the last ten natural time steps there was both no lofting activity and no particle state values indicating a particle was aloft, an extra time step to skip most of the spin-up period is added in. This skip-over step has length Δt equal to 95% of the difference between the norm of ${}_1\boldsymbol{\omega}_{1_t}$ and the lower spin rate threshold value, divided by the norm of the constant angular acceleration ${}_1\boldsymbol{\alpha}_1$. Since nothing is aloft, no particle state adjustment as in the last paragraph is needed with this jump in time. Instead, all particle states in the range $1 \leq \mathbf{x}_{i_t} \leq 36$ are moved to account for the rotation of Alpha during the skip-over step, i.e. the number of bins to move

through, q, and new particle state values are given by

$$q = \text{round} \left\{ \frac{18}{\pi} \left(\frac{1}{2} \|\boldsymbol{\alpha}_1\| \Delta t^2 + \|\boldsymbol{\omega}_{1_t}\| \Delta t - \sqrt{G(m_{1_t} + m_{2_t})/\|\mathbf{r}_t\|^3} \, \Delta t \right) \right\},$$

$$\mathbf{x}_{i_{t+1}} = q - 36 \lfloor q/36 \rfloor \qquad (5.57)$$

Before updating the system's binary states across the skip-over time step, the reason-able assumption is made that damping of non-principal-axis rotation in the primary occurs on a much faster timescale than the primary's spin-up by YORP, and thus a scaling and realignment to rotation about the body principal axis frame's Z-axis is made. This frame is recomputed for Alpha's current mass distribution, with corre-sponding shifts made to $_1 I_{1_t}$ and $_I R_{1_t}$, and then

$$_1\boldsymbol{\omega}_{1_t} = \begin{bmatrix} 0 \, , & 0 \, , & \frac{\left\| \, _I R_{1_t} \, _1 I_{1_t} \, _1 \boldsymbol{\omega}_{1_t} \right\|}{_1 I_{1_t}(3,3)} \end{bmatrix}^T \qquad (5.58)$$

The binary states are then updated using Eqs. 5.51-5.56 with $t_{t+1} - t_t$ now replaced by Δt, and the time t is increased by Δt to get t_{t+1}. Then the regular time interval length is recomputed to account for the changes to the Alpha spin and mutual orbit rates, and system angular momenta are found again from current binary states before resetting the gradual spin-up period detection buffer and proceeding with the next natural time step. As mentioned before, the probabilistic propagation approach sum-marized here can cover very long durations and large particle populations with low computational cost while, most importantly, modeling the effects of the particle mo-tion on the binary states themselves with accuracy inherited from earlier full-detail RF3BP simulations. The application of these methods to the scenarios defined in 5.4.1 yields some interesting results with important implications for binary asteroid studies.

5.4.3 Results and implications

For several batches of RF3BP particle dynamic simulation output, the final dispositions resolved for the particles are broken down as shown in Table 5.4. As can be seen, only for cases with the higher initial Alpha spin rate of 0.000651444 rad/s are lofted particles observed going to outcomes of transfer impact, still lingering in "orbit" (at a two-week cutoff duration), or escape. For all such particles the expected outcome by comparison of the initial Jacobi function value with the L1-analogue equilibrium point Jacobi function value is instead return impact, which would happen without including detailed modelling of the time-varying dynamics for this system. However, dropping the initial Alpha spin rate by only $0.10 - 0.11 \times 10^{-5}$ rad/s produces total return impact probability of unity, for the cases of both same-side lofting position and opposite-side lofting position with 2.5° offset angle between the orbit normal and Alpha's spin pole.

For these latter two cases, with initial Alpha spin rate at the threshold spin rate values, the probability matrices generated are used with the best estimate for KW4 Alpha's YORP acceleration (3×10^{-11} rad/s/year, or $\approx 9.5129 \times 10^{-19}$ rad/s^2, per Scheeres et al [66]) to obtain results for a "nominal" probability-based simulation. The total mass of regolith or surface material free to move or be lofted is an uncertain physical parameter of the system's primary, so this is nominally set to 10 million metric tons, only about 0.43% of Alpha's total estimated mass. How this is discretized into particles with specific masses is also a free parameter. Nominally, 5000 particles of equal mass are used, though different choices for all of these parameters are explored below. The results of a nominal model simulation, extending to a duration of about 2792 years, are shown in Figure 5.5.

As previously mentioned, it is seen that lofting from the same side of Alpha as

Table 5.4: Qualitative trajectory outcomes for RF3BP particle simulation output batches. These are classified by expected outcome based upon the trajectory's initial Jacobi energy level. The table entries are percentages of the total number of particles in each batch (528) reaching the indicated outcome, or the percentage of that number of particles reaching the indicated outcome with the indicated expectation.

$\|{}_1\boldsymbol{\omega}_1\|_o$ (rad/s)	6.51444 $\times10^{-4}$						6.40444 $\times10^{-4}$	6.41444 $\times10^{-4}$
Pole offset, Δ	0.0°		2.5°		5.0°		2.5°	
Lofting side*	same	opp.	same	opp.	same	opp.	same	opp.
Return impact	96.40	91.48	95.83	92.80	95.27	91.66	100	100
Expected	100	100	100	100	100	100	100	100
Uncertain	0	0	0	0	0	0	0	0
Rogue (high J)	0	0	0	0	0	0	0	0
Escape	0.57	0.19	1.33	0.38	0.57	0.19	0	0
Expected	0	0	0	0	0	0	–	–
Uncertain	0	0	0	0	0	0	–	–
Rogue (low J)	100	100	100	100	100	100	–	–
Transfer impact	1.89	4.92	2.08	5.30	2.65	3.98	0	0
"Orbiting"	1.14	3.41	0.76	1.52	1.52	4.17	0	0
Expected	0	0	0	0	0	0	–	–
Rogue (low J)	100	100	100	100	100	100	–	–
Rogue (high J)	0	0	0	0	0	0	–	–

Beta, flight, and return impact occur quickly within short transient lofting episodes, separated by long time spans during which the primary is slowly spun back up by the YORP angular acceleration applied to it. Eventually the lower of the lofting spin rate thresholds is encountered again, and the cycle is repeated. The greater the depression of the Alpha spin rate during any single lofting episode, the longer the time needed for spin-up to lofting again and the longer the following separation time until the next lofting episode becomes. This separation time is seen to follow an exponential distribution, with mean of about 16.6 years for the nominal model given its applied angular acceleration on Alpha.
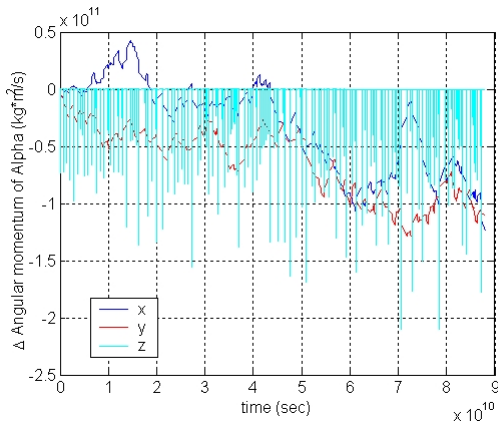
(a) Alpha angular momentum change
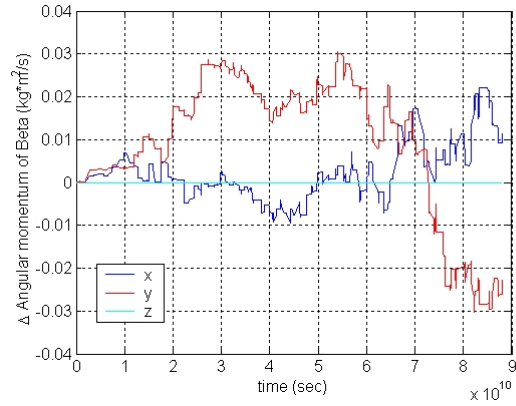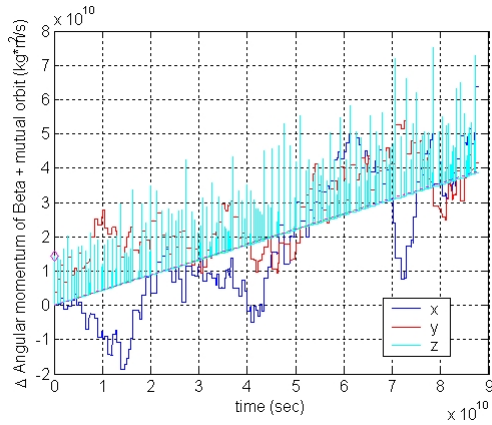
(b) Beta angular momentum change

(c) Combined orbit and Beta angular momentum change
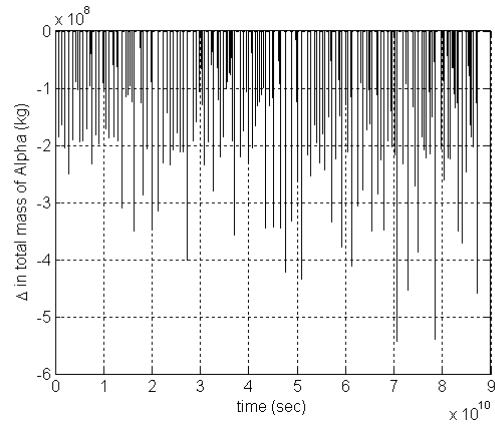
(d) Alpha mass relative to initial value
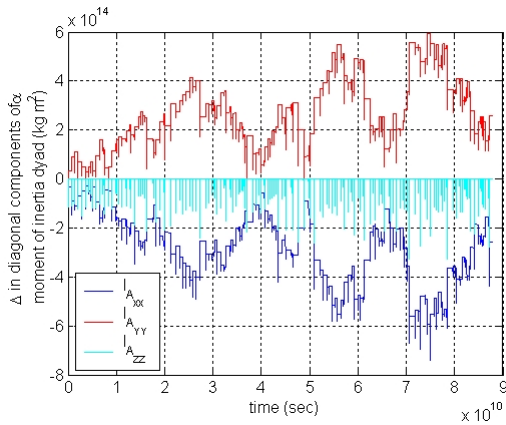
(e) Change in Alpha inertia dyad elements
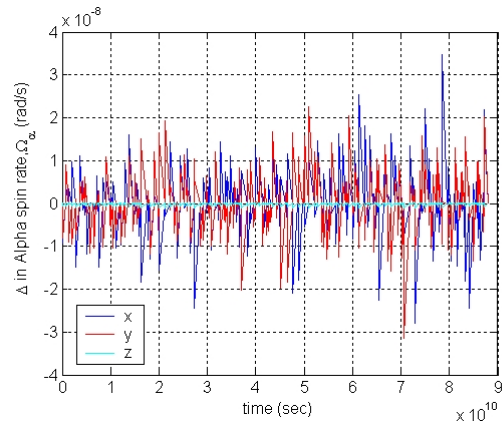
(f) Change in Alpha angular velocity vector

Figure 5.5: Output of probability based simulation of particles in nominal case. For that case we have total regolith mass = 1.0×10^{10} kg, 5000 equal-mass particles, and applied acceleration = 9.5129×10^{-19} rad/s^2.

With the time axis scaled as it is in Figure 5.5, the transient episodes show up as "spikes" in the plotted quantities. Note the vertical scale in panel (b) of Figure 5.5 in comparison to the vertical scales on panels (a) and (c) mean that the angular momentum of Beta experiences only minuscule changes in the fashion of a random walk, and only in the X- and Y-components. Therefore panel (c) really shows exclusively change to the orbit angular momentum, in the form of a steady increase in the main Z-component. The random walk changes in the X- and Y- components for Alpha and the orbit-plus-Beta mirror each other according to total angular momentum conservation for the system in those components. The external angular momentum injected to the system through the angular acceleration applied to Alpha is visibly transferred into expansion of the orbit, as was predicted by the hypothesis.

In addition to the mean separation time between lofting, there are other metrics for the level of particle lofting activity in the system. The duration covered by a simulation given a fixed number of time steps taken is one of these, as more time steps are used in propagating through lofting episodes than to cover even very long spin-up periods, so a shorter duration represents greater activity. In addition, taking the time-integral average of the mass lost from Alpha (as shown in panel (d) of Figure 5.5) gives an average amount of mass aloft, reflecting not only the frequency but individual length of lofting episodes. The total accumulated amount of mass lofted during a simulation divided by the total duration also gives an average mass lofting rate. However, the episodic nature of particle motion, when at low applied Alpha angular acceleration, means these activity metrics should not be misinterpreted to mean certain amounts of material are always hovering above the surface near the equator, or to mean material is continuously being levitated there.

However, it is of interest to examine what happens when the qualification above

of **very low** (i.e. actual YORP-level) angular acceleration no longer applies. This is the hypothetical case that may come about with a similarly-proportioned system of extremely small body sizes and extremely varied primary surface Albedo, or for a more reasonably sized typical asynchronous binary whose primary is artificially spun up using attached propulsive devices for some reason. Similarly, it is interesting to explore various values for the other model parameters of particle mass, number of particles, and their product, total mass available to loft. Table 5.5 shows the degree and frequency of lofting activity within the system, represented by the metrics discussed above, versus the applied angular acceleration and these three material parameters for the material available to loft. The total number of particles and thus total regolith mass is varied while holding particle size constant, then the particle size and number of particles are varied inversely while holding total regolith mass constant, and then particle size and thus total regolith mass is varied while holding the number of particles constant. Some of the trends within the table are also summarized in Figures 5.6–5.9.

It is seen that for the same number of particles but increasing total regolith mass, because the same number of particles come around to loft on the Beta-facing side when the threshold rate is encountered, but each one of those particles is more massive, the depression of Alpha spin rate during the lofting episode is greater, increasing the mean time between episodes and increasing the duration reached. However the time-averaged amount of material aloft and mass lofting rate hold roughly constant, meaning larger mass motion occurring less frequently is the same as smaller mass motion occurring more frequently. The exception comes with moving to the largest total regolith mass case, also the nominal simulation case with output shown in Figure 5.5.

Table 5.5: Several metrics for level and intensity of lofting activity in the binary system, with variation of several probabilistic propagation model parameters, for both initial primary spin rate and discretization of available loose surface material.

$\|_1\boldsymbol{\alpha}_1\|$ (rad/s²)	# of particles	total regolith mass (kg)	particle mass (kg)	simulation duration (s)	mean time between episodes (s)	avg. mass aloft (kg)	avg. lofting rate (kg/s)
1.5×10^{-13}	5000	10^{10}	2×10^{6}	2.568×10^{6}	*	494431652.59	787708.86
1.5×10^{-14}	5000	10^{10}	2×10^{6}	1.103×10^{7}	*	67278217.80	118657.41
1.5×10^{-15}	5000	10^{10}	2×10^{6}	1.015×10^{8}	2.092×10^{5}	528806.13	957.84
1.5×10^{-16}	5000	10^{10}	2×10^{6}	9.309×10^{8}	2.912×10^{6}	43697.12	78.65
1.5×10^{-17}	5000	10^{10}	2×10^{6}	7.977×10^{9}	2.877×10^{7}	3846.66	6.961
9.5129×10^{-19}	5000	10^{10}	2×10^{6}	8.806×10^{10}	5.245×10^{8}	277.98	0.5016
1.5×10^{-19}	5000	10^{10}	2×10^{6}	6.440×10^{11}	4.277×10^{9}	35.34	0.0634
1.5×10^{-20}	5000	10^{10}	2×10^{6}	3.154×10^{12}**	$4.139e10$	3.113	0.00565
9.5129×10^{-19}	50	10^{6}	2×10^{4}	1.873×10^{8}	2.251×10^{5}	177.3	0.3256
9.5129×10^{-19}	500	10^{7}	2×10^{4}	3.836×10^{8}	9.290×10^{5}	185.6	0.3311
9.5129×10^{-19}	5000	10^{8}	2×10^{4}	2.124×10^{9}	8.696×10^{6}	183.4	0.3320
9.5129×10^{-19}	50000	10^{9}	2×10^{4}	1.586×10^{10}	8.424×10^{7}	187.8	0.3393
9.5129×10^{-19}	100	10^{8}	1×10^{6}	3.588×10^{9}	1.422×10^{7}	186.4	0.3316
9.5129×10^{-19}	500	10^{8}	2×10^{5}	2.317×10^{9}	9.089×10^{6}	184.0	0.3363
9.5129×10^{-19}	1000	10^{8}	1×10^{5}	2.130×10^{9}	8.435×10^{6}	183.1	0.3328
9.5129×10^{-19}	5000	10^{8}	2×10^{4}	2.124×10^{9}	8.696×10^{6}	183.4	0.3320
9.5129×10^{-19}	10000	10^{8}	1×10^{4}	1.982×10^{9}	8.169×10^{6}	182.3	0.3304
9.5129×10^{-19}	50000	10^{8}	2×10^{3}	1.970×10^{9}	8.253×10^{6}	183.4	0.3322
9.5129×10^{-19}	5000	10^{5}	20	1.108×10^{8}	1.083×10^{4}	182.7	0.3297
9.5129×10^{-19}	5000	10^{6}	200	1.365×10^{8}	8.523×10^{4}	181.8	0.3289
9.5129×10^{-19}	5000	10^{7}	2000	3.407×10^{8}	8.133×10^{5}	181.8	0.3300
9.5129×10^{-19}	5000	10^{8}	2×10^{4}	2.124×10^{9}	8.696×10^{6}	183.4	0.3320
9.5129×10^{-19}	5000	10^{9}	2×10^{5}	1.510×10^{10}	7.828×10^{7}	185.7	0.3349
9.5129×10^{-19}	5000	10^{10}	2×10^{6}	8.806×10^{10}	5.245×10^{8}	278.0	0.5016

* No separation time is given because material transitions to lofting more or less continually in these cases.

** This duration is equivalent to 10^5 years, an arbitrary duration limit reached rather than the 10000 time step limit.
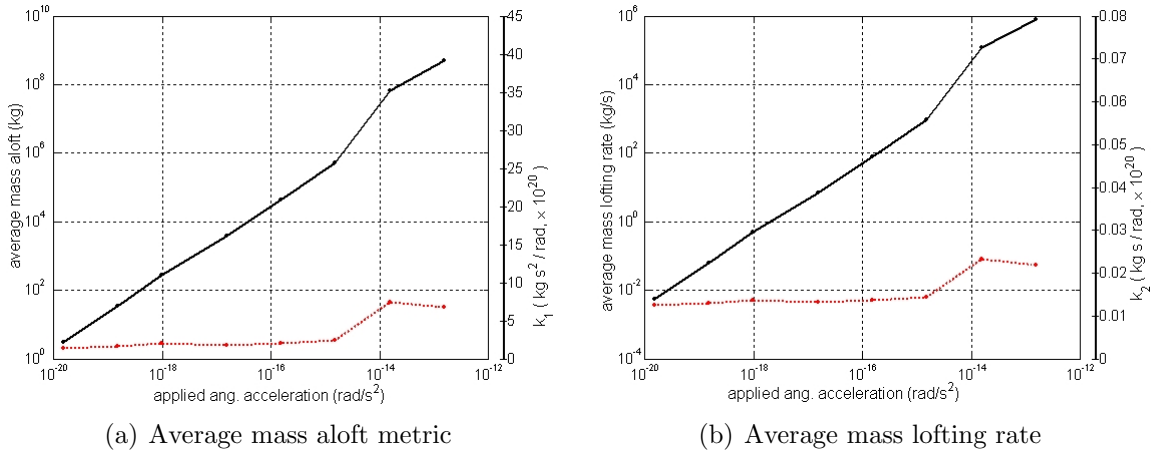
(a) Average mass aloft metric

(b) Average mass lofting rate

Figure 5.6: Trends in the lofting activity metrics versus magnitude of external angular acceleration applied to system primary. The k_1, k_2 quantities are ratios of the metric to the angular acceleration magnitude.

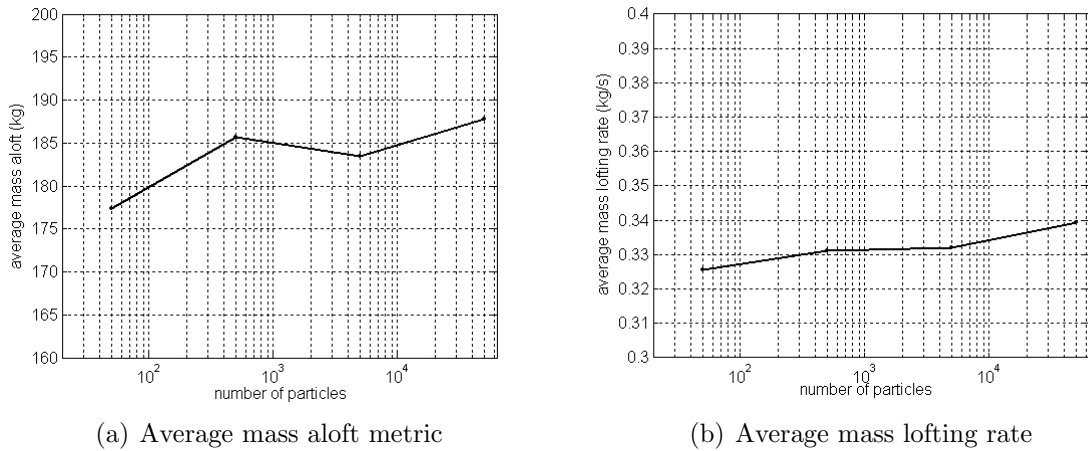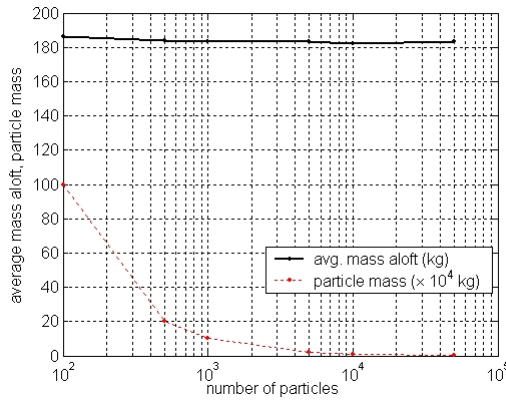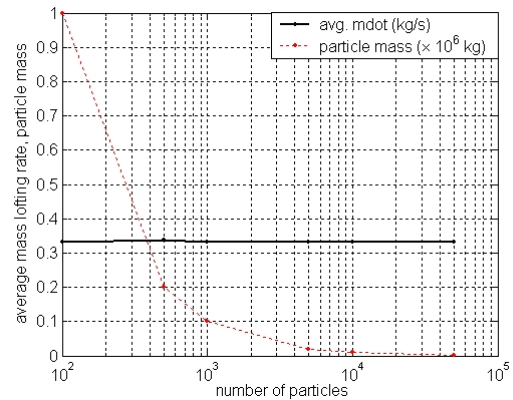(a) Average mass aloft metric

(b) Average mass lofting rate

Figure 5.7: Trends in the lofting activity metrics versus variation in the number of available particles. Meanwhile particle mass (and thus size) is held constant. Total regolith mass varies proportionally with the particle count. The angular acceleration is held constant at the 9.5129×10^{-19} rad/s^2 actual YORP level for KW4.
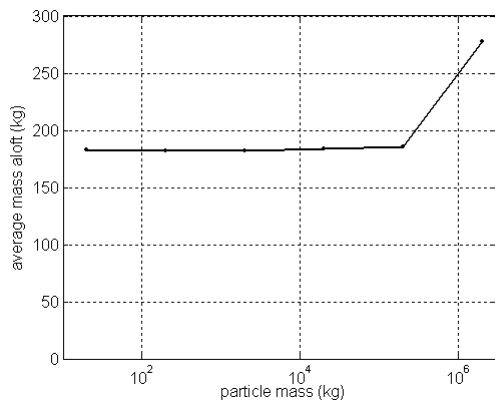
(a) Average mass aloft metric　　　　　(b) Average mass lofting rate

Figure 5.8: Trends in the lofting activity metrics with inverse variation in the number of available particles and particle mass. Meanwhile total regolith mass is held constant, and the angular acceleration is held constant at the 9.5129×10^{-19} rad/s^2 actual YORP level.
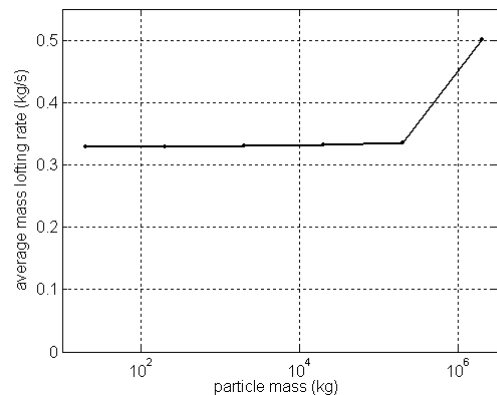
(a) Average mass aloft metric　　　　　(b) Average mass lofting rate

Figure 5.9: Trends in the lofting activity metrics versus variation in particle mass. Meanwhile the total number of particles is held constant. Total regolith mass varies proportionally with the particle size. The angular acceleration is held constant at the 9.5129×10^{-19} rad/s^2 actual YORP level.

The reason for this sharp increase is unclear, as the nature of the angular momenta behavior remains the same for these other cases, as shown in the plots. Holding the total regolith mass constant, fewer but larger particles or pieces to loft also tends to increase the time between lofting episodes and the total duration, though less strongly. This is especially true for the lowest particle counts, with which the coarsest mass discretization and most uneven initial mass distribution around Alpha's equator exist. Since increasing the number of particles each having a fixed mass seems to extend the episode separation times and the duration, overall the effect of having more mass available to launch overpowers the effects of coarser mass discretization. Regardless, the time-averaged mass aloft and mass lofting rate hold roughly constant across all parameter changes for the available material. That is not the case for varying the applied angular acceleration. With low values for this, characteristic of YORP torque on actual binary system primaries in nature, the average mass aloft and average mass lofting rate smoothly vary proportionally with the applied angular acceleration.

Interestingly, for the currently examined KW4 system's body properties, that proportionality goes away once applied angular acceleration increases above $\|\boldsymbol{\alpha}_1\| \approx 10^{-14}$ rad/s^2 (see Figure 5.6). Above this value the angular acceleration is large enough to overwhelm the damping effect of same-side particle lofting on the Alpha spin rate after a certain amount of time has passed. Then a major shift occurs to non-episodic nearly continuous lofting with sustained mass loss from Alpha and sustained changes to it's moments of inertia. As the continuous lofting from the same side as Beta actually balances the applied acceleration less effectively than the prior intermittent lofting, the Alpha spin rate eventually increases through the 1×10^{-6} rad/s separation to the threshold for lofting from the side opposite Beta. Once that particle motion also occurs, the now very large amount of replenishing material aloft

(see Table 5.5) should begin to truly represent a sustained low-lying debris cloud or surface-grazing ring of debris around the equator. A second major shift in the system behavior also occurs at this point in time, beyond another large reduction in Alpha's mass and polar moment of inertia as the lofting region on the opposite side also becomes bare of material. That is, gravitational interaction of particles lofted from the opposite side with both binary components tends to drive the angular momentum transfer in the opposite direction as gravitational interaction of particles lofted from the same side with both binary components, and the former effect overpowers the latter in magnitude. An intuitive explanation for this lies with an understanding of how the usually very low altitude trajectories followed by lofted particles approximate familiar tidal bulges with a lag angle offset from the line of syzygy. Until the lofting on the opposite side begins as well, only the "virtual bulge" on the Beta-facing side exists. But then after the opposite side lofting begins the other "virtual bulge" is also present and may, despite its greater average distance from Beta, exert more of a retarding torque against the mutual orbit than the Beta-facing side "virtual bulge" exerts an accelerating torque on that mutual orbit. Hence the spin rate of Alpha and the Alpha angular momentum rapidly increase while the orbit rapidly decays, after this second major shift occurs. All of this behavior is shown in Figure 5.10 for the most extreme acceleration case in Table 5.5 having $\|\boldsymbol{\alpha}_1\| = 1.5 \times 10^{-13}$ rad/s^2. Note the two major shifts discussed above occurring at approximately 1.0×10^6 and 1.31×10^6 seconds for this case.

Eventually, the Alpha spin rate would increase to a point where the probability matrices derived from the previous full-detail precise dynamical simulation of particles in the binary according to the RF3BP no longer apply. After which the output can no longer be trusted. Instead the probability matrices and matching impact velocity
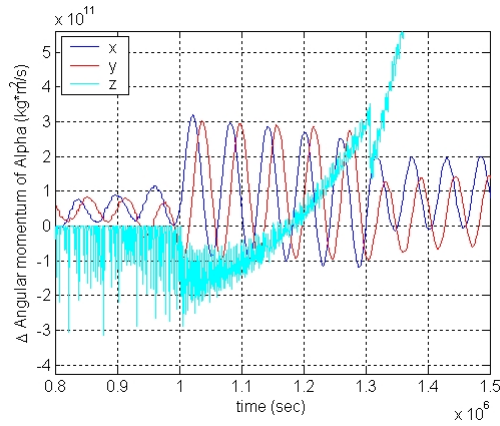
(a) Alpha angular momentum change
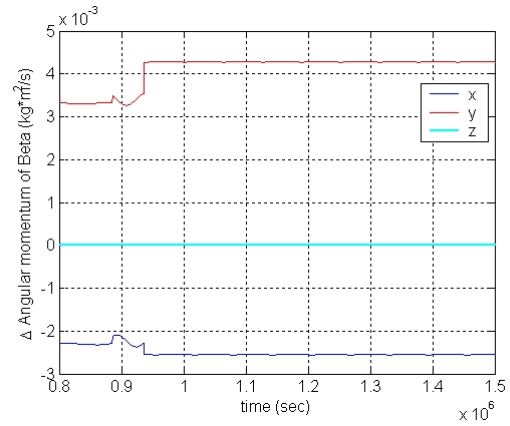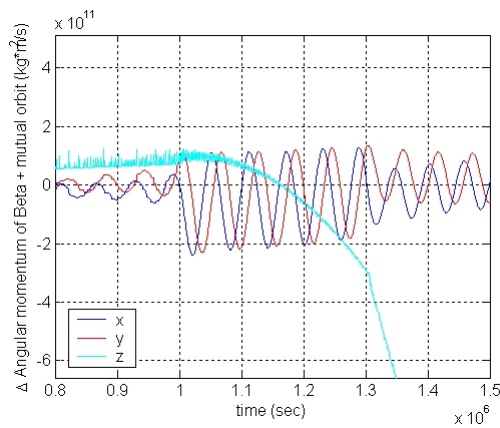
(b) Beta angular momentum change

(c) Combined orbit and Beta angular momentum change
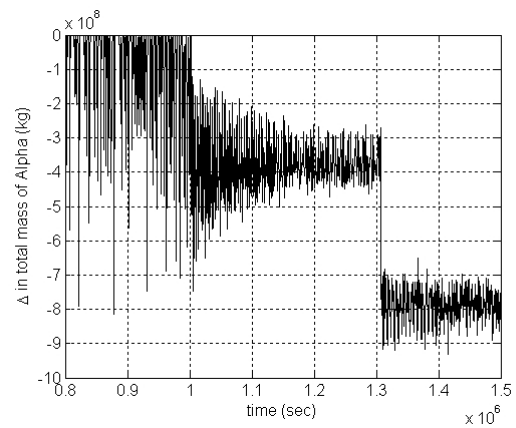
(d) Alpha mass relative to initial value
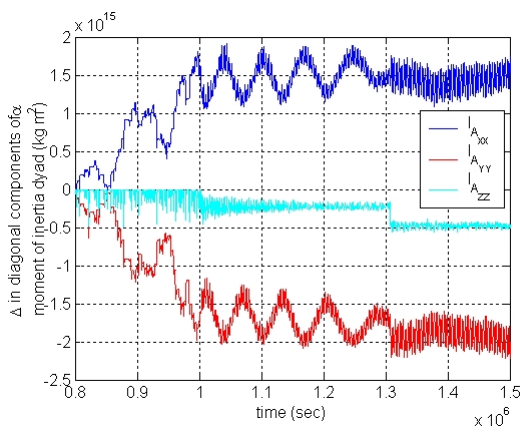
(e) Change in Alpha inertia dyad elements
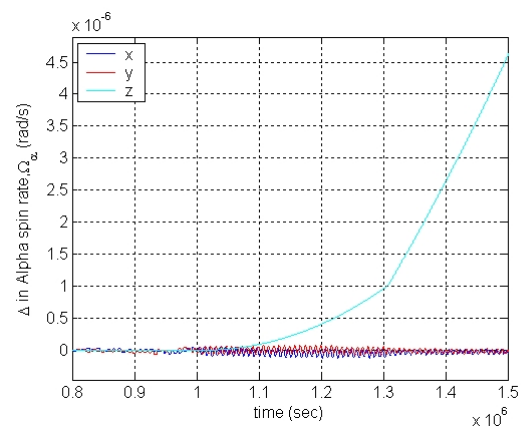
(f) Change in Alpha angular velocity vector

Figure 5.10: Output of probability based simulation of particles for large angular acceleration (1.5×10^{-13} rad/s^2) case. Again this is with total regolith mass = 1.0×10^{10} kg and 5000 equal-mass particles. Note the transitions at approximately 1.0×10^6 and 1.31×10^6 seconds. See text for analysis.

information should be replaced with new versions obtained from such RF3BP dynamic simulation starting at higher initial Alpha spin rates. One may infer from Table 5.4 that using the probability matrices for such higher Alpha spin rate cases will produce steady bleeding away of lofted material from the vicinity of Alpha to the "sinks" of impact with Beta and escape from the system. While this is an interesting new regime of behavior to study, it is not explored further here by repeatedly shifting to new matrices and new data grounded in new full dynamic simulation of particles. The reader is reminded that all of this applies only for hypothetical very large externally applied steady torque on the primary, not found naturally in binary asteroid systems.

For both the nominal case, with angular momentum behavior as shown in the first three panels of Figure 5.5, and all other cases also having $\|\boldsymbol{\alpha}_1\| \ll 10^{-14}$ rad/s^2 and hence having similar-looking plots of angular momentum changes, the slope of the linear fit to the combined orbit plus Beta angular momentum matches that expected. That is, the slope of the linear fit to the numerical output for this quantity, divided by the primary's initial or time-averaged moment of inertia about the Z-axis, recovers the angular acceleration applied to the primary about the Z-axis to within a few percent. Therefore the angular momentum injected to the system is seen to be fully transferred to the orbit, to which Beta is also synchronously locked on-average. The results imply that for any given time, it is true that $\left\| \dot{\mathbf{H}}_{2+\text{orb}} \right\| = {_1}\mathrm{I}_{1_{ZZ}} \|\boldsymbol{\alpha}_1\|$. Here the ${_1}\mathrm{I}_{1_{ZZ}}$ is the Z- principal axis moment of inertia component of the inertia dyad for the primary expressed in its own frame. This relation can be used within a simple equation for the rate of change in the mutual orbit semi-major axis, a, as a function of the YORP angular acceleration acting on the primary body:

$$\dot{a} = \frac{2 \, {_1}\mathrm{I}_{1_{ZZ}} \, \|\boldsymbol{\alpha}_1\|}{\left(\frac{m_1 m_2}{m_1 + m_2} - 3 \, {_2}\mathrm{I}_{2_{ZZ}} / \mathrm{a}^2 \right) \sqrt{\frac{G(m_1 + m_2)}{a}}} \tag{5.59}$$

172

The denominator accounts for the presence of the synchronous secondary. For the nominal results case, the slope fit to the orbit plus Beta angular momentum output is 0.4459 kg m^2/s^2, and when used with the KW4 system parameters in the above this translates to a current 0.882 m/kyr rate of semi-major axis growth for the KW4 system. This orbit expansion is due to the surface particle motion angular momentum transfer mechanism alone and is several times faster than the orbit expansion resulting from the usual solid-body tidal evolution also present in the system. Within this dissertation any accumulated orbit evolution effects of asymmetric thermal absorption and re-radiation to/from the secondary body, or so-called "BYORP", are not addressed. It may also be present in addition to the above two sources of orbit evolution, in which case it may win in the competition for which mechanism dominates in terms of driving the outward evolution of the binary asteroid the fastest.

Integrating Eq. 5.59, one can obtain an expression for the time period required to increase the orbit size by some ratio ζ over an initial orbit size a_o, given just the system evolution effect from angular momentum transfer due to lofting particle motion, assuming that dominates:

$$T_{a_o \mapsto \zeta a_o} = \left[\sqrt{\zeta} - 1 - \frac{2 I_{2_{zz}}}{m \, a_o^2} + \frac{2 I_{2_{zz}}}{m \, \zeta^{\frac{3}{2}} \, a_o^2} \right] \frac{m \, \sqrt{G \, (m_1 + m_2) \, a_o}}{1 I_{1_{zz}} \, \|\boldsymbol{\alpha}_1\|} \tag{5.60}$$

For the general KW4 model as presented in Ostro et al [62] and Scheeres et al [66], this gives the time since the system was at half it's present orbit size, time to double orbit size over the present, and time to double the orbit size again after that, as 1.721±0.471 Myr, 2.487±0.665 Myr, and 3.535±0.939 Myr, respectively. Taking the distance covered by each such stage of orbit growth and dividing it by the time required gives average rates during those stages of 0.740 m/kyr , 1.025 m/kyr, and 1.441 m/kyr, respectively.

From this and simply by looking at Eq. 5.59 it is seen that the expansion rate

increases with larger orbit size, so that the orbit growth is actually accelerating. This likely continues until component separation is large enough that the gravitational interaction of lofted particles with the secondary weakens to the point that the mechanism for angular momentum transfer demonstrated herein must shut down. Once having reached very large separation the likelihood of the secondary being stripped away from the primary by perturbations due to solar gravity interaction and planetary flyby also greatly increases, however. Once such separation occurs, the end state for the system's evolution is then a pair of asteroids with similar heliocentric orbits that may be considered a "divorced" binary pair. Recently, observational evidence for such pairs among NEOs and main-belt asteroids has been obtained from new and archived heliocentric asteroid orbit data, presented by Vokrouhlický and Nesvorný [78].

Meanwhile, as the system is separating, one can safely assume the same YORP angular acceleration continues to act on the primary (though perhaps resurfacing and figure regularization due to the lofting of material from it's surface may gradually change the YORP coefficient and reduce YORP-driven angular acceleration). In this case the primary will continue to spin up but with eventual loss of the regulating effect against further spin-up from the surface material motion, when at large separation. Thus a transition similar to the first seen in the very high applied angular acceleration case output shown above may occur. From the close ring of debris then levitated around the equator and particles thrown off to successively higher altitudes, it is conceivable that enough material may eventually be shed to accumulate and form into another distinct body well interior to the orbit of the departing secondary in the (prior) binary system. Just this process has been modeled through the recent work by Walsh et al [34]. If this in fact occurs before the older secondary has been stripped away, a triple system with a very much closer and smaller younger tertiary body

exists for a certain time. Once the outer satellite body is stripped, the inner satellite body becomes the new secondary, and the new system repeats a similar overall evolution cycle. The body size ratios and relative orbit sizes obtained from recent radar imaging of the first discovered triple NEA system (153591) 2001 SN 263 [79] may indicate just such a scenario is in the process of occurring for that system. Similar conclusions to those stated here regarding the end state for the system's evolution and the possibility of a new secondary's creation are also discussed in Harris, Fahnestock, and Pravec [80]. If the overall evolutionary path for binary asteroids is as described above, new campaigns to find systems at each stage along that path, and characterize where they are along it, become considerably more interesting.

5.5 Investigation of Spacecraft and Debris Trajectory Stability within Binaries

In this section, a third major type of particle motion within a binary asteroid system is examined, which differs from the two types of motion in the previous two sections in that the particle trajectories no longer originate from the surface of either binary component. Rather, the trajectories start from states which match with the particles already initially following orbits through the system, however stable or unstable those orbits may be. Just as the last section shed light on the long timescale dynamical evolution of the components forming a binary system, this section includes results applicable to the very short timescale, rapid dynamical evolution of a planetary debris ring structure that may appear, or be created, within a binary system. However, the primary focus below is on a different application, to the case of an artificial spacecraft flying within the system. This is directly applicable to the execution of future binary NEA in-situ exploration missions that are becoming more likely, for reasons explained in Chapter I.

175

Flying a spacecraft within a binary entails great challenges in navigating and controlling the spacecraft, while subject to the gravity field that is significantly time-varying in any chosen system frame, and subject to the force environment characterized by large perturbations. However, these perturbations are also the prime source of information about the interior structure of the system components themselves.

A key question is how to design a mission flying within a binary system to obtain the most such information, and to maximize the science return considered as a whole. The answer to this entails a trade-off between that which helps get information about the density distribution of the components, and helps increase angular coverage of the components' surfaces by cameras and other instruments, vs. that which helps keep the spacecraft safe and functional for a longer total flight time (i.e. a longer observation time). For the former, it is preferable to allow the spacecraft to propagate with no trajectory actuation (yet have it go through many positions within the binary system, e.g. reach higher latitudes by a path with greater inclination and execute very low altitude passes). Whereas to increase spacecraft safety and mission lifetime, it is preferable to do as many thruster firings as needed to ensure the spacecraft doesn't impact anywhere, while keeping the number of such firings as small as possible to minimize cumulative maneuver ΔV. For this, it may instead be desirable to keep the spacecraft to low inclinations with respect to the binary mutual orbit, neglecting solar radiation pressure considerations. Several other engineering constraints must also be satisfied: maintaining line of sight to Earth, remaining in sunlight for the correct fraction of the time and with correct attitude, etc. The optimal design in the trade-offs involved depends critically on how easily and over what duration a spacecraft initially on an orbit of a certain type enclosed within a comparatively safe region in the binary will be removed from that region.

Thus, in this section, characterization of the stability of orbital trajectories about and within a binary asteroid system, trajectories that are relevant to the execution of scientific missions like that described above, is the emphasized goal. This objective is achieved for the specific example binary system of 1999 KW4 from before, used again because it typifies the small asynchronous binaries class.

5.5.1 System setup and parameter space to be explored

The underlying or "substrate" full two body problem motion results set used for later RF3BP propagation of the massless test particles is one with the highest plausible excitation level identified for the KW4 example system, that being the "most interesting" and most severely perturbing to the test particle motion. In this configuration the initial spin-orbit pole offset angle for the system's Cassini state is $10°$ and the initial eccentricity and mean anomaly are 0.01 and $180°$ (see section 3.3). The state of the binary system itself is interpolated from this "most-excited" case's binary system propagation output files, whenever required for computation of the net force acting on each test particle. That net force is determined as the sum of the forces due to the gravitational interaction of each polyhedral body model with the test particle.

Nominal orbital trajectories are started in six regions of the position and velocity phase space for this system: both prograde and retrograde close orbits about Alpha, prograde and retrograde close orbits about Beta, and prograde and retrograde far-field orbits about the system barycenter. Within each such combination of orbit region and type, nominal trajectory initial states are chosen to sample both radius and inclination, the latter with values of $\{0°, 10°, 20°, 30°, 40°\}$. In all cases the initial position is placed along the extended line of syzygy (the line between the two body centroids), measuring the radius value from the base point (centroid or barycenter,

as appropriate) out along the direction of a vector pointing from Alpha toward Beta. For the radius value, lower bounds of 110% of the maximum radius of any vertex point on the mesh of the body are used, and upper bounds of 80% of the distance from the body centroid to the usual restricted three body problem L1 point, along the line of syzygy, are used. Alternatively, for just the far-field barycentric orbits the lower and upper bounds of 2.0 and 3.0 times the initial centroids separation distance are used. Therefore the normalized radius values sampled for each of the region and type combinations are as indicated in Table 5.6. Here the normalization is by the baseline length of the initial centroids separation. The initial velocity magnitude is chosen as the circular speed using the mass of the body being orbited about or mass of the whole system, as appropriate. The velocity vector with this magnitude is perpendicular to the line of syzygy and simply inclined with respect to the plane of the initial binary mutual orbit by the inclination value.

A nominal trajectory is found by propagating a single test particle from the initial condition of each region-type-radius-inclination case (with 180 cases in all). The states are propagated in an inertial barycentric frame, using a Runge-Kutta Fehlberg 7(8) integrator. (Since the particle's inertial EOM dynamics evolve on a linear space closed

Table 5.6: Normalized (1 = 2540.5 m) initial orbital radius values sampled, for each region and type of orbital trajectory examined.

Alpha-centric, prograde and retrograde	Beta-centric, prograde and retrograde	Barycentric, prograde and retrograde
0.3397	0.1415	2.02
0.39443	0.12821	2.2222
0.44916	0.15479	2.424
0.50389	0.16808	2.626
0.55862	0.18136	2.828
0.61335	0.19465	3.03

under the additive update operation, this choice of integrator is acceptable.) The forces on the particle due to each binary component's mass distribution are computed in the respective body-fixed frame and then transformed back to the integration frame. About each such nominal trajectory a small ($N \approx 20$) Monte-Carlo batch of particles with initial conditions deviated in Gaussian random fashion from the initial condition of the nominal trajectory is also propagated. The perturbations are scaled to approximately the same size as rule-of-thumb spacecraft state uncertainty in an operational scenario ($1\sigma = 10$ m in position, 1 cm/s in velocity).

The particle trajectory outcomes within the simulation duration window (impact, escape, still in flight) are tracked and compared against the expectation for them based on the initial time-varying Jacobi function value compared with the RSE3BP threshold values. Those are in turn the $J_{\mathrm{RSE3BP_{L1}}}$ value from eq. 5.18, and zero. However, the main result of interest here, for stability and lifetime in orbit, is instead a computation of the finite-time Lyapunov Characteristic Exponent (LCE) for every particle. Along with each nominal or perturbed trajectory $\mathbf{x}$, an extremely close shadow trajectory $\mathbf{x}_s$ is propagated, initially offset from $\mathbf{x}$ by a deviation $\delta\mathbf{x}$ of one millimeter in initial position and nothing in velocity. Both trajectories are used in the following to get the LCE at a finite time t:

$$\xi_t = \frac{1}{t} \ln\left(\frac{\|\mathbf{x}_s(t; \mathbf{x}_o + \delta\mathbf{x}, t_o) - \mathbf{x}(t; \mathbf{x}_o, t_o)\|}{\|\delta\mathbf{x}\|} \right) \qquad (5.61)$$

Larger positive values indicate greater instability. The LCE vs. time curves (or the value of the peak, time-integral average, or final value, by order of increasing importance, for these curves) can be compared within a batch of perturbed particles. The nominal trajectory's LCE vs. time curve, or the combined such curve for all nominal and perturbed particles found by averaging at every plotted time, or just the average of the LCE values for all nominal and perturbed particles at one given cutoff
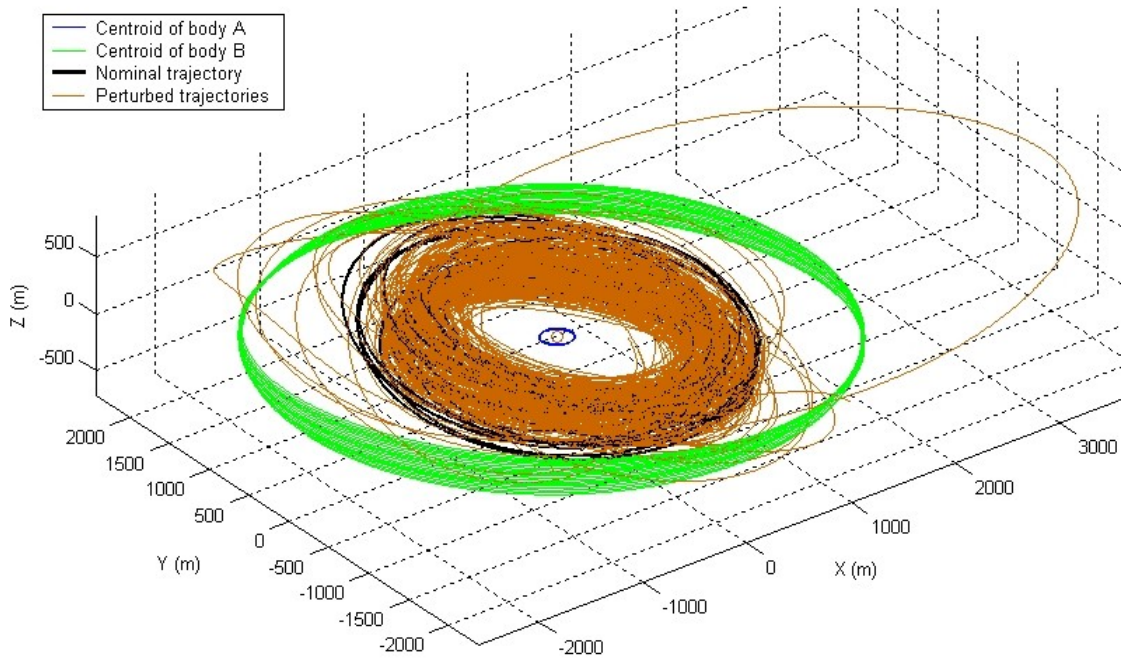
Figure 5.11: Nominal and perturbed trajectories for Alpha-centric, prograde, R_o =0.50389, 0° inclination case. Trajectories are plotted in barycentric inertial space.

time, can all be compared between batches. This yields comparison across initial radius and inclination conditions and regions and types of orbits, to globally map the degree of instability throughout the system, fulfilling this section's primary objective.

In theory, one can also map the representative final LCE value for each perturbed particle onto the planes in phase space in which the initial state perturbations from the nominal trajectory are taken. This should allow for ascertaining the gradients in stability characteristics along each dimension of phase space, in the extreme locality of each case in the parameter space. However, the number of perturbed particles needs to be far higher than the ≈20 used herein, in order for this gradient information to be sufficiently revealed.

5.5.2 Global stability characterization results

As an example of the unprocessed output of the particle propagations, the nominal and perturbed particle trajectories are plotted in the barycentric inertial frame for one case – the Alpha-centric prograde orbit at 0.50389 normalized radius and 0° inclination – within Figure 5.11. These trajectories have their corresponding LCE vs. time curves shown in the fourth (center right) panel of Figure 5.12. What this Figure 5.12 reveals is the difference in spacecraft or particle lifetime and behavior across cases in the same region (about Alpha) and with the same orbit type (prograde) and same inclination (0°) but varying the initial radius parameter from small to large. In addition to the nominal trajectory's LCE being plotted with a thick black solid line, the thin black dashed lines give the extent of the previous (one-step smaller in radius) LCE vs. time curves. Here extent means the region bounded at right by the longest particle flight duration and bounded from below by the minimum particle LCE value (obviously excepting the very initial period). For each case, 25% less than the longest particle flight duration is arbitrarily selected as a cutoff time at which to evaluate the dispositions of the particles, and at which to interpolate and average the LCE values for those particles still having the "lingering in orbit" disposition at that cutoff time. The cutoff time is indicated in Figure 5.12 by the thick black dotted line in each panel. The average of the LCE values for the still in orbit particles at the cutoff time is shown on the thick black dotted line by a circle marker. This average LCE value information is accumulated across many cases in Table 5.7 and in Figure 5.13, in the $\log_{10}$(avg. LCE) column and in the height of the bars/pillars, respectively. The cutoff times are also listed in the appropriate column and used for the color coding of the bar/pillars in the plot.
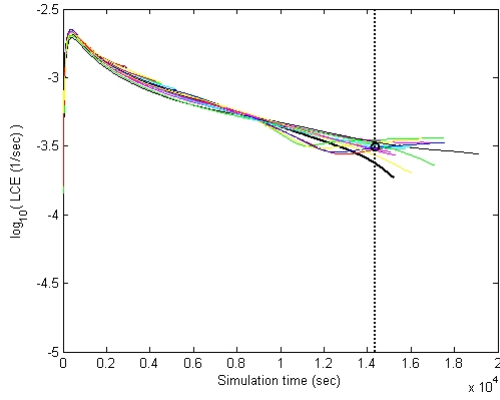
(a) R_o =0.3397
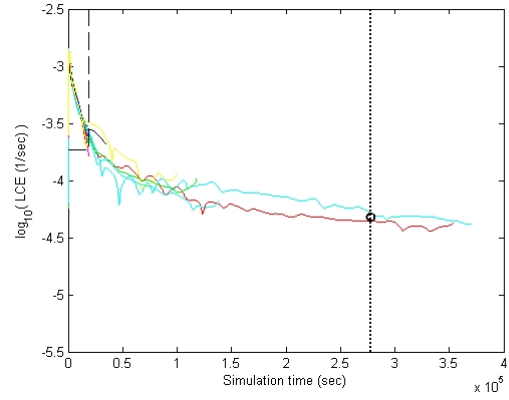
(b) R_o =0.39443
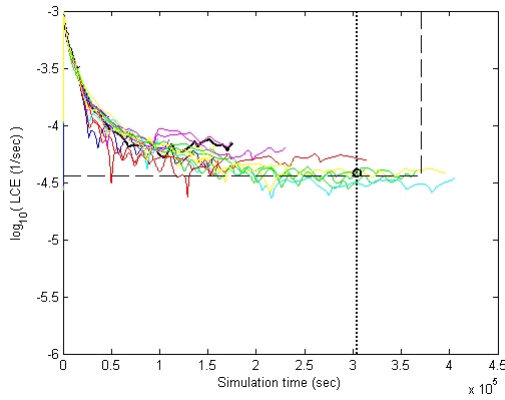
(c) R_o =0.44916
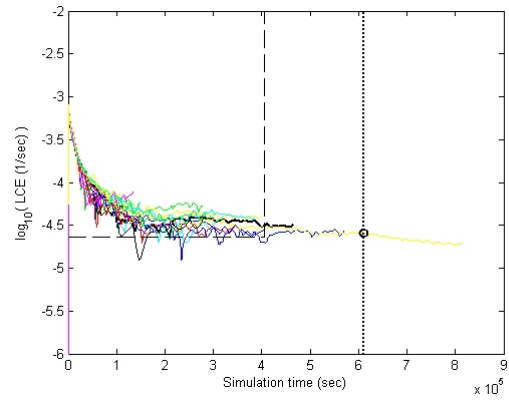
(d) R_o =0.50389
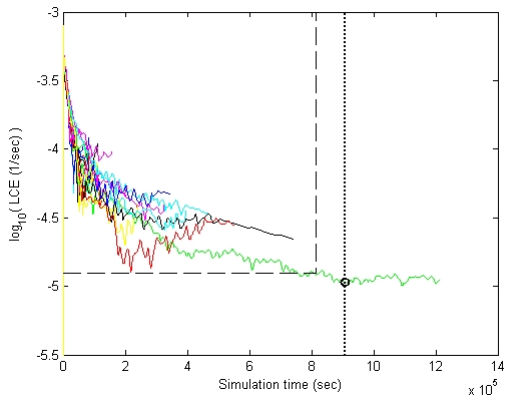
(e) R_o =0.55862
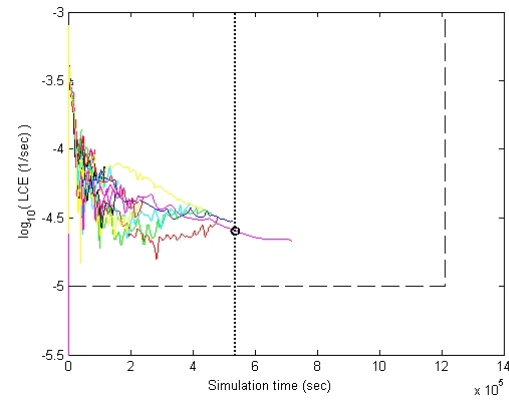
(f) R_o =0.61335

Figure 5.12: Values of the LCE plotted against simulation time, for all Alpha-centric, prograde, 0° inclination cases. Note R_o increases from top left panel. In each case, the nominal trajectory is shown with a thick black solid line, perturbed trajectories are shown with the thin colored solid lines, the bounds on the previous panel's curves (if applicable) are shown with the thin black dashed lines.

Table 5.7: Simulated particle dispositions and LCE values for Alpha-centric, prograde cases.

R_o(DU)	i_o (°)	cutoff time (d:hh:mm:ss)	α^* (%)	β^* (%)	Esc.* (%)	Flight* (%)	$\log_{10}$(avg. LCE)
0.3397	0	0:03:59:31	7 (35)	0 (0)	0 (0)	13 (65)	-3.5075
0.3397	10	0:05:21:25	17 (85)	0 (0)	0 (0)	3 (15)	-3.5927
0.3397	20	0:07:11:07	18 (90)	0 (0)	0 (0)	2 (10)	-3.7151
0.3397	30	1:09:45:56	18 (90)	0 (0)	0 (0)	2 (10)	-4.1239
0.3397	40	1:07:37:21	19 (95)	0 (0)	0 (0)	1 (5)	-4.0465
0.39443	0	3:05:14:49	18 (90)	0 (0)	0 (0)	2 (10)	-4.3169
0.39443	10	2:02: 7:55	15 (75)	2 (10)	0 (0)	3 (15)	-4.115
0.39443	20	5:20:43:55	16 (80)	2 (10)	0 (0)	2 (10)	-4.6408
0.39443	30	4:17:40:39	18 (90)	0 (0)	0 (0)	2 (10)	-4.4241
0.39443	40	10:12:25:25	16 (80)	3 (15)	0 (0)	1 (5)	-5.0003
0.44916	0	3:12:27:26	12 (60)	2 (10)	0 (0)	6 (30)	-4.4166
0.44916	10	5:05:41:06	14 (70)	4 (20)	0 (0)	2 (10)	-4.486
0.44916	20	6:20:22:58	13 (65)	5 (25)	0 (0)	2 (10)	-4.6629
0.44916	30	6:11:52:53	12 (60)	3 (15)	0 (0)	5 (25)	-4.6318
0.44916	40	10:12:25:25	18 (90)	1 (5)	0 (0)	1 (5)	-4.7834
0.50389	0	7:01:51:41	15 (75)	4 (20)	0 (0)	1 (5)	-4.5954
0.50389	10	6:20:27:07	12 (60)	6 (30)	0 (0)	2 (10)	-4.5795
0.50389	20	10:12:25:25	10 (50)	7 (35)	2 (10)	1 (5)	-4.806
0.50389	30	10:12:25:25	13 (65)	5 (25)	0 (0)	2 (10)	-4.7888
0.50389	40	10:12:25:25	8 (40)	0 (0)	0 (0)	12 (60)	-4.9291
0.55862	0	10:12:25:25	13 (65)	6 (30)	0 (0)	1 (5)	-4.9692
0.55862	10	9:23:32:09	14 (70)	5 (25)	0 (0)	1 (5)	-4.848
0.55862	20	10:12:25:25	14 (70)	5 (25)	1 (5)	0 (0)	-4.7876
0.55862	30	10:12:25:25	12 (60)	3 (15)	0 (0)	5 (25)	-4.7731
0.55862	40	10:12:25:25	9 (45)	1 (5)	0 (0)	10 (50)	-4.8722
0.61335	0	6:05:37:24	12 (60)	7 (35)	0 (0)	1 (5)	-4.5952
0.61335	10	10:12:25:25	9 (45)	9 (45)	1 (5)	1 (5)	-4.8668
0.61335	20	10:12:25:25	14 (70)	4 (20)	2 (10)	0 (0)	-4.8524
0.61335	30	10:12:25:25	14 (70)	4 (20)	0 (0)	2 (10)	-4.7727
0.61335	40	10:12:25:25	11 (55)	4 (20)	0 (0)	5 (25)	-4.7696

* Refers to the number (and percentage) of particles reaching this outcome before the duration indicated by the "cutoff time" column has passed. The outcomes are impact onto Alpha, impact onto Beta, escape from the system as a whole, and remaining in flight, from left to right and considered as of the cutoff time.

Figure 5.13: Graphical illustration of cutoff duration and average LCE value at that duration for Alpha-centric, prograde cases.

Similar information is captured for the retrograde orbits about Alpha within Table 5.8 and in Figure 5.14. Note the color scale in Figure 5.14 actually indicates that that all of these cases have the same value for cutoff duration, yet the colors are differentiated between the initial radii to improve the clarity of the figure. The uniform cutoff time is consistent with having at least one particle reach the maximum possible duration, which is limited to the length of the underlying full two body problem propagation, for every retrograde initial orbital condition about Alpha. In other words, all of the retrograde orbital paths artificially saturate at a maximum duration given the methodology used here. Also note that the vertical scales are an order of magnitude different between Figures 5.13 and 5.14, which reveals how much comparatively less unstable the retrograde Alpha-centric orbits are.

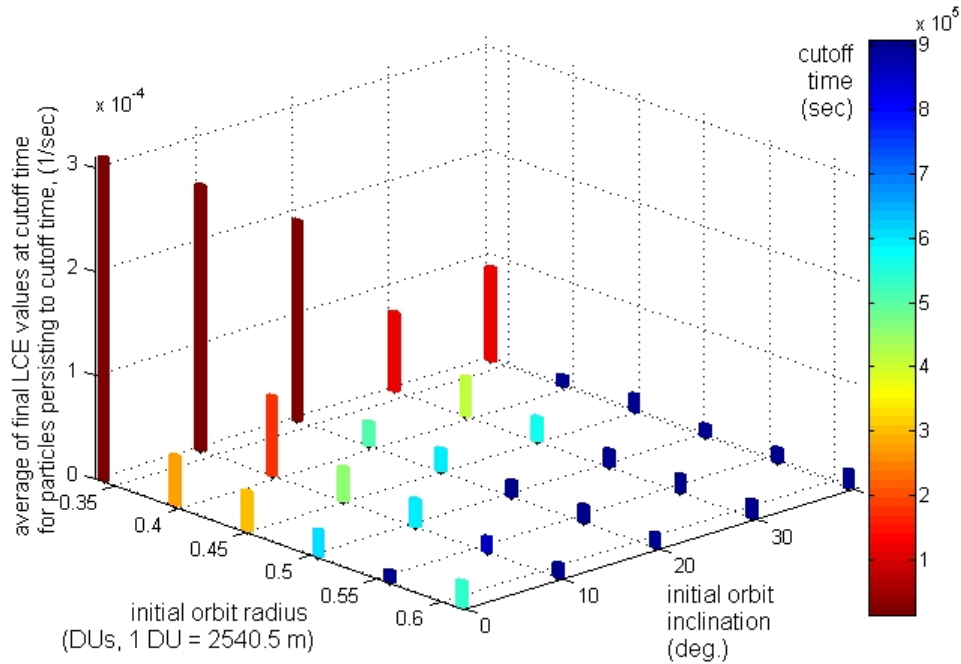From these results, it is concluded that in general, among the Alpha-centric orbits,

184
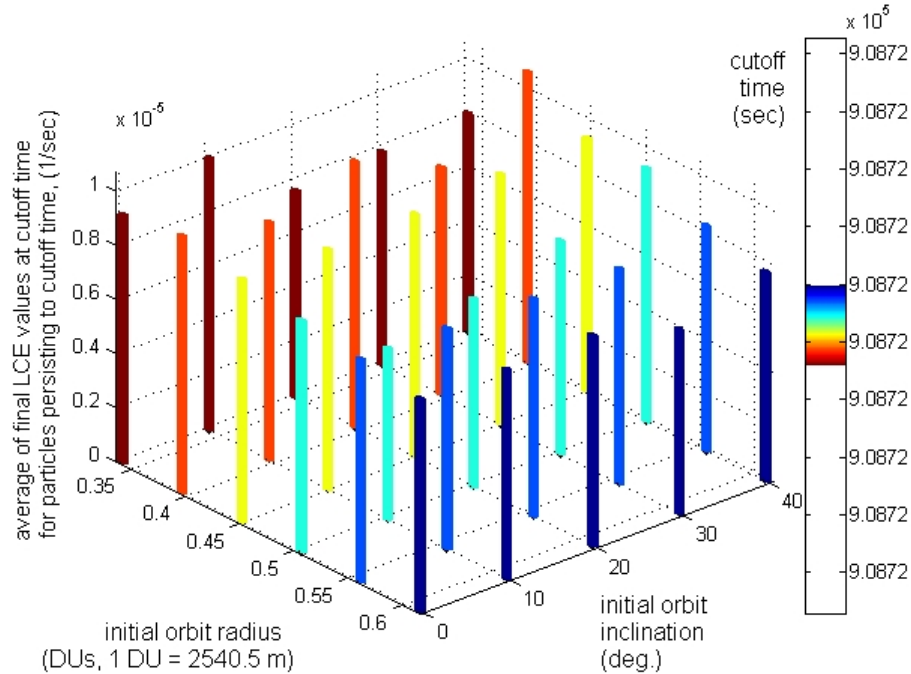
Figure 5.14: Graphical illustration of cutoff duration and average LCE value at that duration for Alpha-centric, retrograde cases.

retrograde orbital paths are more robust to the gravity perturbations of the binary system and enjoy longer lifetimes and lower cutoff LCE values than prograde orbital paths. This is sensible, as the more rapid relative rotation rate of the spacecraft with respect to Alpha's surface accomplishes a better averaging of the non-axisymmetric components of Alpha's gravity field. The same principle applies for effectively better averaging out of the gravitational perturbation from Beta. The retrograde paths also conveniently improve the rate of angular coverage for imaging or similar mapping observations of Alpha's surface.

It is also seen that higher inclination tends to promote longer lifetime in each case, especially for the prograde orbits. This is somewhat surprising, as one might expect that Alpha's oblateness and the gravitational interaction with Beta would more rapidly grow the eccentricity of more highly inclined orbits, producing impact

185

Table 5.8: Simulated particle dispositions and LCE values for Alpha-centric, retrograde cases.

R_o(DU)	i_o (°)	cutoff time (d:hh:mm:ss)	α^* (%)	β^* (%)	Esc.* (%)	Flight* (%)	$\log_{10}$(avg. LCE)
0.3397	0	10:12:25:25	19 (90)	0 (0)	0 (0)	2 (10)	-5.0379
0.3397	10	10:12:25:25	20 (95)	0 (0)	0 (0)	1 (5)	-4.9982
0.3397	20	10:12:25:25	17 (81)	0 (0)	0 (0)	4 (19)	-5.1163
0.3397	30	10:12:25:25	12 (57)	0 (0)	0 (0)	9 (43)	-5.1047
0.3397	40	10:12:25:25	12 (57)	0 (0)	0 (0)	9 (43)	-5.092
0.39443	0	10:12:25:25	15 (94)	0 (0)	0 (0)	1 (6)	-5.0237
0.39443	10	10:12:25:25	13 (93)	0 (0)	0 (0)	1 (7)	-5.0561
0.39443	20	10:12:25:25	12 (92)	0 (0)	0 (0)	1 (8)	-5.0079
0.39443	30	10:12:25:25	11 (92)	0 (0)	0 (0)	1 (8)	-5.0759
0.39443	40	10:12:25:25	10 (91)	0 (0)	0 (0)	1 (9)	-4.9704
0.44916	0	10:12:25:25	8 (73)	2 (18)	0 (0)	1 (9)	-5.0471
0.44916	10	10:12:25:25	6 (55)	4 (36)	0 (0)	1 (9)	-5.0521
0.44916	20	10:12:25:25	9 (82)	1 (9)	0 (0)	1 (9)	-5.0472
0.44916	30	10:12:25:25	9 (82)	1 (9)	0 (0)	1 (9)	-5.0343
0.44916	40	10:12:25:25	11 (92)	0 (0)	0 (0)	1 (8)	-5.0277
0.50389	0	10:12:25:25	0 (0)	0 (0)	0 (0)	21 (100)	-5.0673
0.50389	10	10:12:25:25	6 (55)	4 (36)	0 (0)	1 (9)	-5.1993
0.50389	20	10:12:25:25	5 (45)	5 (45)	0 (0)	1 (9)	-5.1582
0.50389	30	10:12:25:25	7 (64)	3 (27)	0 (0)	1 (9)	-5.1041
0.50389	40	10:12:25:25	8 (73)	2 (18)	0 (0)	1 (9)	-5.0292
0.55862	0	10:12:25:25	0 (0)	0 (0)	0 (0)	21 (100)	-5.0852
0.55862	10	10:12:25:25	0 (0)	0 (0)	0 (0)	21 (100)	-5.0882
0.55862	20	10:12:25:25	0 (0)	0 (0)	0 (0)	21 (100)	-5.0944
0.55862	30	10:12:25:25	0 (0)	0 (0)	0 (0)	21 (100)	-5.0996
0.55862	40	10:12:25:25	1 (5)	0 (0)	0 (0)	20 (95)	-5.0795
0.61335	0	10:12:25:25	0 (0)	0 (0)	0 (0)	21 (100)	-5.1038
0.61335	10	10:12:25:25	0 (0)	0 (0)	0 (0)	21 (100)	-5.1118
0.61335	20	10:12:25:25	0 (0)	0 (0)	0 (0)	21 (100)	-5.108
0.61335	30	10:12:25:25	0 (0)	0 (0)	0 (0)	21 (100)	-5.1671
0.61335	40	10:12:25:25	0 (0)	0 (0)	0 (0)	21 (100)	-5.1113

* See note on Table 5.7.

with Alpha sooner rather than later. A richer set of analysis already exists for three body problem paths staying roughly in the plane of the binary's mutual orbit, but the results observed here indicate a need to also incorporate the $\pm$Z direction. A higher inclination orbit about Alpha is likewise conveniently beneficial for angular coverage

and mapping of not only Alpha, but the polar regions of Beta as well.

Finally, it is observed that in each Alpha-centric case there is also a middle range in the initial radius value sampled that produces the least instability. This is most apparent from Figure 5.12, where for the largest initial radius value the LCE vs. time curves do not drop below the minimum for those curves reached in the previous case with smaller radius. In fact, it appears that the optimal radius is close to or just outside of the radius to produce a 3:1 period resonance between the particle and the binary system orbit.

Now for the trajectories starting from initial conditions for orbit about Beta, in both the prograde and retrograde directions, similar information to that shown before appears in Table 5.9 and in Figure 5.15, for only the smallest radius trajectories (those passing closest to Beta's surface). Beta-centric orbits in general appear to be more easily disrupted than orbits about Alpha, and almost always degrade comparatively

Table 5.9: Simulated particle dispositions and LCE values for Beta-centric, prograde and retrograde cases

PROGRADE

R_o(DU)	i_o (°)	cutoff time (d:hh:mm:ss)	α^* (%)	β^* (%)	Esc.* (%)	Flight* (%)	$\log_{10}$(avg. LCE)
0.1415	0	0:01:30:45	0 (0)	20 (95)	0 (0)	1 (5)	-3.1878
0.1415	10	0:04:44:21	0 (0)	19 (90)	0 (0)	2 (10)	-3.5681
0.1415	20	10:12:25:25	0 (0)	20 (95)	0 (0)	1 (5)	-4.8562
0.1415	30	0:01:30:02	0 (0)	15 (71)	0 (0)	6 (29)	-3.1124
0.1415	40	0:09:02:14	0 (0)	20 (95)	0 (0)	1 (5)	-3.8013

RETROGRADE

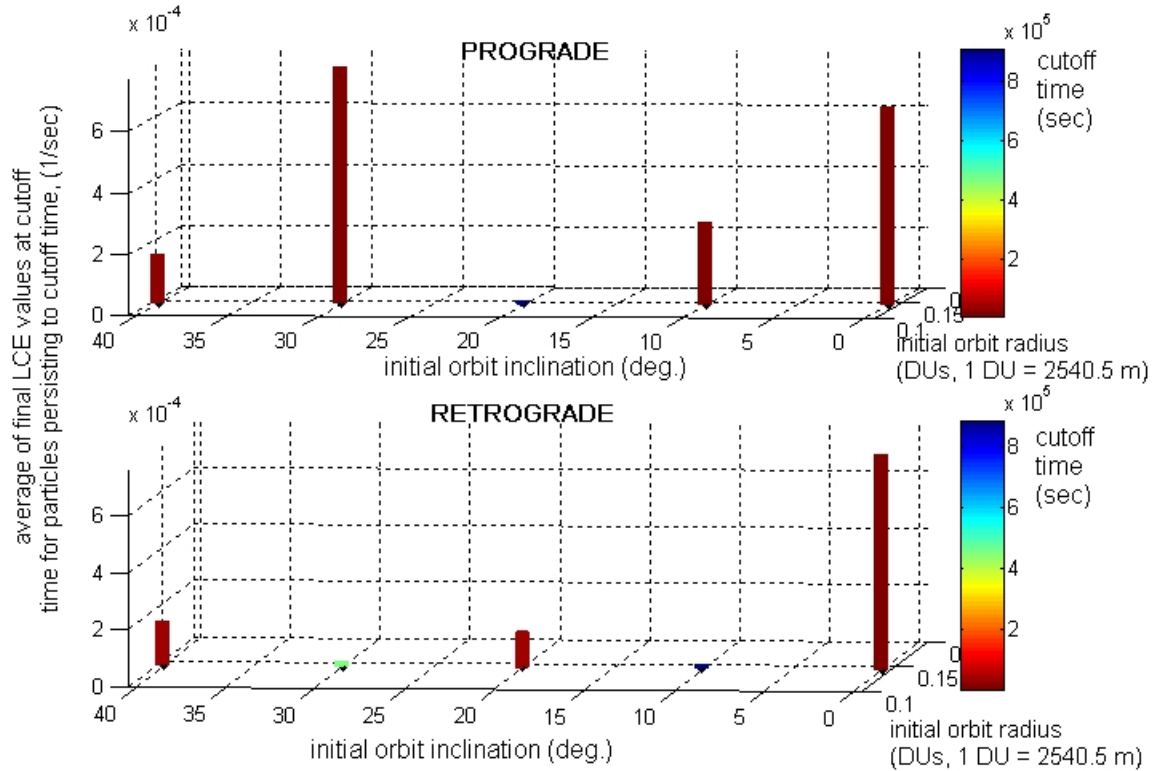|							
0.1415	0	0:01:28:09	0 (0)	19 (90)	0 (0)	2 (10)	-3.1201
0.1415	10	10:06:53:10	0 (0)	20 (95)	0 (0)	1 (5)	-4.8336
0.1415	20	0:10:14:17	0 (0)	20 (95)	0 (0)	1 (5)	-3.8927
0.1415	30	5:04:38:59	0 (0)	20 (95)	0 (0)	1 (5)	-4.6748
0.1415	40	0:09:32:57	0 (0)	20 (95)	0 (0)	1 (5)	-3.8062

* See note on Table 5.7.

Figure 5.15: Graphical illustration of cutoff duration and average LCE value at that duration for Beta-centric orbits, both prograde and retrograde, passing closest to Beta's surface.

rapidly, at least when started with the sampled radius values used herein and assuming matching circular speed for the initial velocity. This likely means that a significantly different initial velocity condition needs to be selected within the context of the three body problem. Note that in this current example system, or in any other member of the general class of small asynchronous binary NEAs formed by spin-up to fission, Beta is not rotating as rapidly as Alpha nor rotating at all (rather, merely librating) with respect to the usual three body problem frame. This may contribute to the quicker trajectory degradation about Beta. Note that for prograde Beta-centric orbits at a fixed radius the performance improves dramatically with increasing inclination, then drops, and then improves again. However, retrograde Beta-centric paths at the

same fixed radius seem to follow a trend in stability performance vs. inclination going in the opposite sense of the trend for prograde paths.

At the opposite extreme in terms of separation from all binary component bodies, the far-field orbits about the binary barycenter at the maximum radius value sampled have cutoff times, and average LCE values at the cutoff times, as shown in Table 5.10 and represented in Figure 5.16. These far-field orbits about the system barycenter unsurprisingly exhibit much greater stability than either the Alpha-centric or Beta-centric paths within the system. However in this case it is seen that there is little change with increasing inclination and also little difference between the retrograde and prograde orbit types. Perhaps differences in duration of the particle trajectories prior to impact or escape would become apparent between orbit types and various inclinations if the duration of propagation for the test particles were not limited to the length of the underlying full two body problem propagation - only a little over

Table 5.10: Simulated particle dispositions and LCE values for barycentric, prograde and retrograde cases

PROGRADE

R_o(DU)	i_o (°)	cutoff time (d:hh:mm:ss)	α^* (%)	β^* (%)	Esc.* (%)	Flight* (%)	$\log_{10}$(avg. LCE)
3.03	0	10:12:25:25	0 (0)	0 (0)	0 (0)	21 (100)	-5.3689
3.03	10	10:12:25:25	0 (0)	0 (0)	0 (0)	21 (100)	-5.3594
3.03	20	10:12:25:25	0 (0)	0 (0)	0 (0)	21 (100)	-5.3516
3.03	30	10:12:25:25	0 (0)	0 (0)	0 (0)	21 (100)	-5.3648
3.03	40	10:12:25:25	0 (0)	0 (0)	0 (0)	21 (100)	-5.3492

RETROGRADE

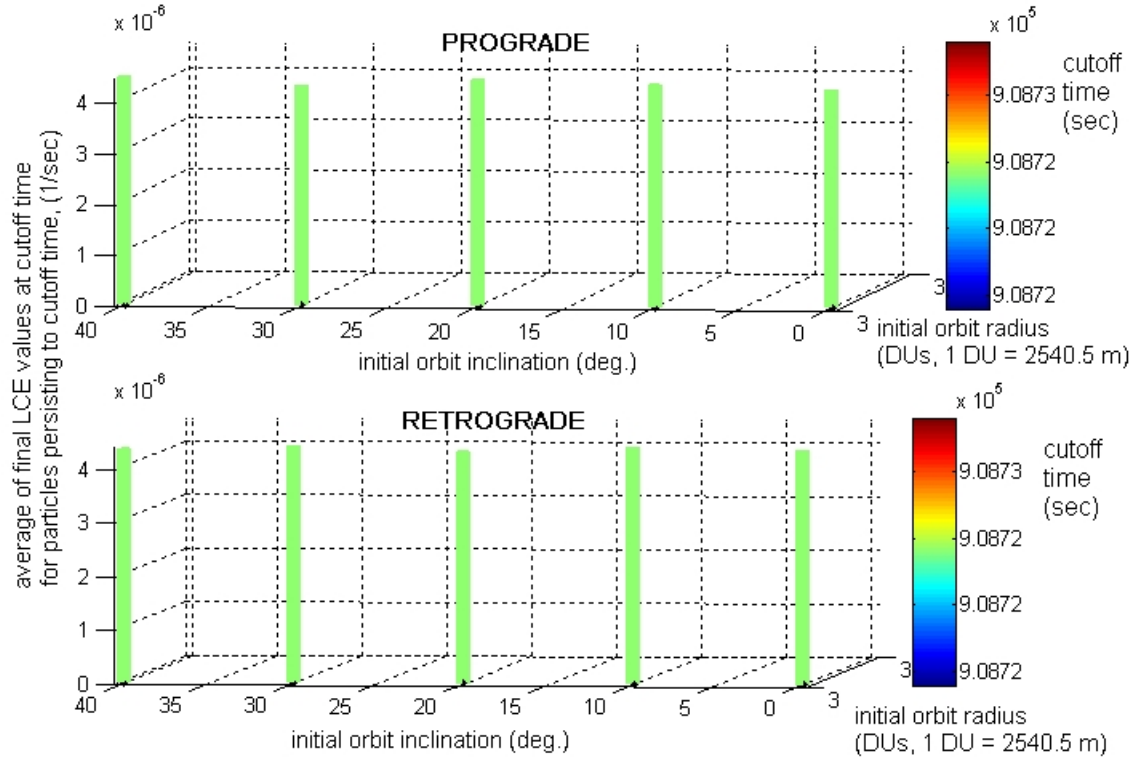|							
3.03	0	10:12:25:25	0 (0)	0 (0)	0 (0)	21 (100)	-5.3604
3.03	10	10:12:25:25	0 (0)	0 (0)	0 (0)	21 (100)	-5.3546
3.03	20	10:12:25:25	0 (0)	0 (0)	0 (0)	21 (100)	-5.3641
3.03	30	10:12:25:25	0 (0)	0 (0)	0 (0)	21 (100)	-5.3562
3.03	40	10:12:25:25	0 (0)	0 (0)	0 (0)	21 (100)	-5.3613

* See note on Table 5.7.

Figure 5.16: Graphical illustration of cutoff duration and average LCE value at that duration for barycentric orbits, both prograde and retrograde, at farthest average distance from the binary barycenter.

two weeks. In this sense, the flight time for the test particles in these far-field orbits seems to be saturated at an artificial limit.

5.5.3 Technique for improvement of local stability characterization

It is desirable to find a way to improve the stability characteristics of the nominal trajectory in each case from the parameter space examined above, by choosing an initial condition which generates a nominal trajectory that is closer to periodic, i.e. closer to repeating the same location in the Poincaré section formed by the plane of syzygy. (This is the plane formed by the instantaneous line of syzygy and binary's instantaneous mutual orbit normal.) The simplest approach to begin with is to refine the initial condition velocity while keeping the initial condition position fixed. This
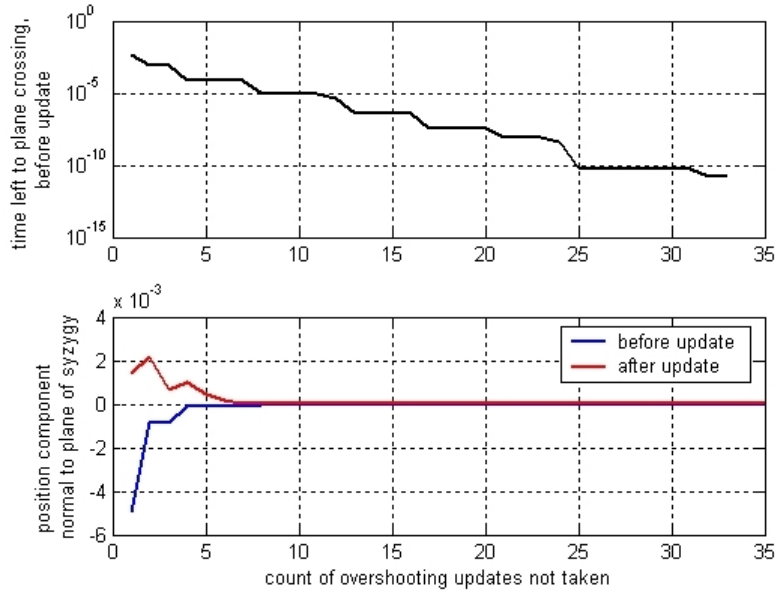
Figure 5.17: Performance in converging to exact time of syzygy plane crossing, for accurate formulation of cost functional.

refinement is done starting from the prior guess, which was velocity direction perpendicular to the initial radial position vector from the orbit center, with the given inclination, and with the velocity magnitude matching circular orbit speed (for which the orbit center is just considered an idealized point mass for each body, or the total system mass all at the system barycenter). The approach taken here is to first vary the velocity magnitude but not the direction, and to first change that magnitude with a linear sweep covering $\pm 9\%$ of the nominal value in 1% increments.

For the propagation of this sweep of trajectories, and other trajectories mentioned below, a switch is implemented in the RF3BP propagation code to detect crossing of the syzygy plane (the Poincaré section) and stop integration at such a crossing. Prior to the update portion of the RKF7(8) integration algorithm, a virtual update is performed instead. Then a check is made using what the particle state would become after that virtual update, and also what the new binary state would become after it, at the end of the current time step. That is, unit vectors of the instantaneous plane of

syzygy frame matching these virtually updated particle and binary states are found. Then the particle position and velocity vectors are decomposed into components in that frame. If the +Y component of position in this frame (the component in the direction of the mutual orbit normal crossed into the line from Alpha to Beta) changes sign relative to its previous value, upon this virtual update, then the actual update is rejected and the usual RKF7(8) step size adjustment is overridden by a halving of the current step size. The computations for the new time step of smaller size and then all of the above checking is repeated again. And so on for as many times as necessary until the actual update portion of the algorithm is allowed to execute. The whole integration is stopped once the step size is reduced below the minimum step size value specified. Figure 5.17 shows first, at top, the simulation time left until the exact time of reaching the syzygy plane (as defined by the plane crossing time eventually converged to) before each update that was not adopted because an overshoot of the plane was detected. At the bottom in the same figure is shown the +Y component of position in this frame, both before (blue) and after (red) each update that was not adopted because an overshoot of the plane was detected. The count of such skipped updates forms the independent variable axis in these plots. Figure 5.17 demonstrates accurate determination of the instant and particle conditions at plane crossing, and demonstrates propagation right up to that instant through the step size being reduced to the minimum step size, stopping the integration.

For a given particle trajectory, all components of the position and velocity expressed in the syzygy frame at the time of next plane crossing, when the propagation stops, can be differenced with the position and velocity expressed in the syzygy frame at the initial time. This gives the position and velocity deviations $\delta\mathbf{d}$ and $\delta\mathbf{v}$ for use

192

in the cost functional

$$J = \frac{1}{2}(\delta \mathbf{d} \cdot \delta \mathbf{d}) + \frac{1}{2}(\delta \mathbf{v} \cdot \delta \mathbf{v}) \tag{5.62}$$

From the sweep of initial velocity magnitudes, the velocity magnitude value resulting in the lowest J is adopted to define a new particle initial state serving as the starting point for iterative refinement. For the iteration, the simple algorithm must first be initialized by propagating to the next syzygy plane crossing new trajectories having initial velocity magnitude 5%, 10%, and 0% above the iteration starting point. Once these three trajectories and their end states and corresponding costs are in hand, one can use the following to perform the actual iteration:

$$\|\mathbf{v}\|_{i+1} = -\frac{b_i}{c_i} \quad , \quad \begin{bmatrix} a_i \\ b_i \\ c_i \end{bmatrix} = \begin{bmatrix} 1.0 & \|\mathbf{v}\|_{i-2} & \frac{1}{2}\|\mathbf{v}\|_{i-2}^2 \\ 1.0 & \|\mathbf{v}\|_{i-1} & \frac{1}{2}\|\mathbf{v}\|_{i-1}^2 \\ 1.0 & \|\mathbf{v}\|_{i} & \frac{1}{2}\|\mathbf{v}\|_{i}^2 \end{bmatrix}^{-1} \begin{bmatrix} J_{i-2} \\ J_{i-1} \\ J_i \end{bmatrix}$$

$$\tag{5.63}$$

With each iteration, i is incremented and the newest cost J_i for the end state of the last propagation, in turn started using $\|\mathbf{v}\|_i$, is incorporated.

From all of the iterated values used for initial velocity magnitude, again the value resulting in the lowest J is adopted to define the initial state for an improved nominal trajectory. This is propagated for the full duration with no syzygy plane crossing detection enabled, with the intent of being able to directly compare the duration reached and long-term LCE value reached between the improved nominal trajectory and the old nominal trajectory, within the same region-type-radius-inclination case.

All of the steps outlined in this section are applied only to a small subset of the full set of cases. In particular, these steps are performed for the Alpha-centric prograde orbits at the lowest radius, highest radius, and radius from the original parameter

space sampling which is nearest to that for the (possibly least unstable) 3:1 period resonance between the particle and binary system orbits. For these three radii, all inclination values are explored.

5.5.4   Local stability characterization results

Comparing the best results obtained with the linear sweep and subsequent iteration in the scalar parameter $\|\mathbf{v}\|$ against the original results obtained, for the nominal trajectories in the subset of cases of particular interest as outlined above, gives Figures 5.18–5.20. These figures show this comparison in the LCE vs. time curves from the propagated trajectories, with the dotted lines being for the "improved" nominal trajectories and solid lines being for the original ones.

Figure 5.18: Comparison, between original and improved nominal trajectories, of the LCE plotted against simulation time, all for the Alpha-centric, prograde, R_o =0.3397 cases. The nominal trajectories are solid lines and the "improved" nominal trajectories produced with sampling and iteration in the initial velocity magnitude parameter are dotted lines.
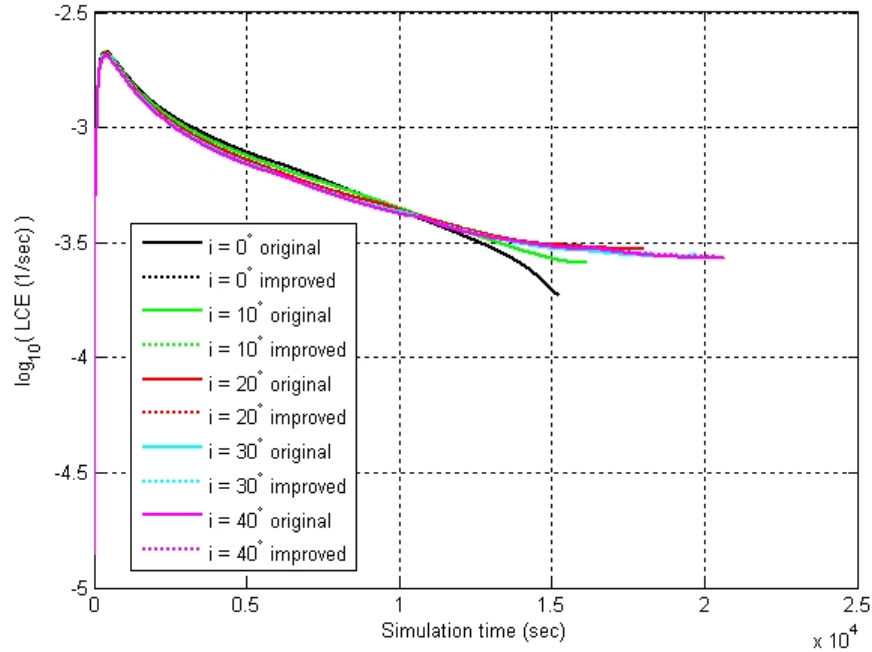
194

Figure 5.19: Comparison, between original and improved nominal trajectories, of the LCE plotted against simulation time, for the Alpha-centric, prograde, R_o =0.50389 cases. The nominal trajectories are solid lines and the "improved" nominal trajectories produced with sampling and iteration in the initial velocity magnitude parameter are dotted lines.

It is seen that while the winner of this comparison varies considerably between cases, with the newer nominal trajectory sometimes performing better and sometimes performing worse, in general there is no net improvement in stability metric performance resulting from the computational effort of the $\|\mathbf{v}\|$ parameter exploration. Over the short (less than about 6 hours) lifetimes for the trajectories starting closest to Alpha's surface, almost no change is observable. Average lifetimes are still about the same for the trajectories starting at the larger radii too. Again, the same 40° inclined trajectory persists longest (and is separated in duration by only a few days in favor of the original initial condition for the case nearest the hypothesized stable resonance). Remedies for this failure to achieve performance improvement may include varying a larger number of initial state components or parameters, to work with more degrees
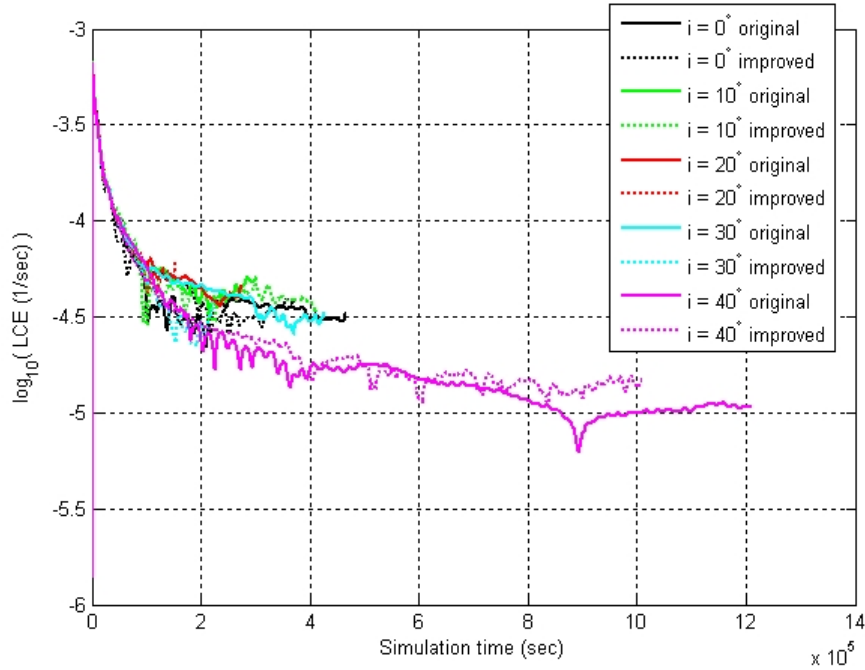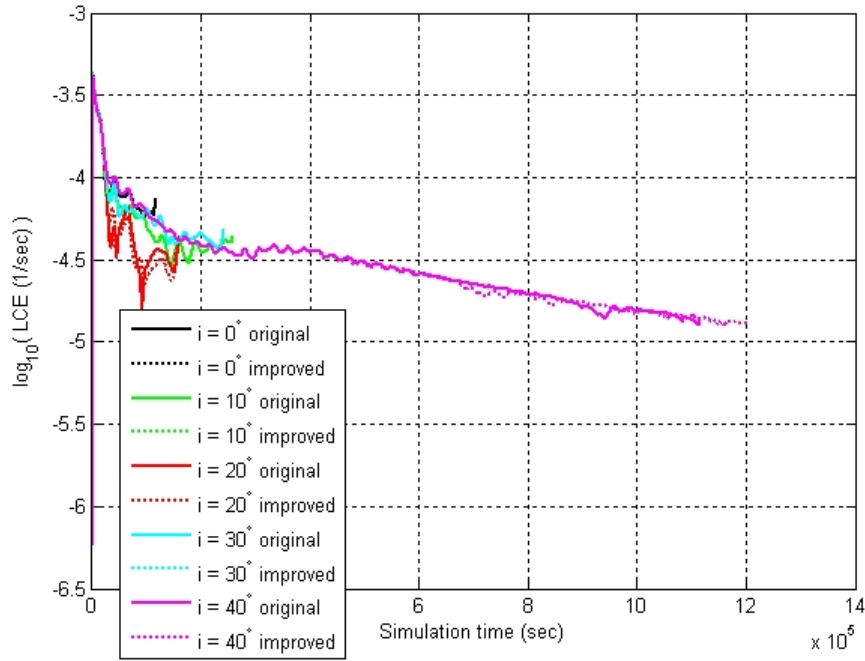
195

Figure 5.20: Comparison, between original and improved nominal trajectories, of the LCE plotted against simulation time, for the Alpha-centric, prograde, R_o =0.61335 cases. The nominal trajectories are solid lines and the "improved" nominal trajectories produced with sampling and iteration in the initial velocity magnitude parameter are dotted lines.

of freedom. Also, it may help to use a more sophisticated gradient-based optimization for the cost functional rather than the simple iterative scheme proposed above (which assumes that the cost is approximately locally quadratic in the single varied parameter of initial velocity magnitude). Of course another explanation for the lack of improvement is that the stability properties of this dynamical system simply do not change strongly with location in phase space, in which case the choice of approach used would have little impact.

5.5.5 Findings applicable to design of future space missions to binary asteroids

The study overviewed in this section is merely the first step towards global characterization of the degree of instability of trajectories within and about any member

of the class of small asynchronous binaries. The simulation of test particles in the RF3BP, for the KW4 example system which typifies that class, has explored only a limited parameter space governing the choice of trajectory initial conditions. Above, trajectories have been explored about both components and about the system as a whole, in both directions with respect to the three body problem frame's mean rotation, with varying scaled proximity to either component plus varying initial departure from the instantaneous plane of the binary mutual orbit. While the impact vs. escape outcomes have been tracked for all test particles, for the main focus herein the finite-time LCE's of their trajectories has been determined as the metric for how unstable those trajectories are. Direct sampling and then an iterative scheme to attempt to refine a single initial condition parameter (initial velocity magnitude) to improve trajectory duration and performance, according to that metric, has produced minimal overall benefit. Further pursuing the orbit refinement path is advisable only with improvements in the methods used for such refinement.

Several insights into the best trajectories within a binary system to use as part of a future scientific mission to such a pair can still be gained from this limited study, however. Orbiting at a distance from the barycenter a few times larger than the separation between the binary component mass centers is the most natural starting point. The low LCE values for such orbits indicate that this choice is good for the goal of flight safety and long observation time at a larger distance, up to at least a few weeks. However, this supposes that the binary as a whole is large enough or dense enough that it's net gravitational force on the spacecraft at this distance is at least an order of magnitude larger than the force on the spacecraft from solar radiation pressure (SRP), which was not incorporated into any of the RF3BP propagations above. The observed insensitivity of stability performance with respect to inclination

from the binary's mutual orbit plane means a higher inclination, up to 40°, can and should be chosen. This serves the goal of bettering the angular coverage in latitude on both bodies, for imaging, spectroscopy, or point-ranging measurement mapping of the surfaces. Further, bearing in mind the actual presence of SRP, this higher inclination should be narrowed to that which places the spacecraft's orbit as close to within the terminator plane perpendicular to the direction of the sun as possible. The direction of the spacecraft orbit should also be retrograde to accommodate transfer into the best choice for close proximity flight within the system, to accomplish detailed gravity mapping and the highest resolution surface observations. This best choice for close proximity flight would be a retrograde orbit that is significantly inclined (helpful for SRP and for Alpha mapping, as well as observing of high latitudes on Beta) and with an orbital radius from Alpha's center of mass about 1/2 the separation between the component mass centers. To obtain the most information about the gravity field and density distribution of the components it seems desirable to persist in these orbits (though they are the safest rather than the most strongly influenced paths) for as long as possible without any trajectory correction thruster actuation. These general guidelines, supported by the results of this section, should be useful for the future design of binary asteroid missions.

CHAPTER VI

Conclusions and Future Research Directions

This dissertation contributes to the general state of understanding about the dynamics, characteristics, and evolution of binary asteroid systems in several ways. The results apply to many discovered objects, and address both the current dynamical "snapshot" for them, the longer term history for them, and how to more effectively explore them in-situ.

6.1 Summary of Research Contributions and Results

Chapter II presents the development of a general methodology for accurate and efficient propagation of the Full Two-Body-Problem, whether applied to a binary asteroid system or any other pair of extended bodies interacting under their mutual potential arising from their distributions of mass, charge, etc. The gradients of the mutual **gravity** potential involved here, with respect to relative position and attitude between the bodies, are given based upon a prior-published highly flexible formulation for that mutual gravity potential when both bodies are modeled as arbitrary closed polyhedra with triangular facets. The derivation of these gradients using succinct tensor expressions is a new contribution of this work, as is their incorporation into simulation code using both traditional continuous equations of motion with a standard integration scheme and the discrete equations of motion comprising the novel LGVI

integration scheme. This dissertation also presents the unique serial and parallel implementation of the methodology, profiles the accompanying dramatic performance improvements since the beginning of this work, and provides validation of these tools for interesting test cases, with varying complexity.

Next, this dissertation presents the first-of-its-kind application of these tools to a specific example binary asteroid system observed in nature, that of (66391) 1999 KW4. This first end-to-end dynamical study has broader applicability due to KW4 being representative of the majority class (containing nearly half of the systems) within the already significant in size NEA population: the class of "small asynchronous binaries" as introduced near the start of Chapter III. The main conclusions drawn from the simulation of KW4's behavior, in configurations spanning various levels of energetic excitation but all plausibly consistent with observations, should be readily transferable to other systems in this class of binaries. Particularly the existence of a variant of the type 2 Cassini-state as a long-period dynamic mode of the coupled motion, and the existence and period relationships for at least three shorter-period dynamic modes of co-orbital and librational motion within the approximate plane of the mutual orbit, may be readily generalized. As with KW4, most systems of this class are likely currently found to be occupying a moderately energetically excited configuration between their most relaxed and plausibly most excited configurations. The long-period mode excitation mechanism of solar tide during perihelion passage, also effectively demonstrated herein for KW4, likely applies only to Aten NEAs with similarly low perihelion distance. However, very infrequent distant flybys of Earth and Mars should have a similar effect. Along with the continuous processes like YORP, events like these and rare impact events upon either component drive shifts in the system excitation level over time. The analytical formulae presented in this

dissertation in Chapter IV relate the frequencies for the modes of motion for any system in this class of small asynchronous binaries to the primary's oblateness and the secondary's triaxial ellipsoid shape. These frequencies are for the long term mutual precession of the primary spin pole and orbit normal, and for the faster coupled Beta libration and orbit dynamics, both as revealed in the output of the F2BP simulation. For the latter, the motion may be properly reduced into the quantities of relative position of Alpha's centroid, relative velocity of Alpha's centroid, and angular velocity of Beta, all represented in the frame fixed to Beta, for the frequencies to be directly manifest. Especially relevant to the conduct of future binary NEA observations and spacecraft missions to such pairs is the fact that these frequencies are able to be captured through a time history of imaging of the binary from a location outside of the binary's own gravitational sphere of influence. The inertia elements of the bodies are in turn related to the frequencies through the formulae, so that the inertia elements can be determined from the motion just as from the shape models. Comparison of these inertias provides a rough first estimation of internal mass distribution and inhomogeneity within the bodies. The ability to obtain this information from standoff observation before entry into the system is significant and useful.

Finally, the consideration herein of the motion of test particles within the time-varying gravity field of the F2BP system (according to the RF3BP), is likewise applicable to any system in this class of small asynchronous binaries, and contributes further understanding of the dynamical environment present within such systems. It highlights the relative effects that may accompany infrequent impact events creating ejecta, in terms of surface material redistribution and mass-normalized angular momentum changes to the system components and mutual orbit. More significantly, examination of lofting motion of surface material on the primary near its equator,

not performed in such detailed fashion prior to the work for this dissertation, provides verification of a long timescale binary evolution mechanism hypothesized herein. This operates in addition to tidal evolution and any effects of BYORP. The pieces of surface material undergo such lofting motion after the primary spin rate exceeds the local "disruption spin rate" due to gradual spin-up of the primary under YORP torque, even if those pieces of material have no initial surface-relative velocity. The gravitational interaction of these particles with both components while in flight causes them to gently re-impact with Alpha with a nonzero surface-relative velocity. It is the difference in the surface-relative motion states between the time of lofting and time of re-impact that causes, in reaction to that re-impact, a reduction in the spin rate of Alpha. The same interaction also transfers angular momentum through the lofted particles into the mutual orbit. All of this is found to occur episodically, with the reduction in Alpha spin rate during each lofting episode being slowly undone by the gradual YORP torque ramping back up the spin rate, until the next episode is triggered. The demonstrated evolution mechanism's strength and metrics for that (such as time-averaged mass aloft) are found to be insensitive to changes in the amount of material available for such motion or that material's discretization (number and size of "particles"), but sensitive to the YORP torque's magnitude. As a whole, all of the angular momentum externally injected into Alpha spin is transported into the mutual orbit, which grows over timescales comparable to or several times faster than standard orbital expansion evolution due to solid body tides alone. The orbit growth rate theoretically would increase with the expansion but in reality may produce other significant changes to the system. These changes and the eventual end-state for such systems may be related to recent observations of the first NEA triple system and divorced binaries in the inner main belt, respectively. Together with such observa-

tions, the work summarized herein provides additional valuable pieces of the puzzle for binary system evolution and life cycle that were not available before.

Also, in Chapter V this dissertation presents a simple but novel direct study of the (in)stability of trajectories approximating spacecraft orbital motion about each of the components, and the system barycenter at large distance, for any member of the small asynchronous binaries class. It is found that among the Alpha-centric trajectories, retrograde orbital paths are more robust to the gravity perturbations of the binary system and enjoy longer lifetimes and a lesser degree of instability than prograde orbital paths. For these Alpha-centric trajectories, it is also seen that, somewhat surprisingly, higher inclination relative to mutual orbit tends to promote longer lifetime, especially for the prograde paths, and a middle range in the initial radius value exists that produces the least instability. Beta-centric trajectories are much more easily disrupted and decay comparatively quickly, while far-field barycentric trajectories exhibit much better performance all around than Alpha-centric ones, insensitive to prograde/retrograde direction and inclination. Practically useful rules of thumb for any spacecraft mission to a binary follow from this work. First the craft should orbit at a distance from the barycenter a few times larger than the separation between the binary component centroids, with a higher inclination chosen as close as possible to that which places the spacecraft's orbit within the terminator plane. The orbit should be retrograde and transfer to a close significantly inclined retrograde orbit about Alpha with a nominal radius from Alpha's center of mass about 1/2 the centroids separation. These guidelines should be valuable for the future design of binary NEA missions.

6.2 Topics for Future Study

Of course the work presented here is by no means complete. In addition to the possibility of addressing some of this work's remaining limitations, many promising directions for further related investigation exist. The limitations most often stem from a lack of computing resources (requiring restriction or coarser sampling of the parameter spaces for the F2BP KW4 studies of Chapter III or the RF3BP studies of Chapter V, for example, or restriction of the particle population sizes within the latter). Otherwise a prime limitation is in the applicability of many results and conclusions herein only to those binary systems satisfying the main conditions and assumptions of small body size and intermediate component size ratio, close separation, on-average synchronous elongated Beta and super-synchronous oblate Alpha rotating near its spin limit. In other words, the choice to narrow the systems studied to those within the small asynchronous binaries class of interest, which bear the signatures of a formation by fission or mass shedding due to slow spin-up. Other major types of binaries exist within the NEA and MBA populations having very different size ratios or angular momentum content (hence different likely origins). Particularly large asteroidal bodies with very small satellites (likely generated by mutual capture of catastrophic disruption products or material separation by impact), a few widely separated small binaries, and a few large double asteroids with roughly equal sized components both in synchronous rotation, per Pravec et al. [63]. Most of the results herein are of limited applicability to these other system types.

One of the specific avenues for further investigation, related to the F2BP simulation methodology developed early on, would be comprehensive examination of and direct comparison between other solitary-body and mutual gravitational potential representations in addition to the polyhedral-based representations used above. The

comparison desired is between final simulation performance, in both computational cost and error accumulation, using the different mutual potential gradient computations matching these representations, within the same EOM and integration scheme, with full parallelization. Any adjustments tailored to each's structure (like tree-code methods for the N point masses packed sphere model $+$ N point masses packed sphere model representation) may also be incorporated. In the present work, based on the reasoning at the start of Chapter II, these other methods are not developed to the same degree and directly compared in performance.

Another area for further investigation would be direct simulation over very long timescales of the effects of the sun's perturbing forces on the KW4 binary's behavior, particularly its Cassini state excitation level, through many successive perihelion passages rather than single perihelion passages in isolation. The purpose of this would be to reveal the true random-walk accumulation of Alpha spin and orbit pole offset angle changes over many perihelion passages, as in the KW4 system in nature, and to find the average offset angle value for that random walk for comparison with the value the system likely occupies as presented earlier. It would be ideal to perform this simulation spanning many successive heliocentric orbits for at least several trials randomized over the observation-derived uncertainty in absolute orientation for the system relative to its heliocentric orbit plane, to get a better statistical result. The perturbations of all other planets may be included in similar fashion to the sun's, without much additional computational effort aside from propagating the planets' heliocentric orbits too, simply by adding additional $\mathbf{C}_{(1,2)}$ terms of the two point mass type for each planet into Eq. 2.58. Alternatively, if an analytical model can be developed for the effects of the perihelion passage, with the same or higher order than that presented for changes to a solitary body's spin state during flybys in Scheeres at

al [81],[82], then that may be used for many successive passages without the cost of such extensive duration simulation including many long aphelion arcs.

With respect to the examination of primary surface material lofting herein, a few additional directions may be pursued. First, it is recognized that although a thorough attempt was made to identify the system parameters and location for which particle lofting motion is most likely to begin, the choice of threshold spin rates following from that, at which such motion is said to "activate", is rather arbitrary. Second, instantly activating such motion precisely when this fixed threshold is crossed is itself unrealistic. So it is of interest to better characterize the conditions under which motion begins for surface material in the identified lofting regions on the primary, accounting for actual physical particle size distribution and contact and friction between the particles and the surface. For example, some level of cohesion between material at the surface and material lying below it, closer to the centroid, may allow for no motion by any of the material until well above the critical spin rate (as locally computed for that location simply by considering the surface-normal component of total acceleration). Then the entire mass will suddenly give way well above the critical spin rate, resulting in different particle trajectories reaching higher altitudes with respect to Alpha. Stochastic modelling of lofting onset, particle-by-particle, within the precise dynamical simulation, may be an important improvement. In addition, it may be significant to include collisional and gravitational interactions between particles of material after they have lofted. This would become a detailed N-body problem in the presence of the binary components. Inclusion of surface charging and electrostatic forces between particles and between the surface and the particles may be a worthwhile addition on top of that inter-particle gravitation and collision.

In the probability-based simulation method, just as for the precise dynamic simu-

lation above, there are more open ended issues awaiting resolution. Over time, regularization of the equatorial figure of Alpha may occur, which may cause the magnitude of the YORP torque on Alpha to change slightly, so that it should not be kept a fixed constant but slowly varied. No realistic shape is included in the probability-based simulation, and by construction of the algorithm "evening out" of material around the equator cannot be directly modeled but only indirectly modeled through more or less mass being allocated into the different rotating barycentric frame longitude bins as the time intervals are discretely mapped forward. Further, those longitude bins are uncoupled from actual longitude on the surface of the asynchronous Alpha. Slowly accumulating (in magnitude) changes to the X- and Y- principle axis components of the Alpha inertia dyad are observed as roughly symmetric and opposite each other, indicating the longitudinal shifts in material within the frame fixed to Alpha. Note that no latitude shift of material in that frame is possible, by construction of the algorithm, which is also not realistic. The open issue is that none of this has been firmly linked back to whether enduring body figure changes are occurring which actually impact the rate of external angular momentum input by YORP.

However, even if all of these potential improvements in the model fidelity for both simulation types are pursued, the basic mechanism for small asynchronous binary evolution supported by this work is not likely to be altered. Though additional energy dissipation would be present with the collision and friction, all of the inter-particle and particle-to-binary-component interactions will not reduce total system angular momentum. They may only transfer angular momentum to the orbit less effectively, by returning a greater portion of angular momentum carried with the particles back to Alpha. In which case the spin rate of Alpha will not be depressed as much over the whole lofting episode, and those episodes will occur more frequently

for the same net effect on the system evolution. All that is adjusted with decreasing angular momentum transfer is increasing lofting activity, until in the limit it would become almost continuous.

It is also observed that there is some drift over time in the X- and Y- components (and especially importantly the norm of those two components) for the Alpha and orbit angular momenta. Further, the drift in that norm is in opposite directions for Alpha and the orbit. This brings up the possibility of spin and orbit pole angular separation being altered through the action of YORP on the primary and transfer of the angular momentum added into the orbit. This would be excitation/damping of the system's Cassini state by such means, in addition to the orbit expansion evolution, and is a phenomena which has yet to be fully addressed.

Another future research direction is to step back and attempt a comprehensive combined modeling of all of the different proposed mechanisms for binary evolution toward separation acting concurrently, with significant adjustments to the approximate probabilistic simulation approach used herein. The aim of this should be to directly see which of these effects dominates the quantitative timescales for such orbit migration.

Finally, it may be valuable to more fully explore the parameter space for the orbital paths about both binary components and the system as a whole. Also, for all points explored in that space, it may be helpful to use the methodology for iterative trajectory initial condition optimization after including more states and parameters, and utilizing a proper gradient-based optimization of the cost functional that does not assume locally quadratic behavior in the cost about the best parameter values.

Exploring some of these topics for further study, together with the anticipated availability and incorporation of significantly more observational data on multiple

asteroid systems in coming years, promises to continue the dramatic progress seen in the past decade, in understanding the dynamics and morphology of such natural examples of the Full Two-Body-Problem.

APPENDIX A

Further remarks on the rule used to obtain the gradient of an attitude matrix with respect to another attitude matrix, for Eqs. (2.24–2.26)

One may resume using the tensor notation of Chapter II and write the rules used to obtain Eqs. (2.24) and (2.26) as follows:

$$\frac{\partial T_{j\,k}}{\partial T_{\phi\theta}} \;=\; \delta_j^\phi \delta_\theta^k \qquad , \qquad \frac{\partial T_{i\,k}^T}{\partial T_{\phi\theta}} \;=\; \delta_k^\phi \delta_\theta^i. \tag{A.1}$$

This is just the most general and intuitive approach for differentiation of an arbitrary matrix with respect to itself, or its transpose. Given that in the application addressed by this document $T_{i\,k}$ is in SO(3), it is more proper to use different rules, namely

$$\frac{\partial T_{j\,k}}{\partial T_{\phi\theta}} \;=\; \delta_j^\phi \delta_\theta^k \;-\; T_{\phi k} T_{j\theta} \qquad , \qquad \frac{\partial T_{i\,k}^T}{\partial T_{\phi\theta}} \;=\; \delta_k^\phi \delta_\theta^i \;-\; T_{\phi i} T_{k\theta}. \tag{A.2}$$

With the latter one must also modify Eq. (2.35) to be

$$E_{\phi\theta} \;=\; G \sum_{a\in A}\sum_{b\in B} \rho_a\, T_a\, \rho_b\, T_b\; \frac{1}{2}\left(\frac{\partial \hat{U}_1}{\partial T_{\phi\theta}} + \frac{\partial \hat{U}_2}{\partial T_{\phi\theta}} + \frac{\partial \hat{U}_3}{\partial T_{\phi\theta}} + \cdots \right).$$

Unlike as stated in Fahnestock and Scheeres [83], both of these approaches are correct and give equivalent results. Note that within $T_{j\,i} \in$ SO(3), the rows are orthogonal to one another and so are the columns, which leads to six constraints that must be satisfied. These constraints can be succinctly summarized with the fact that

$T_{j\,i}^{-1} = T_{j\,i}^{T}$, which leads to

$$T_{j\,i}^{-1}\,T_{i\,k} = T_{j\,i}^{T}\,T_{i\,k} = \delta_{j}^{k}. \tag{A.3}$$

Differentiating the left hand side of Eq. (A.3) with respect to the attitude matrix gives

$$\frac{\partial\left(T_{j\,i}^{T}\,T_{i\,k}\right)}{\partial T_{\phi\theta}} = \frac{\partial T_{j\,i}^{T}}{\partial T_{\phi\theta}}\,T_{i\,k} + T_{j\,i}^{T}\,\frac{\partial T_{i\,k}}{\partial T_{\phi\theta}}. \tag{A.4}$$

Substituting Eqs. (A.1) into this, and using the fact that $\delta_{i}^{\phi} = \delta_{\phi}^{i}$ yields

$$
\begin{aligned}
\frac{\partial\left(T_{j\,i}^{T}\,T_{i\,k}\right)}{\partial T_{\phi\theta}} &= \left(\delta_{i}^{\phi}\delta_{\theta}^{j}\right)T_{i\,k} + T_{j\,i}^{T}\left(\delta_{i}^{\phi}\delta_{\theta}^{k}\right) \\
&= \delta_{\theta}^{j}\,\delta_{\phi}^{i}\,T_{i\,k} + \delta_{\theta}^{k}\,\delta_{\phi}^{i}\,T_{j\,i}^{T} \\
&= \delta_{\theta}^{j}\,\delta_{\phi}^{i}\,T_{i\,k} + \delta_{\theta}^{k}\,\delta_{\phi}^{i}\,T_{i\,j} \\
&= \delta_{\theta}^{j}\,T_{\phi k} + \delta_{\theta}^{k}\,T_{\phi j} \tag{A.5}
\end{aligned}
$$

It has been manually verified by the author that no skew symmetry about the two dimensions referenced by indices j and k exists, so that the last line above is not equal to zero in general, which is inconsistent with the fact that the partial derivative of the right hand side of Eq. (A.3) is zero. Therefore the rules of Eqs. (A.1) do not respect the constraints of $T_{j\,i}$ being in SO(3). Instead substituting Eqs. (A.2) into Eq. (A.4) gives

$$
\begin{aligned}
\frac{\partial\left(T_{j\,i}^{T}\,T_{i\,k}\right)}{\partial T_{\phi\theta}} &= \left(\delta_{i}^{\phi}\delta_{\theta}^{j} - T_{\phi j}T_{i\theta}\right)T_{i\,k} + T_{j\,i}^{T}\left(\delta_{i}^{\phi}\delta_{\theta}^{k} - T_{\phi k}T_{i\theta}\right) \\
&= \delta_{\theta}^{j}\,\delta_{\phi}^{i}\,T_{i\,k} - T_{\phi j}T_{i\theta}\,T_{i\,k} + \delta_{\theta}^{k}\,\delta_{\phi}^{i}\,T_{j\,i}^{T} - T_{j\,i}^{T}T_{\phi k}T_{i\theta} \\
&= \delta_{\theta}^{j}\,\delta_{\phi}^{i}\,T_{i\,k} - T_{\phi j}\left(T_{\theta i}^{T}\,T_{i\,k}\right) + \delta_{\theta}^{k}\,\delta_{\phi}^{i}\,T_{i\,j} - \left(T_{j\,i}^{T}T_{i\theta}\right)T_{\phi k} \\
&= \delta_{\theta}^{j}\,T_{\phi\,k} - T_{\phi j}\left(T_{\theta i}^{T}\,T_{i\,k}\right) + \delta_{\theta}^{k}\,T_{\phi\,j} - \left(T_{j\,i}^{T}T_{i\theta}\right)T_{\phi k}
\end{aligned}
$$

Then substituting the identity in Eq. (A.3) back in where apparent and rearranging

produces

$$\frac{\partial \left(T_{j\,i}^{T}\, T_{i\,k} \right)}{\partial T_{\phi\theta}} \;=\; \delta_{\theta}^{j}\, T_{\phi\,k} \;-\; T_{\phi j}\, \delta_{\theta}^{k} \;+\; \delta_{\theta}^{k}\, T_{\phi\,j} \;-\; \delta_{j}^{\theta} T_{\phi k}$$

$$\;=\; \delta_{\theta}^{j}\, T_{\phi\,k} \;-\; \delta_{\theta}^{j}\, T_{\phi k} \;-\; \delta_{\theta}^{k}\, T_{\phi j} \;+\; \delta_{\theta}^{k}\, T_{\phi\,j}$$

$$\;=\; 0$$

This is clearly consistent with the partial derivative of the right hand side of Eq. (A.3) being zero. Therefore the rules of Eqs. (A.2) do satisfy the orthonormality identity constraints on $T_{j\,i}$, which is why it is stated that they are more proper to use. In practice, due to the slightly lower number of operations involved, the rules of Eqs. (A.1) are used in our codes to obtain the F2BP propagation results presented in Chapter II and thereafter.

APPENDIX B

Mapping of velocity bounds for expected return and expected escape over the full surfaces of KW4 Alpha and Beta

Earlier in section 5.3.1, a method was presented for calculating a conservative upper bound up to which the magnitude of the surface-relative velocity vector for particles launching from the center point of a given facet on a binary component's body mesh could grow, while still expecting return impact of those particles onto the source body. Similarly, small adjustments to that method's equations allow calculation of a conservative lower bound down to which the magnitude of the surface-relative velocity vector for particles launching from such points may be lowered, while still expecting those particles to escape from the binary asteroid system. Here these calculations are performed for the center points of every facet in the body meshes for Alpha and Beta of (66391) 1999 KW4, the main example small asynchronous binary asteroid treated in the research for this dissertation. The assumption for the launch relative velocity vector's direction used in these calculations here is alignment with the face normal vector. Also the calculations make use of the F2BP motion output from the "most-excited" scenario within Table 3.3 in section 3.3. What results are interesting maps of the velocity bounds over the surfaces of Alpha and Beta for this system, presented in latitude-longitude projection in Figures B.1 and B.2 and

in isometric view in Figures B.3 and B.4. Note that a total of 260 roughly evenly spaced instances in time spread out over 35.88 hours, equivalent to $\approx$2.0615 times orbital period or $\approx$13.00 times the shortest (Alpha spin) period were used in this computation, so that the results represent a fairly complete coverage of the modes of motion characterizing the dynamical evolution of the full system. On Alpha, the highest surface normal launch speed bounds for return and escape are observed in a few regions at intermediate lattitude, and the lowest such bounds are observed at the equator. On Beta, there is a significant discrepancy between the leading and trailing faces, in the sense of the Beta's orbital motion, with the leading face having lower velocity bound values accounting for the nominal synchronous orientation of Beta in the system.
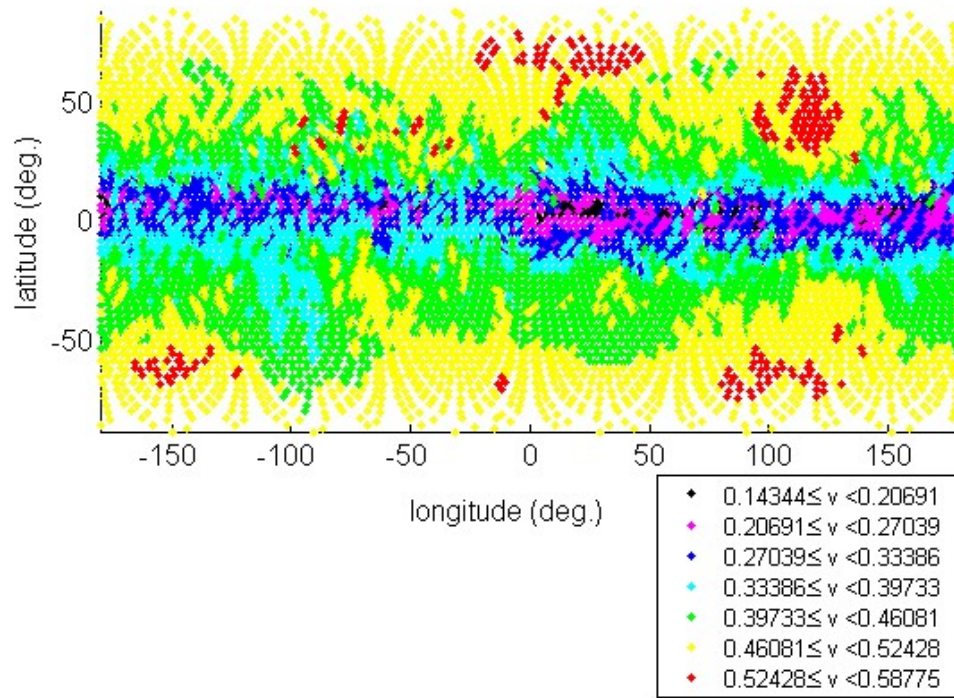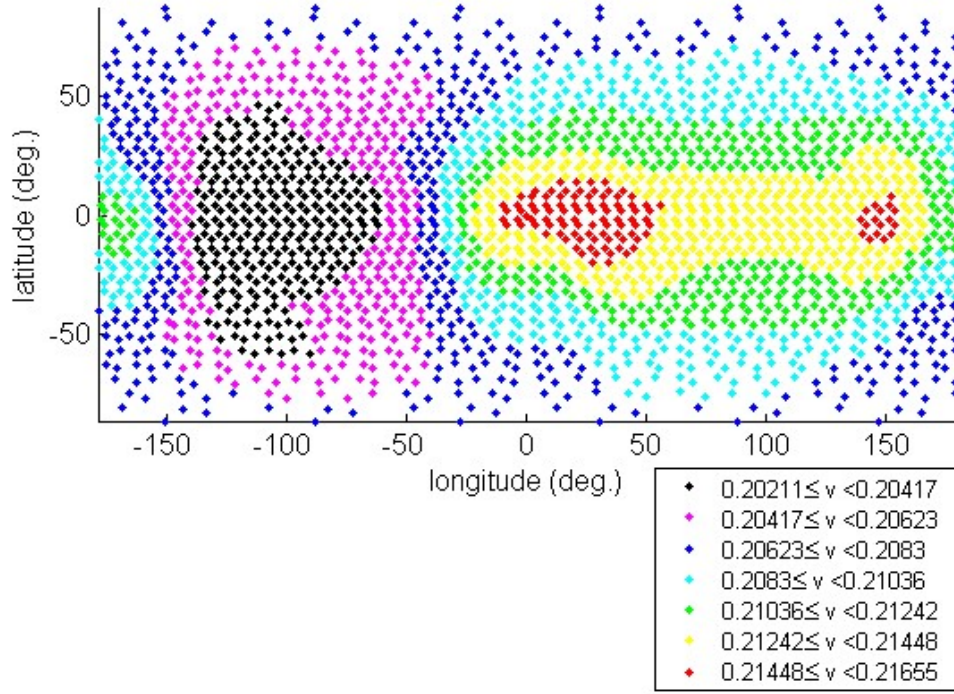
(a) Guaranteed return speed, matching $J_{\mathrm{RSE3BP_{L1}}} = -0.1119978$
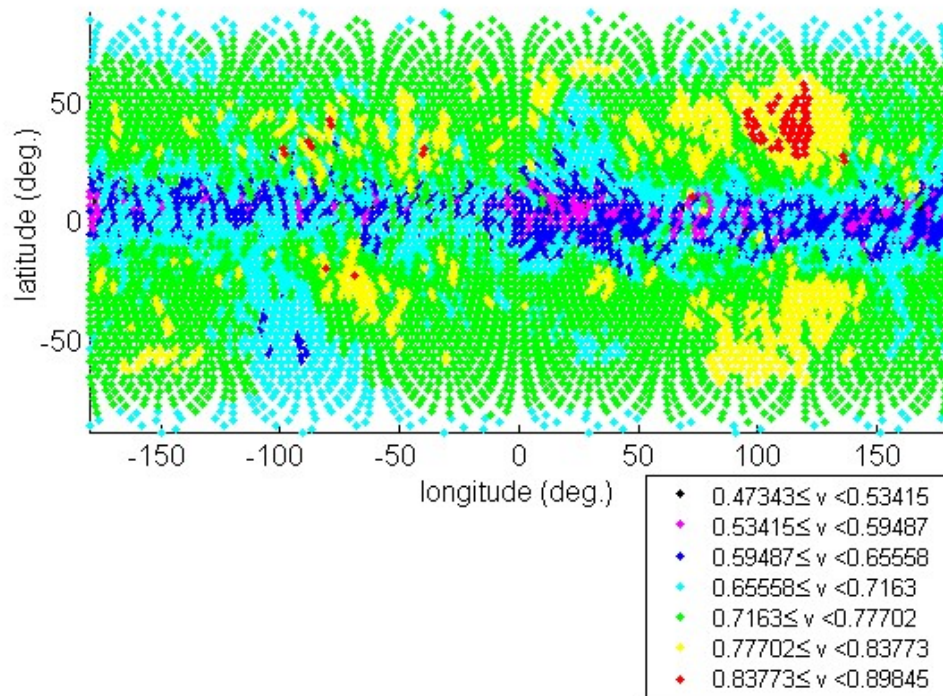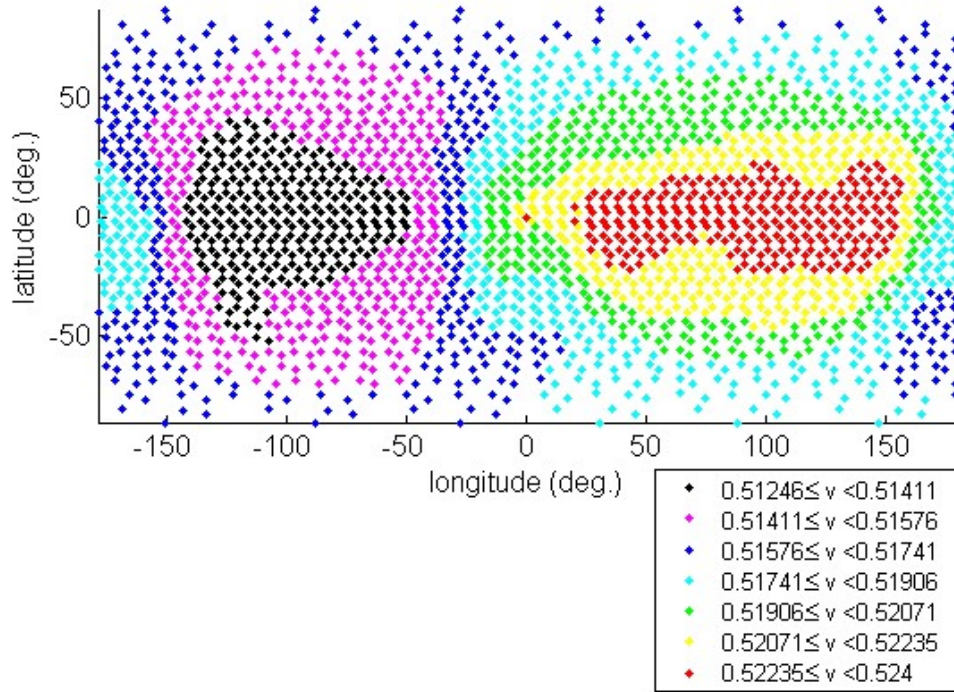

(b) Guaranteed escape speed, matching $J_{\mathrm{RSE3BP_{L1}}} = 0$

Figure B.1: Mapping of surface-normal launch velocity bounds over surface of KW4 Alpha, lat.-long. projection. Velocity units are m/s.

(a) Guaranteed return speed, matching $J_{\mathrm{RSE3BP_{L1}}} = -0.1119978$

(b) Guaranteed escape speed, matching $J_{\mathrm{RSE3BP_{L1}}} = 0$

Figure B.2: Mapping of surface-normal launch velocity bounds over surface of KW4 Beta, lat.-long. projection. Velocity units are m/s.
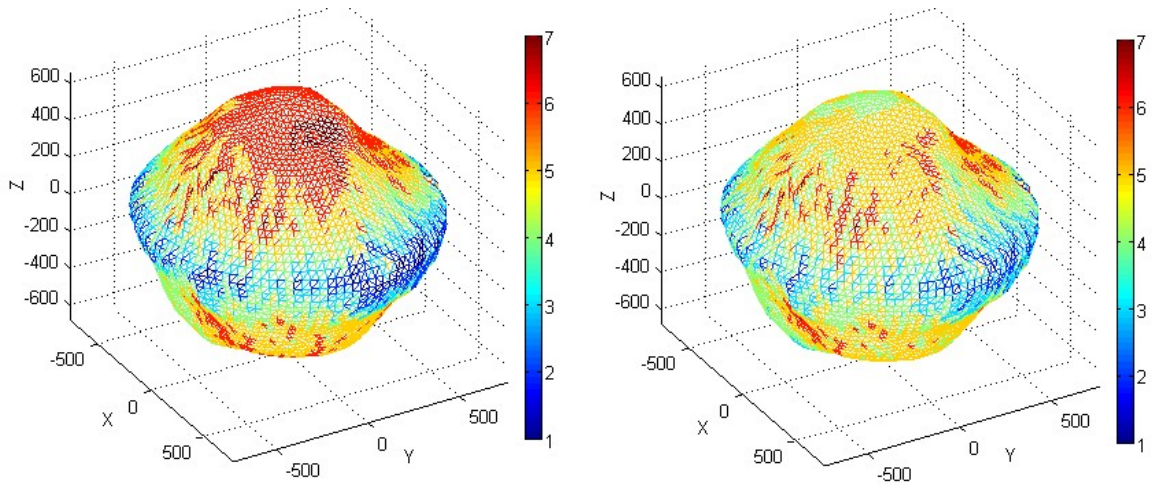
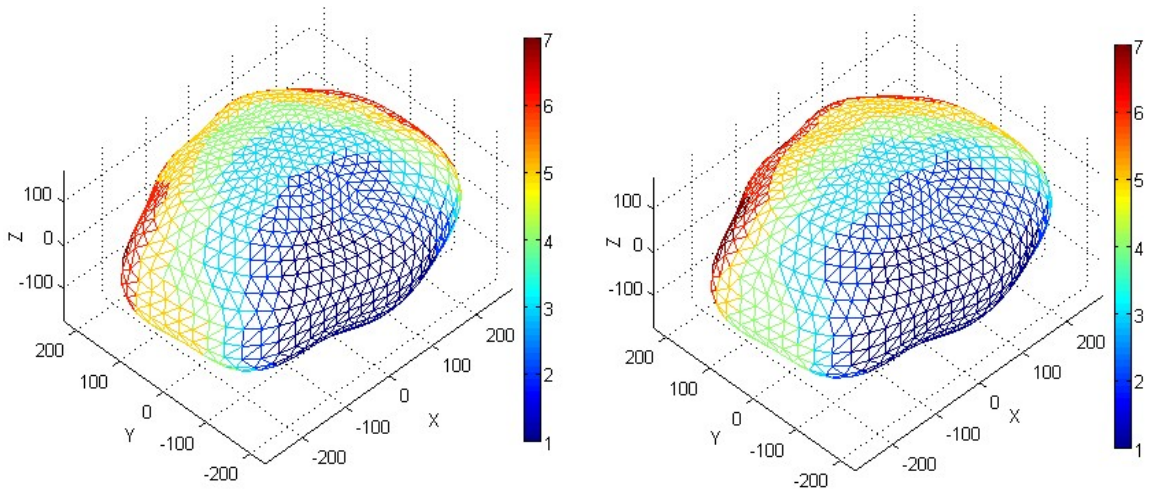(a) Guaranteed return speed, $J_{\mathrm{RSE3BP_{L1}}}$ = -0.1119978

(b) Guaranteed escape speed, $J_{\mathrm{RSE3BP_{L1}}} = 0$

Figure B.3: Mapping of surface-normal launch velocity bounds over surface of KW4 Alpha, isometric view. The numbers on the color scale correspond to the velocity bins in the legend of the matching lat.-long. projection map shown earlier.

(a) Guaranteed return speed, $J_{\mathrm{RSE3BP_{L1}}}$ = -0.1119978

(b) Guaranteed escape speed, $J_{\mathrm{RSE3BP_{L1}}} = 0$

Figure B.4: Mapping of surface-normal launch velocity bounds over surface of KW4 Beta, isometric view. The numbers on the color scale correspond to the velocity bins in the legend of the matching lat.-long. projection map shown earlier.

BIBLIOGRAPHY

[1] Lyon B. King, Gordon G. Parker, Satwik Deshmukh, , and Jer-Hong Chong. Study of interspacecraft coulomb forces and implications for formation flying. *Journal of Propulsion and Power*, 19(3), May 2003.

[2] Lyon B. King, Gordon G. Parker, Satwik Deshmukh, and Jer-Hong Chong. Spacecraft formation-flying using inter-vehicle coulomb forces. Phase I research rep., NASA Institute for Advanced Concepts, Atlanta, GA, January 2002.

[3] Arun Natarajan and Hanspeter Schaub. Linear dynamics and stability analysis of a two-craft coulomb tether formation. *Journal of Guidance, Control, and Dynamics*, 29(4):831–839, 2006.

[4] Ahmed Badawy and Colin R. McInnes. On orbit assembly using superquadric potential fields. *Journal of Guidance, Control, and Dynamics*, 31(1):30–43, 2008.

[5] John Berryman and Hanspeter Schaub. Analytical charge analysis for two- and three-craft coulomb formations. *Journal of Guidance, Control, and Dynamics*, 30(6):1701–1710, 2007.

[6] Eugene G. Fahnestock and Daniel J. Scheeres. Dynamical characterization and stabilization of large gravity tractor designs. *Journal of Guidance, Control, and Dynamics*, 31(3):501–521, 2008.

[7] Bong Wie. Dynamics and control of gravity tractor spacecraft for asteroid deflection. *Journal of Guidance, Control, and Dynamics*, 31(5):1413–1423, 2008.

[8] S. J. Weidenschilling, P. Paolicchi, and V. Zappala. Do asteroids have satellites? In Richard P. Binzel, T. Gehrels, and M.S. Matthews, editors, *Asteroids II*, Space Science Series, pages 653–658. Univ. of Arizona Press, Tucson, 1989.

[9] Clark R. Chapman, J. Veverka, P. C. Thomas, K. Klaasen, M. J. S. Belton, A. Harch, A. McEwen, T. V. Johnson, P. Helfenstein, M. E. Davies, W. J. Merline, and T. Denk. Discovery and physical properties of dactyl, a satellite of asteroid 243 ida. *Nature*, 374:783–785, 1995.

[10] Petr Pravec and G. Hahn. Two-period lightcurve of 1994 aw1: Indication of a binary asteroid? *Icarus*, 127:431–440, 1997.

[11] L.M. Close, W.J. Merline, C. Dumas, C.R. Chapman, F.J. Roddier, F. Ménard, D. Slater, G. Duvert, J. Shelton, and T.H. Morgan. Search for asteroidal satellites using adaptive optics. In P.L. Wizinowich, editor, *Adaptive Optical Systems Technology*, volume 4007 of *Proc. SPIE*, pages 796–802, Bellingham, WA, USA, 2000. SPIE.

[12] W. J. Merline, L. M. Close, C. Dumas, C. R. Chapman, F. Roddier, F. Ménard, D. C. Slater, G. Duvert, C. Shelton, and T. Morgan. Discovery of a moon orbiting asteroid 45 eugenia. *Nature*, 401:565–568, October 1999.

[13] F. Marchis, P. Descamps, D. Hestroffer, J. Berthier, F. Vachier, A. Boccaletti, I. de Pater, and D. Gavel. A three-dimensional solution for the orbit of the asteroidal satellite of 22 kalliope. *Icarus*, 165:112–120, 2003.

[14] Petr Pravec, P. Scheirich, P. Kušnirák, L. Šarounová, S. Mottola, G. Hahn, P. Brown, G. Esquerdo, N. Kaiser, Z. Krzeminski, D. P. Pray, B. D. Warner, A. W. Harris, M. C. Nolan, E. S. Howell, L. A. M. Benner, J.-L. Margot, A. Galád, W. Holliday, M. D. Hicks, Yu. N. Krugly, D. Tholen, R. Whiteley, F. Marchis, D. R. DeGraff, A. Grauer, S. Larson, F. P. Velichko, W.R. Cooney Jr., R. Stephens, J. Zhu, K. Kirsch, R. Dyvig, L. Snyder, V. Reddy, S. Moore, Š. Gajdoš, J. Világi, G. Masi, D. Higgins, G. Funkhouser, B. Knight, S. Slivana, R. Behrend, M. Grenon, G. Burki, R. Roy, C. Demeautis, D. Matter, N. Waelchli, Y. Revaz, A. Klotz, M. Rieugné, P. Thierry, V. Cotrez, L. Brunetto, and G. Kober. Photometric survey of binary Near Earth Asteroids. *Icarus*, 181:63–93, 2006.

[15] L. A. M. Benner, M. C. Nolan, S. J. Ostro, J. D. Giorgini, and J.-L. Margot. 1998 ST27. *IAU Circular*, 2001.

[16] William F. Bottke Jr. and H. J. Melosh. The formation of binary asteroids and doublet craters. *Icarus*, 124:372391, 1996.

[17] William F. Bottke Jr. and H. J. Melosh. The formation of asteroid satellites and doublet craters by planetary tidal forces. *Nature*, 381:5153, 1996.

[18] J. L. Margot, M. C. Nolan, L. A. M. Benner, S. J. Ostro, R. F. Jurgens, J. D. Giorgini, M. A. Slade, and D. B. Campbell. Binary asteroids in the Near-Earth Object population. *Science*, 296:1445–1448, May 2002.

[19] W. J. Merline, S. J. Weidenschilling, D. D. Durda, J. L. Margot, P. Pravec, and A. D. Storrs. Asteroids do have satellites. In William F. Bottke Jr., A. Cellino, P. Paolicchi, and R.P. Binzel, editors, *Asteroids III*, Space Science Series, pages 289–312. Univ. of Arizona Press, Tucson, 2002.

[20] L. A. M. Benner, Michael C. Nolan, Steven J. Ostro, Jon D. Giorgini, Donald P. Pray, Alan W. Harris, Christopher Magri, and Jean-Luc Margot. Near-Earth Asteroid 2005 CR37: Radar images and photometry of a candidate contact binary. *Icarus*, 182:474–481, 2006.

[21] Derek C. Richardson, William F. Bottke Jr., and Stanley G. Love. Tidal distortion and disruption of Earth-crossing asteroids. *Icarus*, 134:47–76, 1998.

[22] K. J. Walsh and D. C. Richardson. Binary Near-Earth Asteroid formation: Rubble pile model of tidal disruptions. *Icarus*, 180:201–216, 2006.

[23] Kieth A. Holsapple and Patrick Michel. Tidal disruptions II. A continuum theory for solid bodies with strength, with applications to the solar system. *Icarus*, 193:283–301, 2008.

[24] Kevin J. Walsh and Derek C. Richardson. Steady-state population of the NEA binaries and YORP spinup models. In *38th Meeting of the AAS Division for Planetary Sciences*, number 53.08, Pasadena, California, USA, October 2006.

[25] David P. Rubincam. Radiative spin-up and spin-down of small asteroids. *Icarus*, 148:2–11, 2000.

[26] D. Vokrouhlický and D. Čapek. YORP-induced long-term evolution of the spin state of small asteroids and meteoroids: Rubincam's approximation. *Icarus*, 159:449–467, 2002.

[27] D. Čapek and D. Vokrouhlický. The YORP effect with finite thermal conductivity. *Icarus*, 172:526–536, 2004.

[28] D. J. Scheeres. The dynamical evolution of uniformly rotating asteroids subject to YORP. *Icarus*, 188:430–450, 2007.

[29] Stephen C. Lowry, Alan Fitzsimmons, Petr Pravec, David Vokrouhlický, Hermann Boehnhardt, Patrick A. Taylor, Jean-Luc Margot, Adrian Galád, Mike Irwin, Jonathan Irwin, and Peter Kušnirák. Direct detection of the asteroidal YORP effect. *Science*, 316:272–274, April 2007.

[30] Patrick A. Taylor, Jean-Luc Margot, David Vokrouhlický, Daniel J. Scheeres, Petr Pravec, Stephen C. Lowry, Alan Fitzsimmons, Michael C. Nolan, Steven J. Ostro, Lance A. M. Benner, Jon D. Giorgini, and Christopher Magri. Spin rate of asteroid (54509) 2000 PH5 increasing due to the YORP effect. *Science*, 316:274–277, April 2007.

[31] William F. Bottke Jr., D. Vokrhouhlický, D. P. Rubincam, and M. Brož. The effect of Yarkovsky thermal forces on the dynamical evolution of asteroids and meteroids. In William F. Bottke Jr., A. Cellino, P. Paolicchi, and R.P. Binzel, editors, *Asteroids III*, Space Science Series, pages 395–408. Univ. of Arizona Press, Tucson, 2002.

[32] D. J. Scheeres. Rotational fission of contact binary asteroids. *Icarus*, 189:370–385, 2007.

[33] D. J. Scheeres, M. Abe, M. Yoshikawa, R. Nakamura, R.W. Gaskell, and P.A. Abell. The effect of YORP on itokawa. *Icarus*, 188:425–429, 2007.

[34] Kevin J. Walsh, Derek C. Richardson, and Patrick Michel. Rotational breakup as the origin of small binary asteroids. *Nature*, 454:188–191, July 2008.

[35] Matija Cuk and Joseph A. Burns. Effects of thermal radiation on the dynamics of binary NEAs. *Icarus*, 176:418–431, 2005.

[36] Matija Cuk. Formation and destruction of small binary asteroids. *The Astrophysical Journal*, 659:L57–L60, April 2007.

[37] C. D. Murray and S. F. Dermott. *Solar System Dynamics*. Cambridge Univ. Press, Cambridge, UK, 1999.

[38] Daniel. J. Scheeres, Eugene G. Fahnestock, and Julie Bellerose. Binary asteroid system dynamics and scientific exploration. In *presented at the 1st International Primitive Body Exploration Working Group (IPEWG) Meeting*, Okinawa, Japan, January14-16, 2008.

[39] Andrzej J. Maciejewski. Reduction, relative equilibria and potential in the two rigid bodies problem. *Celestial Mechanics and Dynamical Astronomy*, 63(1):1–28, 1995.

[40] D. J. Scheeres. Stability in the Full Two-Body Problem. *Celestial Mechanics and Dynamical Astronomy*, 83:155–169, 2002.

[41] D. J. Scheeres. Stability of relative equilibria in the Full Two-Body Problem. In *New Trends in Astrodynamics Conference*, January 2003.

[42] D. J. Scheeres and S. Augenstein. Spacecraft motion about binary asteroids. In *Proc. AIAA/AAS Astrodynamics Specialist Conference*, August 2003.

[43] F. Gabern, Wang S. Koon, and Jerrold E. Marsden. Spacecraft dynamics near a binary asteroid. In *Proceedings of the Fifth International Conference on Dynamical Systems and Differential Equations*, Jun 2004.

[44] D. J. Scheeres and J. Bellerose. The Restricted Hill Full 4-Body Problem: application to spacecraft motion about binary asteroids. *Dynamical Systems: An International Journal*, 20(1):23–44, 2005.

[45] John M. A. Danby. *Fundamentals of Celestial Mechanics*. Willmann-Bell, Richmond, VA, second edition, 1988.

[46] Robert A. Werner and Daniel J. Scheeres. Exterior gravitation of a polyhedron derived and compared with harmonic and mascon gravitation representations of asteroid 4769 Castalia. *Celestial Mechanics and Dynamical Astronomy*, 65(3):313–344, 1997.

[47] N. Borderies. Mutual gravitational potential of N solid bodies. *Celestial Mechanics*, 18(3):295–307, 1978.

[48] C. Von Braun. *The Gravitational Potential of Two Arbitrary, Rotating Bodies with Applications to the Earth-Moon System.* PhD thesis, University of Texas at Austin, 1991.

[49] Helmut Moritz. *Advanced Physical Geodesy.* Abacus Press, 1980.

[50] Paul Geissler, Jean-Marc Petit, Daniel D. Durda, Richard Greenberg, William Bottke Jr., Michael Nolan, and Jeffrey Moore. Erosion and ejecta reaccretion of 243 Ida and its moon. *Icarus*, 120(1):140–157, 1996.

[51] Joshua Ashenberg. Proposed method for modeling the gravitational interaction between finite bodies. *Journal of Guidance, Control, and Dynamics*, 28(4):768–774, 2005.

[52] Robert A. Werner and Daniel J. Scheeres. Mutual potential of homogenous polyhedra. *Celestial Mechanics and Dynamical Astronomy*, 91(3):337–349, March 2005.

[53] Ernst Hairer, Christian Lubich, and Gerhard Wanner. *Geometric Numerical Integration.* Springer, 2000.

[54] J. E. Marsden and M. West. Discrete mechanics and variational integrators. *Acta Numerica*, 10:357–514, 2001.

[55] Arieh Iserles, Hans Z. Munthe-Kaas, Syvert P. Nørsett, and Antonella Zanna. Lie-group methods. *Acta Numerica*, 9:215–365, 2000.

[56] Taeyoung Lee, Melvin Leok, and N. Harris McClamroch. A Lie group variational integrator for the attitude dynamics of a rigid body with application to the 3D pendulum. In *Proceedings of the IEEE Conference on Control Application*, pages 962–967, Toronto, Canada, August 2005.

[57] Taeyoung Lee, Melvin Leok, and N. Harris McClamroch. Lie Group Variational Integrators for the Full Body Problem. *Computer Methods in Applied Mechanics and Engineering*, 196:2907–2924, 2007.

[58] Taeyoung Lee, Melvin Leok, and N. Harris McClamroch. Lie Group Variational Integrators for the Full Body Problem in Orbital Mechanics. *Celestial Mechanics and Dynamical Astronomy*, 98(2):121–144, June 2007.

[59] Donald K. Yeomans and Alan B. Chamberlin. JPL Small-Body Database Browser, September 20, 2008. `http://ssd.jpl.nasa.gov/sbdb.cgi#top`.

[60] L. A. M. Benner, S. J. Ostro, J. D. Giorgini, R. F. Jurgens, J.-L. Margot, and M. C. Nolan. 1999 KW4. *IAU Circular*, 2001.

[61] P. Pravec and L. Šarounová. 1999 KW4. *IAU Circular*, 2001.

[62] Steven. J. Ostro, Jean-Luc Margot, Lance A. M. Benner, Jon D. Giorgini, Daniel J. Scheeres, Eugene G. Fahnestock, Stephen B. Broschart, Julie Bellerose, Michael C. Nolan, Christopher Magri, Petr Pravec, Petr Scheirich, Randy Rose, Raymond F. Jurgens, Eric M. De Jong, and Shigeru Suzuki. Radar imaging of binary Near-Earth Asteroid (66391) 1999 KW4. *Science*, 314:1276–1280, November 2006.

[63] Petr Pravec and Alan W. Harris. Binary asteroid population 1. angular momentum content. *Icarus*, 190:250–259, 2007.

[64] P. Pravec, A.W. Harris, D. Vokrouhlický, B.D. Warner, P. Kušnirák, K. Hornoch, D.P. Pray, D. Higgins, J. Oey, A. Galád, Š. Gajdoš, L. Kornoš, J. Világi, M. Husárik, Yu.N. Krugly, V. Shevchenko, V. Chiorny, N. Gaftonyuk, W.R. Cooney Jr., J. Gross, D. Terrell, R.D. Stephens, R. Dyvig, V. Reddy, J.G. Ries, F. Colas, J. Lecacheux, R. Durkee, G. Masi, R.A. Koff, and R. Goncalves. Spin rate distribution of small asteroids. *Icarus*, 197:497–504, October 2008.

[65] Bernhard Hofmann-Wellenhof and Helmut Moritz. *Physical Geodesy.* Springer-Verlag Wien, 2005.

[66] D. J. Scheeres, Eugene G. Fahnestock, Steven J. Ostro, Jean-Luc Margot, Lance A. M. Benner, Steven B. Broschart, Julie Bellerose, Jon D. Giorgini, Michael C. Nolan, Christopher Magri, Petr Pravec, Petr Scheirich, Randy Rose, Raymond F. Jurgens, Eric M. De Jong, and Shigeru Suzuki. Dynamical configuration of binary Near-Earth Asteroid (66391) 1999 KW4. *Science*, 314:1280–1283, November 2006.

[67] Bret Gladman, D. Dane Quinn, Philip Nicholson, and Richard Rand. Synchronous locking of tidally evolving satellites. *Icarus*, 122:166–192, 1996.

[68] Eugene G. Fahnestock and Daniel J. Scheeres. Dynamical characterization and stabilization of gravity tractor designs for NEO impact risk mitigation. In *2007 Planetary Defence Conference: Protecting Earth from Asteroids*, Washington, DC, March 2007.

[69] Bret Gladman, Patrick Michel, and Christiane Froeschle. The Near Earth Object population. *Icarus*, 146:176–189, 2000.

[70] Daniel J. Scheeres, Steven J. Ostro, R. S. Hudson, and Robert A. Werner. Orbits close to asteroid 4769 castalia. *Icarus*, 121:67–87, 1996.

[71] Daniel J. Scheeres, Steven J. Ostro, R. S. Hudson, Eric M. DeJong, and Shigeru Suzuki. Dynamics of orbits close to asteroid 4179 toutatis. *Icarus*, 132:53–79, 1998.

[72] Julie Bellerose and Daniel J. Scheeres. Stability of equilibrium points in the restricted full three-body problem. *Acta Astronautica*, 60:141–152, 2007.

[73] M. C. Nolan, E. S. Howell, C. Magri, B. Beeney, D. B. Campbell, L. A. M. Benner, S. J. Ostro, J. D. Giorgini, and J.-L. Margot. 2002 BM 26. *IAU Circular*, 2002.

[74] M. C. Nolan, E. S. Howell, and G. Miranda. Radar Images of Binary Asteroid 2003 YT1. In *Bulletin of the American Astronomical Society*, volume 36, pages 1132+, November 2004.

[75] Michael K. Shepard, Jean-Luc Margot, Christopher Magri, Michael C. Nolan, Joshua Schlieder, Benjamin Estes, Schelte J. Bus, Eric L. Volquardsen, Andrew S. Rivkin, , Lance A. M. Benner, Jon D. Giorgini, Steven J. Ostro, and Michael W. Busch. Radar and infrared observations of binary near-Earth Asteroid 2002 CE26. *Icarus*, 184:198–210, 2006.

[76] P. A. Taylor, J. L. Margot, M. C. Nolan, L. A. M. Benner, S. J. Ostro, J. D. Giorgini, and C. Magri. Radar Imaging of Binary Near-Earth Asteroid 2004 DC. In *Bulletin of the American Astronomical Society*, volume 38, pages 577+, September 2006.

[77] L. A. M. Benner, M. W. Busch, M. C. Nolan, S. J. Ostro, J. D. Giorgini, R. Rose, J. S. Jao, G. J. Black, L. M. Carter, M. A. Slade, R. F. Jurgens, and A. A. Hine. Radar Images Of Binary Near-earth Asteroid 2006 VV2. In *AAS/Division for Planetary Sciences Meeting Abstracts*, volume 39, page 432, October 2007.

[78] D. Vokrouhlický and D. Nesvorný. Pairs of asteroids probably of common origin. *The Astronomical Journal*, 136(1):280–290, July 2008. Available: http://www.astro.cz/∼asteroid/paris/material/vokr0221.pdf.

[79] M. C. Nolan, E. S. Howell, L. A. M. Benner, S. J. Ostro, J. D. Giorgini, M. W. Busch, L. M. Carter, R. F. Anderson, C. Magri, D. B. Campbell, J. L. Margot, Jr. R. Vervack, and M. K. Shepard. (153591) 2001 SN263. *IAU Circular*, (8921), 2008.

[80] Alan W. Harris, Eugene G. Fahnestock, and Petr Pravec. On the shapes and spins of "rubble pile" asteroids. *Icarus*, 2008. Available: http://dx.doi.org/10.1016/j.icarus.2008.09.012

[81] D. J. Scheeres. Changes in rotational angular momentum due to gravitational interaction between two finite bodies. *Celestial Mechanics and Dynamical Astronomy*, 81:39–44, 2001.

[82] Daniel J. Scheeres, F. Marzari, and A. Rossi. Evolution of NEO rotation rates due to close encounters with earth and venus. *Icarus*, 170:312–323, 2004.

[83] E. G. Fahnestock, D. J. Scheeres, N. H. McClamroch, and R. A. Werner. Simulation and analysis of binary asteroid dynamics using mutual potential and potential derivatives formulation. In *Proc. AAS/AIAA Astrodynamics Specialist Conference*, Lake Tahoe, CA, August 2005.